

ORE PETROLOGY AND APPLIED MINERALOGY OF THE  
TROUT LAKE MASSIVE SULFIDE DEPOSIT, FLIN FLON, MANITOBA.

by

RAYMOND E. HEALY

A thesis  
presented to the University of Manitoba  
in fulfillment of the  
thesis requirement for the degree of  
MASTER OF SCIENCE  
in  
THE DEPARTMENT OF GEOLOGICAL SCIENCES

Winnipeg, Manitoba

(c) RAYMOND E. HEALY, 1991

 National Library  
of Canada

Bibliothèque nationale  
du Canada

Canadian Theses Service    Service des thèses canadiennes

Ottawa, Canada  
K1A 0N4

The author has granted an irrevocable non-exclusive licence allowing the National Library of Canada to reproduce, loan, distribute or sell copies of his/her thesis by any means and in any form or format, making this thesis available to interested persons.

The author retains ownership of the copyright in his/her thesis. Neither the thesis nor substantial extracts from it may be printed or otherwise reproduced without his/her permission.

L'auteur a accordé une licence irrévocable et non exclusive permettant à la Bibliothèque nationale du Canada de reproduire, prêter, distribuer ou vendre des copies de sa thèse de quelque manière et sous quelque forme que ce soit pour mettre des exemplaires de cette thèse à la disposition des personnes intéressées.

L'auteur conserve la propriété du droit d'auteur qui protège sa thèse. Ni la thèse ni des extraits substantiels de celle-ci ne doivent être imprimés ou autrement reproduits sans son autorisation.

ISBN 0-315-71888-9

Canada

ORE PETROLOGY AND APPLIED MINERALOGY OF THE TROUT LAKE  
MASSIVE SULFIDE DEPOSIT, FLIN FLON, MANITOBA

BY

RAYMOND E. HEALY

A thesis submitted to the Faculty of Graduate Studies of  
the University of Manitoba in partial fulfillment of the requirements  
of the degree of

MASTER OF SCIENCE

© 1991

Permission has been granted to the LIBRARY OF THE UNIVERSITY OF MANITOBA to lend or sell copies of this thesis. to the NATIONAL LIBRARY OF CANADA to microfilm this thesis and to lend or sell copies of the film, and UNIVERSITY MICROFILMS to publish an abstract of this thesis.

The author reserves other publication rights, and neither the thesis nor extensive extracts from it may be printed or otherwise reproduced without the author's written permission.

I hereby declare that I am the sole author of this thesis.

I authorize the University of Manitoba to lend this thesis to other institutions or individuals for the purpose of scholarly research.

RAYMOND E. HEALY

I further authorize the University of Manitoba to reproduce this thesis by photocopying or by other means, in total or in part, at the request of other institutions or individuals for the purpose of scholarly research.

RAYMOND E. HEALY

The University of Manitoba requires the signatures of all persons using or photocopying this thesis. Please sign below, and give address and date.

**DEDICATION**

To family and friends.

## ABSTRACT

The ore mineralogy of the Trout Lake massive sulfide deposit, Flin Flon, Manitoba has been investigated. Nine ore types are defined, of which seven form a differentiation series from the Zn-rich hangingwall ores to the Cu-rich footwall ores. The remaining two ore types are of tectonic origin. Two groups of elements: (1) the Zn-Group (Zn, Cd, Sb, Pb, Ag, Hg, In, Sn and As), and (2) the Cu-Group (Cu, Se, Te, Co and Fe) form the principal geochemical associations of the ores.

Twenty six ore minerals including sulfides, oxides, sulfosalts, sulfantimonides, alloys, intermetallic compounds, tellurides and selenides have been identified. The principal Zn- and Cu-minerals are sphalerite and chalcopyrite, respectively. Twelve Ag-bearing minerals were identified or inferred, of which sulfosalts and tellurides account for <24% of the Ag, Au-Ag-Hg alloy for <19% of the Ag, and galena for 3% of the Ag in the ore. Chalcopyrite, pyrite and sphalerite are inferred to contain 45, 11 and 55ppm Ag, respectively, corresponding to 23, 14 and 19% of the Ag in the ore. The average composition of Au-Ag-Hg alloy (in wt%) is 49.2% Ag, 38.7% Au, 11.0% Hg and 0.70% Fe. 'Invisible' Au in pyrite (0.72ppm Au) and arsenopyrite (30.2ppm Au) account for 6 and 1%, respectively of the Au in the ore; 93% occurs as Au-Ag-Hg alloy.

From image analysis determined grain size data, minimum grinds for liberating sphalerite, chalcopyrite, pyrite, galena and freibergite are calculated as +208um, -175um, -95um, -48um and -60um, respectively. Similarly, the optimum grinds for liberating the above minerals are -52um, -52um, -26um, -9um and -5um, respectively. Predicted minimum liberations are 73% for sphalerite, and 69% for chalcopyrite.

Two textural types of Au-Ag-Hg alloy are recognized: (1) inclusions, grain coatings on, interstitial-fillings and fracture-fillings in, pyrite; and (2) large (<5mm) anastomosing masses. The losses of Au to the tailings are due largely to extremely fine-grained Type 1 Au-Ag-Hg alloy entrapped in pyrite (64%), and Au in solid solution in pyrite and arsenopyrite (36%). The principal Ag losses to the tailings are largely due to Ag in solid solution in pyrite, and poor recovery of pyrargyrite. The environmentally hazardous elements As and Hg are largely rejected to the tailings, and backfilled underground.

Chalcopyrite Stringer and Disseminated Pyrite + Chalcopyrite ore types represent tectonically flattened feeder pipe mineralization. Vein Quartz + Chalcopyrite ore type is evidence of limited sulfide mobilization during metamorphism. Diablastic texture, characterized by myrmekitic intergrowths of chalcopyrite, sphalerite and pyrrotite was produced by a quartz-diorite intrusion of the large Lens 2 of north zone. This texture is not amenable to grinding, and may yield middling particles of chalcopyrite and sphalerite, which will be recovered in the Cu-concentrate.

## ACKNOWLEDGEMENTS

Initially I wish to thank Dr. D. G. W. Smith for his instruction in determinative mineralogical techniques, and his support and recommendation as a referee, without all of which none of the following would have been possible.

Special thanks are extended to Dr. W. Petruk who has provided essential direction and insight into the study, and for making the image analysis system at CANMET available for this study. I am particularly indebted to Dr. Petruk for the many discussions in which he related his wealth of experience in this field of applied research. As co-author of published and unpublished reports and papers which form the kernel of this study, Dr. Petruk has contributed substantially to the scientific content of the thesis.

Prof. A. Turnock is gratefully thanked for his continued and unyielding support, enthusiasm and suggestions throughout the duration of the project. Drs. Lee Groat and Mati Raudsepp are thanked for their assistance and expertise on the mainframe computer at the University of Manitoba. In particular, I wish to thank Mati Raudsepp for his friendship, discursiveness and 'esprit de corps' as a fellow researcher. Ron Chapman is thanked for his patience in familiarizing me with the Mac V and the Cameca SX-50 electron microprobes. The staff members of the Dept. of Geological Sciences at the University of Manitoba are thanked for their encouragement and friendship. In particular, Profs.

A. C. Turnock, P. Cerny, N. Halden, G. S. Clark and F. C. Hawthorne are acknowledged for the enthusiasm they have shown in developing a research environment that fosters continued growth in applied mineralogy.

The staff at Hudson Bay Mining & Smelting Co. Ltd. are thanked for their technical assistance, enthusiasm and affability. In particular, I am grateful to Choong Ko for his assistance and geological expertise above and below the ground. Bernard Barlin, Brian Krysa, Norm McEachern and Karl Hoover are gratefully acknowledged for their contributions through technical assistance and fruitful discussion.

Drs. A. Turnock, N. Halden and W. Petruk are thanked for their insightful comments on, and editorial contributions to, early drafts of the thesis. The editorial contributions of the many referees who critically reviewed early manuscripts of the published reports and papers that comprise much of thesis are also gratefully acknowledged.

The study was in funded by a grant to Hudson Bay Mining & Smelting Co. Ltd. from the Federal Government of Canada via the 1984 CANADA - MANITOBA MINERAL DEVELOPMENT AGREEMENT.

## SYMBOLS AND ABBREVIATIONS

---

Acan	acanthite	Gal	galena
Asp	arsenopyrite	Gud	gudmundite
Boul	boulangerite	Hess	hessite
Bour	bournonite	Mag	magnetite
Cl	clausthalite	Ma	marcasite
Cst	cassiterite	Nau	naumannite
Cos	costibite	Pil	pilsenite
Cp	chalcopyrite	Po	pyrrhotite
Cub	cubanite	Py	pyrite
Dys	dyscrasite	Pyr	pyrargyrite
El	Au-Ag-Hg alloy	Ru	rucklidgeite
Fr	freibergite	Sp	sphalerite
Frs	freieslebenite	Vol	volynskite

---

Gan	gangue	um	micrometer
Qtz	quartz	mm	millimeter
Carb	carbonate	cm	centimeter
Bt	biotite	m	meter
Chl	chlorite	ppm	parts per million
PGE	Platinum group element	wt%	weight %
PGM	Platinum group mineral	at%	atomic %
Iss	Intermediate solid solution	vol%	volume %

---

EMPA	Electron microprobe analysis	Eo	Excitation voltage
IA	Image analysis	Sc	Sample current
EDS	Energy dispersive system	nA	Nanoamperes
EDA	Energy dispersive analysis	kV	Kilovolts
WDS	Wavelength dispersive system	eV	Electron volts
WDA	Wavelength dispersive analysis	ROI	Region of interest
BSE	Backscattered electron	StD	Standard deviation
SEM	Scanning electron microscopy	Z	Average atomic number
SIMS	Secondary ion mass spectrometry		
UoM	University of Manitoba		
MicroPIXE	Micro proton induced X-ray excitation		

---

## CONTENTS

DEDICATION . . . . .	iv
ABSTRACT . . . . .	v
ACKNOWLEDGEMENTS . . . . .	vi
SYMBOLS AND ABBREVIATIONS . . . . .	viii

<u>Chapter</u>	<u>page</u>
I. INTRODUCTION . . . . .	1
II. DISCOVERY, DEVELOPMENT AND PRODUCTION . . . . .	6
III. GEOLOGY . . . . .	11
IV. METHODS OF INVESTIGATION . . . . .	16
SAMPLING . . . . .	16
PETROGRAPHIC ANALYSIS . . . . .	20
MICROPROBE ANALYSIS . . . . .	20
CHEMICAL ANALYSES . . . . .	23
IMAGE ANALYSIS . . . . .	27
V. CLASSIFICATION OF ORES: ORE TYPES . . . . .	30
GENERAL CHARACTERISTICS . . . . .	30
DETAILED CHARACTERISTICS . . . . .	43
MASSIVE SPHALERITE ORE TYPE . . . . .	43
MASSIVE PYRITE ORE TYPE . . . . .	49
LAYERED PYRITE + SPHALERITE ORE TYPE . . . . .	53
MIXED/LAYERED CHALCOPYRITE + SPHALERITE ORE TYPE . . . . .	59
MASSIVE CHALCOPYRITE + PYRRHOTITE ORE TYPE . . . . .	65
CHALCOPYRITE STRINGER ORE TYPE . . . . .	69
DISSEMINATED PYRITE + CHALCOPYRITE ORE TYPE . . . . .	76
SHEARED CHALCOPYRITE + SPHALERITE ORE TYPE . . . . .	82
VEIN QUARTZ + CHALCOPYRITE ORE TYPE . . . . .	89
VI. CHARACTERISTICS OF THE ORE MINERALS . . . . .	92
SULFIDES . . . . .	92
PYRITE . . . . .	92
MARCASITE . . . . .	95
PYRRHOTITE . . . . .	95
CHALCOPYRITE . . . . .	100
CUBANITE . . . . .	103

GALENA . . . . .	103
SPHALERITE . . . . .	105
ACANTHITE . . . . .	114
SULFARSENIDES . . . . .	115
ARSENOPYRITE . . . . .	115
OXIDES . . . . .	118
MAGNETITE . . . . .	118
CASSITERITE . . . . .	121
SULFOSALTS . . . . .	121
FREIBERGITE . . . . .	121
PYRARGYRITE . . . . .	126
BOULANGERITE . . . . .	126
FREIESLEBENITE . . . . .	127
BOURNONITE . . . . .	132
SULFANTIMONIDES . . . . .	132
GUDMUNDITE . . . . .	132
COSTIBITE . . . . .	135
ALLOYS AND INTERMETALLIC COMPOUNDS . . . . .	135
Au-Ag-Hg ALLOY . . . . .	135
Grain Size Distribution of Au-Ag-Hg Alloy . . . . .	137
Chemical Composition of Au-Ag-Hg Alloy . . . . .	140
The Ag-Au-Hg Ternary System . . . . .	142
Zoning and Distribution of Type 2 Au-Ag-Hg Alloy . . . . .	144
DYSCRASITE . . . . .	152
TELLURIDES . . . . .	153
HESSITE . . . . .	153
PILSENITE . . . . .	156
RUCKLIDGEITE . . . . .	158
VOLYNSKITE . . . . .	161
SELENIDES . . . . .	163
CLAUSTHALITE-GALENA SOLID SOLUTION . . . . .	163
NAUMANNITE . . . . .	169
<b>VII. GEOCHEMISTRY AND METAL ACCOUNTING . . . . .</b>	<b>174</b>
CORRELATION ANALYSIS . . . . .	180
THE Zn-GROUP (HANGINGWALL ASSOCIATION) . . . . .	187
THE Cu-GROUP (FOOTWALL ASSOCIATION) . . . . .	191
FACTOR ANALYSIS . . . . .	194
INVISIBLE GOLD . . . . .	204
DISTRIBUTIONS OF Au-Ag-Hg ALLOY AND OF INVISIBLE GOLD . . . . .	206
SUMMARY . . . . .	210
<b>VIII. DISCUSSION . . . . .</b>	<b>215</b>
PREDICTION OF MINERAL LIBERATIONS . . . . .	215
ORE TEXTURES AND METAMORPHISM . . . . .	224
RELICT TEXTURES . . . . .	226
CHANGES IN MINERALOGY DUE TO METAMORPHISM . . . . .	228
Inversion . . . . .	228
Exsolution . . . . .	229
Composition . . . . .	231
Replacement . . . . .	233

CHANGES IN FABRIC DUE TO METAMORPHIC RECRYSTALLIZATION . . . . .	237
CHANGES IN FABRIC DUE TO DEFORMATION . . . . .	241
SULFIDE MOBILIZATION . . . . .	248
Au-Ag-Hg Alloy and the Transport of Gold, Silver and Mercury . . . . .	249
<b>IX. CONCLUSIONS . . . . .</b>	<b>260</b>

<b>BIBLIOGRAPHY . . . . .</b>	<b>277</b>
-------------------------------	------------

<u>Appendix</u>	<u>page</u>
A. SAMPLE LOCATIONS AND DESIGNATED ORE TYPES . . . . .	287
B. GRAIN SIZE DISTRIBUTIONS OF THE MINERALS OF INTEREST . . . . .	290
C. CHEMICAL COMPOSITION (MICROPROBE DATA) OF SPHALERITE IN UNBROKEN ORE SAMPLES . . . . .	295
D. CHEMICAL COMPOSITION (MICROPROBE DATA) OF SPHALERITE IN THE FLOTATION FEED . . . . .	297
E. AU AND AS CONCENTRATIONS IN PYRITE (SIMS DATA) FROM THE TROUT LAKE CONCENTRATOR TAILINGS . . . . .	299
F. AU CONCENTRATIONS IN ARSENOPYRITE (SIMS DATA) IN THE TROUT LAKE FLOTATION TAILINGS . . . . .	300
G. CHEMICAL COMPOSITION (MICROPROBE DATA) OF FREIBERGITE . . . . .	301
H. CHEMICAL COMPOSITION (MICROPROBE DATA) OF AU-AG-HG ALLOY . . . . .	302
I. CHEMICAL COMPOSITION (MICROPROBE DATA) OF AU-AG-HG ALLOY IN TLN.1-89I . . . . .	304
J. CHEMICAL COMPOSITION (MICROPROBE DATA) OF SPHALERITE AND GALENA-CLAUSTHALITE IN TLN.1-87 . . . . .	305
K. LETTER OF WAIVER OF COPYRIGHT FROM DR. W. PETRUK . . . . .	308

## LIST OF TABLES

<u>Table</u>	<u>page</u>
1. Grades and Tonnages of the Six Proven Ore Lenses . . . . .	9
2. Trout Lake Production and Reserves as of January 1st 1986 . . .	10
3. Trout Lake Circuit Balance on February 5th 1986 . . . . .	10
4. Ore Minerals Identified in the Trout Lake Ores . . . . .	22
5. Precision and Accuracy Tests of the Chemical Analyses . . . . .	26
6. List of Ore Types Defined at Trout Lake . . . . .	32
7. The Chemical Composition of the 27 Representative Ore Samples . . . . .	33
8. Mineral Quantities (in wt%) of the 27 Representative Ore Samples . . . . .	34
9. Average Chemical Compositions of Each Ore Type . . . . .	35
10. Partial Chemical Compositions of the Ore Samples Calculated from Mineralogical Compositions . . . . .	36
11. Average Mineral Quantities for Each Ore Type . . . . .	39
12. Interpreted Mineralogical Composition of the Ore Types . . . . .	40
13. Representative Chemical Compositions (Microprobe Data) of Pyrrhotite . . . . .	97
14. Representative Chemical Compositions (Microprobe Data) of Sphalerite . . . . .	108
15. Representative Chemical Compositions (Microprobe Data) of Arsenopyrite . . . . .	117
16. Representative Chemical Compositions (Microprobe Data) of Magnetite . . . . .	120
17. Representative Chemical Compositions (Microprobe Data) of Freibergite . . . . .	124
18. Chemical Compositions (Microprobe Data) of Freieslebenite . .	129

19.	Chemical Compositions (Microprobe Data) of Gudmundite . . . . .	134
20.	Representative Compositions (Microprobe Data) of Au-Ag-Hg Alloy. . . . .	145
21.	Chemical Compositions (Microprobe Data) of Au-Ag-Hg Alloy in Section TLN.1-89i. . . . .	149
22.	Chemical Compositions (Microprobe Data) of Hessite . . . . .	155
23.	Chemical Compositions (Microprobe Data) of Pilsenite(?) . . . . .	157
24.	Chemical Compositions (Microprobe Data) of Rucklidgeite . . . . .	160
25.	Chemical Compositions (Microprobe Data) of Volynskite . . . . .	162
26.	Chemical Compositions (Microprobe Data) of Clausthalite-Galena from TLS.3-47 . . . . .	165
27.	Basic Statistical Parameters of the Element Distributions . . . . .	176
28.	Correlation Coefficient Matrix of the Chemical Analyses . . . . .	183
29.	Correlation Coefficient Matrix of the Chemical Analyses . . . . .	184
30.	Coherence of the Geochemical Associations . . . . .	186
31.	Principal Factor Matrix of the Chemical Analyses . . . . .	196
32.	Prinicpal Factor Matrix of the Chemical Analyses . . . . .	197
33.	Bulk Au Assays, Modal Quantities and Au Assays Assigned to Pyrite, Asrenopyrite and Au-Ag-Hg Aloy . . . . .	208
34.	Minimum and Optimum Grinds for the Minerals of Interest . . . . .	219

## LIST OF FIGURES

<u>Figure</u>	<u>page</u>
1. Location Map of the Proterozoic Flin Flon - Snow Lake Greenstone Belt. . . . .	8
2. A Schematic Zonation of the Six Proven Trout Lake Ore Lenses. . . . .	15
3. Idealized Longitudinal Vertical Projection of the North Zone. . . . .	18
4. Idealized Longitudinal Vertical Projection of the South Zone. . . . .	19
5. Sphalerite-Chalcopyrite-Pyrrhotite+Pyrite Triangular Diagram. . . . .	41
6. Triangular Diagram of Bulk Chemical Compositions in the Zn-Cu-Fe System. . . . .	42
7. Grain Size Distributions in the Massive Sphalerite Ore Type. . . . .	47
8. PLATE OF PHOTO-MICROGRAPHS. . . . .	48
9. Grain Size Distributions in the Massive Pyrite Ore Type. . . . .	52
10. Grain Size Distributions in the Layered Pyrite + Sphalerite Ore Type. . . . .	56
11. PLATE OF PHOTO-MICROGRAPHS. . . . .	57
12. Grain Size Distributions in the Mixed/Layered Chalcopyrite + Sphalerite Ore Type. . . . .	62
13. PLATE OF PHOTO-MICROGRAPHS. . . . .	63
14. Grain Size Distributions in the Massive Chalcopyrite + Pyrrhotite Ore Type. . . . .	68
15. Grain Size Distributions in the Chalcopyrite Stringer Ore Type. . . . .	73
16. PLATE OF PHOTO-MICROGRAPHS. . . . .	74

17.	Grain Size Distributions in the Disseminated Pyrite + Chalcopyrite Ore Type. . . . .	79
18.	PLATE OF PHOTO-MICROGRAPHS. . . . .	80
19.	Grain Size Distributions in the Sheared Chalcopyrite + Sphalerite Ore Type. . . . .	86
20.	PLATE OF PHOTO-MICROGRAPHS. . . . .	87
21.	Grain Size Distributions in the Vein Quartz + Chalcopyrite Ore Type. . . . .	91
22.	Histograms of Au Concentrations in Arsenopyrite and Au and As Concentrations in Pyrite. . . . .	94
23.	PLATE OF PHOTO-MICROGRAPHS. . . . .	98
24.	Cumulative Grain Size Curves of Chalcopyrite and Sphalerite in each of the Nine Ore Types. . . . .	102
25.	PLATE OF PHOTO-MICROGRAPHS. . . . .	110
26.	PLATE OF PHOTO-MICROGRAPHS. . . . .	112
27.	PLATE OF PHOTO-MICROGRAPHS . . . . .	130
28.	PLATE OF PHOTO-MICROGRAPHS. . . . .	138
29.	Histograms of the Grain Size Distributions of Au-Ag-Hg Alloy. . . . .	141
30.	Histograms of Au, Ag, Hg and Fe Concentrations in Trout Lake Au-Ag-Hg Alloy. . . . .	146
31.	Schematic Isothermal Section of the Au-Ag-Hg Ternary System (in wt%). . . . .	147
32.	Element Concentration Profiles Across Type 2 Au-Ag-Hg Alloy. .	150
33.	PLATE OF PHOTO-MICROGRAPHS. . . . .	171
34.	Histogram of Se Concentrations in Clausthalite-Galena Solid Solution. . . . .	173
35.	Scatter Diagrams of Selected Element Pairs from the Chemical Analyses. . . . .	178
36.	Scatter Diagrams of Selected Element Pairs from the Chemical Analyses. . . . .	179
37.	Mineralogical Department of Gold in a Sample of Trout Lake Concentrator Tailings. . . . .	209

38.	Average Grain Size Distributions for Trout Lake Minerals of Interest. . . . .	218
39.	Grain Size Distributions of Minerals of Interest in TLS.5-64. . . . .	223
40.	Possible Pathways of Compositional Evolution of Paragenetically Latest Au-Ag-Hg Alloy. . . . .	254

## Chapter I

### INTRODUCTION

Volcanogenic massive sulfide deposits constitute one of the principal sources of the metals Cu, Zn, Pb, Ag, Au and Cd. In addition, the elements Co, Ni, As, Se, Sn, In, Sb, Te, Hg and Bi may be present in significant concentrations, such that they are economically recoverable as by-products, or strongly influence the processing of the ores from a mineral beneficiation, metallurgical or environmental standpoint (Chen & Petruk 1980, Petruk 1985). Typically Fe is the most abundant metal in these deposits and principally occurs in pyrite or pyrrhotite, both of which constitute economically unrecoverable forms of that metal. These polymetallic ores are commonly fine-grained, texturally complex and are often referred to as complex sulfide ores (Petruk 1985).

The initial step in the processing of complex sulfide ores involves mineral beneficiation, whereby the ores undergo grinding to liberate the valuable mineral(s), and concentrating these minerals into mineral-specific products termed concentrates. Ideally, such a concentrate consists of a specific mineral or minerals, with the minimum of dilution or contamination from other minerals present in the ore. This can only be achieved if the mineral(s) of interest occur as free grains or in composite particles with minimal amounts of other minerals (Petruk 1984). It therefore becomes critical during processing that the mineral(s) of interest occur predominantly as free grains and that these

grains are preferentially concentrated in a given product. Thus, the ability of even the most efficient processing plant to produce high grade concentrates with simultaneously high metal recovery hinges on the degree of liberation of the mineral(s) of interest.

Optimum plant efficiency can only be achieved by maximizing the recovery of free grains (Petruk 1984). However, analytical chemistry, the conventional method of evaluating metallurgical products from ore processing plants, fails to address the mineralogical nature of the material, and its control on the chemistry of the products. Critical information pertaining to mineral composition, mode of occurrence, particle size and degree of liberation of the mineral(s) of interest remains neglected or undetermined (Ahlrichs 1984). Because mineral processing operates by exploiting the physico-chemical characteristics of the ore minerals, and not that of their contained metals, 'Applied' or 'Process' Mineralogy is gaining recognition as an integral component in the overall process of extracting metals from ore. In the present highly competitive world market, and with the need to work progressively lower grade and mineralogically complex deposits, with the additional need to select processes that are sensitive to the environment, the procurement of mineralogical control on process selection, design, monitoring, evaluation and optimization is essential to economic viability and sustainable development.

Process mineralogy utilizes advanced analytical techniques such as electron microprobe analysis (EMPA), image analysis (IA) and secondary ion mass spectrometric (SIMS) analysis in order to understand, evaluate, optimize and diversify industrial processes. Two of the more important

types of process mineralogical studies are: (1) assess ore and predict it's behaviour during processing; and (2) examine it's behaviour in existing plants, and hence evaluate process performance.

The objective of 'ore assessment' is to determine the mineralogical characteristics of the ore that affect the behaviour of the valuable minerals, and hence metals, during beneficiation. Thus, mineral and metal behaviour during beneficiation can be predicted, the potential viability of a deposit can be assessed, and applicable processes and optimum circuit configuration can be selected. Some of the key factors considered include: (1) grinding characteristics; (2) ore mineral identification, chemistry and quantities; (3) grain size and degree of intergrowth of the ore minerals; (4) host mineralogy of the precious metals or PGE's, and their amenability to recovery; (5) occurrence of minerals that are likely to interfere with the process; and (6) heterogeneity of the ore, and problems likely to be encountered when processing specific ore types, lenses or veins. These data are also critical to understanding laboratory bench tests that precede process selection and design and plant production or modification.

The objective of 'process evaluation' is to examine the behaviour of minerals through circuits, by material balance modelling any specific category of mineral or particle (e.g., free grains of sphalerite) through the circuit under simulated steady-state conditions. Thus, circuit performance can be quantitatively modelled and the distribution process parameters or variables (e.g., chemical assays, mineral abundances, grain sizes and liberations) can be assessed. Problem areas in circuit performance can thus be identified, and remedial actions can

be proposed such as: (1) pre-concentration; (2) adjust grinding conditions; (3) selection of regrind; (4) optimum reagent conditions; and (5) others. Such studies may be undertaken for circuit optimization, periodic monitoring or trouble shooting on a 'one of a kind' basis. Importantly, process optimization not only aims at improving metal recoveries, but also in reducing process costs and environmentally hazardous emissions.

A research project entitled "The mineralogical characteristics that affect metal recoveries from the Cu, Zn, Pb and Ag ores from Manitoba" was established under the auspices of 1984 CANADA-MANITOBA MINERAL DEVELOPMENT AGREEMENT. The objective of the project was to establish whether the volcanogenic massive sulfide deposits of Manitoba contain unique mineralogical characteristics, and to determine whether these characteristics can be utilized to modify metallurgical practises, so that recovery could be optimized. The first deposit selected for study was the Trout Lake mine. Trout Lake was selected because: (1) it is the richest deposit in the Flin Flon - Snow Lake mining camp; (2) the Cu-concentrate commonly assays 5 wt% Zn, corresponding to losses of 15% Zn; (3) approximately 30% of the Au and of the Ag are lost to the tailings; and (4) the ore is processed in a separate, dedicated concentrator circuit, permitting direct translation of mineralogical data from the ore to the plant environment. The Trout Lake deposit consists of complex sulfide ores that contain economically recoverable quantities of the metals Cu, Zn, Au, Ag, Pb and Cd.

The study was divided into two parts: Part 1, to define the mineralogical characteristics that could have a bearing on mining and

mineral processing (Healy & Petruk 1988), and Part 2, a mineralogical study of the behaviour of the minerals in the concentrator (Healy & Petruk 1989). Part 1 involved collecting a representative suite of samples from the deposit, fitting them into a classification based largely on that developed by the mine geologist, and characterizing the ore from each classification. The ore characterization involved identifying the minerals, determining mineral quantities, determining the average chemical composition, defining the host mineral(s) for each element of interest, determining the size distribution of the minerals in the unbroken ore, and noting mineral textures that might have a bearing on mineral beneficiation. Importantly, although this study defines mineralogical characteristics that affect processing, many of these same characteristics also provide fundamental information on ore genesis. This thesis is a synthesis of several reports and papers that were done under Part 1 of the study (Healy & Petruk 1988, 1990a, 1990b, In Prep.), and additionally incorporates some of the findings of Part 2 where these superscede those of Part 1.

## Chapter II

### DISCOVERY, DEVELOPMENT AND PRODUCTION

The Trout Lake deposit is located 5km northeast of Flin Flon (Fig. 1). The deposit was discovered by Granges Exploration in the winter of 1976 during a diamond drilling follow-up program to airborne and ground geophysical surveys (Muzylowski 1979). The mine is a joint venture of Hudson Bay Mining & Smelting Co. Ltd. (HBM&S), Granges Exploration, Manitoba Mineral Resources and Outokumpu Oy. The mine was brought into production by HBM&S (operator) in 1982 at a cost of \$30.3 million (Duval 1985). As of the 1st of January 1986 six lenses had been proven and developed, the grades and tonnages of which are given in Table 1

Because the mine underlies Trout (Embury) Lake it is accessed by a decline, and uses largely trackless vehicles. These include 40 ton Toro ore trucks, which haul the ore to the primary crusher just below the surface. From here the minus 6 inch ore is conveyed to two 300 ton ore bins in the load-out building on surface, from where trucks haul it to Flin Flon. Further proven and probable ore has been delineated at depth necessitating a \$20 million shaft development to the 560 m level, with hoisting of ore to start in 1991. The operation presently produces approximately 3,400 ton per day, and employs a mechanized 'Cut and Fill' mining method. Mining costs are approximately \$19 per ton, and average productivity is 4.2 tons per manhour, making Trout Lake one of the lowest-cost, and the most productive underground base metal mines in the

world (Yungwirth 1988). Based on the average metal content per ton, and average market price received in 1988 (Inspiration Resources 1989), it is apparent that the 'simplified market value' of \$152 greatly exceeds the combined mining (approximately \$19) and processing (approximately \$10) costs per ton, making Trout Lake one of HBM&S' most lucrative operations.

To simplify accounting with its partners in the Trout Lake Joint Venture, HBM&S process the ore in a separate concentrator circuit in their concentrator-smelter complex in Flin Flon. The ore is crushed to minus 1.75 inch and fed to the rod mill and ball mill in a closed circuit configuration (Wells 1985). The grind is generally set at 60 to 65% minus 325 mesh (43um), and after reagent conditioning is fed to the head of the flotation circuit. HBM&S practise standard flotation, with chalcopyrite recovery in the Cu-circuit, followed by  $\text{CuSO}_4$  activation and recovery of sphalerite in the Zn-circuit. A secondary ball mill is used to regrind one of several streams so as to increase liberation at those points in the circuit. Both the Cu- and the Zn-concentrates are combined with the corresponding concentrates from the main HBM&S circuit, which presently processes ore from the Callinan mine, and are fed to the Cu-Smelter and Zinc Plant, respectively. The circuit tailings are trucked back to the mine for use as hydraulic backfill. The combined production and ore reserves, and the remaining proven ore reserves as of January 1st 1986 (Ko, 1986) are presented in Table 2. The concentrate and tailings grades and the metal recoveries are presented in Table 3.

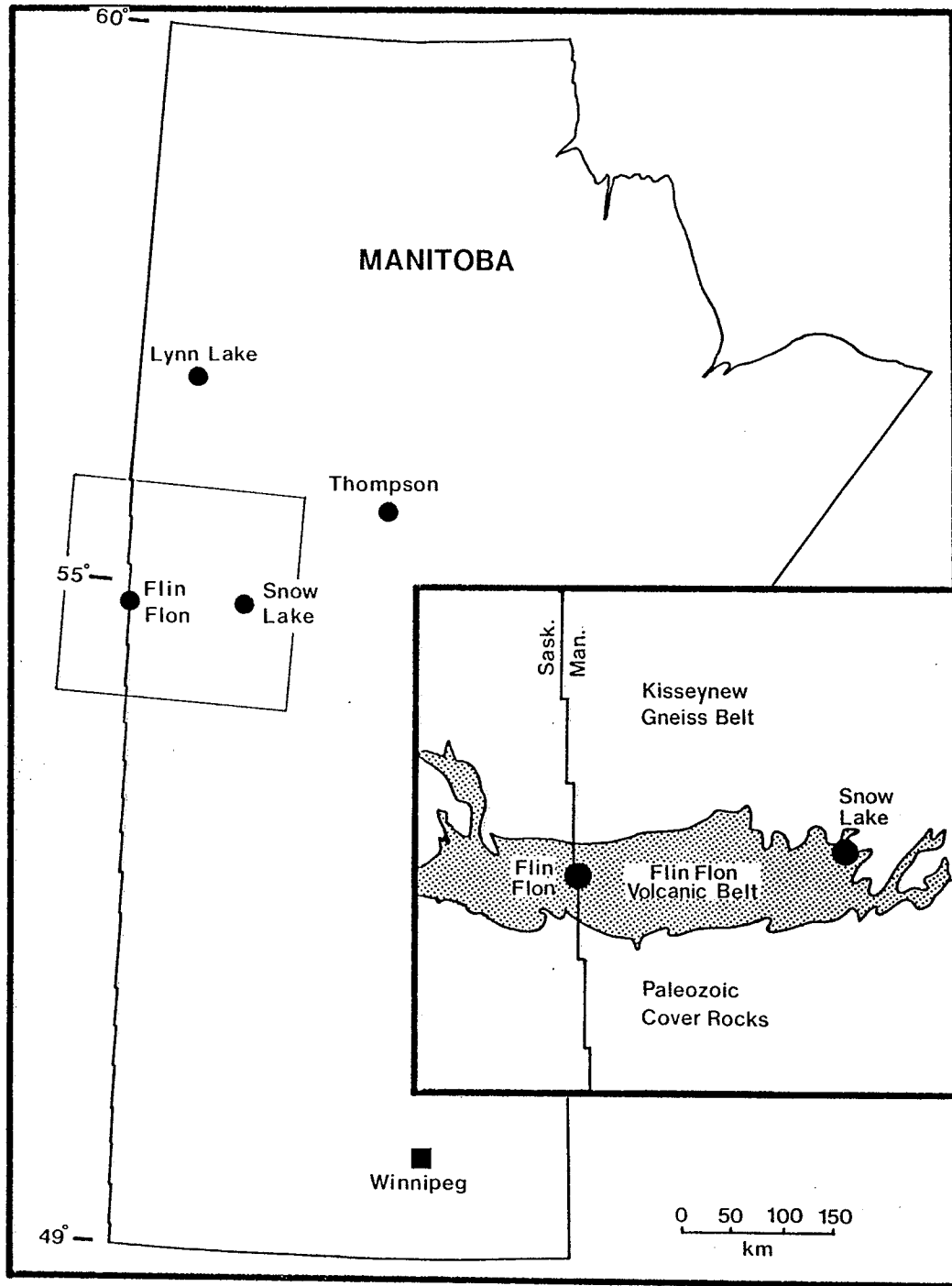


Figure 1: Location Map of the Proterozoic Flin Flon - Snow Lake Greenstone Belt. The insert shows the location of the Flin Flon and Snow Lake mining camps within the east-west trending greenstone belt, which straddles the Manitoba - Saskatchewan border. Redrawn from Ko (1986).

TABLE 1

## Grades and Tonnages of the Six Proven Ore Lenses

Lense	Tonnage (1000's)	Au Grade (ppm)	%	Ag Grade (ppm)	%	Cu Grade (wt%)	%	Zn Grade (wt%)	%
North Zone									
No. 1 Lens	487	1.303	6.	13.03	6.	2.22	8.	4.0	6.
No. 2 Lens	2213	2.367	48.	17.49	39.	2.69	41.	7.4	47.
South Zone									
No. 1 Lens	1098	1.715	17.	18.87	21.	2.25	17.	4.2	13.
No. 2 Lens	307	1.372	4.	20.24	6.	0.84	2.	6.1	5.
No. 3 Lens	1591	1.303	19.	7.546	12.	2.81	31.	4.2	19.
No. 5 Lens	613	1.029	6.	25.38	16.	0.29	1.	6.0	11.

- Notes: 1. '%' denotes percentage of total inventory of that metal (Ko 1986).  
2. Precious metal data is given in ppm, and is recalculated from oz/t using a conversion factor of 34.3.

TABLE 2

Trout Lake Production and Reserves as of January 1st 1986

	Tons (million)	Au (ppm)	Ag (ppm)	Cu (%)	Zn (%)
Combined Production and Reserves	6.31	1.715	15.78	2.28	5.6
Proven Reserves	4.63	1.749	16.81	2.32	6.1

Note: Data includes 15% dilution and 92.9% mining recovery (Ko 1986).

TABLE 3

Trout Lake Circuit Balance on February 5th 1986

Product	Assays					
	wt %	Au(ppm)	Ag(ppm)	Cu(%)	Zn(%)	Pb(%)
Head	100.000	2.230	12.35	2.16	2.07	0.038
Cu Conc.	7.064	18.69	84.86	28.00	3.99	0.070
Zn Conc.	4.485	7.580	59.92	1.67	47.29	0.381
Tailings	88.451	0.652	4.150	0.12	0.19	0.018
		Recovery(%)				
Cu Conc.		59.22	48.49	91.74	10.96	13.09
Zn Conc.		15.25	21.74	3.47	82.47	45.59
Tailings		25.54	29.77	4.80	6.57	41.40

Note: Data from Healy & Petruk (1989).

## Chapter III

### GEOLOGY

The Trout Lake deposit is hosted in the Amisk Group volcanic strata of the Proterozoic Flin Flon greenstone belt (Fig. 1). The Flin Flon belt is part of the southern Churchill structural province and was deformed and metamorphosed prior to 1,750 Ma during the Hudsonian Orogeny (Syme et al. 1982). The metamorphic grade of the rocks in the Flin Flon area corresponds to greenschist facies and progressively increases northward where the almandine-amphibolite metamorphic grade has been recognized in the Kisseynew gneisses (Syme et al. 1982). Aggarwal & Nesbitt (1987) estimate that temperatures reached between 400 and 450°C in the vicinity of Flin Flon, which includes the Trout Lake locality.

The Flin Flon belt consists of a sequence of volcanic rocks with associated subordinate sediments, an overlying sequence of terrestrial sediments and a diversity of intrusive rocks. The Amisk Group comprises the lower stratigraphic elements of the Flin Flon belt. This group is dominated by subaqueous and subaerial volcanics of tholeiitic and calc-alkaline affinity, and are interpreted as having been deposited in an island arc setting (Syme et al. 1982). The volcanics consist of massive to pillowed basalt and andesite flows, overlain by pyroclastic andesite breccias and rhyolitic and dacitic quartz-porphyry (Koo & Mossman 1975). The Amisk Group underwent plutonism, uplift and deformation prior to the

deposition of the unconformably overlying fluviatile sedimentary strata of the Missi Group (Syme et al. 1982). The Missi Group constitutes sediments derived from the uplifted and deeply eroded Amisk terrain, including unroofed pre-Missi felsic plutons. Numerous small intrusives are interpreted as being correlative with the Amisk volcanism, whilst the larger intrusive bodies are less clearly syn-volcanic, or are interpreted as being post-volcanic (Price 1977).

The metamorphic peak occurred during the second of three deformational events associated with the Hudsonian Orogeny (Price 1977). The earliest deformation event (D1) resulted in east-trending tightly closed folds with steeply dipping axial surfaces and non-penetrative metamorphism. The second deformation event (D2) resulted in north-trending isoclinal folding about steep to vertical dipping axial surfaces (Price 1977). This folding was associated with penetrative metamorphism (axial foliation) as well as the emplacement of syn-tectonic plutons (Koo 1973). The latest deformation event (D3) resulted in refolding the rocks about the northeast trending Embury Lake antiform and associated shearing and drag-folding along northwesterly trending faults (Price 1977, Koo & Mossman 1975). There is no evidence of post-tectonic magmatism in the Flin Flon area (Price 1977).

The Trout Lake deposit consists of a series of steeply dipping stacked lenses (6 proven) occurring in two (North and South) zones. The zones strike at  $140^{\circ}$  azimuth and have a relatively constant dip of  $60-70^{\circ}$  to the northeast. Each lens consists of two principal types of mineralization: massive mineralization occurring in quartz-sericite schists, and disseminated mineralization occurring in chlorite schists,

where the hostrock types represent the metamorphosed equivalents of hydrothermally altered quartz-porphyry fragmental pyroclastics. The lenses generally consist of massive sulfides which are commonly separated by zones of disseminated pyrite and chalcopryite. The massive mineralization is interpreted as exhalative mineralization deposited on the seafloor proximal to a fumarolic vent. The disseminated mineralization, which does not constitute ore, together with chalcopryite stringer ore (described in Chapter 5) are interpreted as the metamorphosed equivalent of the feeder pipe stockwork mineralization (C. Ko, pers. comm., 1985).

The footwall contact of the stockwork ore is diffuse, whereas the hangingwall contact of the massive ore is sharp. The margins of the lenses commonly display open to tightly closed and isoclinal folding with shearing and dislocations on a mesoscopic scale. The relative distribution of the massive and stockwork mineralization strongly suggests intense shearing of the highly chloritized footwall rocks, the stringer ore and disseminated mineralization (C. Ko, pers. comm., 1985).

The lenses generally exhibit a zonation from a graphitic argillite in the hangingwall, to massive sphalerite, to massive pyrite, to massive chalcopryite + pyrite + sphalerite + pyrrhotite to footwall semi-massive chalcopryite stringers and disseminated pyrite and chalcopryite (Fig. 2). This zonation is locally reversed or disturbed by folding, as well as by emplacement of quartz-diorite intrusions. Generally, increases in the Cu/Cu+Zn ratio correlate with higher Au and lower Ag values. The metal zonation can be generalized as high Ag and Pb values associated with low Cu/Cu+Zn ratios in the hangingwall, and high Au, low Ag values

with high Cu/Cu+Zn ratios in the footwall. The intensity of the zonation is manifested in the highly differentiated appearance of the ores in terms of the sphalerite and chalcopyrite content, with spectacular semi-massive coarse-grained chalcopyrite stringer ores in the footwall and massive sphalerite ores in the hangingwall. The zonation of the ores is characteristic of many volcanogenic massive sulfides (Sangster 1972, Large 1977, Franklin et al. 1981). High Cu values are associated with the more proximal elements of the hydrothermal cell (stockwork ore and immediate vent area), whereas increasing Zn values are observed upwards and outwards away from the vent towards the margins of the lens. Large (1977) explains the zonation in terms of the chemical evolution of hydrothermal metal-bearing fluids progressively mixing with the seawater, either just below or above the exhalative vent, with increasing distance from the vent, and with time during the evolution of the hydrothermal cell. Conversely, Eldridge et al. (1983) explain the zonation in terms of the outward and upward migration of Cu-rich sulfide facies replacing Zn-rich facies in response to the chemical and thermal evolution of the hydrothermal fluids with time.

As each of the lenses possesses a footwall stockwork ore with a highly chloritized alteration zone, each lens is interpreted as being of the proximal type, having formed in the immediate vent area. In addition, as each lens exhibits the primary metal zonation the lenses are interpreted as representing an entire hydrothermal cycle, possibly fed by one or more hydrothermal cells separated in time and/or space. The consistent occurrence of stockwork ores in the footwall and the metal zonation also mitigates any form of downslope transportation or reworking of the sulfide mound (Jambor 1980).

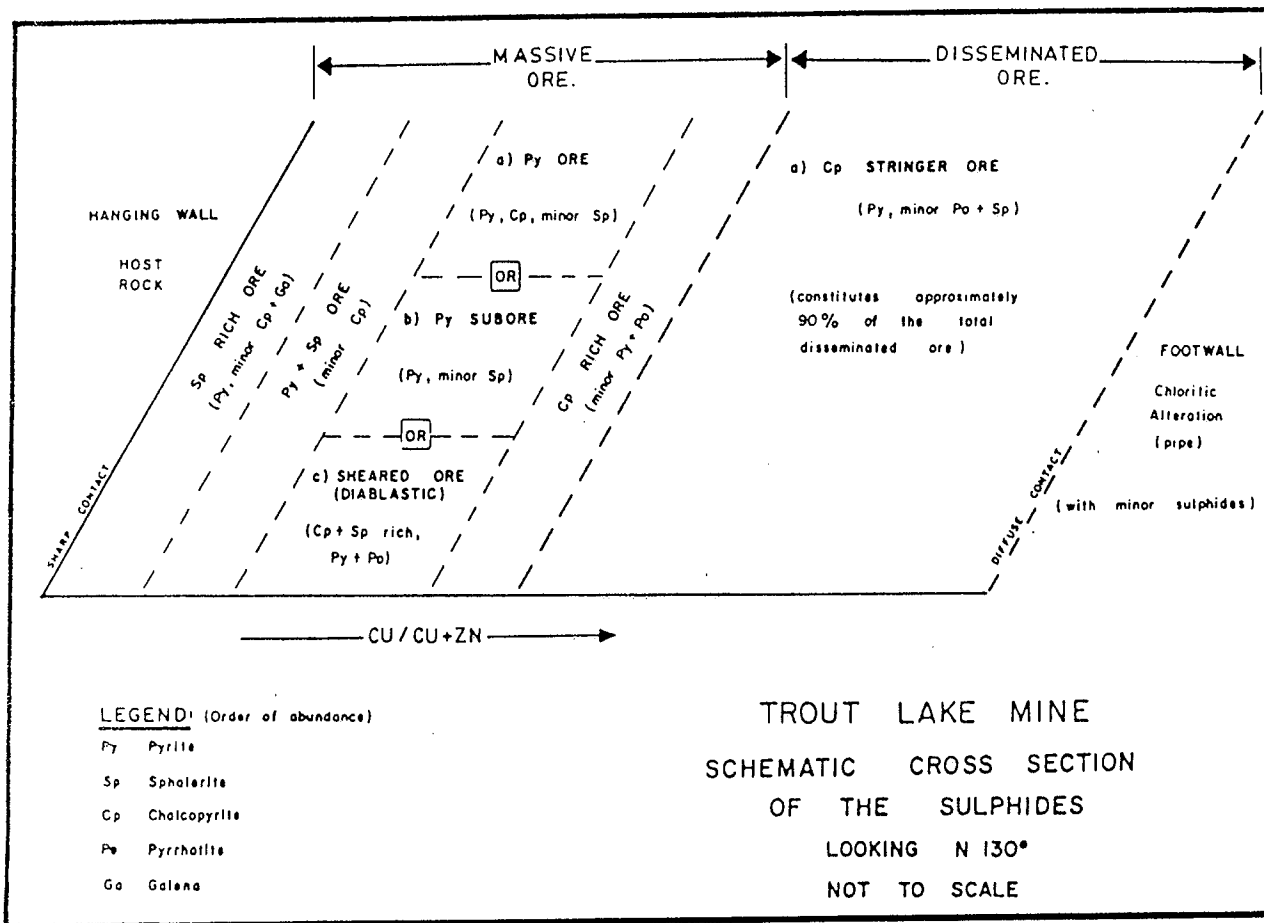


Figure 2: A Schematic Zonation of the Six Proven Trout Lake Ore Lenses. Cross-section of an idealized ore lense showing the mineralogical zonation from hangingwall to footwall. Redrawn from Ko (1986).

**Chapter IV**  
**METHODS OF INVESTIGATION**

**4.1 SAMPLING**

A total of 112 hand-specimen samples were collected during three underground sampling campaigns in June, September and December of 1985. Sampling was conducted in such a manner as to obtain the maximum spatial coverage of each lens, as well as to acquire samples that fully encompass the range of ore types at each sample location. Thus, depending on the character of the lens at a selected site, anywhere from 1 to 6 samples were collected with an average of 2.5 samples per site. However, the spatial coverage was constrained by the extent to which each lens could be accessed by drifts, crosscuts and stopes. The spatial coverage of Lens 1 in the North Zone and Lens 2 and 3 of the South Zone is considered to be thorough, whereas Lens 2 of the North Zone and Lens 1 and 5 of the South Zone are inadequately covered (Figs. 3 and 4).

Samples were also collected at sites where geological, chemical and/or metallurgical data suggested that the mineralogical characteristics of the ore differed significantly from that of their assumed ore type. For example, 4 samples were collected from stope 2451 on the 210m level of Lens 5 of the South Zone, because of high Zn and Ag losses to the tailings when these ores were previously processed in the concentrator. The sample numbers were prefixed with TL to designate

Trout Lake, N or S to designate North or South zone, and a number to designate the lens from which the sample was taken. Thus for example, TLN.1-89 is the 89th sample, and was taken from the (N)umber (1) lens of the (N)orth (Z)one.

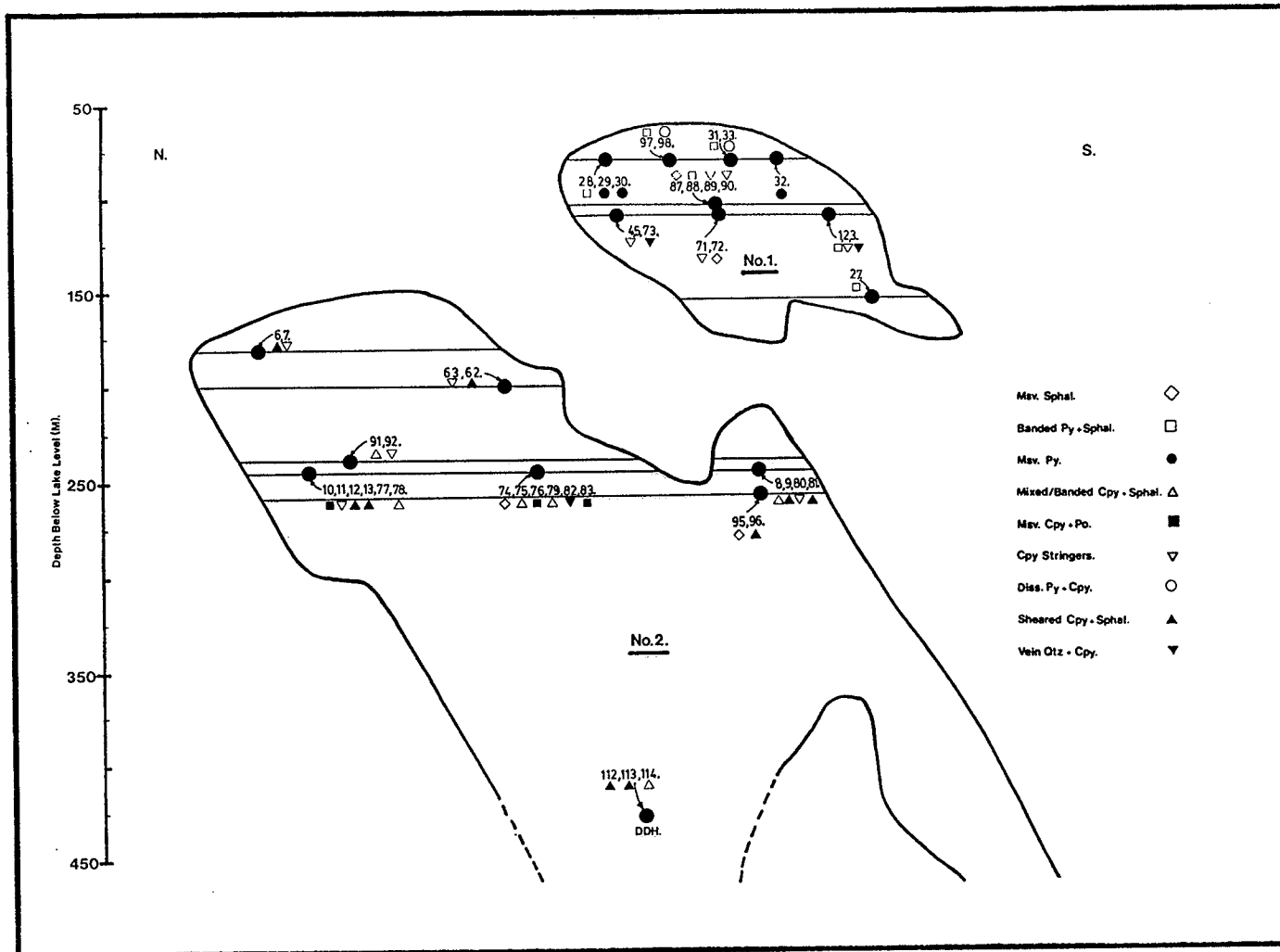


Figure 3: Idealized Longitudinal Vertical Projection of the North Zone. The zone consists of two proven ore lenses. The sample locations and designated ore types are plotted on the projection. Lens 2 is open at depth.

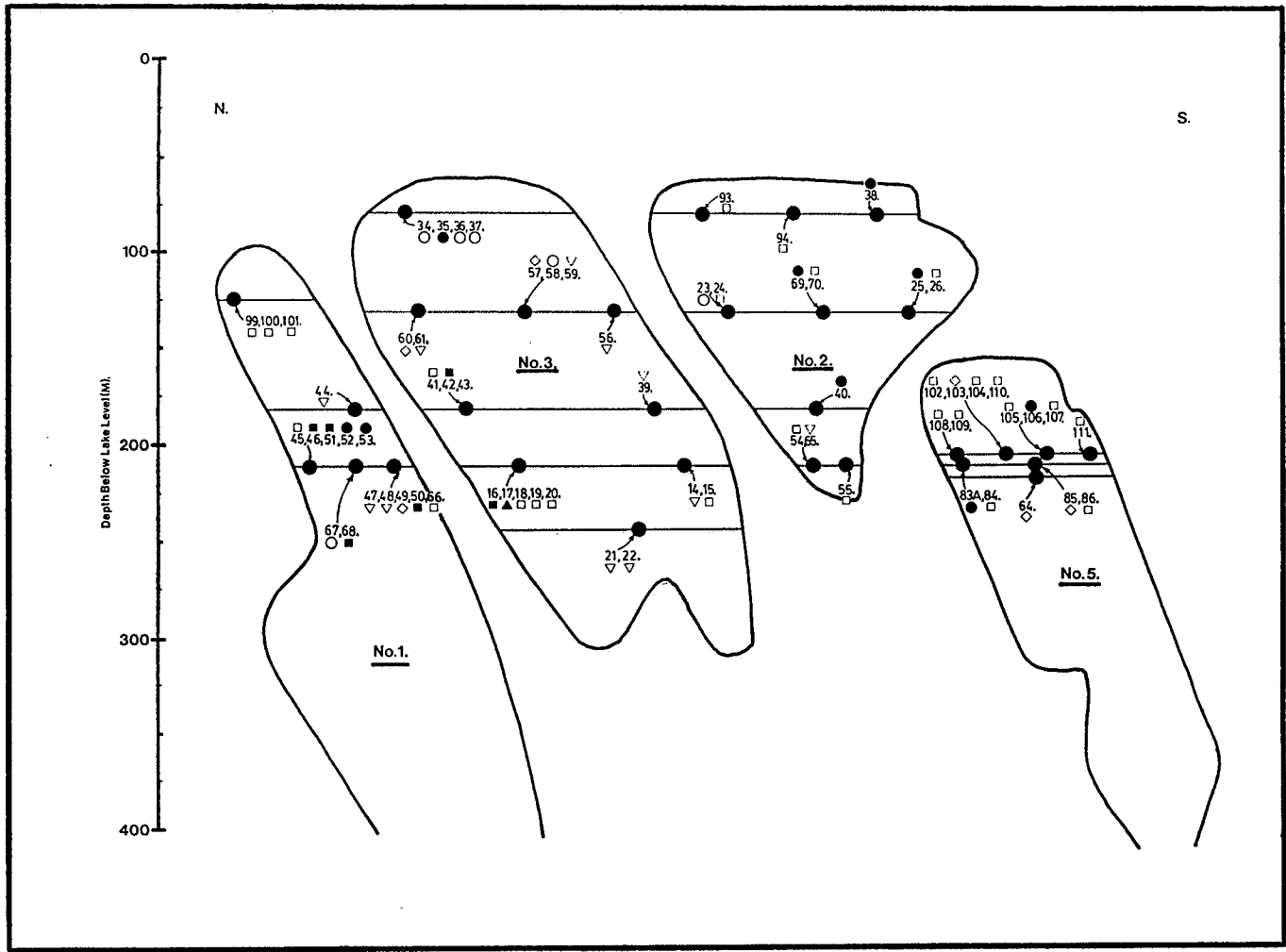


Figure 4: Idealized Longitudinal Vertical Projection of the South Zone. The zone consists of four proven ore lenses. The sample locations and designated ore types are plotted on the projection. Les 1 and 5 are open at depth

## 4.2 PETROGRAPHIC ANALYSIS

A total of 118 polished sections and polished thin sections representing the 112 samples were examined under reflected light using a Reichert Orthoplan research microscope. The purpose of the petrography was to classify the samples, to identify the constituent ore minerals, to note specific textures and to select samples for detailed characterization of each ore type. Each section was thoroughly examined for several hours in an attempt to locate and identify all precious metal-bearing minerals (Au-Ag-Hg alloy, freibergite, etc) > 0.5um in size. Subsequently, the sections were examined with emphasis on mineral distributions and textures. The mineral identities were later confirmed by EMPA at the UoM, and during IA using the MP-SEM-IPS Image Analysis System at CANMET. A total of twenty six ore minerals<sup>1</sup> were identified (See Table 4).

## 4.3 MICROPROBE ANALYSIS

The chemical composition of the ore minerals (except dyscrasite, costibite, bournonite, volynskite, naumanite and acanthite were determined using the EDS on the now decommissionaed MAC-V electron microprobe at the UoM. The EDS consisted of a Kevex Micro-X 7000 analytical spectrometer with a Si(Li) detector and a 1024-multichannel analyser. The bulk of the analyses were collected with an excitation voltage (Eo) of 15 kV, specimen current (Sc) of 5 nA, a vacuum of

---

<sup>1</sup> Ore minerals are informally defined here as minerals characteristic of the ore zone, but are not necessarily of economic value e.g., sulfides, alloys, sulfosalts, selenides, tellurides, etc. Similarly, gangue is informally defined here as non-sulfide minerals characteristic of the surrounding hostrocks, and of no economic value i.e., silicates, carbonates and phosphates.

approximately  $1.1 \times 10^{-4}$  Torr, and a sample collection time of 200 live seconds. A library of working standard spectra, and several fayalite calibration standard spectra were collected and stored at the initiation of the project. Several fayalite spectra were collected during each analytical run, thus permitting calibration in terms of  $E_0$ ,  $S_c$ , peak shape and peak position by reference to the original fayalite spectra, using the 'FAYREF' program.

Routine data processing including full matrix (ZAF) corrections were done using the Magic 5 program of J.W. Colby. Overlap corrections were applied by stripping off the respective peak of a reference standard spectra that had been scaled to the sample spectra, by normalizing on another non-overlapped peak of the overlapping element (Groat et al. 1985). This was not possible for certain overlapping peak pairs i.e.,  $HgM\alpha-AuM\alpha$  (Au-Ag-Hg alloy),  $PbM\alpha-BiM\alpha$  (rucklidgeite and pilsenite) and  $PbM\alpha-SK\alpha$  (boulangerite, clausthalite and pilsenite), because (1) of the absence of a second non-overlapped peak for the overlapping element that could be used for normalization (e.g., no  $SL\alpha$ ), or (2) the overlapping peak centroids were within approximately 50-100 eV, and could not be resolved satisfactorily without serious degradation of peak shape. Consequently, rucklidgeite and pilsenite were analysed with a 20 kV  $E_0$  using the  $L\alpha$  and  $L\beta$  lines.

The MAC-V was decommissioned in the Fall of 1988 and replaced by a new Cameca SX-50 scanning electron microprobe with a Kevex Delta EDS and a three-spectrometer WDS. The compositions of sphalerite and galena-clausthalite solid solution in sample TLN.1-87 were determined by WDA using the Cameca SX-50. These analyses were collected with a 20kV  $E_0$ , a

TABLE 4

## Ore Minerals Identified in the Trout Lake Ores

NAME	FORMULA	ABUNDANCE
<b>SULFIDES</b>		
Pyrite	FeS <sub>2</sub>	Ubiquitous, Major/Minor
Chalcopyrite	CuFeS <sub>2</sub>	Ubiquitous, Major/Minor
Sphalerite	ZnS	Ubiquitous, Major/Minor
Pyrrhotite	Fe <sub>(1-x)</sub> S	Common, Major/Trace
Marcasite	FeS <sub>2</sub>	Common, Major/Trace
Galena	PbS	Common, Major/Trace
Cubanite	CuFe <sub>2</sub> S <sub>3</sub>	Less Common, Trace
Acanthite	Ag <sub>2</sub> S	Rare, Trace
<b>OXIDES</b>		
Magnetite	Fe <sub>3</sub> O <sub>4</sub>	Less Common, Major/Minor
Cassiterite	SnO <sub>2</sub>	Rare, Trace
<b>SULFARSENIDES</b>		
Arsenopyrite	FeAsS	Common, Major/Trace
<b>SULFOSALTS</b>		
Freibergite	(Cu,Ag,Fe,Zn) <sub>12</sub> (Sb,As) <sub>4</sub> S <sub>13</sub>	Less Common, Minor/Trace
Pyrargyrite	Ag <sub>3</sub> SbS <sub>3</sub>	Rare, Trace
Freieslebenite	Ag <sub>2</sub> Sb <sub>2</sub> Pb <sub>2</sub> S <sub>6</sub>	Rare, Trace
Boulangerite	Pb <sub>5</sub> Sb <sub>4</sub> S <sub>11</sub>	Rare, Trace
Bournonite	PbCuSbS <sub>3</sub>	Rare, Trace
<b>ALLOYS AND INTERMETALLIC COMPOUNDS</b>		
Au-Ag-Hg Alloy	Ag,Au,Hg	Common, Trace
Dyscrasite	Ag <sub>3</sub> Sb	Rare, Trace
<b>SULFANTIMONIDES</b>		
Gudmundite	FeSbS	Less Common, Trace
Costibite	CoSbS	Rare, Trace
<b>TELLURIDES</b>		
Hessite	Ag <sub>2</sub> Te	Rare, Trace
Rucklidgeite	(Bi,Pb) <sub>3</sub> Te <sub>4</sub>	Rare, Trace
Pilsenite	(Bi,Pb) <sub>8</sub> (Te,Se) <sub>7</sub>	Rare, Trace
Volynskite	BiAgTe <sub>2</sub>	Rare, Trace
<b>SELENIDES</b>		
Clausthalite	PbSe	Less Common, Minor/Trace
Naumannite	Ag <sub>2</sub> Se	Rare, Trace

Presented in order of decreasing abundance of the mineral groups, and of the minerals in each group.

20nA Sc (as measured on the Faraday Cup) and a sample collection time of 20 seconds on the peaks, and 10 seconds on both high and low backgrounds.

The compositions of Au-Ag-Hg alloy, volynskite, naumannite and dyscrasite were analyzed by WDA on the Jeol 733 'Superprobe' at CANMET, Ottawa (Petruk 1987). These analyses were collected with a 20kV Eo, a 15nA Sc (as measured on the Faraday Cup) and a sample collection time of 60 seconds or less, if acceptable counting statistics (StD = 0.5) were achieved for each element on standards and unknowns before the 60 second limit was reached. The concentrations of Ag, Au, Hg and Fe were determined during routine WDA of Au-Ag-Hg alloy. Fe was sought as it had been observed consistently in EDS spectra on the Mac V. High-contrast, BSE imagery was used to select all analytical points. The detection limit for Au, Ag, Hg and Fe is 0.05 wt%. Cu and S were also determined in twenty of the analyses. Furthermore, several profiles of Au, Ag and Hg concentrations were generated by continuous, qualitative, wavelength dispersive traverses across masses of Au-Ag-Hg alloy were generated on the Cameca SX-50.

#### **4.4 CHEMICAL ANALYSES**

A suite of twenty seven samples were selected for detailed characterization of each ore type. These were analysed chemically for Au, Ag, Cu, Zn, Ni, Cd, Co, Mn, Bi, Pb, Fe and S at the HBM&S Assay Laboratory, Flin Flon, and for As, Se, Te, Hg, Sn, Sb and In by Bondar-Clegg, Ottawa. The samples were prepared for chemical analysis at the Manitoba Department of Energy & Mines facility on Logan Ave., Winnipeg.

Approximately 400g of sample was passed through the jaw crusher, and then through the disc-grinder equipped with standard grade cast iron plates. High quality silica sand was used to clean the surfaces of the plates prior to each sample pass, as well as to evaluate the potential contaminants due to the cast iron plates.

An aqua regia leach of the silica sand, followed by Atomic Absorption indicated contamination by Cu, Ni, Mn and Fe. The Cu, Ni and Mn are probably due to cross-contamination from the previous sample, whereas Fe is largely due to abrasion of the plates with each pass. Nonetheless, the contamination is considered insignificant.

The crushed samples and the CANMET reference ore standard CZN-1 were sealed in labelled vials as unknowns, and submitted to the respective laboratories for analysis. Precision of analysis was tested by duplicate analyses of several submitted samples. Excellent precision was achieved by HBM&S. with the exception of Au (See Table 5). The duplicate analyses gave a precision of  $0.131 \pm 0.03$  oz/ton Au, which corresponds to an uncertainty of 23%. This high uncertainty probably reflects the 'particle sparcity' or 'nugget' effect of Au, and the difficulty in acquiring a representative, yet manageable sample aliquot (Boyle 1978, Bacon et al. 1989). The duplicate analyses done by Bondar-Clegg also exhibit relatively good precision.

The accuracy of the analyses was evaluated by including reference ore standard CZN-1 as an unknown, and comparing the measured with the certified, recommended and non-certified values. Good agreement between the recommended and the measured values was obtained for the elements

determined by both HBM&S and Bondar-Clegg (See Table 5), indicating that acceptable accuracy was achieved by both laboratories.

TABLE 5

## TEST OF PRECISION AND ACCURACY OF THE CHEMICAL ANALYSES.

## TEST OF PRECISION BY DUPLICATE ANALYSES.

SAMPLE	Au	Ag	Cu	Zn	Ni	Cd	Co	Mn	Pb	Fe	S	As	Se	Te	Hg	Sn	Sb	In
	ppm																	
TLN.2-91	4.150	44.08	4.7	10.6	0.002	0.025	0.015	0.27	0.002	18.7	16.6							
DUPLICATE	4.802	45.11	4.7	10.6	0.002	0.025	0.015	0.27	0.002	18.7	16.6							
TLS.1-49													6.			44.	109.	
DUPLICATE													7.			40.	112.	
TLN.2-96																9.	15.	
DUPLICATE																2.	17.	

## TEST OF ACCURACY BASED ON ANALYSES OF REFERENCE ORE STANDARD CZN-1 (SUBMITTED AS AN UNKNOWN).

HBM&S ASSAY LABORATORY			BONDAR-CLEGG COMMERCIAL LABORATORY		
ELEMENT	ANALYSIS	RECOMMENDED/CERTIFIED VALUE	ELEMENT	ANALYSIS	RECOMMENDED/CERTIFIED VALUE
Au	nd.	0.09 ppm (Non-Certified)	As	268 ppm	260 ± 20 ppm
Ag	94.84 ppm	93. ppm ± 3 ppm	Se	1 ppm	5 ppm (Non-Certified)
Cu	0.15 wt%	0.144 ± 0.003 wt%	Te	0.2 ppm	- (Not Quoted)
Zn	45.2 wt%	44.74 ± 0.11 wt%	Hg	46 ppm	43 ± 4 ppm
Ni	0.001 wt%	- (Not Quoted)	Sn	102 ppm	74 ppm (Non-Certified)
Cd	0.15 wt%	0.132 ± 0.002 wt%	Sb	407 ppm	520 ± 30 ppm
Co	0.001 wt%	- (Not Quoted).	In	71 ppm	86 ppm (Non-Certified)
Mn	0.21 wt%	0.219 ± 0.07 wt%			
Bi	0.004 wt%	0.003 (Non-Certified)			
Pb	7.7 wt%	7.45 ± 0.05 wt%			
Fe	11.1 wt%	10.93 ± 0.06 wt%			
S	30.0 wt%	30.2 ± 0.2 wt%			

#### 4.5 IMAGE ANALYSIS

The twenty seven ore samples were analysed by image analysis to determine the quantities and grain size distributions of the constituent ore minerals. The Leitz Tass Plus Image Analyser, Department of Engineering, UoM was proposed initially for this aspect of the work. However, this system is equipped with an optical microscope such that the image produced is based on the reflectance of the constituent ore minerals. Because of the anisotropic nature of many ore minerals, the reflectance values vary with the orientation of the constituent grains, resulting in adjacent or overlapping ranges in the reflectance values for different minerals. Consequently, many of the minerals of interest could not be unambiguously discriminated e.g., chalcopyrite from pyrrhotite and galena.

The image analysis was done at CANMET, Ottawa on the MP-SEM-IPS image analysis system, which was developed by Petruk (Petruk 1987, 1988). MP-SEM-IPS is an abbreviation for an 'Electron Microprobe' interfaced with a Kontron 'SEM-IPS' Image Analyser and a Tracor Northern TN2000 EDS, to form an integrated Image Analysis System. The SEM capabilities of the Jeol 733 electron microprobe, the image-producing component or 'front-end' of the system, permits the generation of high resolution BSE images of the polished sample surface. The BSE signal (or grey level) of each constituent mineral is dependent on its average atomic number (Z). Consequently, each mineral occurs within a characteristic narrow range or grey level window (for standardized operating conditions), and thus provides the basis for discrimination of the minerals (Mainwaring & Petruk 1984, Petruk 1985).

The BSE image of a single field of the sample surface is transferred to the Kontron SEM-IPS image analyser and digitized. Those areas of the image detected within the grey level window of each mineral are transformed into separate binary images. These mineral-specific binary images are filtered and enhanced by binary image functions (e.g., erode, dilate, median, close, etc.; See Petruk 1988, 1989a), and are stored in the image memory assigned to each mineral or mineral group. At this point the various parameters are measured, and the procedure is repeated for successive fields.

The polished sections were analyzed by PRGM #30, a macro routine customized specifically for this suite of sections. PRGM #30 determined (1) the quantities of each mineral (or mineral group) of interest; and (2) grain size distributions for minerals of interest. The minerals or mineral groups of interest are gangue, pyrite, pyrrhotite, chalcopyrite, sphalerite, arsenopyrite, freibergite and galena. Because of overlapping grey levels, minor magnetite and marcasite contribute to the pyrite grey level window, cubanite to the chalcopyrite grey level window, Au-Ag-Hg alloy to the galena grey level window, and pyrargyrite, hessite, gudmundite and many of the other trace and ultra-trace minerals to the freibergite grey level window. These minerals are difficult to discriminate because they are fine-grained and have similar Z values and thus cannot be differentiated from each other in the BSE image (Healy & Petruk 1987, Petruk 1988). The minerals can only be discriminated by scanning, with the electron beam, those areas of the image that show the grey level range characteristic of this 'family' of minerals and determining their chemical composition and hence identity by EDA (Petruk 1988, Healy & Petruk 1987).

Image analysis was done on each of the twenty seven samples of the representative ore suite, as well as on sample TLN.1-89a. A magnification of x100 (pixel size = 1.348um) was used over an analytical area of approximately 40 to 100 fields per sample, until a statistically valid number of measurements for the minerals was obtained. The mineral quantities are determined by measuring the relative area% of each mineral or mineral group within the polished section. The area% is stereologically equivalent to vol%, and is recalculated to wt% of the mineral by correcting for the mineral's specific gravities. From the wt% values and the composition of the minerals as determined by EMPA, metal and sulfur contents (partial compositions) of the sample can be calculated.

The grain size distributions of the minerals of interest were determined by chord analysis. Chord analysis scans the image along finitely-spaced horizontal lines and measures the intercept lengths for the mineral(s). These intercept lengths are equivalent to the grain diameter (Petruk 1985), and are classified using size ranges that approximate to the Tyler mesh series from 3.3um to 208um (i.e., 208um equivalent to 65 Mesh). Thus, a grain size distribution for each of the minerals of interest was generated for each sample. Stereological corrections for the 'slicing effect' (Petruk 1976, Jones 1987) were not applied to the grain size data.

## Chapter V

### CLASSIFICATION OF ORES: ORE TYPES

#### 5.1 GENERAL CHARACTERISTICS

The ores were classified into nine ore types on the basis of the relative abundance and textures of the ore minerals (See Table 6). These ore types correspond closely to ore types recognized by the mine geology staff (C. Ko, pers. comm., 1985), seven of which also approximate to metamorphic equivalents of the classical ore types recognized from the Kuroko volcanogenic deposits of Japan (Lambert and Sato 1974). The other two ore types (the Sheared Chalcopyrite + Sphalerite and the Vein Quartz + Chalcopyrite ore types) are interpreted as having been produced by tectonic forces, and have no equivalent in the definitions for the Kuroko deposits.

In general, the seven 'non-tectonic' ore types are represented in each lens, and occur in the following generalized stratigraphic sequence from hangingwall to footwall: Massive Sphalerite; Massive Layered Pyrite + Sphalerite; Massive Pyrite; Mixed/Layered Chalcopyrite + Sphalerite; Massive Chalcopyrite + Pyrrhotite; Chalcopyrite Stringers and Disseminated Pyrite + Chalcopyrite. The lenses in the Trout Lake deposit have an average thickness of 10 m; the maximum recorded thickness is approximately to 25 m (Ko 1986). Each lens is largely vertically stratified and generally comprising all the ore types, although locally

only one ore type comprises the full vertical width of a lens. The distribution of the ore types is reflected in the samples that were taken (Figs. 3 and 4). However, the relative abundance of the ore types could not be determined within the scope of this work. Healy & Petruk (1989) determined the relative abundances of the ore types being fed to the concentrator circuit on February 16th 1986, by hand-sorting the rod mill feed. Although their results are only strictly valid for the ore being mined at the time of sampling, these data provide a 'best estimate' of the relative abundances of the ore types in the deposit as a whole.

Twenty seven samples were selected as a representative suite of the nine ore types. These were analysed chemically and with the image analyser to determine the average chemical compositions, and the quantities and size distributions of the ore minerals, respectively, in each ore type. The chemical compositions for each sample are given in Table 7, and the mineral quantities in Table 8. The average chemical composition for each ore type was calculated from Table 7, and the results are given in Table 9. Using microprobe determined average mineral compositions, partial chemical compositions were also calculated from the mineral quantities data in Table 8, in order to assess whether the analysed samples were representative (See Table 10). In general, good agreement was obtained, especially as the polished sections represent a very small area of the sample, and a single representative section may be unobtainable if the sample is coarse-grained and/or inhomogeneous. The material submitted for chemical analysis represents a larger and more homogeneous (finely ground) aliquot of the sample, and is therefore assumed to be more representative.

TABLE 6

## LIST OF ORE TYPES DEFINED AT TROUT LAKE.

ORE TYPE	STRATIGRAPHIC LOCATION	UNMETAMORPHOSED KUROKO EQUIVALENT (Lambert and Sato, 1974)	PRINCIPAL ORE MINERALS
Massive Sphalerite	Hangingwall	Kuroko (Black) Ore	Sp+Py+Cp+Po+Gal+Asp+Ma+Fr
Layered Pyrite + Sphalerite	Hangingwall	Kuroko (Black) Ore	Py+Sp+Cp+Po+Asp+Gal+Ma+Fr
Massive Pyrite	Hangingwall/Center	Ryukako (Pyrite) Ore	Py+Sp+Cp+Po+Ma+Gal
Mixed/Layered Chalcopyrite + Sphalerite	Center	Oku (Yellow) Ore	Cp+Sp+Po+Py+Mag
Massive Chalcopyrite + Pyrrhotite	Footwall/Center	Oku (Yellow) Ore	Cp+Po+Py+Sp+Mag
Chalcopyrite Stringers	Footwall	Keiko (Siliceous) Ore	Cp+Po+Py+Sp+Po+Ma
Disseminated Pyrite + Chalcopyrite	Footwall	Keiko (Siliceous) Ore	Py+Cp+Sp+Po+Ma
Sheared Chalcopyrite + Sphalerite	Tectonic Control	No equivalent	Cp+Sp+Po+py
Vein Quartz + Chalcopyrite	Tectonic Control	No equivalent	Cp+Sp+Py+Po+Ma+Cub

TABLE 7  
THE CHEMICAL ANALYSES OF THE 27 REPRESENTATIVE ORE SAMPLES.

SAMPLE	Au	Ag	Cu	Zn	Ni	Cd	Co	Mn	Pb	Fe	S	As	Se	Te	Hg	Sn	Sb	In
	ppm																	
MASSIVE SPHALERITE ORE TYPE.																		
TLS.1-49	0.69	27.27	0.11	37.4	0.003	0.077	0.015	0.056	0.031	10.8	24.9	550.	6.	nd.	19.	44.	109.	37.
TLS.5-64	2.06	445.9	0.06	38.6	0.001	0.052	0.001	0.030	12.1	10.7	24.3	1400.	nd.	nd.	45.	47.	30.	61.
TLN.2-74	2.74	21.44	4.4	41.3	0.001	0.093	0.017	0.067	0.035	13.2	29.7	6.	5.	0.2	22.	46.	89.	48.
TLN.2-95	0.52	28.98	2.3	34.3	0.001	0.079	0.005	0.15	0.29	11.6	22.4	3.	62.	1.2	21.	40.	84.	27.
LAYERED PYRITE + SPHALERITE ORE TYPE.																		
TLN.2-24	0.86	27.44	2.00	15.0	0.002	0.034	0.007	0.072	0.001	27.9	35.1	165.	80.	1.5	60.	53.	60.	36.
TLN.2-26	0.52	275.8	0.05	30.3	0.002	0.050	0.001	0.027	4.1	14.9	28.8	485.	nd.	nd.	114.	46.	377.	53.
TLN.2-54	0.86	9.26	0.34	16.1	0.002	0.034	0.003	0.096	0.132	30.8	39.3	500.	15.	0.2	66.	41.	69.	27.
TLN.2-55	13.75	8.06	0.02	18.0	0.002	0.041	0.006	0.096	0.051	26.4	32.0	54000.	13.	nd.	65.	39.	162.	25.
MASSIVE PYRITE ORE TYPE.																		
TLN.2-25	0.52	12.52	0.07	6.6	0.002	0.014	0.001	0.020	0.008	39.9	45.0	330.	70.	0.3	44.	34.	56.	27.
TLN.1-52	1.82	5.66	0.46	1.98	0.002	0.005	0.038	0.042	0.008	38.6	36.2	306.	44.	0.2	44.	35.	37.	23.
TLN.5-83A	1.37	112.9	0.04	1.44	0.002	0.001	0.001	0.028	0.85	35.9	37.3	2600.	1.	nd.	28.	30.	135.	41.
MIXED/LAYERED CHALCOPYRITE + SPHALERITE ORE TYPE.																		
TLN.2-78	3.64	72.03	6.17	25.0	0.002	0.051	0.025	0.078	0.013	23.6	33.7	893.	4.	0.7	43.	42.	98.	46.
TLN.2-91	4.49	44.59	4.7	10.6	0.002	0.025	0.015	0.27	0.002	18.7	16.6	32.	24.	1.0	24.	31.	40.	43.
MASSIVE CHALCOPYRITE + PYRRHOTITE ORE TYPE.																		
TLN.3-42	2.78	28.81	7.99	0.27	0.002	0.001	0.123	0.064	0.004	44.0	28.1	1500.	90.	2.5	62.	42.	40.	25.
TLN.1-50	1.48	44.08	19.74	0.37	0.002	0.001	0.009	0.099	0.005	32.9	28.7	nd.	302.	3.5	37.	45.	54.	30.
TLN.2-83	5.83	45.28	8.73	0.54	0.006	0.001	0.027	0.20	0.003	35.1	30.2	175.	94.	5.0	34.	43.	27.	40.
CHALCOPYRITE STRINGER ORE TYPE.																		
TLN.1-2	4.29	68.94	5.3	9.9	0.003	0.026	0.038	0.063	0.029	24.6	28.5	11100.	134.	0.5	67.	36.	92.	63.
TLN.2-11	2.57	28.64	18.81	0.29	0.002	0.001	0.009	0.027	nd.	36.3	29.6	2.	209.	3.5	38.	53.	34.	37.
TLN.2-65	0.76	27.78	3.6	0.62	0.002	0.002	0.008	0.042	0.15	17.6	6.2	84.	57.	2.5	17.	6.	18.	12.
TLN.1-71	1.51	28.30	21.89	0.19	0.002	0.001	0.006	0.026	0.004	31.4	31.6	2.	219.	4.5	31.	52.	36.	43.
DISSEMINATED PYRITE + CHALCOPYRITE ORE TYPE.																		
TLN.3-36	0.69	4.63	0.59	9.0	0.002	0.019	0.005	0.035	0.009	7.5	9.8	132.	37.	0.5	14.	nd.	30.	11.
TLN.1-67	1.27	8.06	2.04	0.64	0.003	0.002	0.020	0.100	0.015	25.5	21.6	332.	17.	0.5	24.	20.	43.	14.
SHEARED CHALCOPYRITE + SPHALERITE ORE TYPE.																		
TLN.2-12	0.38	11.49	0.71	44.7	0.002	0.126	0.010	0.135	0.010	10.3	27.6	270.	28.	nd.	22.	40.	116.	32.
TLN.2-62	6.35	84.89	6.66	25.6	0.003	0.057	0.025	0.069	0.004	19.6	28.2	138.	19.	1.2	37.	50.	78.	52.
TLN.2-63	8.23	132.4	11.02	19.2	0.002	0.042	0.017	0.088	0.010	22.3	27.7	410.	72.	2.5	33.	54.	73.	54.
TLN.2-96	12.52	30.36	3.2	3.3	0.002	0.006	0.003	0.26	0.024	15.7	7.8	30.	18.	0.8	14.	9.	15.	14.
VEIN QUARTZ + CHALCOPYRITE ORE TYPE.																		
TLN.1-3	6.17	13.21	3.2	0.43	0.003	0.001	0.001	0.014	0.005	5.6	3.9	19.	16.	1.5	7.	nd.	2.	nd.

TABLE 8

## Mineral Quantities (in wt%) of the 27 Representative Ore Samples

ORE TYPE/SAMPLE ID.	Pyrite	Chalcopyrite	Sphalerite	Pyrrhotite	Galena	Freibergite	Arsenopyrite	Gangue
MASSIVE SPHALERITE.								
TLS. 1-49.	3.55	0.96	82.72	3.28	0.02	0.01	0.02	9.42
TLS. 5-64.	3.60	0.05	70.59	1.79	12.45	0.01	0.02	11.50
TLN. 2-74.	0.00	13.27	70.65	4.74	0.02	0.00	0.00	11.32
TLN. 2-95.	0.00	1.06	61.53	1.10	0.84	0.01	0.00	35.47
LAYERED PYRITE + SPHALERITE.								
TLS. 2-24.	48.86	4.30	26.43	0.05	0.00	0.00	0.00	20.37
TLS. 2-26.	22.80	0.07	64.77	0.01	5.09	0.09	0.30	6.87
TLS. 2-54.	66.78	0.12	19.44	0.01	0.02	0.00	0.07	13.54
TLS. 2-55.	48.26	0.04	18.92	0.00	0.02	0.00	20.10	12.66
MASSIVE PYRITE.								
TLS. 2-25.	86.17	0.05	2.15	0.01	0.00	0.00	0.00	11.63
TLS. 1-52.	73.94	0.57	0.02	0.03	0.00	0.00	0.00	25.42
TLS. 5-83A.	60.90	0.00	2.19	0.00	3.81	0.10	0.14	32.84
MIXED/LAYERED CHALCOPYRITE + SPHALERITE.								
TLN. 2-78.	24.34	24.64	27.24	6.94	0.00	0.00	0.03	16.09
TLN. 2-91.	0.03	15.06	7.57	8.04	0.00	0.00	0.00	69.31
MASSIVE CHALCOPYRITE + PYRRHOTITE.								
TLS. 3-42.	51.74	16.09	0.31	12.06	0.00	0.00	0.00	19.75
TLS. 1-50.	0.08	61.37	0.30	27.73	0.00	0.00	0.00	10.48
TLN. 2-83(#2).	9.27	28.51	1.42	27.88	0.00	0.00	0.00	32.92
CHALCOPYRITE STRINGERS.								
TLN. 1-2.	18.82	33.82	22.65	0.20	0.00	0.00	0.21	24.31
TLN. 2-11.	0.12	25.68	0.22	23.84	0.00	0.00	0.00	50.14
TLS. 2-65.	1.72	10.92	0.34	1.08	0.15	0.00	0.00	85.74
TLN. 1-71.	23.59	55.65	0.16	0.43	0.00	0.00	0.00	20.17
TLN. 1-89.	7.86	38.50	0.56	0.96	0.00	0.00	0.00	52.50
DISSEMINATED PYRITE + CHALCOPYRITE.								
TLS. 2-36(#2).	28.67	1.60	0.98	0.04	0.02	0.00	0.02	68.66
TLS. 1-67.	39.79	1.78	0.19	0.02	0.02	0.00	0.00	58.22
SHEARED CHALCOPYRITE + SPHALERITE.								
TLN. 2-12.	0.00	4.92	67.87	9.45	0.00	0.00	0.00	17.76
TLN. 2-62.	3.41	14.76	36.15	4.17	0.00	0.00	0.00	41.51
TLN. 2-63.	1.32	35.88	35.17	10.83	0.00	0.00	0.00	16.79
TLN. 2-96.	11.50	17.79	7.69	19.37	0.00	0.00	0.00	43.62
VEIN QUARTZ + CHALCOPYRITE.								
TLN. 1-3.	3.28	68.08	1.05	0.90	0.00	0.00	0.00	26.69

Note: 1. Data generated by image analysis using the MP-SEM-IPS-IAS, CANMET, Ottawa.

2. Pyrite includes marcasite and magnetite, because these minerals have similar average atomic numbers (Z) and hence occur in the same grey level window in the BSE image; the marcasite and magnetite contents are minor.

**TABLE 9**  
**AVERAGE CHEMICAL COMPOSITION OF EACH ORE TYPE.**

Ore Type	Au ppm	Ag	Cu	Zn	Ni	Cd	Co wt%	Mn	Pb	Fe	S	As	Se	Te	Hg	Sn	Sb	In
Msv Sp.	1.51	131.	1.72	37.9	0.002	0.075	0.009	0.076	3.11	11.6	25.3	490.	18.	0.4	27.	44.	148.	43.
Layered Py+Sp.	4.01	80.	0.60	19.9	0.002	0.040	0.004	0.073	1.071	25.0	33.8	13940.	27.	0.4	76.	45.	167.	35.
Msv Py.	1.02	44.	0.19	3.34	0.002	0.007	0.013	0.030	0.289	38.1	39.5	1080.	38.	0.2	39.	10.	76.	22.
Mix/L. Cp+Sp.	4.05	58.	5.43	17.8	0.002	0.038	0.020	0.174	0.007	21.1	25.1	460.	14.	0.8	26.	37.	69.	45.
Msv Cp+Po.	3.36	39.	12.15	0.39	0.003	0.001	0.053	0.121	0.004	37.3	29.0	560.	162.	3.7	44.	43.	40.	32.
Cp Stringers.	2.26	38.	12.4	2.75	0.001	0.007	0.015	0.039	0.046	27.5	24.0	2800.	155.	2.7	38.	38.	45.	39.
Diss Py+Cp.	1.27	8.1	2.04	0.64	0.003	0.002	0.020	0.100	0.015	25.5	21.6	332.	17.	0.5	24.	20.	43.	14.
Sheared Cp+Sp.	6.86	65.	5.24	23.2	0.002	0.058	0.014	0.138	0.012	17.0	22.8	210.	34.	1.1	27.	38.	71.	38.
Vein Qtz+Cp.	6.17	13.2	3.2	0.43	0.003	0.001	0.001	0.014	0.005	5.6	3.9	19.	16.	1.5	7.	nd.	2.	nd.

Note: Composition of Diss. Py + Cpy Ore Type based on TLS.1-67 only, because the chemical composition of TLS.2-26(#2) is inconsistent with the mineral quantity analysis and the defined ore type; inhomogeneous sample.

TABLE 10

Partial Chemical Compositions of the Ore Samples Calculated from  
Mineralogical Compositions

Sample ID.	S	Fe	Cu	Zn	Pb
Massive Sphalerite					
TLS.1-49.	30.90	9.66	0.33	49.63	0.02
TLS.5-64.	27.76	7.64	0.02	42.35	10.70
TLN.2-74.	29.87	11.90	4.51	42.39	0.02
TLN.2-95.	21.14	5.30	0.36	36.92	0.72
Massive Layered Pyrite + Sphalerite					
TLS.2-24.	37.12	25.20	1.46	15.86	0.00
TLS.2-26.	34.65	14.82	0.02	38.86	4.38
TLS.2-54.	43.19	31.46	0.04	11.66	0.02
TLS.2-55.	37.22	30.09	0.01	11.35	0.02
Massive Pyrite					
TLS.2-25.	48.13	38.96	0.02	1.29	0.00
TLS.1-52.	40.89	33.47	0.19	0.01	0.00
TLS.5-83A.	34.78	27.61	0.00	1.31	3.28
Mixed/Layered Chalcopyrite + Sphalerite					
TLN.2-78.	33.78	24.60	8.38	16.34	0.00
TLN.2-91.	11.01	10.03	5.12	4.54	0.00
Massive Chalcopyrite + Pyrrhotite					
TLS.3-42.	39.01	35.53	5.47	0.19	0.00
TLS.1-50.	32.71	35.73	20.87	0.19	0.00
TLN.2-83.	26.70	29.84	9.69	0.85	0.00
Chalcopyrite Stringer					
TLN.1-2.	29.75	20.66	11.50	13.59	0.00
TLN.2-11.	18.67	21.76	8.11	0.13	0.00
TLS.2-65.	5.33	4.83	3.71	0.20	0.13
TLN.1-71.	32.68	28.14	18.92	0.10	0.00
TLN.1-89.	18.37	16.10	13.09	0.34	0.00
Disseminated Pyrite + Chalcopyrite					
TLS.3-36.	16.67	13.49	0.54	0.59	0.03
TLS.1-67.	22.58	18.48	0.61	0.11	0.02
Sheared Chalcopyrite + Sphalerite					
TLN.2-12.	27.90	11.95	1.67	40.72	0.00
TLN.2-62.	20.65	11.15	5.02	21.69	0.00
TLN.2-63.	29.23	20.67	12.20	21.10	0.00
TLN.2-96.	22.85	22.86	6.05	4.61	0.00
Vein Quartz + Chalcopyrite					
TLN.1-3.	26.34	23.20	23.15	0.63	0.00

Average mineral quantities for each ore type were calculated from Table 8 and are given in Table 11). However, as noted above, there are differences between the compositions determined by chemical assay and image analysis. It is assumed that the most representative mineral content is one derived from a combination of chemical composition and image analysis data. The average mineral quantities were therefore recalculated using both the average chemical composition and the mineral quantities as follows. The sphalerite, chalcopyrite, galena, arsenopyrite, Au-Ag-Hg alloy and gangue (by difference) were calculated from the average chemical composition using 60 wt% Zn for sphalerite, 34.5 wt% Cu for chalcopyrite, 86.7 wt% Pb for galena, 43 wt% As for arsenopyrite and 40 wt% Au for Au-Ag-Hg alloy. The average gangue content was determined from the chemical composition (by difference), and the pyrite + marcasite + magnetite content was adjusted to normalize the total to 100%. A close correlation was obtained between the analysed pyrite and gangue contents reported in Table 11, and the calculated values from chemical analyses. This suggests that the calculated values for the pyrite and gangue are relatively accurate. The results are therefore given as 'interpreted mineralogical compositions' of each ore type in the Trout Lake deposit (See Table 12). Table 12 contains check marks (i.e., 'X') to indicate all trace minerals that were observed during petrological and image analysis. This table is therefore considered to provide the most complete mineralogical compositions of the ore types.

Triangular diagrams for Sphalerite-Chalcopyrite-Pyrrhotite+Pyrite (the latter includes marcasite and magnetite) and Zn-Cu-Fe were

constructed from the data in Tables 9 and 12. These diagrams show the mineralogical and chemical compositions of each ore type, respectively (Figs. 5 and 6). Comparing the two diagrams, it is apparent that the Sphalerite-Chalcopyrite-Pyrrhotite+Pyrite diagram which is based on mineralogy, shows slightly less overlaps of fields, providing superior discrimination between the ore types, than the Zn-Cu-Fe diagram. This is primarily due to the many Fe-bearing minerals, occurring in a large number of minerals including chalcopyrite and sphalerite, and thereby being indiscriminant.

TABLE 11

AVERAGE MINERAL QUANTITIES OF THE ORE MINERALS IN EACH ORE TYPE.

ORE TYPE.	Py	Cp	Sp	Po.	Gal	Fr	Asp	Gang
MASSIVE SPHALERITE.	1.86	3.84	71.63	2.75	3.53	0.01	0.00	16.39
LAYERED PYRITE + SPHALERITE.	46.68	1.13	32.39	0.02	1.28	0.02	5.12	13.36
MASSIVE PYRITE.	73.67	0.21	1.45	0.01	1.27	0.03	0.05	23.30
MIXED/LAYERED CHALCOPYRITE + SPHALERITE.	13.62	20.93	18.83	7.71	0.00	0.00	0.02	38.89
MASSIVE CHALCOPYRITE + PYRRHOTITE.	21.21	34.33	0.66	21.31	0.00	0.00	0.00	22.46
CHALCOPYRITE STRINGERS.	11.25	34.22	5.19	5.01	0.00	0.00	0.00	44.33
DISSEMINATED PYRITE + CHALCOPYRITE.	34.37	1.73	0.58	0.03	0.02	0.00	0.02	63.25
SHEARED CHALCOPYRITE + SPHALERITE.	3.94	18.49	37.20	10.97	0.00	0.00	0.00	29.39
VEIN QUARTZ + CHALCOPYRITE.	3.28	68.08	1.05	0.90	0.00	0.00	0.00	26.69

TABLE 12

## INTERPRETED MINERALOGICAL COMPOSITION OF THE ORE TYPES.

MINERAL	Massive Sp	Layered Py+Sp	Massive Py	Mixed/Layered Cp+Sp	Massive Cp+Po	Cp Stringers	Dissem. Py+Cp	Sheared Cp+Sp	Vein Qtz+Cp
Gangue	20.16	18.11	18.42	30.28	20.92	32.96	61.54	31.52	86.84
Pyrite	5.15	42.44	74.85	16.30	21.31	20.35	38.46	3.33	2.14
Pyrrhotite	2.70	0.02	0.01	7.70	21.30	5.00	0.03	11.00	0.90
Sphalerite	63.20	33.17	5.57	29.60	0.70	4.60	0.58	38.70	0.72
Chalcopyrite	5.10	1.77	0.56	16.00	35.70	36.50	3.90	15.40	9.40
Galena	3.60	1.25	0.34	0.01	0.00	0.05	0.01	0.01	0.00
Arsenopyrite	0.09	3.24	0.25	0.08	0.07	0.54	0.05	0.04	0.00
Au-Ag-Hg Alloy	0.00036	0.00098	0.00025	0.00097	0.00080	0.00054	0.00024	0.00165	0.00148
Cubanite				X	X	X	X		X
Freibergite	X	X	X						
Gudmundite	X	X						X	
Pyrargyrite	X	X							
Dyscrasite	X								
Boulangerite		X							
Freieslebenite		X							
Costibite								X	
Clausthalite	X			X		X			
Hessite						X		X	
Rucklidgeite						X			
Pilsenite						X			

Note 1. Volume% data determined by image analysis and calculations from assays; Au-Ag-Hg alloy is here assumed to be the sole Au-bearing mineral, and thus includes minor 'invisible' gold in pyrite and arsenopyrite.

2. Pyrite data includes minor marcasite and magnetite.

3. Chalcopyrite data includes trace cubanite.

4. Bournonite, Volynskite, Naumannite and Acanthite were observed in the mill products only; omitted.

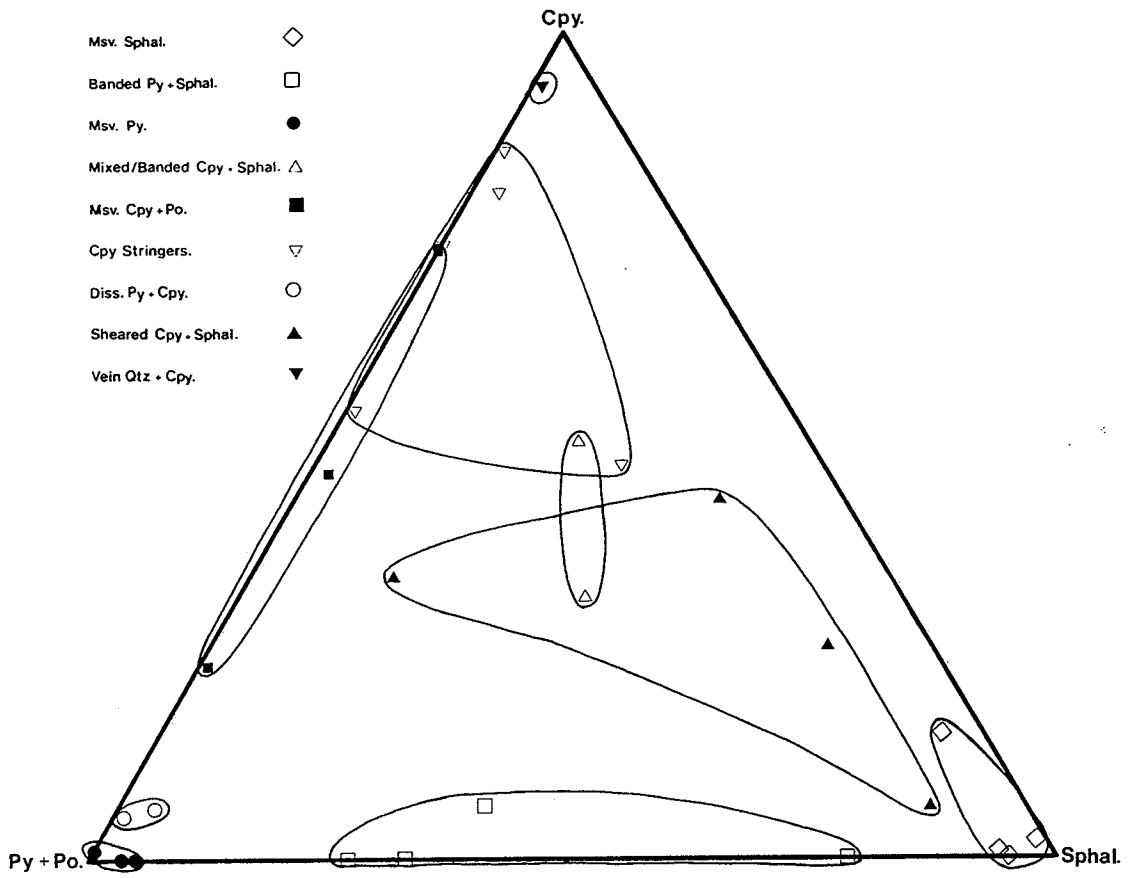


Figure 5: Sphalerite-Chalcopyrite-Pyrrhotite+Pyrite Triangular Diagram. The mineralogical composition of each sample in the suite of representative ore samples is designated by ore type and plotted. Compositional fields of the ore types are outlined.

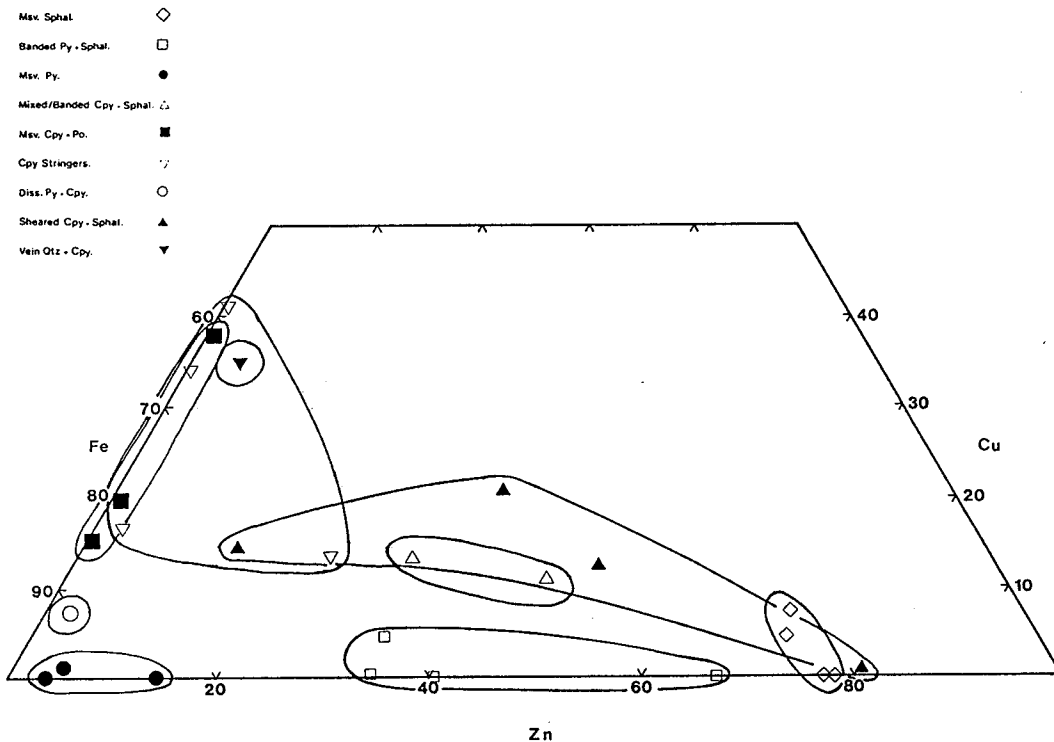


Figure 6: Triangular Diagram of Bulk Chemical Compositions in the Zn-Cu-Fe System. The chemical composition of each sample in the suite of representative ore samples is designated by ore type and plotted.

## 5.2 DETAILED CHARACTERISTICS

### 5.2.1 MASSIVE SPHALERITE ORE TYPE

The Massive Sphalerite ore type occurs in the immediate hangingwall of the ore lenses. Ten samples corresponding to this ore type were taken from the ore lenses 1N<sup>2</sup>, 2N, 1S, 3S and 5S. The average chemical composition of 4 representative samples of this ore type is 37.9 wt% Zn, 1.72 wt% Cu, 3.11 wt% Pb, 131ppm Ag and 1.5ppm Au (See Table 9). The average mineralogical composition for the same samples is 63.2 wt% sphalerite, 5.2 wt% pyrite (includes trace magnetite and marcasite), 5.1 wt% chalcopyrite, 3.6 wt% galena and trace amounts of freibergite, pyrargyrite and Au-Ag-Hg alloy (See Table 12). It is interpreted that the gold occurs largely in Au-Ag-Hg alloy, and the silver in sphalerite, freibergite, pyrargyrite, galena and pyrite. This ore type plots near the sphalerite apex of the Sphalerite-Chalcopyrite-Pyrrhotite + Pyrite triangular diagram and the Zn apex of the Zn-Cu-Fe triangular diagram (See Fig. 5 and Fig. 6, respectively).

The ore consists of semi-massive to massive sphalerite. The massive sphalerite envelopes the gangue, pyrite and other minor to trace minerals (Fig. 8A). Size analysis data shows that 55% of the sphalerite occurs in grains that are larger than 208um (Fig. 7). The gangue is foliated and consists of lenses and rafts of carbonate (calcite), quartz, chlorite, sericite and biotite. The foliation is commonly defined by schistose flakes of chlorite, sericite and/or biotite disseminated throughout the ore.

---

<sup>2</sup> The names of the lenses have been abbreviated to a two-character term, in which the first character designates the lens number, and the second character designates the zone e.g., 1N denotes No. 1 lens of the north zone.

The pyrite occurs as small disseminated grains and metacrysts in sphalerite (Fig. 8A). The disseminations are concentrated in zones which form diffuse, thin laminae, and which may define the primary banding of the ore. The metacrysts are variably corroded and rounded by the surrounding sphalerite and this leads to the development of 'atoll texture' (Fig. 8B), where the pyrite is replaced by sphalerite, and more rarely galena and pyrrhotite. The pyrite is less commonly fractured and invaded by sphalerite, and some is replaced by fine-grained marcasite.

The chalcopyrite occurs as blebs and rods along crystallographically oriented planes in sphalerite, and as interstitial-fillings between sphalerite grains (Fig. 8C). The blebs and rods of chalcopyrite in sphalerite are referred to here as chalcopyrite-disease<sup>3</sup>. Commonly a gradation is discernible from the chalcopyrite-disease to abundant interstitial blebs and films which coalesce to form masses of chalcopyrite (See Fig. 8D). The cumulative size distribution curve for chalcopyrite shows a change in slope at 13 $\mu$ m (Fig. 7). It is interpreted from this size distribution data that most of the chalcopyrite smaller than 13 $\mu$ m occurs as chalcopyrite-disease, whereas the remainder is interstitial fillings between sphalerite grains. It follows from this interpretation that about 40% of the chalcopyrite in the Massive

---

<sup>3</sup> Chalcopyrite intergrowths in sphalerite can be produced by exsolution, coprecipitation, epitaxy, replacement, recrystallization and segregation, decomposition of a metastable Cu-Zn-S phase, and supergene processes (Eldridge et al. 1983, 1988). Barton & Bethke (1987) use the term chalcopyrite-disease strictly to describe chalcopyrite intergrown with Fe-poor sphalerite that is replacing Fe-rich sphalerite. Scott (1983) notes that the crystallographically rational intergrowth of chalcopyrite in sphalerite from metamorphic deposits is probably the product of recrystallized chalcopyrite-disease. Nonetheless, the term is used here for convenience to describe the texture of the latter process of metamorphic recrystallization.

Sphalerite ore type occurs as chalcopyrite-disease. Some of the interstitial chalcopyrite occurs as elongate masses which parallel the preferred orientation of the chalcopyrite-disease within the foliated and twinned sphalerite. Both features define a foliation in the sphalerite which is parallel to the schistosity defined in the gangue minerals, and to the probable primary mineralogical banding of the ore.

Galena occurs as disseminated blebs (<10um) and grains in sphalerite, and as interstitial fillings between sphalerite grains (Fig. 8E). The cumulative size distribution curve for galena shows three slopes (Fig. 7). It is interpreted that the slope for galena below 10um represents blebs in sphalerite, the 10 to 37um slope represents discrete grains in sphalerite, and the third slope, which parallels the chalcopyrite size distribution curve in that region, represents galena masses in the interstices between sphalerite grains. This analysis suggests that 25% of the galena occurs as blebs, 50% as grains, and 25% as interstitial masses. The galena, like chalcopyrite, defines a foliation by occurring along sphalerite-sphalerite, sphalerite-pyrite and sphalerite-gangue grain boundaries, which are themselves parallel to the schistosity. Freibergite, gudmundite and pyrargyrite occur as inclusions in galena; the freibergite as fine-grained (<30um) rounded inclusions forming marginally within galena; gudmundite as subhedral bladed inclusions; and the pyrargyrite as anhedral, fine-grained (<20um) inclusions associated with pyrrhotite.

Pyrrhotite occurs as masses and rounded inclusions in chalcopyrite; in composite grains and blebs of chalcopyrite + galena + pyrrhotite; and as oriented blebs and rods in sphalerite, analogous to the chalcopyrite-

disease. Chalcopyrite and pyrrhotite exhibit straight to curved contacts with sphalerite, though carious to myrmekitic interpenetrative contacts are less commonly developed due to recrystallization during and after shearing (Fig. 8F for example of carious to myrmekitic textures).

Arsenopyrite occurs as diffuse laminations of fine-grained euhedral to subhedral grains disseminated in sphalerite. These laminations in sphalerite probably represent primary mineralogical banding inherited from the initial ore-forming process (Fig. 8G).

One grain of Au-Ag-Hg alloy was observed in sample TLS.1-52. The grain measured 15 x 15um and occurred as a rounded inclusion in an unfractured pyrite porphyroblast. EMPA of this grain gave the highest Hg content (i.e., 30.9 wt% Hg) in the Au-Ag-Hg alloy from Trout Lake.

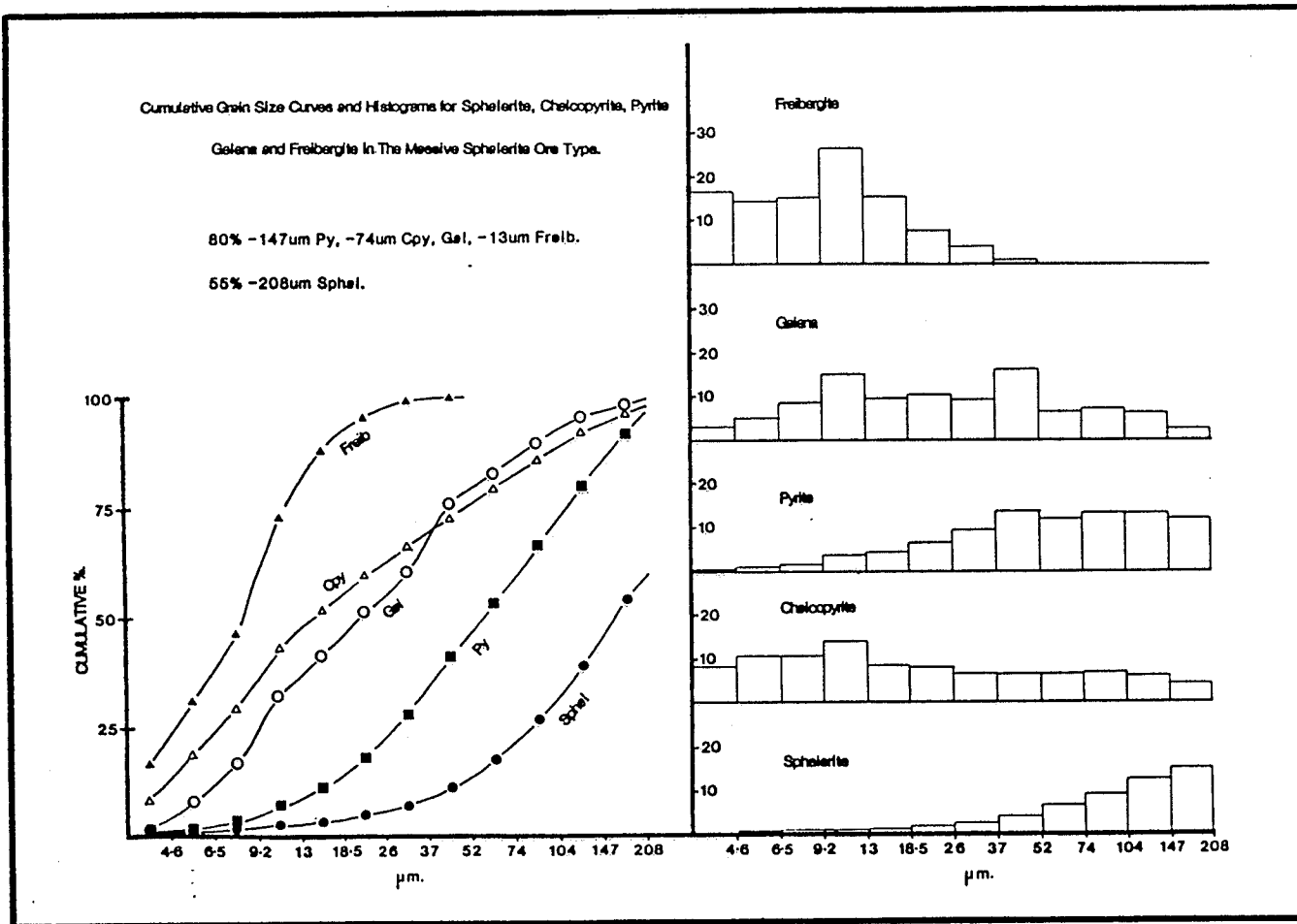


Figure 7: Grain Size Distributions in the Massive Sphalerite Ore Type. Cumulative curves and histograms of the grain size distributions of pyrite, chalcopyrite, sphalerite, galena and freibergite are shown. The 80% passing size of each mineral is given, except sphalerite for which the 55% passing size is given.

**FIGURE 8: PLATE OF PHOTO-MICROGRAPHS.**

A. Sample TLS.5-111: A Massive Sphalerite (Sp) ore with disseminated pyrite (Py) grains and foliated gangue grains. Plane Polarized Reflected Light (PPRL). Scale bar = 325um.

B. Sample TLS.2-55: Pyrite euhedra that have well developed atoll texture, disseminated in a matrix of sphalerite. Note the arsenopyrite (Asp) metacrysts and porphyroclasts with fractures, pits and reticulate replacements of sphalerite. PPRL. Scale bar = 160um.

C. Sample TLN.2-114: Sphalerite with interstitial chalcopyrite (Cp) and exquisitely formed chalcopyrite disease. Chalcopyrite blebs are alligned along the straight to slightly curved twin lamellae in the sphalerite. PPRL with the Illuminator Field Diaphragm virtually closed. Scale bar = 325um.

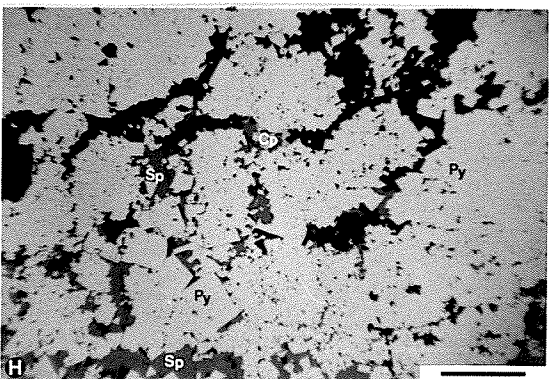
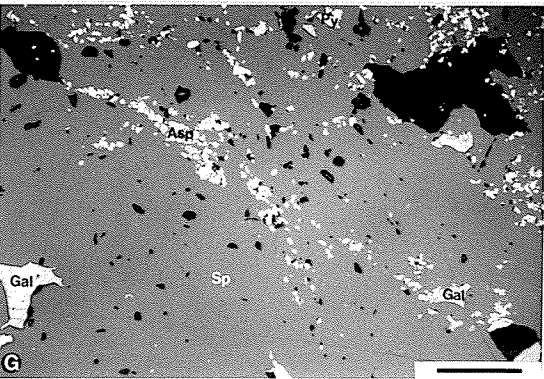
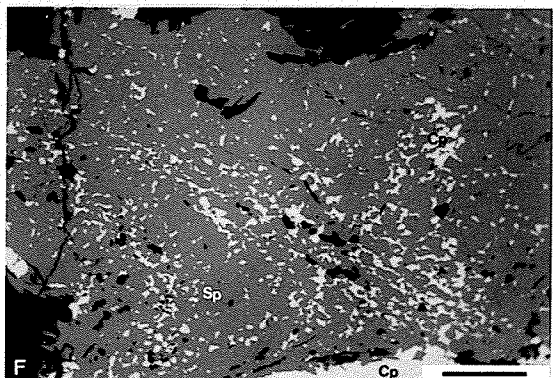
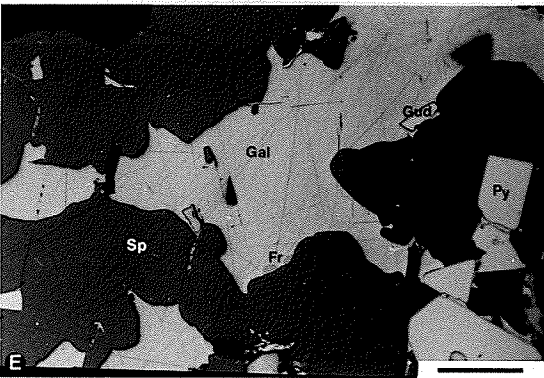
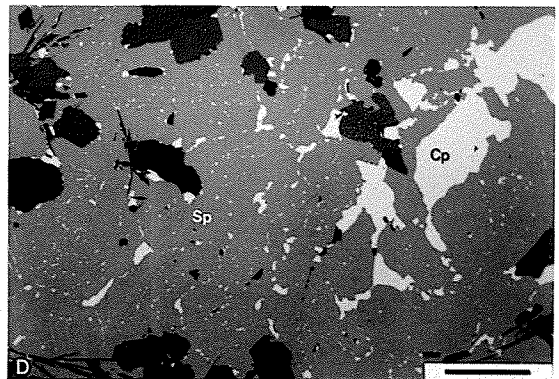
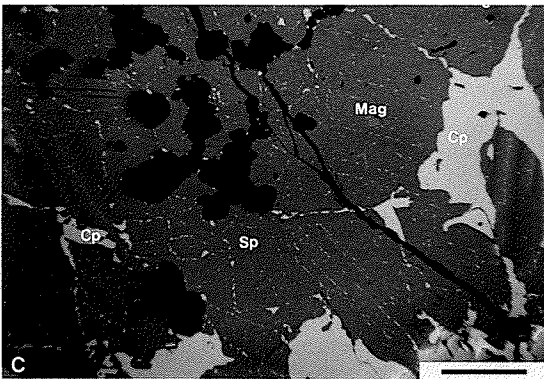
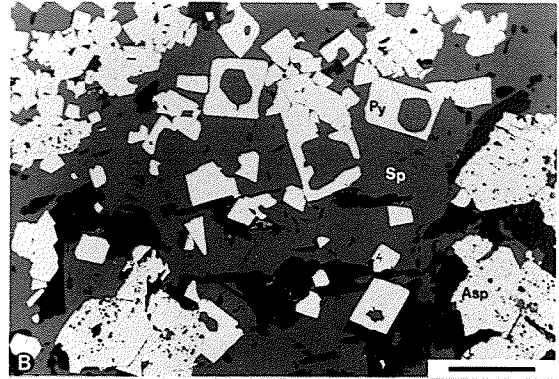
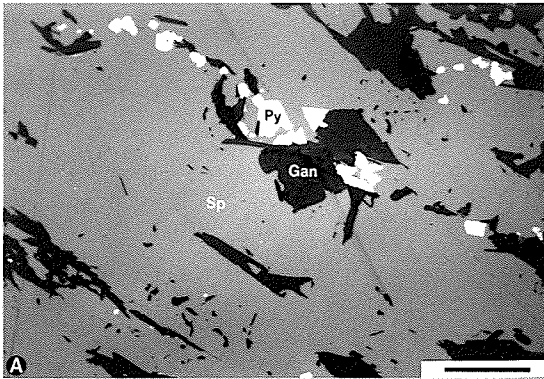
D. Sample TLN.2-74: Interstitial blebs, films and wedges of chalcopyrite and lesser pyrrhotite (Po) coalescing between and partially enveloping sphalerite grains. Note the well developed chalcopyrite-disease, and the smooth, straight to curved sphalerite-chalcopyrite grain contacts. PPRL. Scale bar = 160um.

E. Sample TLS.5-64: A Massive Sphalerite ore with an interstitial mass of galena (Gal) which contains inclusions of gudmundite (Gud) and freibergite (Fr). Note the fine-grained rounded inclusions of freibergite formed on the margin of the galena. PPRL. Scale bar = 160um.

F. Sample TLN.2-12: Carious blebs of chalcopyrite in massive sphalerite. Note the WNW trending foliation in the blebs, interpreted as a shear plane. PPRL. Scale bar = 160um.

G. Sample TLS.2-26: A diffuse lamination consisting of clusters of fine-grained, euhedral, rhombic arsenopyrite grains in a sphalerite matrix. Note the disseminated anhedral galena, and corroded pyrite grains. PPRL. Scale bar = 160um.

H. Sample TLS.2-69: A Massive Pyrite ore with interstitial sphalerite, chalcopyrite and gangue (black). PPRL Scale bar = 325um.



### 5.2.2 MASSIVE PYRITE ORE TYPE

The Massive Pyrite ore type generally occurs in the hangingwall to central parts of the ore lenses. Eleven samples corresponding to this ore type were taken for study from lenses 1N, 1S, 2S, 3S and 5S (Fig. 3 and Fig. 4). This ore type has an average grade of 3.34 wt% Zn, 0.19 wt% Cu, 0.29 wt% Pb, 44ppm Ag and 1.24ppm Au (See Table 9). It contains 74.9 wt% pyrite (includes trace magnetite + marcasite), 5.6 wt% sphalerite and 0.6 wt% chalcopyrite, 0.34 wt% galena, 0.25 wt% arsenopyrite, 0.01 wt% pyrrhotite and trace amounts of freibergite and Au-Ag-Hg alloy. The gold is interpreted to occur largely in Au-Ag-Hg alloy and to a lesser extent in pyrite, whereas much of the silver occurs in pyrite and freibergite. This ore type plots near the pyrite + pyrrhotite apex on the Sphalerite-Chalcopyrite-Pyrrhotite + Pyrite triangular diagram, and the Fe apex of the Zn-Cu-Fe triangular diagram (See Figs. 5 and 6, respectively).

The ore consists of semi-massive to massive pyrite with interstitial sphalerite, chalcopyrite, and lesser galena, freibergite and pyrrhotite (Fig. 8H). The pyrite occurs as polygonal masses that are composed of individual pyrite grains, and as porphyroblasts that are up to 500um in diameter. Commonly the pyrite has been granulated and fractured and the cleavages and fractures are infilled with interstitial minerals, particularly chalcopyrite. Minor amounts of marcasite commonly occur along grain boundaries of fractured pyrite. In addition, in semi-massive samples, the pyrite is occasionally smeared out to produce schistose

pyrite and/or web-like to dendritic fringes on pyrite, or remobilised into veinlets. These textures suggest locally intense deformation. Image analysis shows that most of the pyrite grains range from 10 to 208um in diameter; 98 wt% are smaller than 208um; the mean size is about 45um; and the median size is approximately 65um in diameter (See Fig. 9). The size analysis was done in such a manner that the size is the uninterrupted length on the pyrite surface between grain boundaries, fractures and inclusions. The grain sizes are therefore the sizes of unbroken regions within pyrite grains. Thus, coarse-grained pyrite porphyroclasts are likely be measured as being finer-grained, because of fractures and inclusions in the porphyroclasts.

The sphalerite, chalcopyrite and lesser galena, pyrrhotite and freibergite occur as (1) interstitial fillings in massive pyrite (Fig. 11A), (2) as replacements of pyrite along fractures and cleavages (Fig. 11B), (3) as replacements of individual grains in the massive pyrite, and (4) as rounded inclusions in pyrite (Fig. 11C). The replacement of pyrite grains by sphalerite produces an intricate network of sphalerite in pyrite (Fig. 11D). This network will be referred to in this report as 'dendritic-like replacements'. It is interpreted that the rounded inclusions in pyrite, shown in Figure 11C, represent grains that were entrapped during recrystallization of pyrite. Size analysis of the chalcopyrite and sphalerite, determined with the image analyser provide the general size distributions for interstitial minerals in this ore. The median size for both minerals is approximately 11um. The chalcopyrite, however, has a larger -4.6um fraction, which probably reflects the veinlets in pyrite. Conversely, the sphalerite has a

larger +18.5um fraction, because it contains proportionally less veinlets and a greater predominance of interstitial fillings. Magnetite occurs as subhedral to anhedral equant grains that are commonly fractured, embayed and invaded, dominantly by chalcopyrite and sphalerite.

Au-Ag-Hg alloy was observed in 3 of the 10 samples studied petrographically. It is generally associated with sphalerite and chalcopyrite, and occurs as fracture-fillings in, inclusions in, and in the interstitial spaces between, pyrite grains.

Abundant interstitial masses of tetrahedrite + galena + sphalerite + arsenopyrite + chalcopyrite were observed in sample TLS.2-40(#2), which is transitional between the Massive Pyrite and the Layered Pyrite + Sphalerite ore types. Interestingly, abundant Au-Ag-Hg alloy is intimately associated with these masses (Fig. 11E).

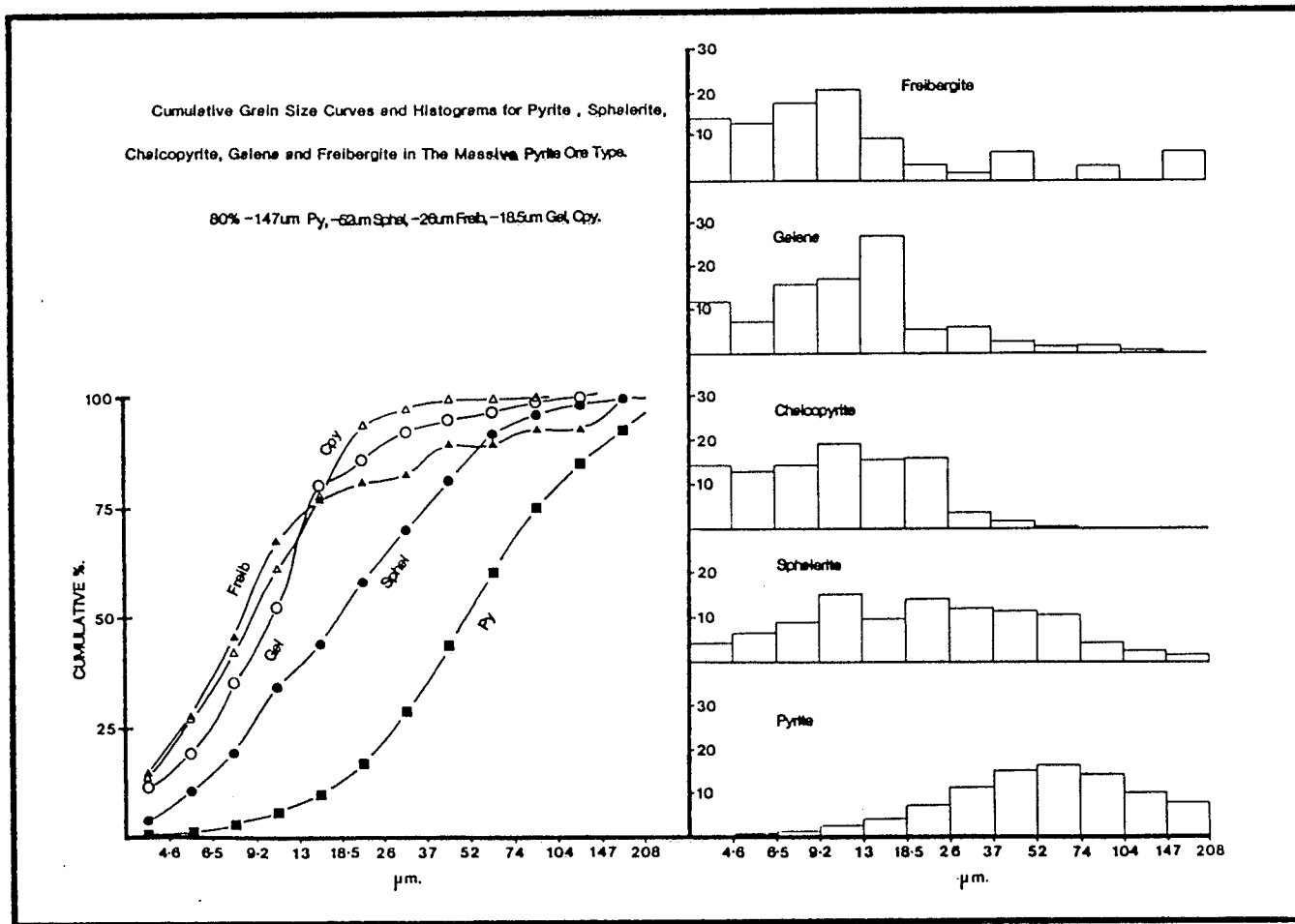


Figure 9: Grain Size Distributions in the Massive Pyrite Ore Type. Cumulative curves and histograms of grain size distributions of pyrite, chalcopyrite, sphalerite, galena and freibergite are shown. The 80% passing size of each mineral is given.

### 5.2.3 LAYERED PYRITE + SPHALERITE ORE TYPE

The Layered Pyrite + Sphalerite ore type occupies the intermediate range between the Massive Pyrite and the Massive Sphalerite ore type in terms of composition, texture and stratigraphic location. It occurs in the hangingwall to central parts of the lenses. This ore type contains an average composition of 19.9 wt% Zn, 0.6 wt% Cu, 1.07 wt% Pb, 80ppm Ag and 4.0ppm Au (See Table 7). It is composed of approximately 51 wt% pyrite (includes trace magnetite and marcasite), 27 wt% sphalerite, 1.4 wt% chalcopyrite, 1 wt% galena, minor to trace freibergite, and trace amounts of gudmundite, pyrargyrite, Au-Ag-Hg alloy, dyscrasite, freieslebenite and boulangerite (See Table 12). This ore type plots as a thin band on, or adjacent to, the sphalerite-pyrrhotite + pyrite join of the Sphalerite-Chalcopyrite-Pyrrhotite + Pyrite triangular diagram, and similarly on the Zn-Fe join of the Zn-Cu-Fe triangular diagram (See Figs. 5 and 6, respectively). The ore consists of finely (<1mm) to coarsely (<1cm) banded pyrite and sphalerite laminae (Fig. 11F). Mineralogical banding may also be manifest as laminae of gangue superimposed on the pyrite-sphalerite banding. The gangue, however, is generally distributed diffusely, or as pods and rafts in the ore.

The pyrite laminae consist essentially of pyrite and gangue in a matrix of sphalerite. The pyrite occurs as annealed masses, porphyroblasts, and as diffusely laminated disseminations in sphalerite. The annealed masses display the same features as in the Massive Pyrite ore type (previous section), and contain sphalerite, chalcopyrite, galena and pyrrhotite in the interstices. These laminae commonly contain fractured pyrite that is invaded and/or replaced along fractures and

cleavages by sphalerite, chalcopyrite, galena, pyrrhotite and marcasite. Dendritic replacements of pyrite by sphalerite, galena and chalcopyrite are also common. Similarly, individual pyrite grains in sphalerite have features that are common in the Massive Sphalerite ore type. In particular, the pyrite is generally unfractured, while 'atoll-texture' is commonly developed in pyrite grains, where the pyrite is embayed and the cores have been preferentially replaced by sphalerite and associated lesser minerals.

The sphalerite occurs as massive sphalerite in the sphalerite laminae, and as the predominant interstitial mineral in the pyrite laminae. The median grain size of the sphalerite is approximately 90 $\mu$ m. The sphalerite contains negligible to abundant chalcopyrite-disease. The sphalerite laminae contain chalcopyrite, galena and/or pyrrhotite as interstitial fillings between the sphalerite grains. The chalcopyrite and galena grain size distributions give median sizes of approximately 11 $\mu$ m for both minerals, and reflects the predominance of chalcopyrite-disease and fine-grained blebs and wedges of chalcopyrite and galena.

The galena tends to be preferentially concentrated in the pyrite laminae forming interstitial masses that envelope, invade, cement and/or corrode the pyrite grains (Fig. 11G). Less commonly the galena occurs associated with freibergite in foliated scaly masses of marcasite that are interpreted to have formed in shear zones (Fig. 11H). Freibergite, gudmundite, pyrargyrite, freieslebenite, boulangierite and dyscrasite occur exclusively associated with galena, either as fine-grained inclusions (Fig. 13A), or in the case of freibergite only, as discrete grains adjacent to or intimately associated with the galena (Fig. 13B).

The grain size distributions for freibergite indicates a strong break of slope at approximately 30um, with a median size of approximately 45um. The -40um material probably corresponds to the fine-grained inclusions in galena, whereas the +30um material corresponds to the coarser-grained inclusions in galena, and the discrete interstitial grains. Thus, approximately 50% of the freibergite occurs as fine-grained rounded inclusions in galena.

Both arsenopyrite and magnetite occur as metacrysts and porphyroblasts, and exhibit a mineral banding that is superimposed on the pyrite-sphalerite banding. The arsenopyrite occurs as unfractured, fine-grained disseminations defining thin laminations within the sphalerite laminae, and as diffuse laminae of commonly fractured grains within the massive pyritic laminae (Fig. 13C). The magnetite commonly occurs as fractured and corroded equant grains that are enveloped and invaded by sphalerite and chalcopyrite (Fig. 13D), and which also contains rounded inclusions of pyrite, chalcopyrite and sphalerite.

Au-Ag-Hg alloy was observed in 7 of the 24 samples of this ore type, and occurs as inclusions in pyrite, along grain boundaries and in fractures in pyrite. It also occurs as inclusions in freibergite and galena within the interstices between pyrite grains.

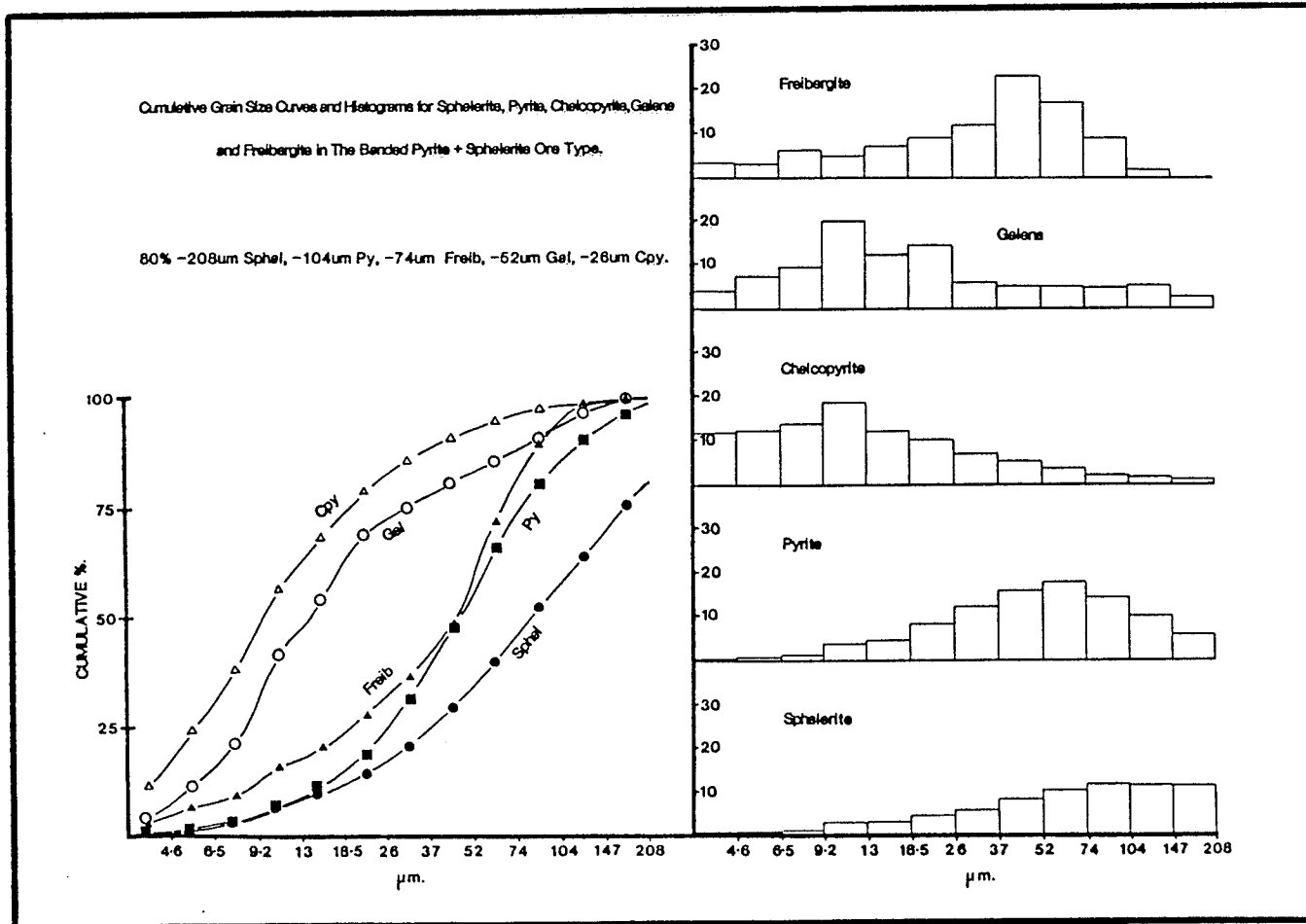


Figure 10: Grain Size Distributions in the Layered Pyrite + Sphalerite Ore Type. Cumulative curves and histograms of the grain size distributions of pyrite, chalcopyrite, sphalerite, galena and freibergite are shown. The 80% passing size of each mineral is given.

**FIGURE 11: PLATE OF PHOTO-MICROGRAPHS.**

A. Sample TLS.5-83A: Interstitial galena (Gal), freibergite (Fr) and sphalerite (Sp) enveloping, invading and corroding fractured and partially granulated pyrite (Py). Plane Polarized Reflected Light (PPRL). Scale bar = 160um.

B. Sample TLS.1-48: Interstitial chalcopyrite (Cp) enveloping, invading and replacing deformed and fractured pyrite along fractures and cleavages. PPRL. Scale Scale = 325um.

C. Sample TLS.3-35(#2): Fine-grained rounded inclusions of sphalerite in partially deformed and corroded pyrite. PPRL. Scale bar = 160um.

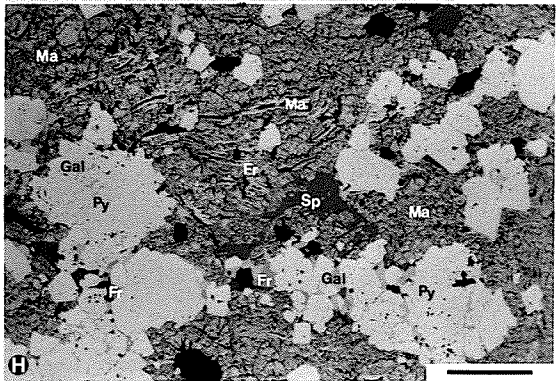
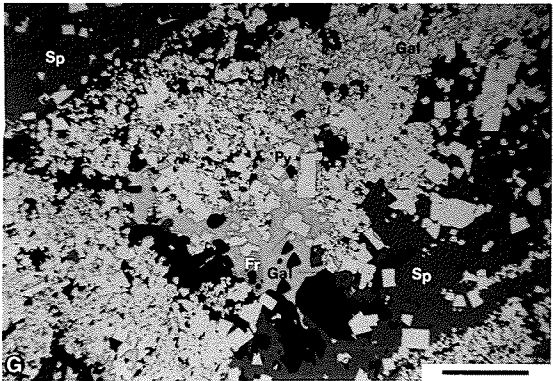
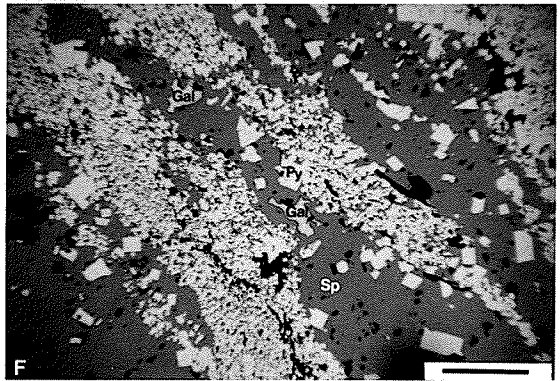
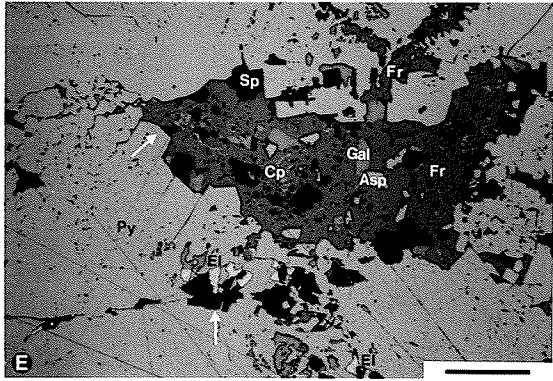
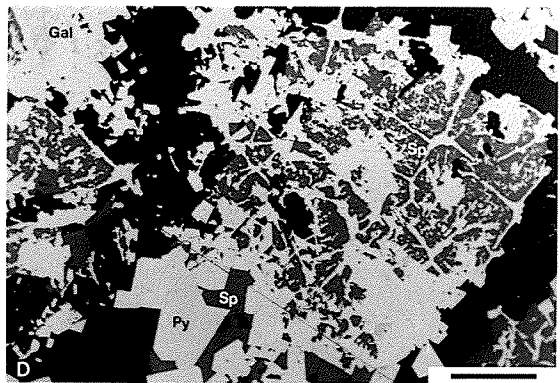
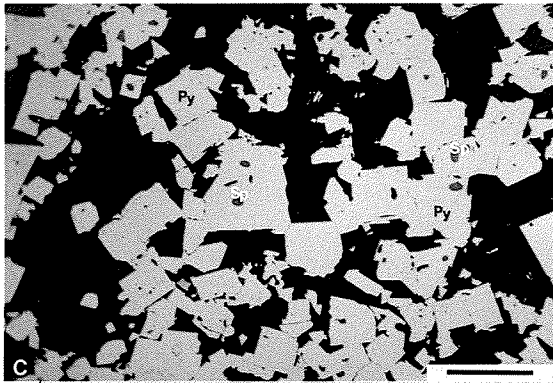
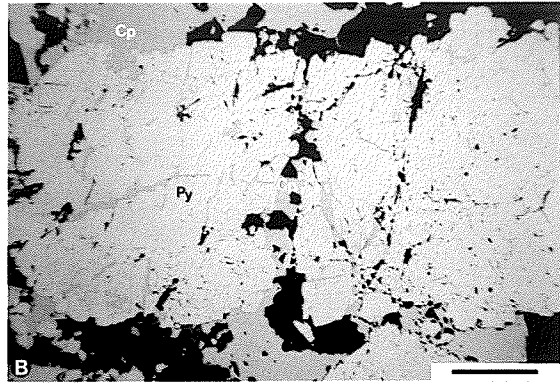
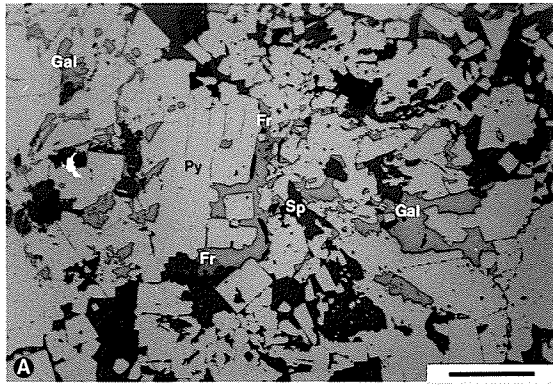
D. Sample TLS.5-111: Dendritic sphalerite and subordinate galena replacing deformed and ruptured pyrite. Note unfractured pyrite grain at bottom left is not replaced by sphalerite. PPRL. Scale bar = 160um.

E. Sample TLS.2-40(#2): A large interstitial mass of freibergite (Fr) in massive annealed pyrite. The freibergite contains arsenopyrite (Asp), galena, sphalerite, exsolved chalcopyrite and disseminations of extremely fine-grained Type 1 Au-Ag-Hg alloy (El). The alloy also occurs as coarser-grained interstitial grains and fracture-fillings associated with freibergite and galena in pyrite. PPRL. Scale bar = 160um.

F. Sample TLS.2-26: Mineral banding of pyrite and sphalerite that is characteristic of the Layered Pyrite + Sphalerite ore types. Note rare anhedral grains of galena in both the sphalerite and pyrite laminae. PPRL. Scale bar = 325um.

G. Sample TLS.2-26: Interstitial galena with inclusions of freibergite enveloping and corroding annealed pyrite. Note the absence of galena and freibergite in the sphalerite laminae. PPRL. Scale bar = 325um.

H. Sample TLS.1-100: Scaly masses of marcasite (Ma) associated with freibergite, galena, sphalerite and pyrrhotite (Po), enveloping and replacing pyrite. Note the foliated wisps of marcasite. PPRL. Scale bar = 160um.



#### 5.2.4 MIXED/LAYERED CHALCOPYRITE + SPHALERITE ORE TYPE

The Mixed/Layered Chalcopyrite + Sphalerite ore type was found to occur across virtually the entire width of the massive exhalative ore (i.e., excluding the stockwork ore) in lens 2N, and all 5 samples of this ore type were taken from lens 2N. The apparently exclusive occurrence of this ore type in lens 2N is significant because this lens exhibits (1) pronounced disturbance of the generalized Cu/(Cu+Zn) distribution, (2) loss of the stratigraphic control on ore type location within the lens, and (3) intrusion by a quartz-diorite sill. The average chemical composition of 2 representative samples is 17.8 wt% Zn, 5.43 wt% Cu, 0.01 wt% Pb, 58ppm Ag and 4.05ppm Au. The average mineralogical composition for the same samples is 29.6 wt% sphalerite, 16.0 wt% chalcopyrite, 0.01 wt% galena (includes clausthalite), 16.3 wt% pyrite (includes minor magnetite), 7.7 wt% pyrrhotite, and trace amounts of arsenopyrite and Au-Ag-Hg alloy. Sphalerite and chalcopyrite are interpreted to be the main hosts of the Ag in this ore type, whereas Au is hosted in Au-Ag-Hg alloy. This ore type plots in the center of the Sphalerite-Chalcopyrite-Pyrrhotite + Pyrite triangular diagram, and centrally towards the Fe-Zn join of the Zn-Cu-Fe triangular diagram (See Figs. 5 and 6, respectively).

The ore consists of massive to semi-massive sulfides with pods, bands or rafts of gangue, or with diffusely distributed gangue. The sphalerite, chalcopyrite and pyrrhotite envelope and occur interstitially to the gangue and pyrite, and can be considered as forming the matrix (Fig. 13E).

The pyrite varies from fine-grained to less commonly coarse-grained, granulated, fractured and rounded grains. The grains are invariably enveloped, invaded and replaced by the matrix sulfides, commonly as a texture that may be described as 'rounded islands of pyrite in a sea' of chalcopyrite, sphalerite and pyrrhotite (Fig. 13F). Chalcopyrite and sphalerite also occur as dendritic-replacements in pyrite, whereas magnetite forms reticulate-textured fringes and zones in the pyrite (See Fig. 13G, and MAGNETITE section). The grain size distribution of pyrite is 80%  $-26\mu\text{m}$ , and the median size is approximately  $15\mu\text{m}$  (Fig. 12); this is the most fine-grained pyrite of all the ore types. The break of slope in the pyrite size distribution at  $26\mu\text{m}$  is interpreted to reflect the granulated, fractured and corroded pyrite comprising the  $-26\mu\text{m}$  material, and which forms 75% of the pyrite. The remaining 25% corresponds to relatively undeformed  $+26\mu\text{m}$  pyrite.

The sulfide matrix consists essentially of sphalerite and chalcopyrite with lesser pyrrhotite, where the latter generally forms granular masses and disseminated anhedral grains in the chalcopyrite. The chalcopyrite also occurs as well developed chalcopyrite-disease in sphalerite. The contacts of these three matrix minerals are generally straight to curved, though mutually carious to myrmekitic contacts are developed along localised zones, which are interpreted to be shear planes (Fig. 8F for example of carious to myrmekitic contacts). The sphalerite and chalcopyrite grain size distributions give a median size of approximately  $125\mu\text{m}$  and  $65\mu\text{m}$ , respectively.

Minor magnetite commonly occurs as disseminated, medium-grained, fractured and corroded grains, or as clusters of grains enveloped in

matrix chalcopyrite and/or sphalerite. Arsenopyrite occurs as rare disseminated subhedral grains enveloped in the sphalerite and/or chalcopyrite. Clausthalite (identified on the basis of its higher reflectance relative to galena) was observed as rare interstitial films and fracture-fillings in fractured masses of pyrite.

Au-Ag-Hg alloy was observed in 3 of the 5 samples, and in all cases occurred spatially associated with pyrite. The Au-Ag-Hg alloy occurred along fractures and embayments in pyrite, as partial grain coatings on pyrite, as interstitial films between pyrite grains, and as inclusions in pyrite. The occurrence of Au-Ag-Hg alloy as interstitial films between pyrite grains typifies the 99 grains of Au-Ag-Hg alloy observed in sample TLN.2-8, which was taken from the ore contact with the quartz-diorite sill.

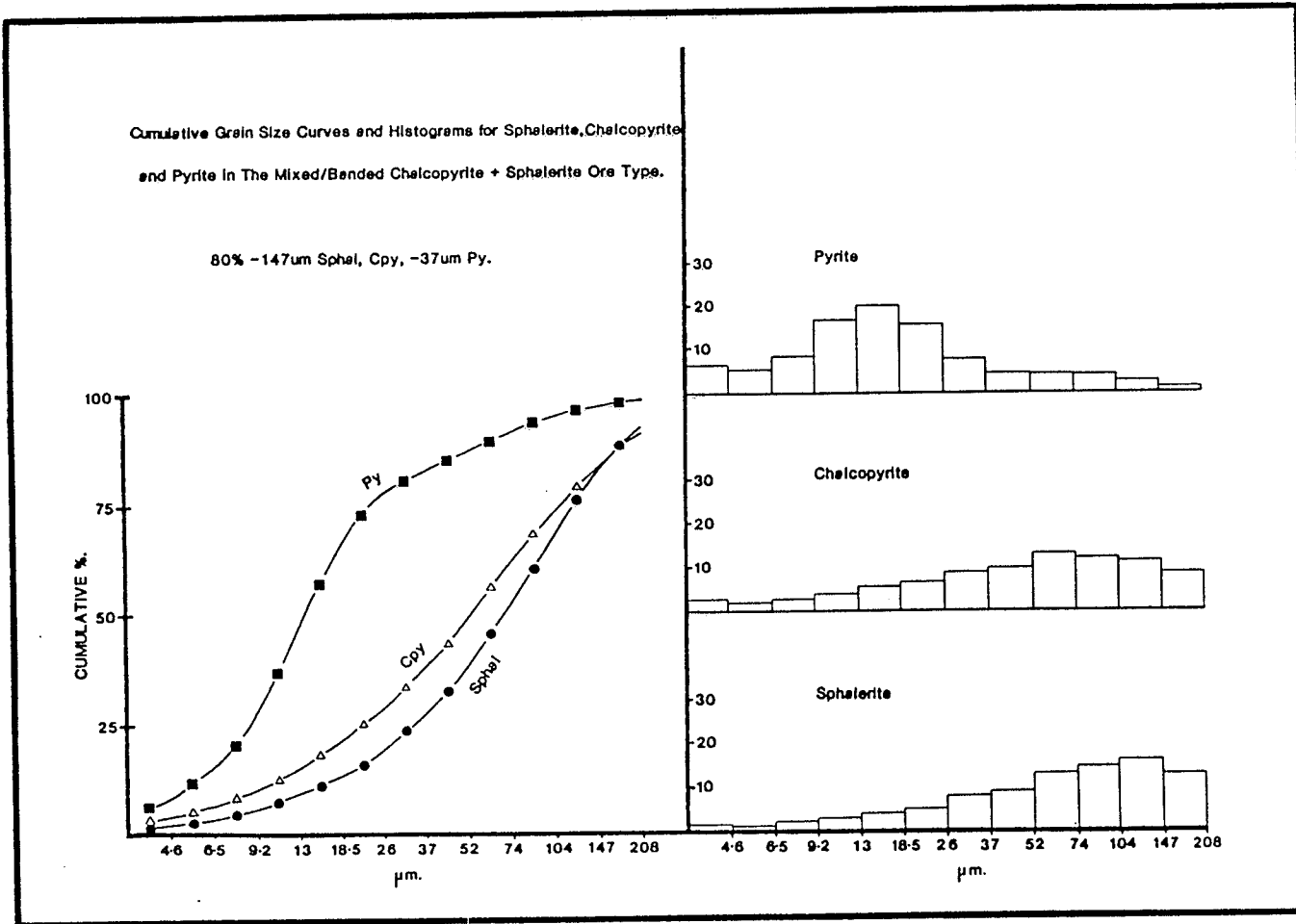


Figure 12: Grain Size Distributions in the Mixed/Layered Chalcopyrite + Sphalerite Ore Type. Cumulative curves and histograms of the grain size distributions of pyrite, chalcopyrite and sphalerite are shown. The 80% passing size of each mineral is given.

**FIGURE 13: PLATE OF PHOTO-MICROGRAPHS.**

A. Sample TLS.5-84: A Massive Sphalerite (Sp) ore with a mass of galena (Gal) that contains inclusions of gudmundite (Gud), freibergite (Fr), pyrargyrite (Pyr) and freieslebenite (Frs). Note the intimate spatial association of the freibergite, pyrargyrite and freieslebenite. Plane Polarized Reflected Light (PPRL). Scale bar = 40um.

B. Sample TLS.2-26: Medium-grained freibergite and associated galena in a Layered Pyrite (Py) + Sphalerite ore. PPRL. Scale bar = 160um.

C. Sample TLS.2-55: Fine-grained reticulate-textured sphalerite in an arsenopyrite (Asp) porphyroclast, which together with fine-grained pyrite are disseminated in the sphalerite matrix. PPRL. Scale bar = 160um.

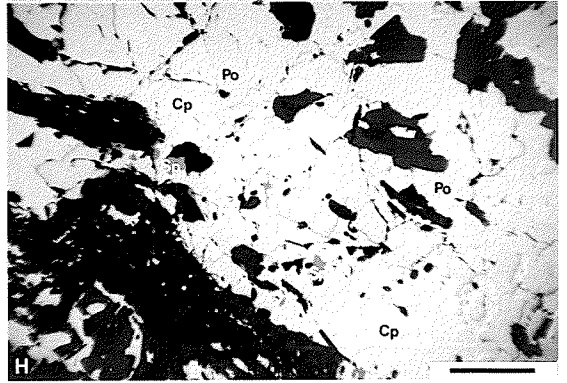
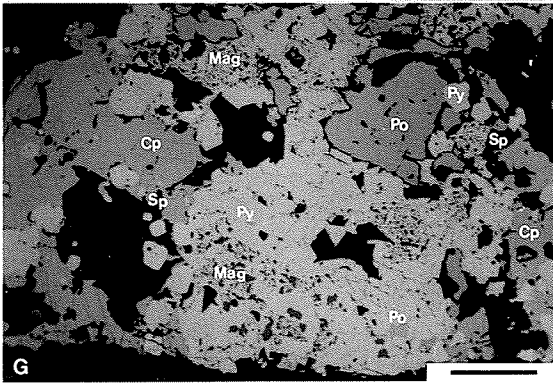
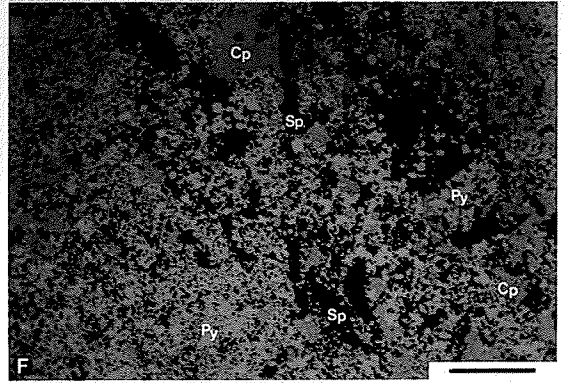
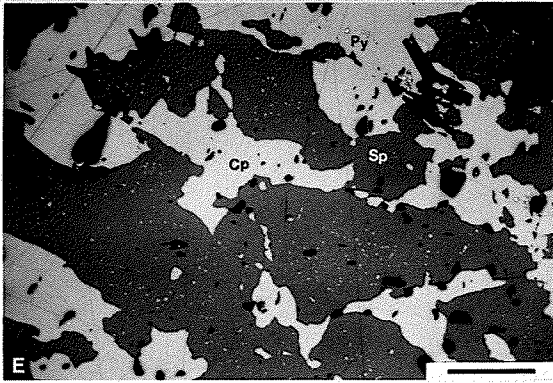
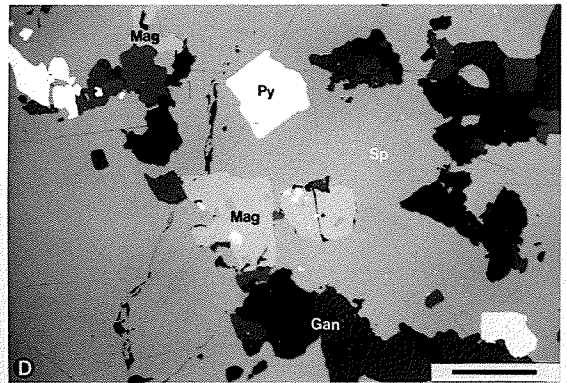
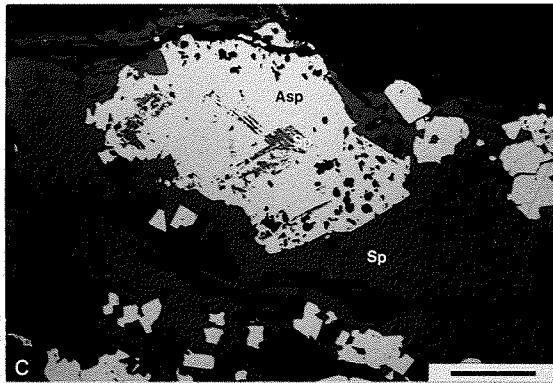
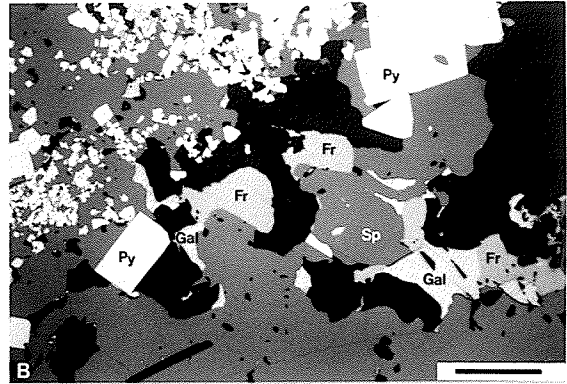
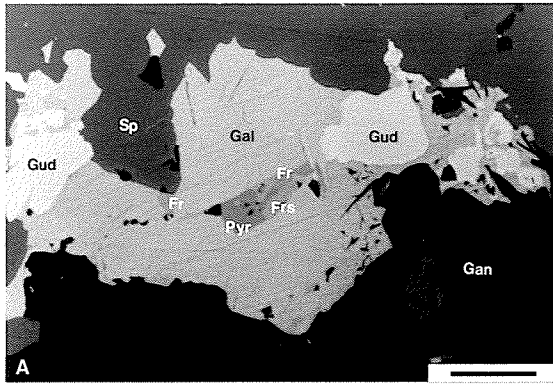
D. Sample TLS.5-41(#2): Rounded grains of magnetite (Mag) disseminated in the sphalerite matrix of a Layered Sphalerite + Pyrite ore. Note the rounded inclusions of pyrite in magnetite, and that the pyrite metacrysts are corroded by the sphalerite. PPRL. Scale bar = 160um.

E. Sample TLN.2-78: Interstitial chalcopyrite and pyrrhotite between grains of the sphalerite matrix in a Mixed/Layered Chalcopyrite + Sphalerite ore. PPRL. Scale bar = 160um.

F. Sample TLN.2-78: A Mixed/Layered Chalcopyrite (Cp) + Sphalerite ore with rounded islands of pyrite enveloped and corroded by a matrix of chalcopyrite, sphalerite and trace pyrrhotite (Po). PPRL. Scale bar = 325um.

G. Sample TLS.3-46: Granular mass of pyrite containing patches of fine-grained reticulate-textured magnetite (pyrite-magnetite sympectite) which is engulfing and replacing coarse-grained pyrrhotite. Note rounded 'islands' of pyrite enveloped in the matrix chalcopyrite (far left of field). PPRL. Scale bar = 160um.

H. Sample TLS.1-50: A Massive Chalcopyrite + Pyrrhotite ore consisting of matrix chalcopyrite containing anhedral, granular pyrrhotite and trace sphalerite, and enveloping and invading the ruptured gangue rafts. PPRL. Scale bar = 325um.



### 5.2.5 MASSIVE CHALCOPYRITE + PYRRHOTITE ORE TYPE

The Massive Chalcopyrite + Pyrrhotite ore type occurs at the center through to the base of the massive ore (exhaled ore), and stratigraphically immediately above the Chalcopyrite Stringer ore type (stockwork ore). Nine samples of this ore type were taken from lenses 2N, 1S and 3S. The average chemical composition of 3 representative samples of this ore type is 0.39 wt% Zn, 12.15 wt% Cu, 0.004 wt% Pb, 39ppm Ag and 3.36ppm Au. The average mineralogical composition for these same samples is 0.7 wt% sphalerite, 35.7 wt% chalcopyrite, 21.3 wt% pyrite (includes trace magnetite and marcasite), 21.3 wt% pyrrhotite, minor to trace magnetite and marcasite, and trace cubanite and Au-Ag-Hg alloy. It is interpreted that Au-Ag-Hg alloy hosts the Au, whereas the principal host of the Ag is probably chalcopyrite. Galena, Sb-sulfosalts and hessite were not observed in samples of this ore type, and Au-Ag-Hg alloy can only account for 10% of the Ag in the ore. This ore type plots on the centre part of the chalcopyrite-pyrrhotite + pyrite join of the Sphalerite-Chalcopyrite-Pyrrhotite + Pyrite triangular diagram, and similarly towards the Fe apex on the Fe-Cu join of the Zn-Cu-Fe triangular diagram (See Figs. 5 and 6, respectively).

The ore consists of massive to semi-massive sulfides that are mineralogically banded, principally with respect to chalcopyrite-pyrrhotite, (Fig. 13HH), and to a lesser extent with respect to chalcopyrite-sphalerite. Layers rich in magnetite and/or pyrite may be also prominent. The sulfide banding is commonly very coarse (<2cm). The gangue varies from unfoliated quartzose pods and laminae to foliated

chloritic schist laminae and rafts. The ore is very heterogeneous in terms of the relative abundance of pyrite, magnetite and sphalerite (i.e., pyrite varies from approximately 30 vol% to <0.05 vol%).

The pyrite is typically deformed, occurring as: (1) anhedral, fractured, granulated and/or rounded coarse-grained porphyroblasts; (2) rounded, corroded, embayed and fractured medium-grained disseminations; (3) ruptured annealed masses; and (4) fine-grained disseminations, particularly within rafts of gangue. Chalcopyrite, pyrrhotite and/or sphalerite typically envelope, invade and replace the pyrite, locally leading to rounded islands of fine-grained relict pyrite enveloped in chalcopyrite, pyrrhotite and/or sphalerite (Fig. 16A). Rare pyrite grains exhibit radial replacement by chalcopyrite + pyrrhotite, and circular cross-sections, suggesting relict primary spheroidal pyrite (Fig. 16B). The pyrite commonly exhibits zones and fringes of fine-grained reticulate-textured magnetite (i.e., pyrite-magnetite symplectite), and more rarely clouded patches of submicroscopic flecks of marcasite (Fig. 16C). The grain size distribution of pyrite gives a median size of approximately 65 $\mu$ m (See Fig. 14).

The chalcopyrite with subordinate pyrrhotite and minor sphalerite, envelope and occur interstitially to the gangue and the pyrite. This sulfide matrix is generally coarse-grained and banded, with laminae of granular to foliated masses of pyrrhotite enveloped by chalcopyrite. The sphalerite occurs as disseminated grains, pods and diffuse to discrete laminae of massive sphalerite with intense chalcopyrite-disease, and with chalcopyrite forming in the interstices between the sphalerite grains. The mutual contacts of chalcopyrite, pyrrhotite and

sphalerite are generally straight, though less commonly and/or locally, carious (and more rarely myrmekitic) with the development of diablastic texture. The chalcopyrite less commonly contains slightly bent exsolution lamellae of cubanite. The grain size distributions of chalcopyrite and sphalerite give median sizes of approximately 90um and 22um, respectively.

Magnetite occurs as disseminations and diffuse laminae of corroded, embayed and/or fractured porphyroblasts, as well as pods and laminae of annealed polygonal magnetite grains (Fig. 16D). The magnetite commonly contains rounded inclusions of chalcopyrite and pyrite. Magnetite commonly envelopes and invades fractured pyrite. Chalcopyrite and lesser pyrrhotite are commonly observed invading and replacing magnetite.

Au-Ag-Hg alloy was observed in 5 of the 9 samples of this ore type, and occurs as fracture-fillings in, or interstitially along the grain margins of pyrite, and is associated with interstitial chalcopyrite, sphalerite and/or pyrrhotite.

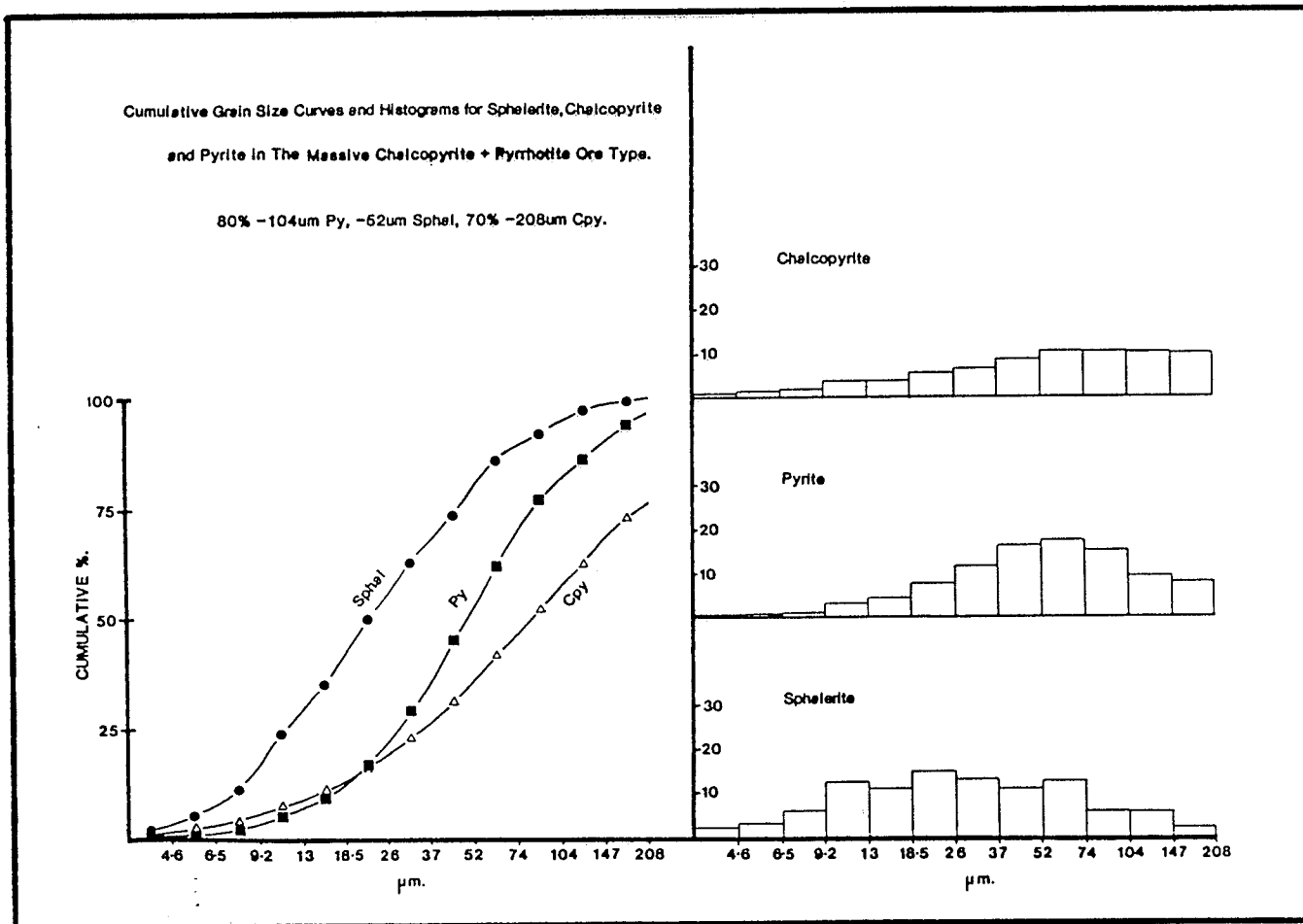


Figure 14: Grain Size Distributions in the Massive Chalcopyrite + Pyrrhotite Ore Type. Cumulative curves and histograms of the grain size distributions of pyrite, chalcopyrite and sphalerite are shown, whereas that of pyrrhotite was erased during data collection. The 80% passing size of each mineral is given.

### 5.2.6 CHALCOPYRITE STRINGER ORE TYPE

The Chalcopyrite Stringer ore type underlies, with a sharp contact, the massive ore (exhalative ore) and together with the Disseminated Pyrite + Chalcopyrite ore type (next section) constitutes the footwall stockwork mineralization. The Chalcopyrite Stringer ore grades into the Disseminated Pyrite + Chalcopyrite ore type downwards and laterally towards the margins of the lenses. Eighteen samples corresponding to this ore type were taken from lenses 1N, 2N, 1S, 2S and 3S. The average chemical composition of 4 representative samples is 2.75 wt% Zn, 12.4 wt% Cu, 0.05 wt% Pb, 38ppm Ag and 2.26ppm Au. The average mineralogical composition of the same samples is 4.60 wt% sphalerite, 36.5 wt% chalcopyrite, 0.05 wt% galena (plus clausthalite), 20.35 wt% pyrite (includes trace marcasite and magnetite), 5.0 wt% pyrrhotite, major to trace marcasite, and trace amounts of cubanite, Au-Ag-Hg alloy, hessite, pilsenite and rucklidgeite. The Au-Ag-Hg alloy is interpreted to be the host of the Au, whereas Ag is mainly carried in chalcopyrite, hessite, Au-Ag-Hg alloy and galena (plus clausthalite). This ore type plots towards the chalcopyrite apex of the Sphalerite-Chalcopyrite-Pyrrhotite + Pyrite triangular diagram, and towards the Fe apex on the Fe-Cu join of the Zn-Cu-Fe triangular diagram (See Figs. 5 and 6, respectively).

The ore consists of semi-massive to disseminated sulfides in the gangue. The sulfide matrix is composed of coarse-grained chalcopyrite with lesser pyrrhotite and sphalerite, all of which envelope the pyrite and gangue (See Fig. 16E). The gangue is generally highly foliated, consisting of chloritic-schist laminae, which are generally

interstratified with laminae of the massive sulfides. These chloritic-schist laminae are commonly folded, sheared and dislocated to form rafts in a 'sea of sulfides'. The stratification is interpreted as being formed by metamorphic segregation under conditions of intense shearing within a highly chloritized 'plastic' zone, rather than representing primary mineral banding. The gangue also occurs as discrete grains distributed diffusely throughout the sulfide matrix, and swirling around pyrite porphyroblasts.

The pyrite occurs as (1) anhedral, granulated, fractured porphyroclasts with variably developed deformation cleavage; (2) large, granulated and disrupted annealed masses of fine- to medium-grained pyrite; and (3) disseminated corroded and rounded grains in the chalcopyrite matrix. The grain size distribution of pyrite gives a median size of approximately 45 $\mu$ m (See Fig. 15). The pyrite contains fine-grained, reticulate-textured magnetite (pyrite-magnetite symplectite), and contains anhedral inclusions of pyrrhotite, marcasite and sphalerite. The marcasite commonly occurs as fine-grained flecks associated with pyrrhotite in pyrite, as disseminated bladed, subhedral grains, and rarely as abundant ( $\leq 10$  vol%) fresh, bladed grains and interlocking aggregates replacing pyrite (Fig. 16G). Rare lobes with concentric rings of 'sooty-textured' marcasite replace pyrrhotite at the contact with pyrite in a texture referred to by Ramdohr (1980) and Craig & Vaughan (1981) as 'birds eye texture' (Fig. 16H).

Chalcopyrite is the dominant sulfide and it envelopes and invades the gangue and pyrite. The mineral occurs as coarse-grained, anhedral grains and commonly contains barely discernible spindle-shaped inversion twins,

rare exsolution lamellae of cubanite, and poorly formed sphalerite stars (Fig. 18A). These three textures indicate the existence of the high temperature chalcopyrite-like cubic phase intermediate solid solution (Iss). The solid solubility of Zn in Iss is significant at high temperatures (i.e., 3.3 at% Zn at 500°C), but decreases with temperature (i.e., 1.2 at% Zn at 300°C), resulting in exsolution of sphalerite, which nucleates as stars (Kojima & Sugaki 1985). Iss inverts to chalcopyrite on cooling resulting in inversion twins, and the formation of cubanite exsolution lamellae (Kullerud et al. 1969, Craig & Scott 1976).

Pyrrhotite occurs as fine-grained rounded disseminations and granular masses in the chalcopyrite, whereas sphalerite occurs as rounded inclusions and rarely as coarse-grained, anhedral grains enveloped and embayed by the chalcopyrite, and displaying well developed chalcopyrite-disease. Sphalerite and/or lesser pyrrhotite also occur as trails (parallel to the foliation) of carious blebs and myrmekitic masses in the chalcopyrite, are formed by collection crystallization during and after shearing; a process termed diablatic growth by Ramdohr (1980). Chalcopyrite, pyrrhotite and sphalerite commonly occur invading, cementing or replacing pyrite along grain boundaries, fractures and cleavages. The grain size distribution of chalcopyrite and sphalerite give median sizes of approximately 125µm and 11µm, respectively. This reflects the general occurrence of sphalerite as inclusions in chalcopyrite.

Galena and clausthalite occur as fine-grained trace phases, generally as inclusions in pyrite or as anhedral grains in the chalcopyrite and

pyrrhotite matrix. In TLS.2-65 the galena is associated with sphalerite forming intergrown masses that envelope and corrode pyrrhotite and chalcopyrite. Abundant fine-grained rucklidgeite, clausthalite and lesser Au-Ag-Hg alloy were observed in sample TLS.3-14. These trace minerals along with chalcopyrite and/or pyrrhotite fill and replace deformed pyrite along fractures and grain boundaries, as interstitial wedges and films, and also as rounded, lenticular and commonly composite inclusions in the pyrite (Fig. 18B and C).

Hessite was observed as a rare inclusion in galena, whereas in sample TLS.1-47 it is associated with trace pilsenite, both occurring as fine-grained, anhedral, tabular inclusions in chalcopyrite (Fig. 18D).

Au-Ag-Hg alloy was observed in 6 of the 18 samples. It occurs in two distinct textural types; (1) Au-Ag-Hg alloy forming inclusions and fracture-fillings along with chalcopyrite, sphalerite, pyrrhotite and trace tellurides and selenides in pyrite, and (2) large ( $\leq 2\text{mm}$ ) anastomosing masses crystallizing along the contact between laminae of massive chalcopyrite and chlorite schist, and enveloping and corroding chalcopyrite and lesser pyrrhotite, sphalerite and pyrite (Fig. 18E).

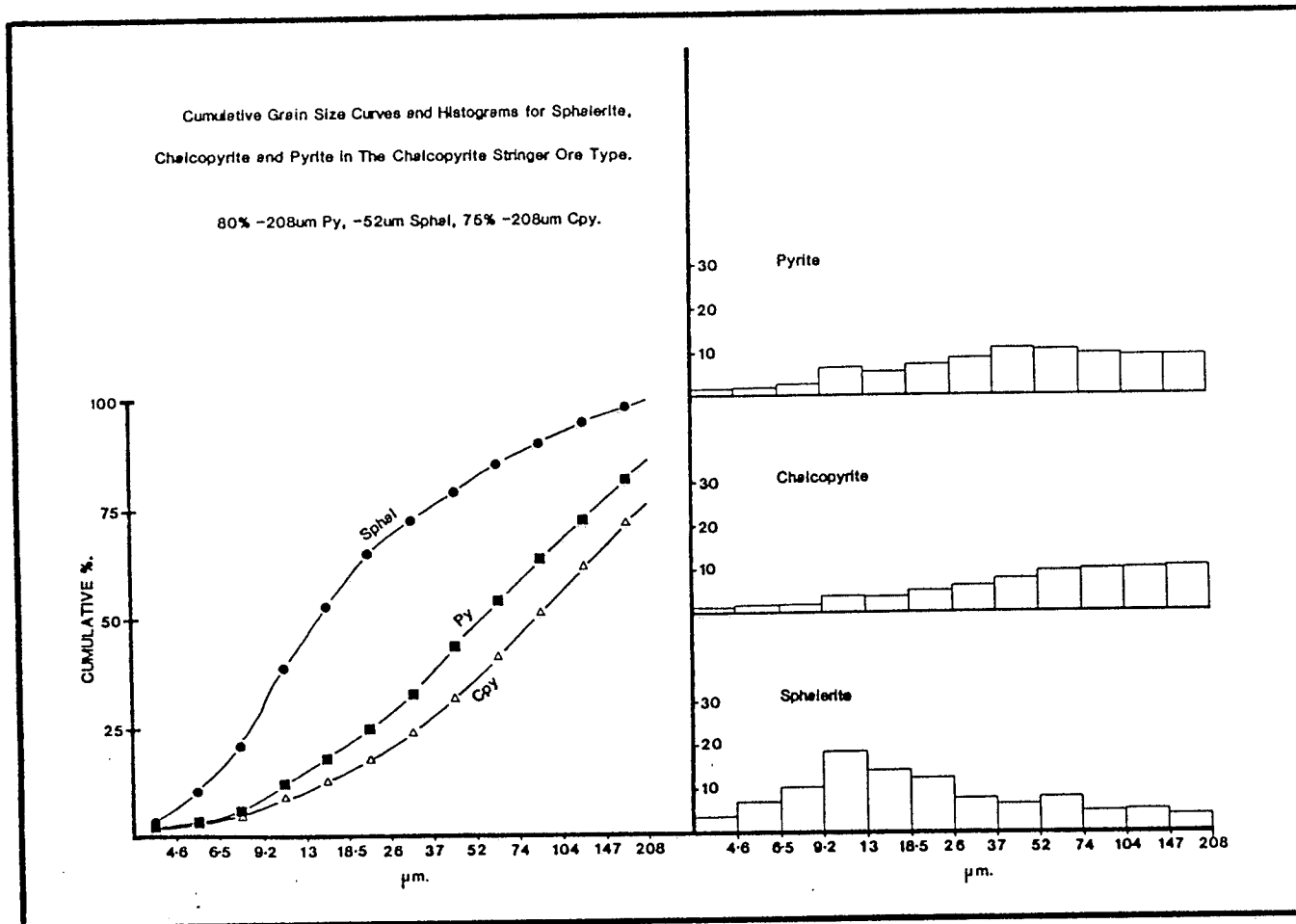
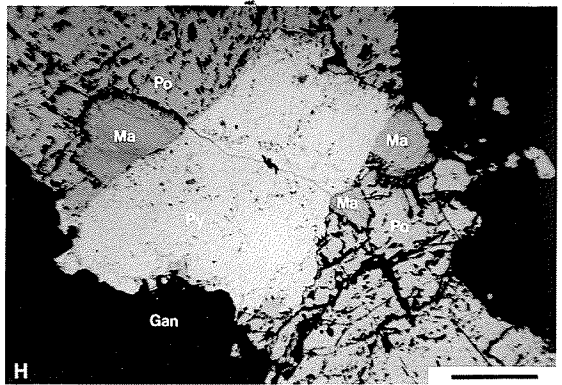
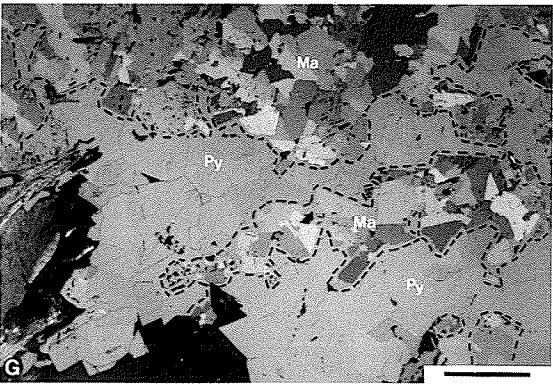
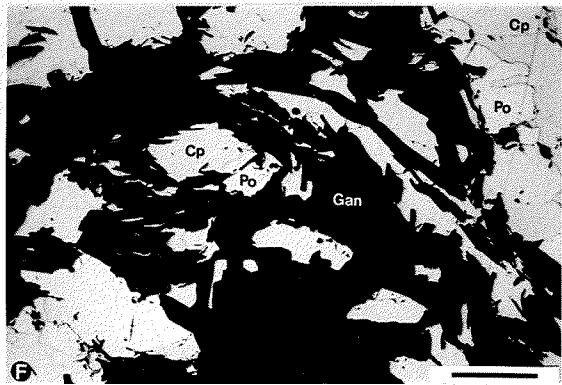
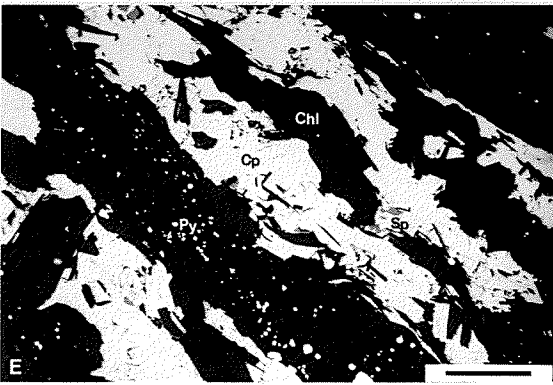
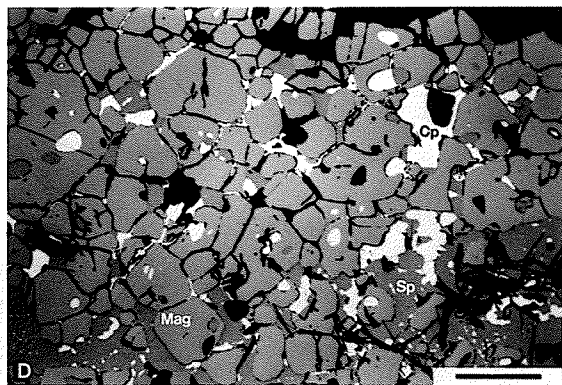
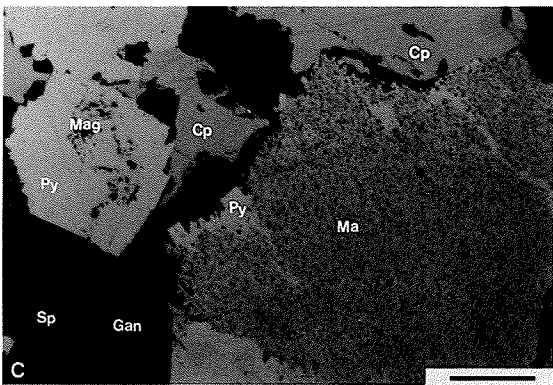
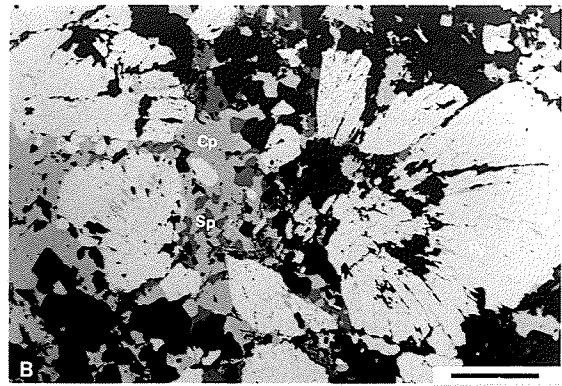
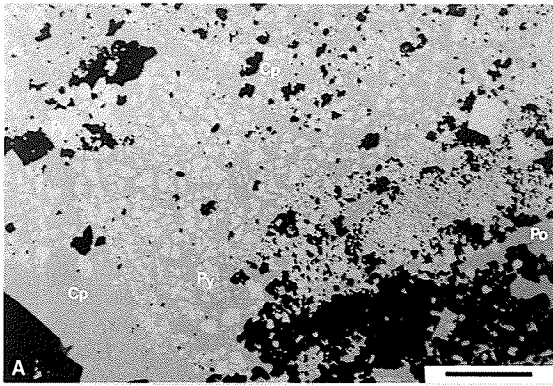


Figure 15: Grain Size Distributions in the Chalcopyrite Stringer Ore Type. Cumulative curves and histograms of the grain size distributions of pyrite, chalcopyrite and sphalerite are shown. The 80% passing size of pyrite and sphalerite is given, whereas the 75% passing size of chalcopyrite is given.

FIGURE 16: PLATE OF PHOTO-MICROGRAPHS.

- A. Sample TLS.3-46: Fractured and corroded pyrite (Py) grains enveloped in, and forming rounded islands in a matrix of chalcopyrite (Cp). Plane Polarized Reflected Light (PPRL). Scale bar = 160um.
- B. Sample TLN.2-112: Spheroidal pyrite enveloped and invaded by chalcopyrite, which is replacing the pyrite radially. Note the curious sphalerite (Sp) in the interstitial chalcopyrite. PPRL. Scale bar = 160um.
- C. Sample TLS.3-14: Pyrite (Py) with fine-grained reticulate magnetite (Mag) in the characteristic symplectite texture (center left), and 'clouded' pyrite due to replacement by fine-grained marcasite (Ma) flecks (bottom right). Chalcopyrite is the dominant matrix sulfide. PPRL. Scale bar = 40um.
- D. Sample TLN.2-114: A lamination of fractured and rounded magnetite grains with interstitial sphalerite and chalcopyrite. Several preserved  $120^\circ$  triple junctions are evident in the annealed magnetite. PPRL. Scale bar = 160um.
- E. Sample TLS.2-65: Discontinuous banding of chalcopyrite and chlorite schist (Gan) laminae in a Chalcopyrite Stringer ore. The chalcopyrite contains trace, fine-grained sphalerite. PPRL. Scale bar = 160um.
- F. Sample TLN.2-11: A Chalcopyrite Stringer ore showing chalcopyrite and pyrrhotite (Po) enveloping and invading fractures in folded and ruptured laminae of chlorite schist. PRPL. Scale bar = 160um.
- G. Sample TLN.1-2: Interlocking granular aggregates of marcasite (outlined by dashed line) replacing polygonal pyrite. Note the marked anisotropy of the pyrite. Partially Crossed Polars. Reflected Light. Scale bar = 160um.
- H. Sample TLN.2-7: 'Birds eye' textured lobes of a fine-grained mixture of marcasite and pyrite replacing pyrrhotite (heavily pitted - poor polish). Note the texture develops at the pyrite-pyrrhotite contact. PPRL. Scale bar = 325um.



### 5.2.7 DISSEMINATED PYRITE + CHALCOPYRITE ORE TYPE

The Disseminated Pyrite + Chalcopyrite ore type occurs in the footwall stockwork mineralization, forming a diffuse envelope around the Chalcopyrite Stringer ore type. It grades into barren wallrock downwards and towards the margins of the ore lenses. Eight samples corresponding to this ore type were taken from lenses 1N, 1S, 2S and 3S. The chemical composition of this ore type, based on only one sample (TLS.1-67) is 0.64 wt% Zn, 2.04 wt% Cu, 0.02 wt% Pb, 8.1ppm Ag and 1.3ppm Au. The average mineralogical composition is based on two samples, including TLS.1-67, and is 0.58 wt% sphalerite, 3.9 wt% chalcopyrite, 0.01 wt% galena and clausthalite, 38.46 wt% pyrite (including magnetite and marcasite), 0.03 wt% pyrrhotite, and trace amounts of cubanite and Au-Ag-Hg alloy. This ore type does not consistently attain ore grade, though it is at least partly included in the mining width of the lenses. It plots adjacent to the pyrrhotite + pyrite apex of the Sphalerite-Chalcopyrite-Pyrrhotite + Pyrite triangular diagram, and similarly adjacent to the Fe apex of the Zn-Cu-Fe triangular diagram (See Figs. 5 and 6, respectively).

The ore consists of disseminated to locally semi-massive pyrite in a gangue matrix of chlorite, carbonate, quartz and sericite (Fig. 18F). The pyrite occurs as (1) euhedral to anhedral, fine- to coarse-grained metacrysts and porphyroblasts, (2) as annealed polygonal masses, and (3) as disseminated, fine-grained, anhedral grains. In relatively undeformed samples, annealed masses of pyrite exhibit 120° triple junctions between equant grains. The fine-grained, anhedral disseminations of pyrite in the gangue exhibit feather-like to dendritic habit, streaked to

anastomosing forms, and also occur as veinlets. The pyrite typically exhibits development of cleavage and fractures, marginal granulation, and disruption of annealed masses. Rare occurrences of radial-anisotropy in pyrite suggests primary medium-grained spheroidal textured pyrite (Fig. 18G). Rare pyrite porphyroblasts exhibit radial pitting, fractures and replacement by chalcopyrite, pyrrhotite and sphalerite along radial features that may be inherited from primary spheroidal pyrite. The grain size distribution of pyrite gives a median size of between 52 and 74 $\mu$ m (See Fig. 17). Chalcopyrite, sphalerite and pyrrhotite occur interstitially to the pyrite and the gangue, and are observed invading and replacing pyrite along fractures, and rounding and corroding the pyrite along grain boundaries. Advanced stages of this replacement result in rounded islands of relict pyrite enveloped in chalcopyrite, and dendritic-textured chalcopyrite and sphalerite in pyrite (Fig. 18H). The sphalerite typically contains fine-grained blebs of chalcopyrite in the form of weakly developed chalcopyrite-disease. Chalcopyrite, sphalerite and pyrrhotite are all found as fine-grained, rounded inclusions in pyrite. The grain size distributions of chalcopyrite and sphalerite give median sizes of approximately 65 $\mu$ m and 90 $\mu$ m, respectively.

Fine-grained flecks to medium-grained subhedral to anhedral grains of marcasite are observed replacing pyrite along fractures and as fringes on pyrite grains, particularly in what are interpreted to be shear zones. Marcasite is observed as subhedral grains disseminated in the gangue, and rarely enveloping and replacing pyrite porphyroclasts. Rare fractured, medium- to fine-grained magnetite grains with rims and cross-

cutting veinlets of pyrite, are observed. Galena and clausthalite occur as rare interstitial, fine-grained films and wedges in the annealed pyrite masses. Au-Ag-Hg alloy was observed in 3 of the 8 samples, and typically occurs associated with chalcopyrite and pyrrhotite along the grain boundaries of, filling fractures in, and as fine-grained ( $\leq 2\mu\text{m}$ ) inclusions in, pyrite.

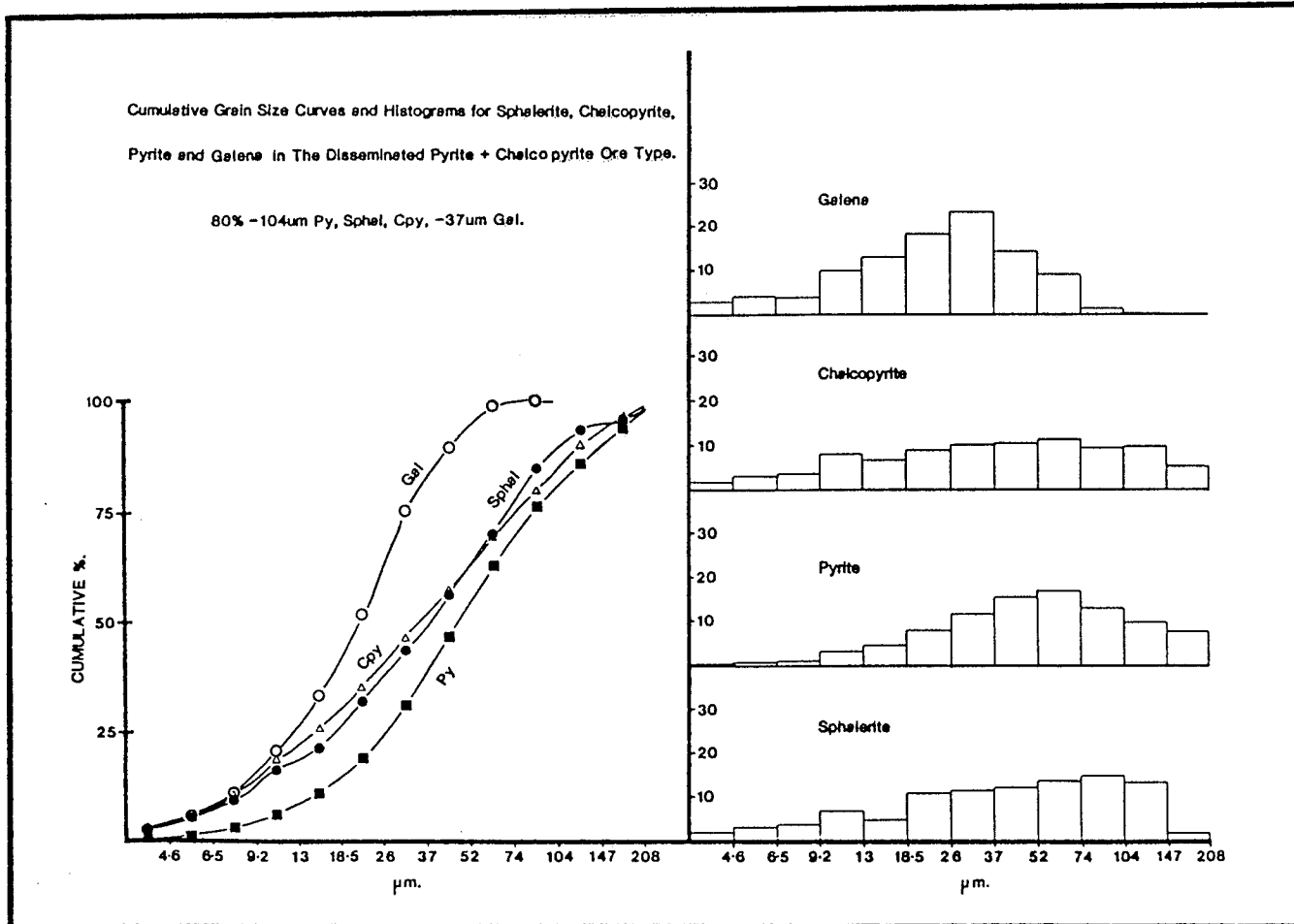


Figure 17: Grain Size Distributions in the Disseminated Pyrite + Chalcopyrite Ore Type. Cumulative curves and histograms of the grain size distributions of pyrite, chalcopyrite, sphalerite and galena are shown. The 80% passing size of each mineral is given.

FIGURE 18: PLATE OF PHOTO-MICROGRAPHS.

A. TLN.2-83: Exquisite, exsolved, composite lamellae of cubanite (Cub), and fine-grained poorly formed sphalerite (Sp) stars in a matrix of coarse-grained chalcopyrite (Cp). Reflected Light. Partly Crossed Polars. Scale bar = 160um.

B. Sample TLS.3-14: A large (diameter = 5mm) pyrite (Py) porphyroclast containing inclusions (commonly composite) of chalcopyrite, pyrrhotite (Po), rucklidgeite (Ru), clausthalite (Cl) Au-Ag-Hg alloy (El) and sphalerite. Note the composite inclusion of clausthalite and Au-Ag-Hg alloy. Plae Polarized Reflected Light (PPRL). Scale bar = 160um.

C. Sample TLS.3-14: Highly anisotropic subhedral pyrite grains with inclusions (commonly composite) of chalcopyrite, pyrrhotite and rucklidgeite (Ru). Chalcopyrite is the sole matrix sulfide. PPRL. Scale bar = 160um.

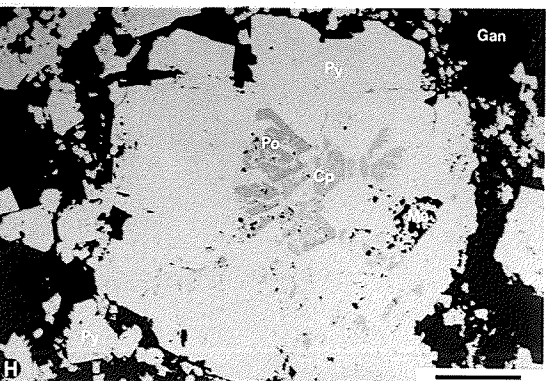
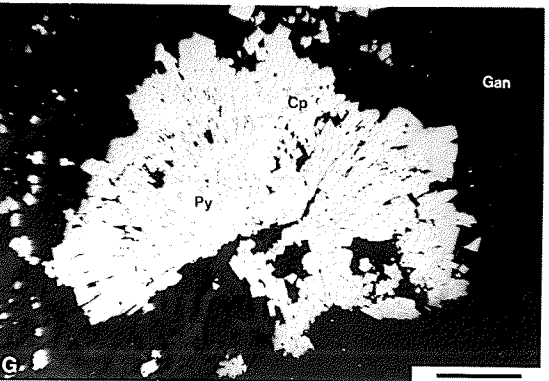
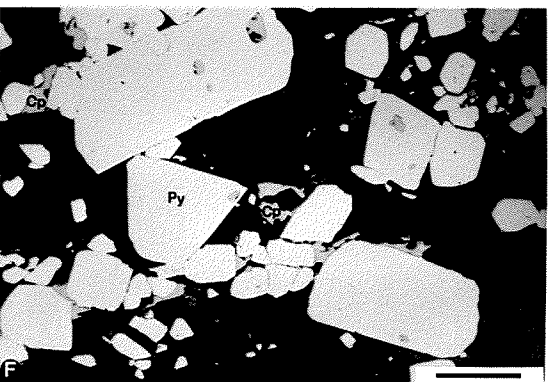
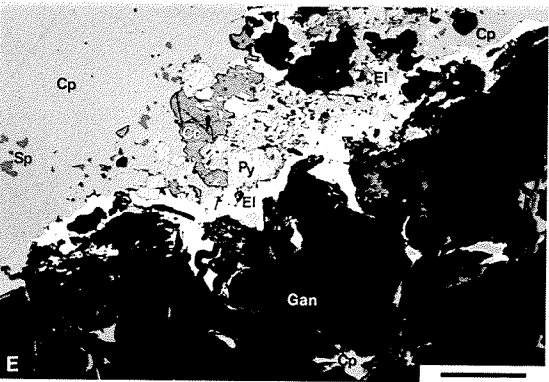
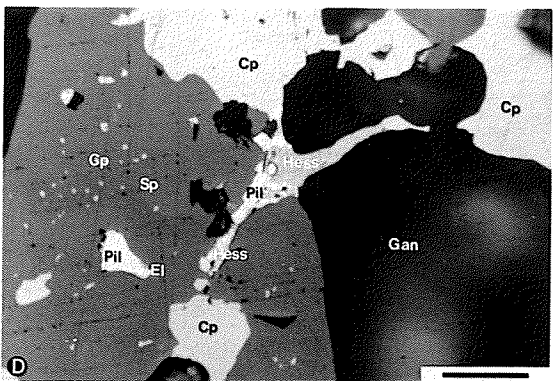
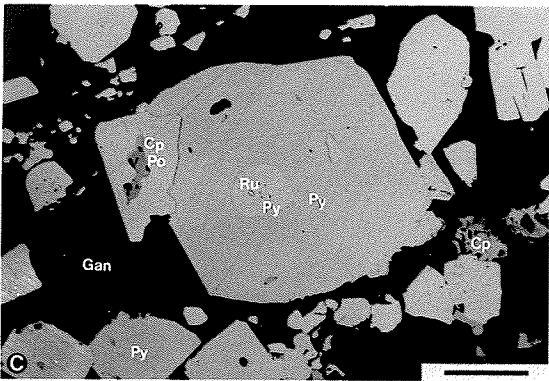
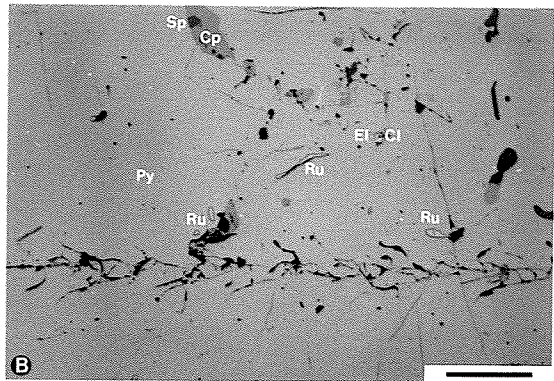
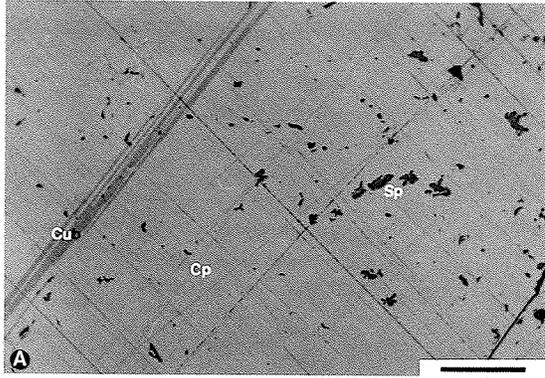
D. Sample TLS.1-47: Chalcopyrite, pilsenite (Pil), hessite (Hess) and Au-Ag-Hg alloy invading and replacing sphalerite. Note the intergrowth of hessite in pilsenite, and the chalcopyrite-disease in sphalerite. PPRL. Scale bar = 40um.

E. Sample TLN.1-89: A 2mm long anastomosing mass and lesser disseminations of Type 2 Au-Ag-Hg alloy that invades and corrodes the chalcopyrite along the contact of laminae of chalcopyrite and chlorite schist. Note the carious blebs of sphalerite at the far left of field. Cc denotes persistent carbon coat. PPRL. Scale bar = 160um.

F. Sample TLN.2-14: A Disseminated Pyrite + Chalcopyrite ore consisting of pyrite grains disseminated in the gangue, and containing minor interstitial chalcopyrite. PPRL. Scale bar = 160um.

G. Sample TLS.1-37: Spheroidal pyrite showing radial-textured pits, gangue and blebs of chalcopyrite and lesser pyrrhotite. PPRL. Scale bar = 325um.

H. Sample TLN.1-30: Dendritic chalcopyrite and pyrrhotite in a pyrite porphyroclast. The fine pits around the margins of th grain, and the pits at right of center of the grain are due to plucking (during polishing) of marcasite (Ma) flecks. PPRL. Scale bar = 160um.



#### 5.2.8 SHEARED CHALCOPYRITE + SPHALERITE ORE TYPE

The Sheared Chalcopyrite + Sphalerite ore type occurs with negligible stratigraphic control. The sole stratigraphic control is that sufficient (>5 vol%) of both sphalerite and chalcopyrite must be present in the ore to warrant its definition due to the intricate intergrowth of the valuable minerals chalcopyrite and sphalerite. This tends to restrict the occurrence of the ore type to the central parts of the massive ore lenses. Ten samples of the Sheared Chalcopyrite + Sphalerite ore type were taken; 1 from lens 3S and 9 from lens 2N. The average chemical composition of 4 representative samples is 23.2 wt% Zn, 5.24 wt% Cu, 0.01 wt% Pb, 65ppm Ag and 6.86ppm Au. The average mineralogical composition of the same samples is 38.7 wt% sphalerite, 15.4 wt% chalcopyrite, 0.01 wt% galena, 11.0 wt% pyrrhotite, 3.33 wt% pyrite (includes trace magnetite), and trace amounts of arsenopyrite, cubanite, magnetite, hessite, gudmundite and Au-Ag-Hg alloy. It is interpreted that Au-Ag-Hg alloy is the host of the Au, whereas sphalerite, chalcopyrite, hessite, galena and Au-Ag-Hg alloy are probably the major hosts of the Ag. This ore type plots in a broad field extending from adjacent to the sphalerite apex to the central portions of the Sphalerite-Chalcopyrite-Pyrrhotite + Pyrite triangular diagram (Fig. 5), and in a wide field close to the Fe-Zn join of the Zn-Cu-Fe triangular diagram (Fig. 6).

This ore type is defined as a chalcopyrite plus sphalerite ore that contains more than 5 vol% of each mineral, and where bulk of the chalcopyrite and sphalerite in the ore occur as an intricately intergrown and interpenetrating, fine-grained matrix. This texture is

interpreted as a deformational texture, which is produced by collection crystallization during and after shearing, and termed diablastic growth (Ramdohr 1980). The gangue in this ore type is commonly schistose- to augen-textured with sericite and/or chlorite forming in the vortices of compression around the augens ('eyes'). The textures of these ores are characteristic of the penetrative deformation that is developed by internal rotational movements, and is termed 'Durchbewegung' (Vokes 1969). Two such deformational textures that are commonly observed are the total disaggregation of primary banding, and the intense deformation and ultimate breakdown of pyrite. Since the origin of the ore type is deformational it lacks strong stratigraphic control, although it tends to be restricted in occurrence to the central parts of the ore lenses.

The Sheared Chalcopyrite + Sphalerite ore type consists of chalcopyrite, sphalerite and pyrrhotite which form a highly foliated sulfide matrix and exhibit various degrees of deformation and intensity of the characteristic diablastic texture (Fig. 20AA). Commonly the chalcopyrite (with rare exsolution lammellae of cubanite), sphalerite (with chalcopyrite-disease) and/or pyrrhotite occur as medium-grained masses with mutually carious to myrmekitic interpenetrative contacts (Fig. 20B and C) and well developed zones of diablastic texture. The matrix, commonly consists of fine-grained myrmekitic chalcopyrite, sphalerite and pyrrhotite, with medium-grained masses forming in the pressure shadows at the terminations of the augens in intensely deformed samples (Fig. 20D). The matrix sulfides commonly invade the fractured augens of rolled and folded gangue, as well as the dilated cleavages of micaceous minerals (Fig. 20E). The grain size distributions of the

chalcopyrite and the sphalerite give median sizes of approximately 45um, and between 65um, respectively (Fig. 19).

Pyrite varies from not observed to a major constituent, occurring as anhedral, fine-grained disseminations and coarse-grained porphyroblasts. The mineral is granulated and fractured, and is invaded, replaced and cemented by the matrix sulfides. A deformation cleavage is often highlighted by the invading matrix sulfides, particularly in the rare examples of 'blow apart' textured pyrite (Fig. 20F). Development of 'atoll' texture is rare. Rounded islands of fine-grained relict pyrite and skeletal pyrite enveloped in a chalcopyrite matrix are common. Pyrite commonly contains reticulate-textured fringes and zones of magnetite. The pyrite in samples of less intense deformation tend to deform by rounding to produce 'pyrite pebbles', rather than by deforming brittly (Fig. 20G). Rare carious contacts with sphalerite, as well as pyrite injected into fractures and the bent and dilated cleavage traces of micaceous minerals suggests that the pyrite has been locally mobilised. The pyrite is interpreted as having partly broken down during the formation of pyrrhotite. The pyrite grain size distribution gives a median size of approximately 65um. Rare, anhedral, disseminated grains of arsenopyrite are observed enveloped in the sulfide matrix.

The galena commonly occurs associated with chalcopyrite, sphalerite and/or pyrrhotite invading deformed pyrite. In sample TLN.2-9 the galena occurs as carious blebs in the diablastic matrix of chalcopyrite, sphalerite and pyrrhotite, and also associated with chalcopyrite and inclusions of hessite forming veinlets and disseminations in the gangue rafts (Fig. 20HH). Inclusions of gudmundite in granular masses of

pyrrhotite were observed within a rim of massive sphalerite adjacent to a large quartz vein.

Au-Ag-Hg alloy was observed in 6 of the 10 samples. It occurs with chalcopyrite and/or sphalerite infilling and replacing pyrite along fractures and cleavages. However, in sample TLN.2-9 the alloy (14 grains observed) exhibited no spatial relationship with the pyrite, but instead occur in the matrix chalcopyrite and/or pyrrhotite. This sample contains trace pyrite, all of which is hosted in rafts of gangue. The general decrease in the pyrite content and increase in the pyrrhotite content with increased deformation in these ores, suggests that the pyrrhotite forms, at least in part, by the breakdown of pyrite and results in the release of trace Au present in solid solution in the pyrite, with the resultant crystallization of Au-Ag-Hg alloy.

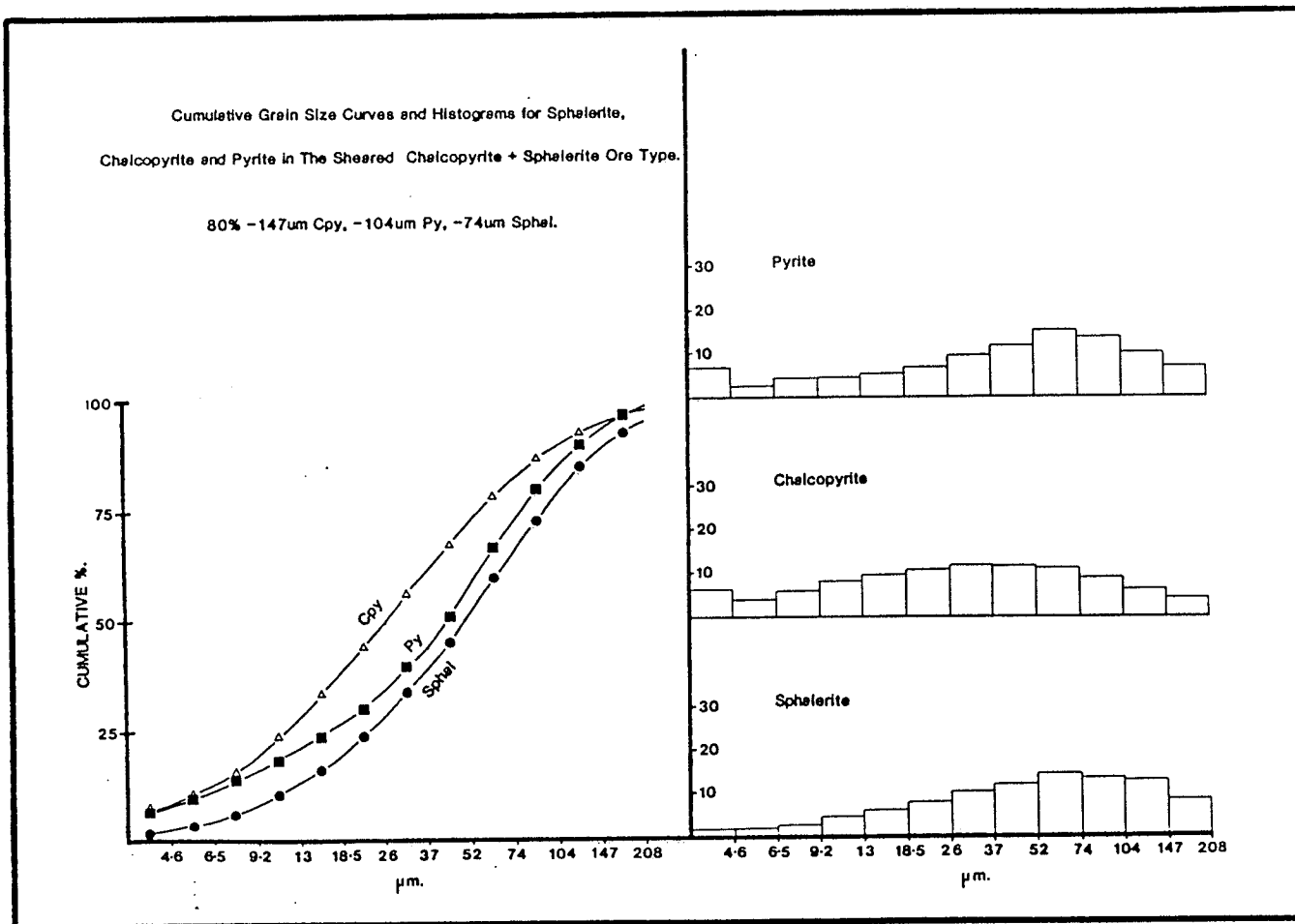


Figure 19: Grain Size Distributions in the Sheared Chalcopryite + Sphalerite Ore Type. Cumulative curves and histograms of the grain size distributions of pyrite, chalcopyrite and sphalerite are shown. The 80% passing size of each mineral is given.

FIGURE 20: PLATE OF PHOTO-MICROGRAPHS.

A. TLN.2-12: Diablastic-textured chalcopyrite (Cp), sphalerite (Sp) and pyrrhotite (Po), consisting of fine-grained, myrmekitic intergrowths of sphalerite with chalcopyrite, and pyrrhotite occurring essentially as inclusions in chalcopyrite. Plane Polarized Reflected Light (PPRL). Scale bar = 40um.

B. Sample TLN.2-63: Diablastic-textured ore consisting of augen-textured rafts of gangue (Gan), and foliated grains of sphalerite with carious contacts with chalcopyrite and subordinate pyrrhotite. Texture was probably produced by shearing and 'smearing-out' of sphalerite-rich ore with abundant interstitial films and grains of chalcopyrite, which underwent collection crystallization to produce these carious grain contacts. PPRL. Scale bar = 160um.

C. Sample TLN.2-12: Disrupted and fractured gangue rafts within a diablastic-textured chalcopyrite, sphalerite and pyrrhotite matrix, which swirls around the augens in a truly tectonized or 'Durchbewegung' style of deformation. PPRL. Scale bar = 325um.

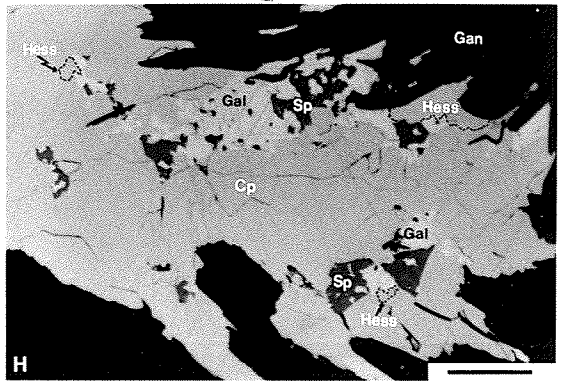
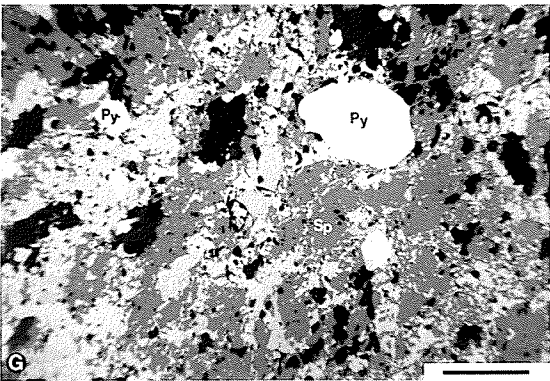
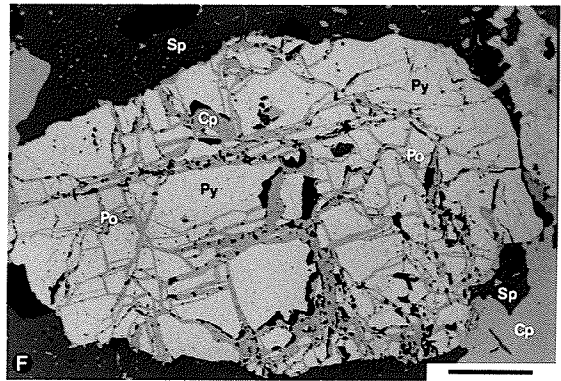
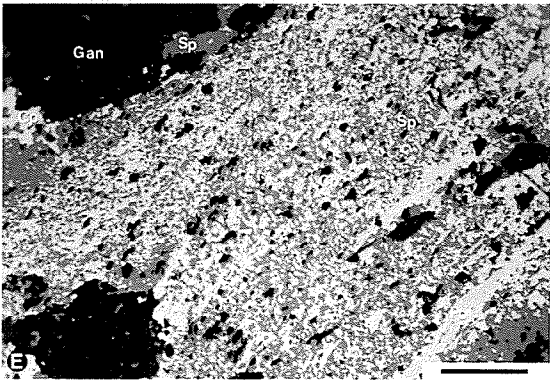
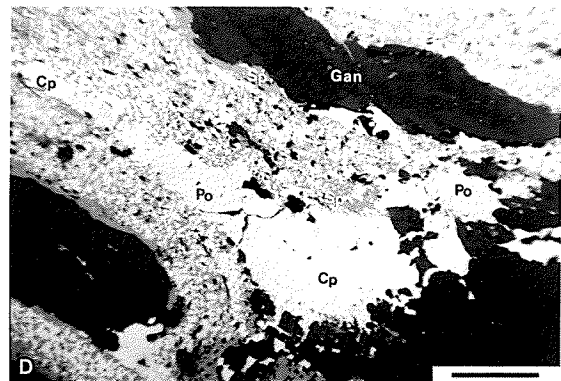
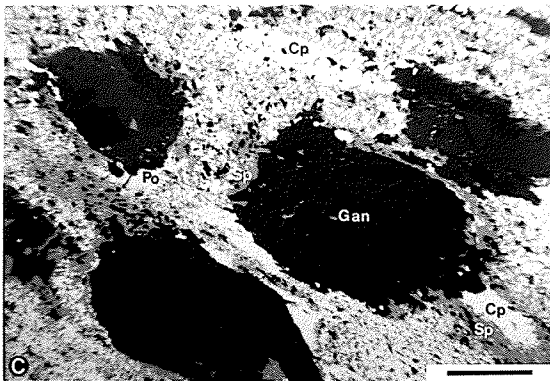
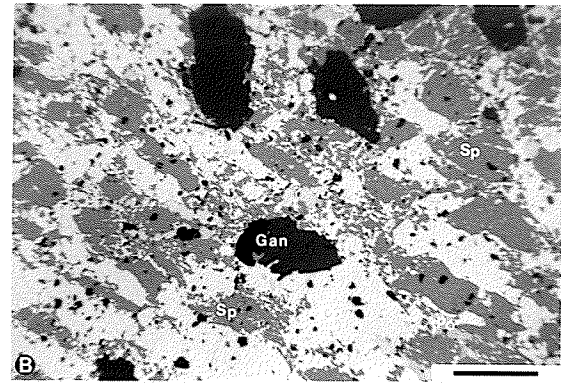
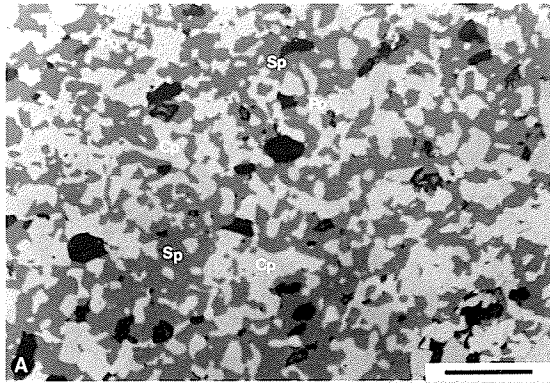
D. Sample TLN.2-12: Augen-textured rafts of gangue 'floating in a sea' of diablastic-textured chalcopyrite, sphalerite and pyrrhotite. Note the coarse-grained chalcopyrite and sphalerite in the 'pressure shadows' at the terminations of the augens. PPRL. Scale bar = 325um.

E. Sample TLN.2-113: Diablastic-textured sphalerite, chalcopyrite and pyrrhotite bearing ore from the 425m drillhole intersection of Lens 2 of the north zone. Note the sphalerite and chalcopyrite invading the gangue rafts at top of field. PPRL. Scale bar = 160um.

F. Sample TLN.2-114: A matrix of sphalerite and chalcopyrite containing a 'blow-apart' textured pyrite (Py) porphyroclast (diameter = 1.25mm) cemented by chalcopyrite and trace pyrrhotite. Note there is negligible replacement of the pyrite along the dilated fracture surfaces. PPRL. Scale bar = 160um.

G. Sample TLN.2-63: Rounded pyrite porphyroclasts (pyrite pebbles) in a matrix of diablastic-textured sphalerite, chalcopyrite and pyrrhotite, all of which exhibit the carious to myrmekitic texture. PPRL. Scale bar = 325um.

H. Sample TLN.2-9: A Sheared Chalcopyrite + Sphalerite ore with masses of fine-grained galena (Gal), sphalerite and hessite (Hess - outlined by dashed line) hosted in chalcopyrite, which is invading fractured and ruptured gangue rafts. PPRL. Scale bar = 40um.



### 5.2.9 VEIN QUARTZ + CHALCOPYRITE ORE TYPE

The Vein Quartz + Chalcopryrite ore type exhibits no stratigraphic control, and is tectonic in origin. This ore type was defined because of the common occurrence of mineralized quartz veins within the ore lenses. These veins exhibit a textural uniqueness of some of the sulfides, and have the potential for concentration of precious metal phases. It is noteworthy that similar quartz veins were observed in the Flin Flon deposit, and may result from hydrothermal remobilization during metamorphism (Koo 1973).

The chemical composition of this ore type based on sample TLN.1-3 is 0.43 wt% Zn, 3.20 wt% Cu, 0.005 wt% Pb, 13ppm Ag and 6.16ppm Au. The mineralogical composition of the same sample is 0.72 wt% sphalerite, 9.4 wt% chalcopryrite, 2.14 wt% pyrite (includes trace marcasite), 2.14 wt% pyrrhotite, and trace cubanite and galena. Au-Ag-Hg alloy is interpreted to be the host of the Au, whereas chalcopryrite, sphalerite, galena and Au-Ag-Hg alloy host the bulk of the Ag. This ore type plots adjacent to the chalcopryrite apex of the Sphalerite-Chalcopryrite-Pyrrhotite + Pyrite triangular diagram, and centrally on the Fe-Cu join of the Zn-Cu-Fe triangular diagram (See Figs. 5 and 6).

The gangue consists predominantly of coarse-grained quartz with pronounced wavy extinction, and subordinate calcite, sericite, chlorite and trace tourmaline. The sulfides, consisting predominantly of chalcopryrite, occupy the interstitial spaces between the quartz grains.

The chalcopryrite is the dominant sulfide and is coarse-grained with spindle-shaped inversion twins. The chalcopryrite also contains abundant

sphalerite stars, typically 20um in diameter, although less commonly as large as 90um in diameter (Fig. 23A). The sphalerite stars are concentrated along twin planes, and along grain boundaries of the chalcopyrite. Rare exsolution lamellae of cubanite up to 5mm in length and 50um in width occur in the chalcopyrite (Fig. 18A). These three textures suggest that Iss crystallized during the metamorphic peak and equilibrated on cooling. The sphalerite also occurs as minor medium-grained, anhedral grains with intense chalcopyrite-disease, and is enveloped and severely embayed by the matrix chalcopyrite. The grain size distributions for chalcopyrite and sphalerite give maximum grain sizes greater than 208um, and median grain sizes of approximately 65um, respectively.

Pyrite occurs as a minor constituent, but as large ( $\leq 5$ mm) granulated and fractured annealed polygonal masses that are invaded and replaced by chalcopyrite and lesser sphalerite. Minor anhedral inclusions of pyrrhotite are typically associated with marcasite, where the latter occurs as less common subhedral, bladed grains replacing the pyrite masses. In TLN.1-3, the pyrite exhibits a 'clouded' texture associated with fine-grained, comb-textured flecks of marcasite replacing pyrite along grain boundaries. Galena occurs as rare, disseminated, anhedral grains in the chalcopyrite. No precious metal-bearing minerals or sulfosalts were observed in samples of this ore type.

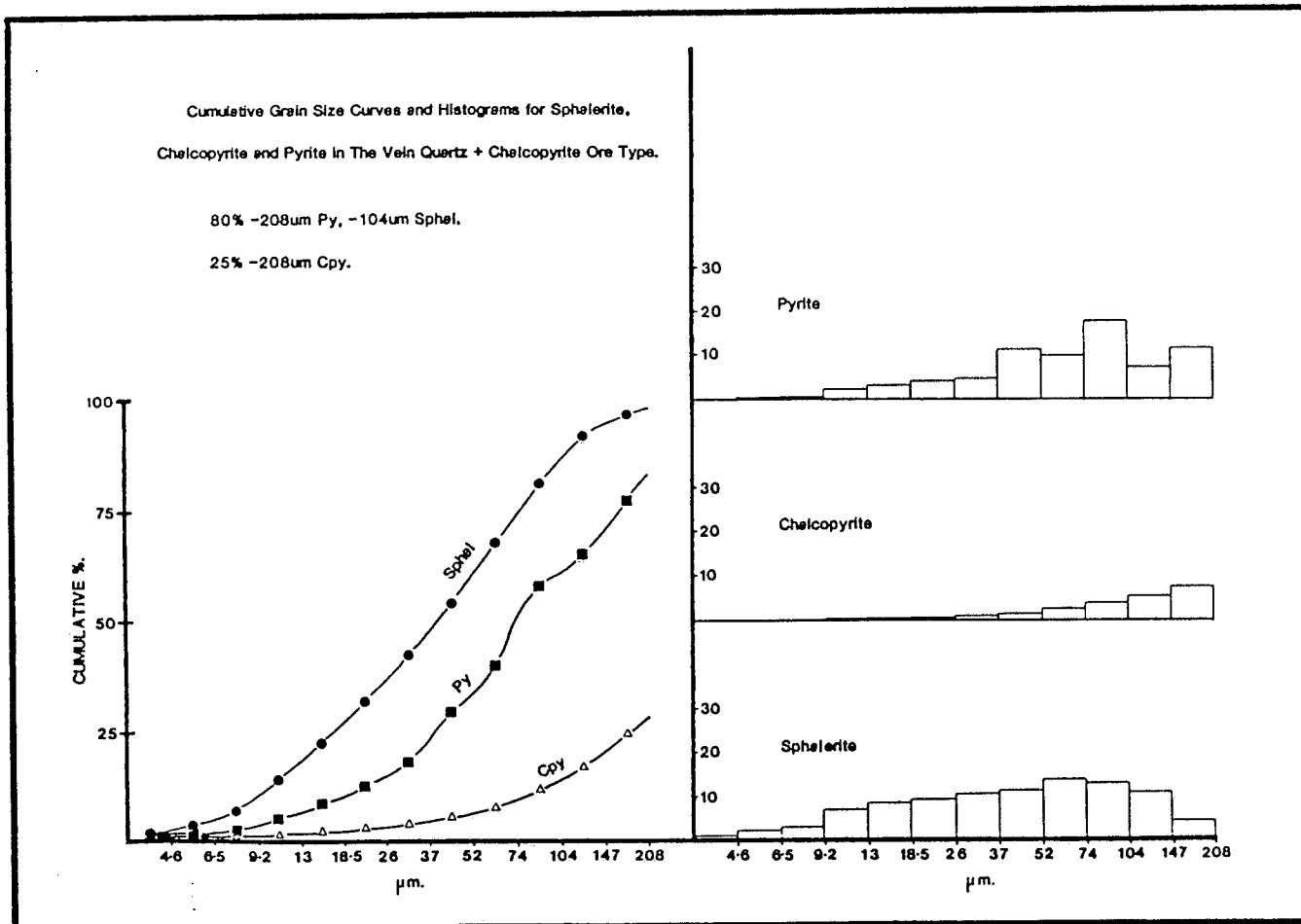


Figure 21: Grain Size Distributions in the Vein Quartz + Chalcopyrite Ore Type. Cumulative curves and histograms of the grain size distributions of pyrite, chalcopyrite and sphalerite are shown. The 80% passing size of pyrite and sphalerite is given, whereas the 25% passing size of chalcopyrite is given.

## Chapter VI

### CHARACTERISTICS OF THE ORE MINERALS

Twenty six ore minerals were observed in the ores, and these are listed in Table 4. The minerals are classified into mineral groups, and listed in order of decreasing abundance of the groups and of the minerals in each group. These are discussed in detail in this chapter.

#### 6.1 SULFIDES

##### 6.1.1 PYRITE

Pyrite is the most abundant mineral in the ore (See Table 11), and was observed in each ore type. It exhibits five principal textural styles; (1) annealed, medium-grained, polygonal masses (See Figs. 16G and 23B), (2) disseminated porphyroblasts and metacrysts (Fig. 23C), (3) granulated, rounded, fractured, anhedral porphyroclasts (fractured porphyroblasts) with variably developed deformation cleavage (Fig. 11B), (4) streaked, smeared, schistose, deformed pyrite (Fig. 23D), and (5) remobilized pyrite in veinlets, fractures and cleavages of gangue minerals (Fig. 23E). These textures demonstrate that the pyrite has been recrystallized during the metamorphism, variably sheared and fractured by tectonism, and has been replaced by other minerals. The grain size distribution of the pyrite in all the ore types gives the median size of approximately 65um.

The matrix sulfides sphalerite, chalcopyrite, pyrrhotite, galena and/or freibergite occur interstitially to the pyrite, invade fractures and cleavages and may cement or replace the pyrite. The dominant replacement textures of pyrite are (1) corrosion, embayment and development of atoll texture, where sphalerite is the dominant matrix sulfide (Fig. 8B)); (2) fine-grained, dendritic replacement by sphalerite, chalcopyrite and/or galena in the Massive Pyrite and the Layered Pyrite + Sphalerite ore types (Fig. 11D); (3) replacement by chalcopyrite, pyrrhotite and/or sphalerite along grain boundaries, fractures and cleavages (Fig. 11B); (4) envelopment and corrosion to form rounded, fine-grained, relict islands of pyrite in matrix chalcopyrite and/or pyrrhotite (Fig. 16A)); and (5) replacement by marcasite in a variety of textures (See section MARCASITE).

Quantitative microprobe analyses failed to detect any trace elements or significant variation in pyrite stoichiometry. However, on the basis of 46 grain discrete SIMS analyses of pyrite in a sample of Trout Lake tailings, it was determined that Au concentrations ('invisible') in pyrite vary from below detection (i.e. <0.01) to 6.80ppm Au, with an average of 0.72ppm Au (See Fig. 22, INVISIBLE GOLD section, and Appendix E). The SIMS analyses also gave a range in As concentrations from below detection (i.e. <10) to 4100ppm As, with an average of 500ppm As. Furthermore, Healy & Petruk (1989) have inferred that pyrite contains 11ppm Ag, accounting for 14% of the Ag in the ore.

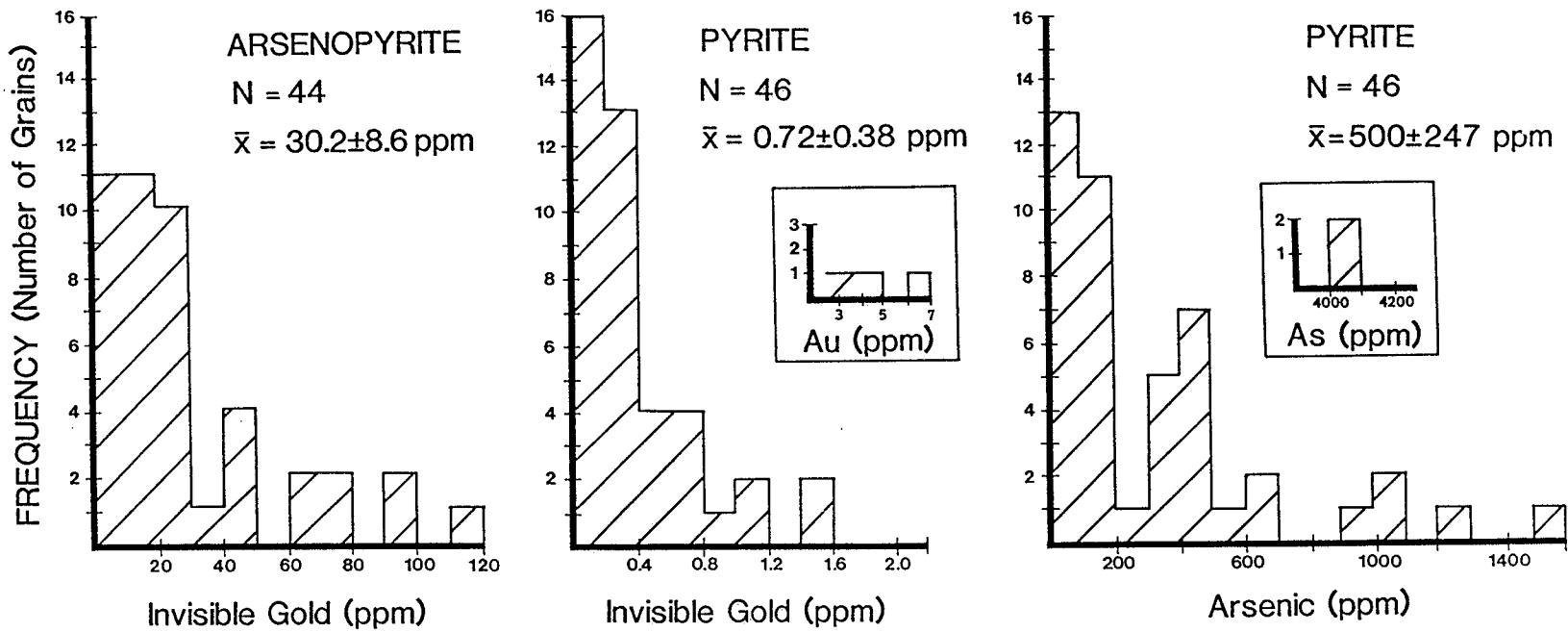


Figure 22: Histograms of Au Concentrations in Arsenopyrite and Au and As Concentrations in Pyrite. Compositional data determined by SIMS analyses of these minerals in a sample of Trout Lake concentrator tailings.

### 6.1.2 MARCASITE

Marcasite is generally a trace constituent of the ores, although it has been observed as a major constituent, reaching approximately 15 vol% in sample TLN.1-2, a Chalcopyrite Stringer ore. Marcasite always occurs as a replacement of pyrite and is generally more abundant where the pyrite has undergone intense deformation, particularly along shear zones. The dominant textures of marcasite are (1) fine-grained flecks and bladed inclusions in pyrite and as fringes on pyrite (Fig. 23F); (2) clouded or sooty-textured pyrite (sub-microscopic marcasite), occasionally with comb-textured marcasite forming on the pyrite grain boundaries (Fig. 16C); (3) fine- to medium-grained subhedral grains and interlocking aggregates with simple, and rarely repeated lamellar twinning (Fig. 16G); and (4) foliated, scaley masses of marcasite intergrown with galena, freibergite and pyrrhotite, and enveloping and replacing deformed and fractured pyrite (Fig. 11H).

### 6.1.3 PYRRHOTITE

Pyrrhotite is an abundant ore mineral, and is a major constituent in some ore types, particularly the Massive Chalcopyrite + Pyrrhotite ore type. The mineral is commonly associated with chalcopyrite and tends to be concentrated in the Massive Chalcopyrite + Pyrrhotite, the Sheared Chalcopyrite + Sphalerite and the Chalcopyrite Stringer ores. The pyrrhotite content of the Sheared Chalcopyrite + Sphalerite ores tends to increase with the apparent intensity of deformation, and inversely to the pyrite content. This suggests that some pyrrhotite forms during the breakdown of pyrite during and after the deformation that followed the porphyroblastic growth of pyrite.

Pyrrhotite is invariably anhedral, and commonly occurs as an interstitial mineral. The dominant textural styles of pyrrhotite are (1) inclusions, interstitial material, and fracture-fillings cementing or replacing pyrite (Fig. 20F); (2) disseminated rounded grains and granular to gneissic-textured masses in chalcopyrite (Fig. 13H); (3) oriented blebs and rods, and disseminated grains in sphalerite (Fig. 23); (4) carious blebs and myrmekitic intergrowths with chalcopyrite and/or sphalerite, which is characteristic of diablastic texture e.g., in the Sheared Chalcopyrite + Sphalerite ores; and (5) as inclusions in interstitial galena (Fig. 23H).

The composition of pyrrhotite from four microprobe analyses are presented below in Table 13. The compositions give an average unit formula of  $Fe_{6.8}S_{8.0}$ , which corresponds to monoclinic pyrrhotite and/or hexagonal pyrrhotite of the 1C or MC type (Craig & Scott 1976). Monoclinic pyrrhotite, unlike hexagonal pyrrhotite, is strongly ferrimagnetic, and this is in agreement with the strong magnetic response of all magnetite-free, pyrrhotite-rich polished sections. In the absence of an x-ray diffraction study or etching, the presence of hexagonal pyrrhotite remains unverified.

TABLE 13

Representative Chemical Compositions (Microprobe Data) of Pyrrhotite

wt%	1	2	3	4	Uncertainty (95% Confidence)
S	39.34	40.33	40.15	40.30	± 0.2
Fe	59.69	59.29	59.54	59.30	± 0.5
Total	99.03	99.62	99.69	99.60	
at%					
S	53.45	54.23	54.01	54.21	
Fe	46.55	45.77	45.99	45.79	
Number of atoms					
S	1.00	1.00	1.00	1.00	
Fe	0.87	0.84	0.85	0.85	

\* Unit formula calculated on the basis of 1 sulfur atom.

\* A pyrite standard was employed for both Fe and S.

FIGURE 23: PLATE OF PHOTO-MICROGRAPHS.

A. Sample TLN.1-3: A large well-formed sphalerite (Sp) star exsolved in a coarse-grained chalcopyrite (Cp). Plane Polarized Reflected Light (PPRL). Scale bar = 160um.

B. Sample TLN.1-12: Identical view as Fig. 16G, except PPRL was used in this photograph. Note the 120° triple junctions in the annealed polygonal pyrite (Py) in the areas indicated by A and B. Note the areas of pitting due to plucking of marcasite (Ma). PPRL. Scale bar = 160um.

C. Sample TLS.5-105: A cluster of pyrite euhedra with a matrix of sphalerite and carbonate gangue (Gan). PPRL. Scale bar = 160um.

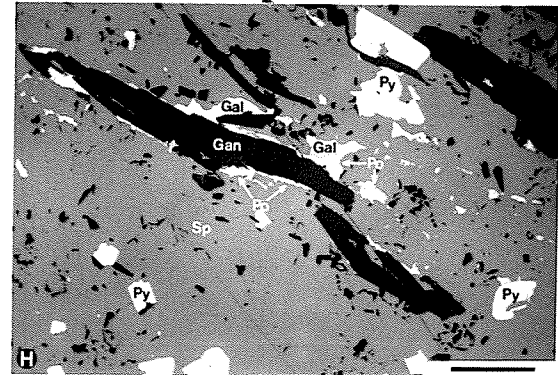
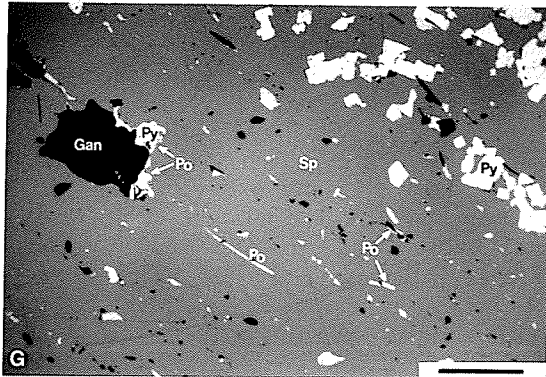
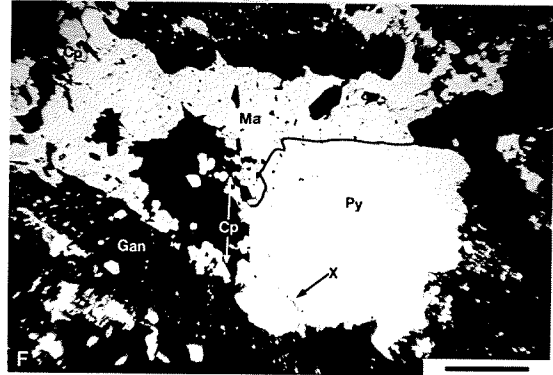
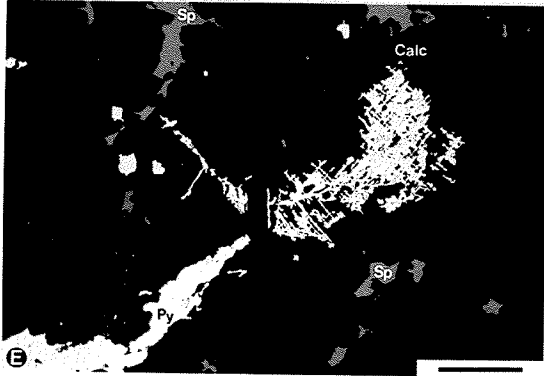
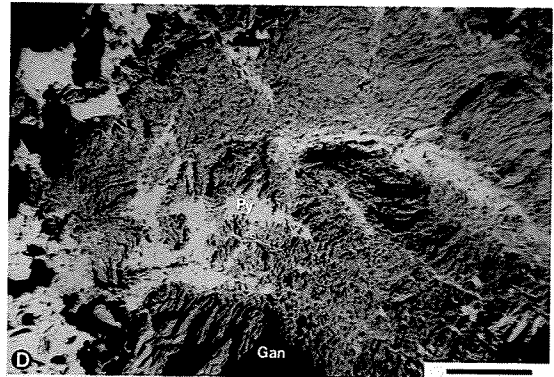
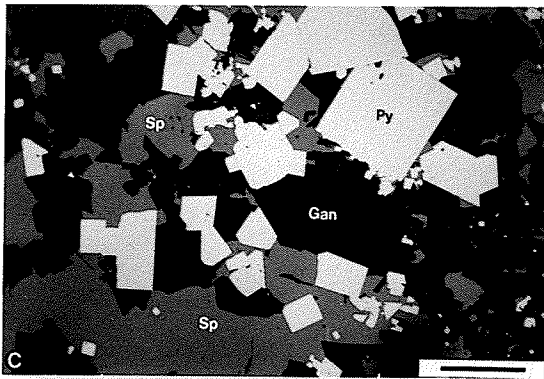
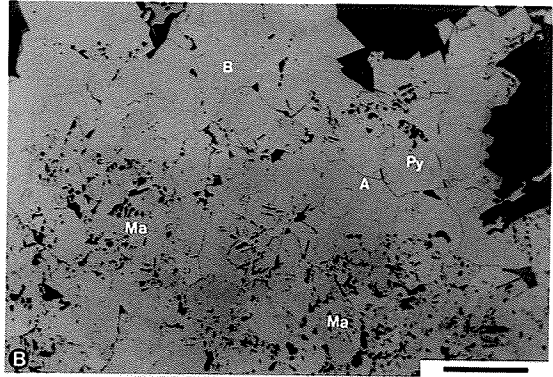
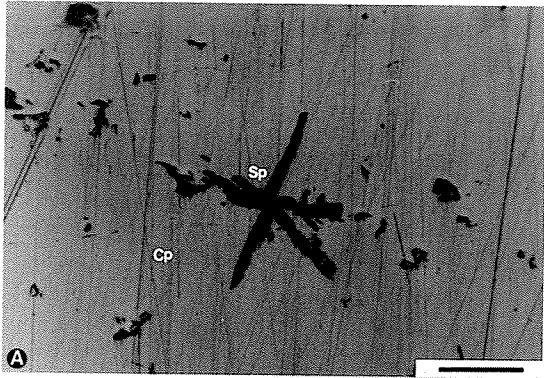
D. Sample TLN.1-29: Highly deformed and sheared pyrite developed locally as swirled patches of 'schistose' pyrite. PPRL. Scale bar = 325um.

E. Sample TLN.1-98: Pyrite (Py) invading and replacing calcite (Calc) along grain boundaries, cleavages and twin lamellae. Sphalerite also invades and corrodes calcite and other gangue minerals. PPRL. Scale bar = 160um.

F. Sample TLS.3-36(#2): A large pyrite porphyroclast enveloped by a granular mass of marcasite. Note the fracture at bottom left corner of pyrite porphyroclast contains fine-grained chalcopyrite and Au-Ag-Hg alloy (not discernible). PPRL. Scale bar = 325um.

G. Sample TLN.1-27: A matrix of massive sphalerite containing oriented blebs and rods of pyrrhotite (Po), often nucleated on foliated gangue grains. PPRL. Scale bar = 160um.

H. Sample TLS.5-84: A massive sphalerite ore containing bent and foliated grains and rafts of gangue, with galena preferentially nucleating along the gangue-sphalerite contacts. Note that the galena contains inclusions of pyrrhotite, and that the pyrite is fractured and corroded. PPRL. Scale bar = 160um.



#### 6.1.4 CHALCOPYRITE

Chalcopyrite is the main Cu-bearing mineral in the ore, with cubanite, freibergite and bournonite constituting the remaining, yet volumetrically insignificant Cu-bearing minerals. The chalcopyrite and hence Cu, tends to be concentrated in the footwall massive exhalative ores, and particularly in the highly differentiated and spectacular Chalcopyrite Stringer ores.

Chalcopyrite is invariably anhedral, and commonly occurs as an interstitial mineral. It is variably coarse-grained (up to 1 cm in the Vein Quartz + Chalcopyrite ore type) to fine-grained, with the grain size decreasing with the relative abundance; the chalcopyrite occupies smaller and more restricted interstitial spaces between the phases with higher crystallinity. Both chalcopyrite and sphalerite constitute the dominant matrix sulfides in the ore. However, because of the lower crystallinity of chalcopyrite and the higher rate of re-equilibration (relative to sphalerite), chalcopyrite displays a diversity of textural styles.

The textural styles of chalcopyrite are (1) massive coarse-grained matrix chalcopyrite with granuloblastic- to gneissic-textured masses and disseminations of pyrrhotite, and with cubanite lamellae and/or sphalerite stars, particularly in the Massive Chalcopyrite + Pyrrhotite, Chalcopyrite Stringer and the Vein Quartz + Chalcopyrite ore types (Fig. 13H); (2) massive chalcopyrite enveloping, invading and/or replacing all other major constituents, including the gangue and excluding galena (Fig. 16F); (3) chalcopyrite associated with other matrix sulfides

invading and cementing or replacing fractured pyrite (Fig. 20F); (4) irregular interstitial material between sphalerite grains (Fig. 8D); (5) crystallographically oriented blebs and rods of chalcopyrite in sphalerite termed chalcopyrite-disease (Fig. 8C); (6) fine-grained, dendritic replacements of pyrite (Fig. 18H); (7) myrmekitic intergrowths of chalcopyrite with sphalerite and/or pyrrhotite, characteristic of diablastic texture, especially in the Sheared Chalcopyrite + Sphalerite ores (Fig. 20A); and (8) extremely rare exsolved blebs and networks in freibergite (Fig. 11E).

It is interpreted from the size analysis data that the chalcopyrite occurring as inclusions in pyrite, as interstitial blebs, wedges and films between pyrite grains, as fracture-fillings in pyrite, and as chalcopyrite-disease in, carious blebs in, and interstitial material between sphalerite dominate the  $-18.5\mu\text{m}$  fraction. This fraction corresponds to approximately 20% of the chalcopyrite in the ore. The remaining 80%  $+18.5\mu\text{m}$  fraction corresponds to the massive matrix chalcopyrite with a median grain size approximately  $90\mu\text{m}$ . The cumulative grain size curves for chalcopyrite in each ore type are presented in Figure 24.

Quantitative microprobe analyses of the chalcopyrite showed no detectable trace elements, nor significant variation in stoichiometry, although Healy & Petruk (1989) have inferred that chalcopyrite contains 45ppm Ag, accounting for 23% of the Ag in the ore.

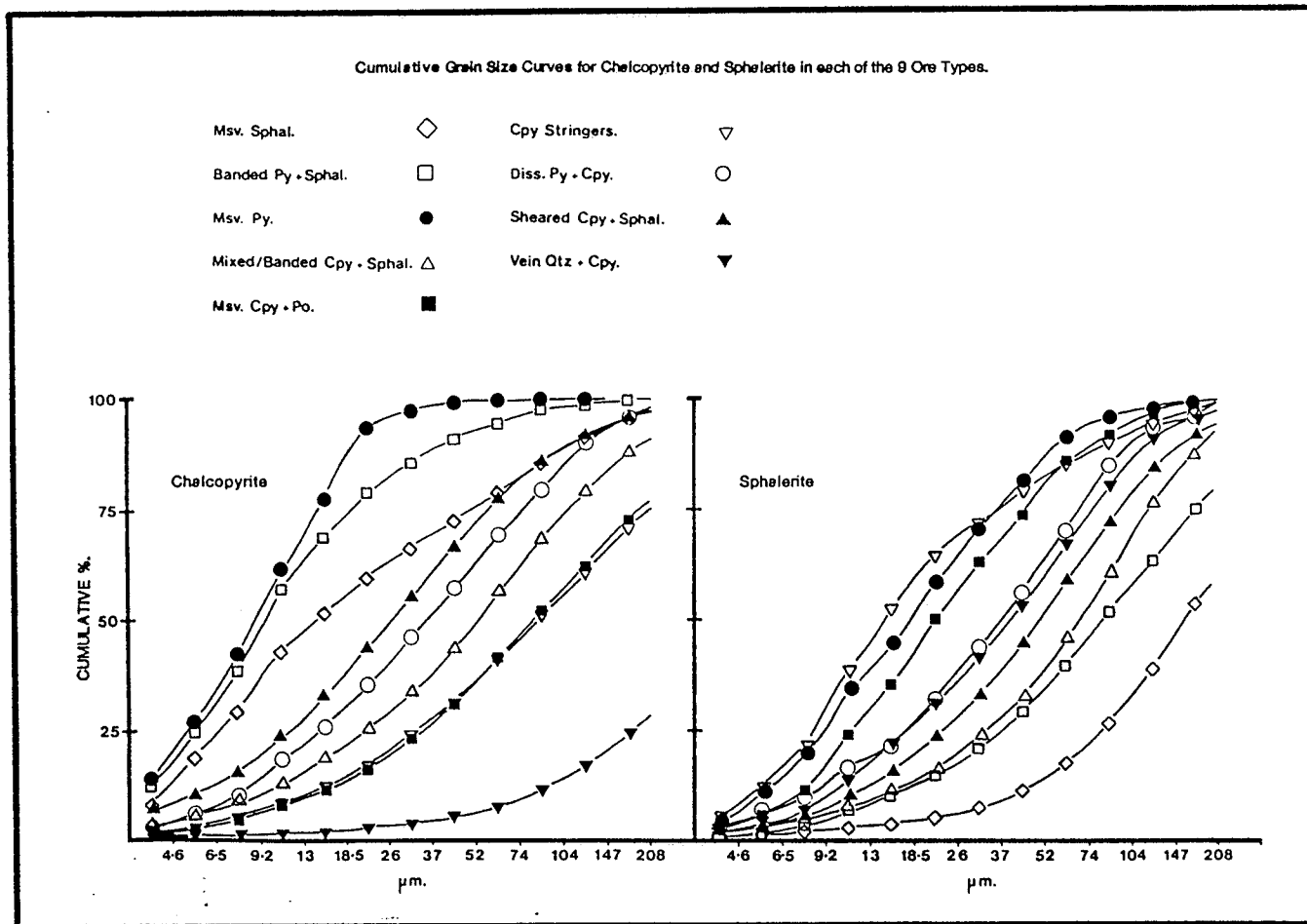


Figure 24: Cumulative Grain Size Curves of Chalcopyrite and Sphalerite in each of the Nine Ore Types.

### 6.1.5 CUBANITE

Cubanite is a trace constituent of the ores. The mineral tends to be concentrated with chalcopyrite in the footwall massive exhalative ores, the Chalcopyrite Stringer and the Vein Quartz + Chalcopyrite ore types. Cubanite occurs in two textures, and these are (1) thin lamellae in massive chalcopyrite, and measuring up to 5mm x 50um, as well as exhibiting composite or finely-lamellar habit (Fig. 18A); and (2) rare fine-grained flame-textured inclusions in chalcopyrite that is replacing pyrite. The lamellae exsolved from a high temperature chalcopyrite-like phase Iss, which decomposed on cooling.

The cubanite was found to contain neither detectable trace elements, nor significant variations in stoichiometry.

### 6.1.6 GALENA

Galena is generally a trace constituent of the ores, although occasionally it is a minor, and rarely a major constituent (See Table 11). The mineral tends to be concentrated in the hangingwall Massive Sphalerite ore type, and particularly in the Layered Pyrite + Sphalerite ore type. The relationship of galena with sphalerite-rich ores may be described as permissive; galena occurs as a major constituent exclusively, but infrequently in sphalerite-rich ores. The occurrence of the Sb-minerals (i.e., sulfosalts, sulfantimonides and alloys) freibergite, pyrargyrite, gudmundite, boulangerite, freieslebenite, bournonite and dyscrasite, as inclusions in interstitial galena is the most pronounced association of the ores. Except for rare grains of

gudmundite these minerals and dyscrasite occur exclusively as inclusions in galena, or in the case of freibergite only, also intimately spatially associated with galena.

Galena is a common constituent of the ores, occurring invariably as an anhedral, interstitial mineral with the lowest crystallinity of the common sulfides (Vokes 1969). It is generally fine-grained, though more rarely coarse-grained ( $\leq 1\text{mm}$ ), with the grain size generally increasing with the relative abundance of the galena. Because of galena's low crystallinity, it occurs in a variety of textures. These are (1) interstitial films, wedges and masses in massive pyrite (Figs. 11G and 25A); (2) irregular interstitial material between grains of massive sphalerite (Fig. 8E); (3) invading, cementing and/or replacing fractured pyrite (Fig. 11A); (4) dendritic replacements of pyrite (Fig. 25B and C); (5) fine-grained inclusions in pyrite; (6) associated with freibergite, pyrrhotite and scaly masses of marcasite that envelope and replace fractured pyrite (Fig. 11H); (7) disseminated grains in chalcopyrite + pyrrhotite matrix; (8) carious blebs to myrmekitic intergrowths with sphalerite and pyrrhotite in highly sheared Layered Pyrite + Sphalerite ores (Fig. 25D and E); and (9) carious blebs in diablastic-textured chalcopyrite, pyrrhotite and sphalerite in the Sheared Chalcopyrite + Sphalerite ores (Fig. 25F).

The grain size data of the galena from 4 ore types gives a cumulative grain size curve defined by 80% -52 $\mu\text{m}$ , with a somewhat bimodal distribution. This reflects (1) the inclusions in pyrite, interstitial blebs and films between pyrite and/or sphalerite grains, and the fracture-fillings of galena in pyrite; and (2) the coarser-grained

masses that are interstitial to and envelope pyrite and sphalerite, particularly in the Layered Pyrite + Sphalerite and the Massive Sphalerite ore types.

The bulk of the qualitative microprobe analyses of galena, done on the MAC V, failed to show the presence of any trace elements (i.e., Ag, Bi, Fe, Se and Te). However, analyses of rare graphic-textured galena in Fe-poor sphalerite, and of grains of galena with a slightly blue-white colour (when a daylight filter is interposed) and high reflectivity, indicated the presence of compositions across a wide range of the clausthalite-galena solid solution (PbSe-PbS). In addition, Ag and Te were detected in these blue-white coloured galenas, and all (rare) occurrences of galena with this characteristic colour were assumed to lie intermediate within the clausthalite-galena solid solution. These rare and optically and/or texturally distinct varieties are treated separately under the CLAUSTHALITE-GALENA SOLID SOLUTION section, whereas this section only considers the minor element-free, stoichiometric, common variety of galena, as determined on the MAC V at the UoM. However, Pinard & Petruk (1989) using WDA on the JEOL 733 at CANMET, determined the concentration of Ag in Trout Lake galena. The analyses indicated an average of 660ppm Ag in galena, with a maximum value of 1,200ppm Ag.

#### 6.1.7 SPHALERITE

Sphalerite is a ubiquitous mineral, and was observed in all the samples examined, generally occurring as a major, and more rarely as a minor or trace constituent. Sphalerite and hence Zn and Cd tend to be

concentrated in the hangingwall massive exhalative ores, specifically in the Massive Sphalerite and the Layered Pyrite + Sphalerite ore types.

Sphalerite is generally anhedral, and occurs typically as an interstitial or matrix mineral. The mineral varies from coarse-grained ( $\leq 3\text{mm}$ ) to fine-grained, with the grain size generally increasing with the relative abundance of the sphalerite. The dominant textures of sphalerite are (1) as massive coarse-grained matrix sphalerite that is interstitial to both the gangue and pyrite, particularly in the Massive Sphalerite and Layered Pyrite + Sphalerite ore types (Fig. 8A); (2) massive coarse-grained sphalerite with interstitial blebs, films, wedges and irregular masses of chalcopyrite and/or galena in the Massive Sphalerite and the Layered Pyrite + Sphalerite ore types (Fig. 8D); (3) the generally abundant to less commonly absent chalcopyrite-disease (Fig. 8C); (4) embayments and development of atoll-textured pyrite by matrix sphalerite (Fig. 8B); (5) sphalerite invading and replacing pyrite along fractures and deformation cleavages (Fig. 25G); (6) fine-grained inclusions (Fig. 25H) and dendritic replacements in pyrite (Fig. 11D); and (7) fine-grained carious blebs and myrmekitic intergrowths with chalcopyrite and pyrrhotite in the Sheared Chalcopyrite + Sphalerite ore type (Fig. 20A).

The coarse-grained sphalerite of the Massive Sphalerite and Layered Pyrite + Sphalerite ore types particularly, commonly display straight to curved repeated lamellar twinning in unetched, but poorly polished sections with high relief (Fig. 8C). These twins are interpreted to be the product of either the initial sphalerite growth and/or more probably twin gliding in response to stress. Fine-grained (approximately 10 to

15um) oriented blebs and rods of chalcopyrite (chalcopyrite-disease) are observed lying on these twin planes, where the latter are discernible. The chalcopyrite-disease is the most common and distinctive textural characteristic of the sphalerite, and its abundance generally increases with the degree of deformation and abundance of matrix chalcopyrite. It is typically most abundant in the Sheared Chalcopyrite + Sphalerite ore type. In agreement with Scott (1983), this texture is interpreted as a metamorphically recrystallized variety of the classical 'chalcopyrite-disease' of Barton & Bethke (1987), who attribute the latter to replacement of sphalerite by Cu-rich fluids. The presence of composite blebs of chalcopyrite, galena, and/or pyrrhotite are consistent with this interpretation. Less commonly however, abundant rods and blebs of pyrrhotite analogous to chalcopyrite-disease are interpreted as exsolution of FeS from Fe-rich sphalerite during equilibration to lower temperatures (Ramdohr 1980).

Microprobe analysis showed that sphalerite contains several minor and trace elements, namely Fe, Cd and Cu. However, Mn, Ag, In and Hg were also sought, but were not detected. Seven representative chemical compositions of sphalerite are presented in Table 14, whereas a complete table of analyses is given in Appendix C.

The seven compositions in Table 14 are representative of the total of 59 analyses collected from 18 samples of unbroken ore, and give a mean analysis of 33.25% S, 59.76% Zn, 6.57% Fe, 0.16% Cd and 0.06% Cu (mean total = 99.84%). This corresponds to the unit formula  $(Zn_{0.882}, Fe_{0.114}, Cd_{0.002}, Cu_{0.001}) S_{1.000}$ ; stoichiometric Fe-rich sphalerite  $(Zn, Fe, Cd, Cu)_{0.999} S_{1.000}$ . Cu was detected in 5 of the 59 analyses. However, it

TABLE 14

## Representative Chemical Compositions (Microprobe Data) of Sphalerite

wt%	1	2	3	4	5	6	7	Uncertainty (95% Confidence)
S	33.10	34.08	32.24	33.00	33.27	33.35	33.44	± 0.2
Fe	5.39	8.24	4.85	2.30	6.42	1.72	7.76	± 0.2
Zn	60.26	58.34	61.59	63.58	60.21	65.61	58.67	± 1.2
Cd	-----	0.14	0.12	0.41	-----	0.39	-----	± 0.2
Cu	0.85	-----	-----	-----	-----	-----	-----	± 0.3
Total	99.60	100.80	98.81	99.28	99.90	101.07	99.87	

## Number of atoms

S	1.00	1.00	1.00	1.00	1.00	1.00	1.00
Fe	0.09	0.14	0.09	0.04	0.11	0.03	0.13
Zn	0.89	0.84	0.94	0.95	0.89	0.97	0.86
Cd	-----	0.001	0.001	0.004	-----	0.003	-----
Cu	0.013	-----	-----	-----	-----	-----	-----

\* Unit formula calculated on the basis of 1 sulfur atom.

\* A sphalerite standard was employed for Zn and S, whereas a pyrite, chalcopyrite and a Cd-metal standard were employed for Fe, Cu and Cd, respectively.

is interpreted that the Cu is an analytical contaminant from blebs of chalcopyrite (i.e., chalcopyrite-disease) beneath the surface and hence not visible at the point of analysis, rather than Cu in solid solution. The solid solubility of CuS in sphalerite at the maximum temperature of equilibration of Trout Lake sphalerite (i.e., 450°C) is less than 1 mole% (Scott 1983), and is thus inconsistent with values in the range of 0.80 wt% Cu.

Cd was detected in 34 of the 59 analyses at concentration levels which approximate to the detection limits and gives analytical uncertainties of the order of  $\pm 100\%$  of the determined value. The analyses for Cd are included for completeness only, and cannot be considered as being quantitative. However, assuming that sphalerite is the sole Zn-bearing mineral, the assays of 0.11% Cd and 47.6% Zn in the 1983 Zn-concentrates, gives a calculated 0.14% Cd content in the sphalerite. Thus, the concentrate assays and the microprobe determined compositions suggest that sphalerite is the sole host of the Cd, and that the concentration level in sphalerite approximates to 0.15% Cd. This is confirmed by the more precise and accurate WDA (generated on the Cameca SX-50) of the common variety Fe-rich sphalerite in sample TLN.1-87, which gave a mean value of 0.13 wt% Cd. (See appendix C, D, and J for a complete listing of chemical compositions of sphalerite).

The Fe-content of the sphalerite varies from 1.72 to 8.28%, which gives an average composition of 6.57% Fe, but includes 3 analyses of Fe-poor sphalerite that are optically and texturally distinct from all other sphalerites. These 3 analyses were collected from an orange-coloured (when viewed under transmitted light) sphalerite with graphic-

**FIGURE 25: PLATE OF PHOTO-MICROGRAPHS.**

A. Sample TLS.5-84: A lamination of annealed pyrite (Py) with interstitial galena (Gal), sphalerite (Sp) and freibergite (Fr). Note the rounded and apparently corroded margins of the pyrite in contact with galena. Plane Polarized Reflected Light (PPRL). Scale bar = 160um.

B. Sample TLS.5-111: Dendritic galena and lesser freibergite replacing a pyrite porphyroclast along a zone of shearing. Note the interstitial freibergite filling a large fracture in the pyrite (top center). PPRL. Scale bar = 160um.

C. Sample TLS.5-111: Dendritic galena and lesser sphalerite replacing a pyrite porphyroclast within a zone of shearing. PPRL. Scale bar = 160um.

D. Sample TLS.1-115: A highly sheared Layered Pyrite + Sphalerite ore with deformed, fractured and highly corroded pyrite porphyroclasts in a matrix of sphalerite. The sphalerite contains abundant carious blebs and myrmekitic masses of galena and pyrrhotite (Po), both of which infill fractures and embayments in the pyrite. PPRL. Scale bar = 160um.

E. Sample TLS.1-115: A highly sheared Layered Pyrite + Sphalerite ore with deformed, fractured and highly corroded pyrite porphyroclasts in a matrix of sphalerite (as shown in Fig. 25D). Note that the galena and pyrrhotite cement the pyrite grains together. PPRL. Scale bar = 160um.

F. Sample TLN.2-9: A Sheared Chalcopyrite (Cp) + Sphalerite ore with carious blebs of galena (outlined with a dashed line) and sphalerite in coarse-grained matrix chalcopyrite. PPRL. Scale bar = 40um.

G. Sample TLS.5-84: Galena and sphalerite and trace freibergite envelop, invade and replace a deformed pyrite porphyroclast along grain boundaries, fractures and cleavages. PPRL. Scale bar = 160um.

H. Sample TLS.3-35(#2): Entrapped, fine-grained, rounded inclusions of sphalerite in pyrite. PPRL. Scale bar = 160um.

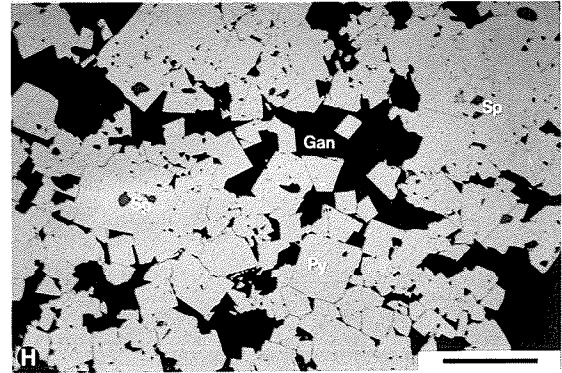
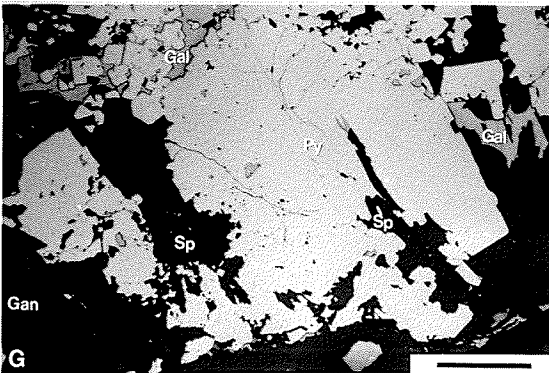
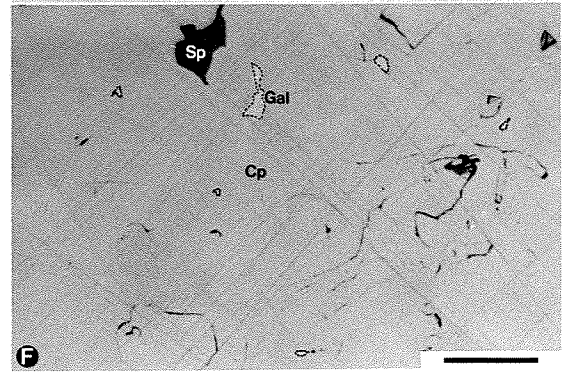
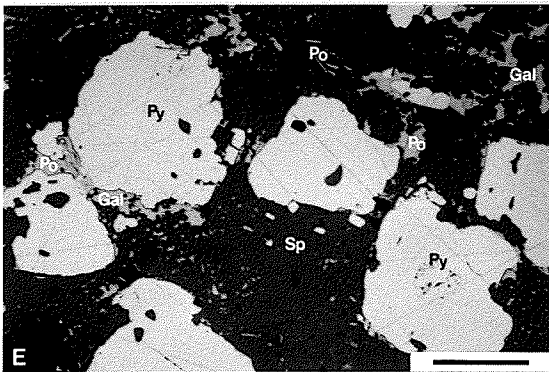
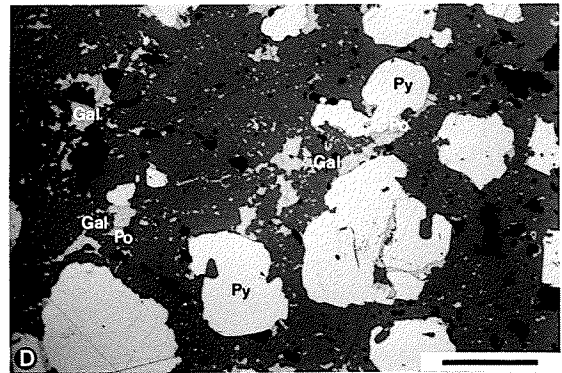
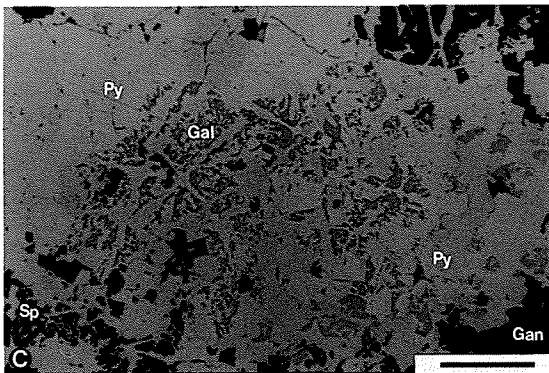
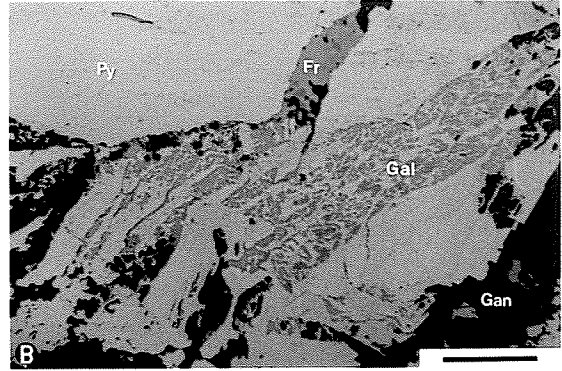
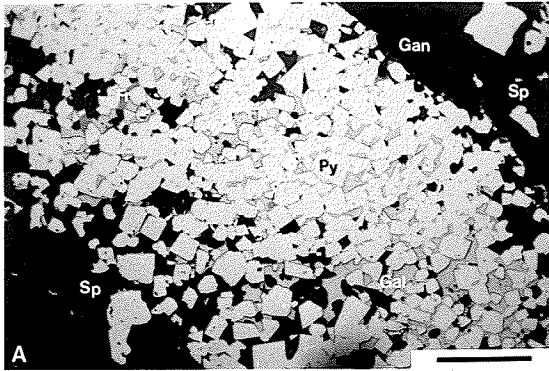
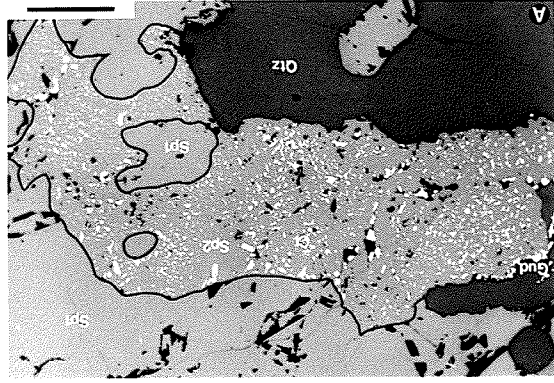
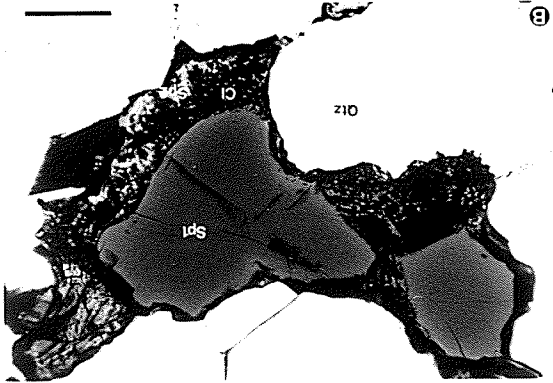
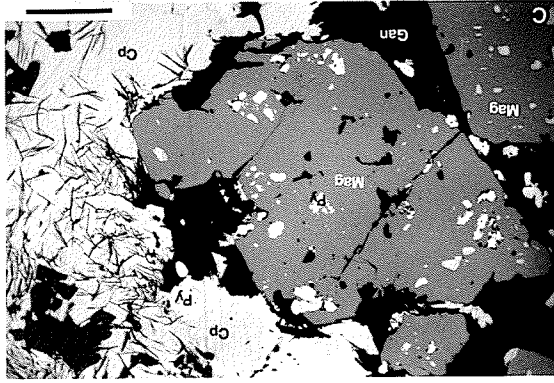
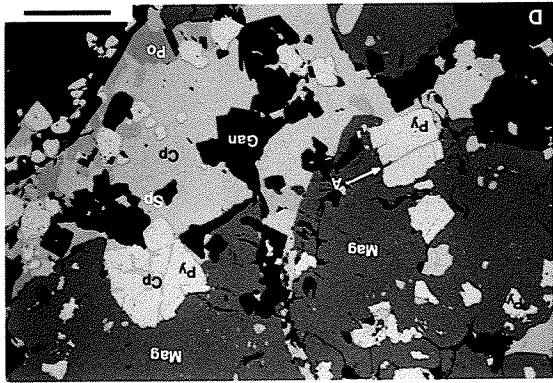
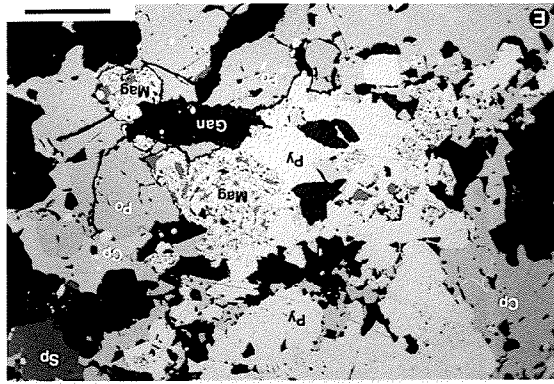
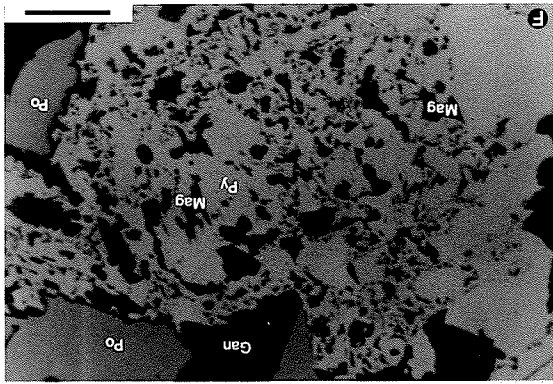
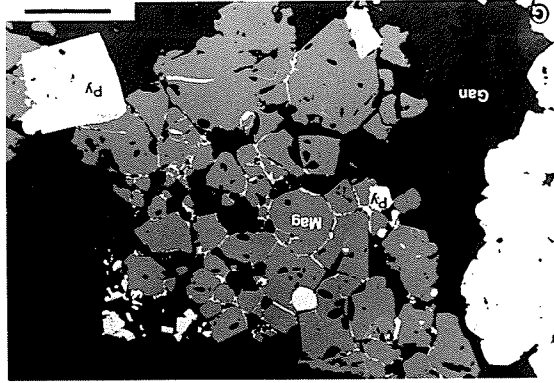
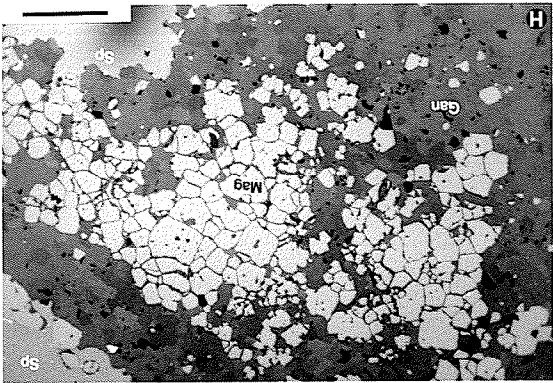


FIGURE 26: PLATE OF PHOTO-MICROGRAPHS.

- A. Sample TLN.1-87: Graphic clausthalite-galena solid solution (Cl) associated with Fe-poor sphalerite (Sp2 - outlined by solid black line) enveloping, invading and replacing Fe-rich common matrix variety sphalerite (Sp1). Note corroded remnant islands of Sp1 enveloped in Sp2, and rim of gudmundite (Gud) on Sp2 at far right margin of field. Plane Polarized Light. Scale bar = 160um.
- B. Sample TLN.1-87: Graphic clausthalite-galena solid solution (Cl - black) associated with Fe-poor sphalerite (Sp2 - light grey) engulfing corroded grains of Fe-rich common matrix variety sphalerite (Sp1 - dark grey) interstitial to quartz (Qtz - white). Transmitted Plane Polarized light. Scale bar = 160um.
- C. Sample TLS.1-53: Anhedral, fractured magnetite (Mag) porphyroclasts engulfing inclusions of fine-grained, rounded pyrite (Py). Chalcopyrite (Cp) is the dominant form the interstitial sulfide matrix around the magnetite. Note the swirls of fine-grained wisp-like gangue. PPRL. Scale bar = 160um.
- D. Sample TLS.3-42: Anhedral, fractured magnetite porphyroclasts enveloping and invading (indicated by arrow) deformed pyrite along fractures and cleavages. Chalcopyrite and lesser pyrrhotite (Po) and sphalerite form the interstitial sulfide matrix around the magnetite, and invade and corrode fractures in both the magnetite and pyrite. PPRL. Scale bar = 160um.
- E. Sample TLS.3-46: A granular mass of pyrite with zones and fringes of reticulate-textured magnetite (pyrite-magnetite symplectite) formed by the alteration of matrix pyrrhotite. Sulfide matrix consists of coarse-grained chalcopyrite, remnant pyrrhotite and minor sphalerite. PPRL. Scale bar = 160um.
- F. Sample TLS.3-46: A zone of reticulate-textured pyrite-magnetite symplectite after pyrrhotite. Matrix consists largely of chalcopyrite and remnant pyrrhotite. PPRL. Scale bar = 40um.
- G. Sample TLS.1-53: Anhedral, fractured magnetite porphyroclasts enveloping rare pyrite grains and being enveloped, invaded and corroded by a thin film of late pyrite. PPRL. Scale bar = 160um.
- H. Sample TLN.1-114: A disrupted pod of annealed magnetite in a matrix of carbonate gangue (Gan) and sphalerite. Note the preserved 120° triple junctions and the relatively equigranular and mosaic texture of the polygonal mass. PPRL. Scale bar = 160um.



textured clausthalite-galena solid solution that was only observed in sample TLN.1-87 (Fig. 26A). The Fe-poor sphalerite (II) invades and replaces the red-coloured common variety of sphalerite (I), along grain boundaries and twin planes (See section CLAUSTHALITE-GALENA SOLID SOLUTION and Appendix J). Excluding these three analyses, the Fe-content of the common variety sphalerite varies from 3.75 to 8.28%, with an average composition of 33.26% S, 59.53% Zn, 6.82% Fe, 0.15% Cd and 0.06% Cu.

#### 6.1.8 ACANTHITE

Acanthite constitutes a trace mineral, having been observed in only one polished section. It was detected during image analysis of the Trout Lake Zn-rougher concentrate, using a EDS-assisted routine for the identification of minor minerals (Healy & Petruk 1989). Because it was observed in a concentrator product, and not in an unbroken ore sample, it cannot be ascribed to any ore type.

The acanthite occurs as a mass (approximately 50um in diameter) that envelopes and cements several enclosed grains of sphalerite and pyrite. Associated with the acanthite were 3 grains ( $\leq 5\mu\text{m}$ ) of silver amalgam(?). Qualitative microprobe analyses of the amalgam failed to detect Au, and indicated approximately 30 wt% Hg, suggesting the amalgam possibly constitutes a distinct phase relative to the common Au-Ag-Hg alloy. Semi-quantitative microprobe analyses of the acanthite indicated stoichiometric proportions of Ag (2) and S (1), and failed to detect any minor or trace elements. The acanthite and silver amalgam(?) may constitute additional trace Ag-bearing minerals in the ore, or possibly

precipitates formed in the pulp during the processing of the ore. This suggests dissolution, at least in part, of one or more Ag-bearing minerals during processing (W. Petruk, pers. comm., 1986).

## 6.2 SULFARSENIDES

### 6.2.1 ARSENOPYRITE

The arsenopyrite constitutes a minor to trace mineral, and only assumes the abundance of a major constituent in the hangingwall Massive Sphalerite and the Layered Pyrite + Sphalerite ore types (See Table 11). The arsenopyrite tends to be distributed along discrete to diffuse laminae within the pyrite- and/or sphalerite-rich bands of these ore types and is suggestive of primary mineral banding. Arsenopyrite is generally not spatially associated with freibergite, which is also abundant in these ore types. However, in one sample of Massive Pyrite ore, euhedral, medium-grained arsenopyrite occurs enveloped in Ag-poor freibergite (approximately 13 to 15% Ag, i.e., tetrahedrite), and where the latter contained networked blebs of chalcopyrite, interpreted to be an exsolution texture (Fig. 11E).

Arsenopyrite is generally medium- to fine-grained, though less commonly grains measuring up to 500um have been observed. It also varies from euhedral, rhombic porphyroblasts and smaller metacrysts to fractured and granulated, anhedral grains, as well as granular masses disseminated within annealed polygonal pyrite masses/bands. The dominant textures exhibited by arsenopyrite are (1) thin laminae of disseminated, medium- to fine-grained, euhedral (i.e., characteristically rhombic) grains in sphalerite (Fig. 8G); (2) laminae of fractured coarse-grained,

subhedral to anhedral porphyroblasts that are invaded by, and contain reticulate replacements of sphalerite (Fig. 8B); and (3) medium- to fine-grained granular masses in massive polygonal pyrite.

Microprobe analysis of arsenopyrite showed that the mineral contained no detectable trace elements (Sb and Co were specifically sought for), but did show minor variation in stoichiometry. Occasionally minor Zn was detected, but this is interpreted as an analytical contaminant from common reticulate replacements of arsenopyrite by sphalerite. The compositions of six microprobe analyses are given in Table 15.

The variation in stoichiometry relates to the diadochic substitution of S for As, and results in a slightly As-deficient mean composition (i.e.,  $\text{Fe}_{0.98}\text{As}_{0.96}\text{S}_{1.06}$ ). The slight cation deficiency ( $\text{As} + \text{S} = 2.02$ ,  $\text{Fe} = 0.98$ ) probably reflects minor inaccuracy in the calibration of the microprobe operating conditions.

SIMS analyses of 44 grains of arsenopyrite in the Trout Lake tailings show that the concentration of Au in arsenopyrite varies from 2 to 112ppm Au, with an average of 30.2ppm Au (See Fig. 22, and Appendix F).

TABLE 15

## Representative Chemical Compositions (Microprobe Data) of Arsenopyrite

wt%	1	2	3	4	5	6	Uncertainty (95% Confidence)
S	22.39	21.12	22.32	20.65	19.91	21.68	± 0.2
Fe	35.42	33.76	34.27	33.64	33.57	33.64	± 0.5
As	43.15	45.30	43.70	46.19	44.95	45.34	± 1.1
Zn	-----	-----	-----	-----	-----	1.08	± 0.4
Total	100.96	100.18	100.29	100.48	98.43	101.75	
Number of atoms							
S	1.10	1.06	1.10	1.04	1.02	1.07	
Fe	1.00	0.97	0.97	0.97	0.99	0.95	
As	0.90	0.97	0.93	0.99	0.99	0.96	
Zn	-----	-----	-----	-----	-----	0.03	

\* Unit formula calculated on the basis of 3 atoms.

\* An arsenopyrite standard was employed for S, Fe and As, whereas a sphalerite standard was employed for Zn.

## 6.3 OXIDES

### 6.3.1 MAGNETITE

Magnetite is observed in several samples, but where present, it generally constitutes a major to less commonly a trace constituent. The magnetite is observed in many of the more differentiated ore types including the footwall Chalcopyrite Stringer and the hangingwall Layered Pyrite + Sphalerite ore types, and does not exhibit any distinct mineralogical association. It occurs as disseminated grains, in clusters, and in laminae within the sulfides and the gangue (Fig. 26G), and whose distribution is suggestive of primary mineral banding. It is interpreted that the magnetite is not a primary product of the original ore deposition, but is a metamorphic product, whose distribution is controlled by the mineralogical and hence chemical banding of the ores.

The magnetite typically occurs as dodecahedral porphyroblasts (Fig. 26C and D), which are generally medium- to fine-grained, and less commonly coarse-grained ( $\leq 2\text{mm}$ ). The porphyroblasts generally contain inclusions of pyrite, chalcopyrite and sphalerite, and are observed occasionally enveloping and invading fractured pyrite (Fig. 26C). The magnetite is thus interpreted to postdate the porphyroblastic growth of pyrite, and its subsequent deformation. However, in sample TLS.1-53 severe deformation has resulted in the mobilization of pyrite into veinlets that infill the interstices of, and crosscut, fractured magnetite (Fig. 26G). Rare pods and lenses of polygonal magnetite are also observed (See Fig. 16D and 26H). In addition, fringes and zones of fine-grained, reticulate-textured magnetite in pyrite, referred to as pyrite-magnetite symplectite, are common in many of the ore types (Figs.

13G, 16C and 26E and F). This texture is the product of oxidation of pyrrhotite, with the simultaneous growth of pyrite and magnetite under conditions of higher oxygen activity (Kieft et al. 1987).

Ten microprobe analyses of magnetite revealed no detectable minor or trace elements, and only slight apparent variation in stoichiometry. The 10 analyses gave an average composition of 72.15% Fe and 27.85% O, which is in good agreement with the ideal composition of 72.36% Fe and 27.64% O for pure end-member magnetite. Three compositions encompassing the observed range in composition are given in Table 16.

TABLE 16

Representative Chemical Compositions (Microprobe Data) of Magnetite

wt%	1	2	3	Uncertainty (95% Confidence)
Fe	72.35	71.60	72.59	± 0.6
O	27.65	28.40	27.41	
at%				
Fe	42.84	41.94	43.13	
O	57.16	58.06	56.87	

\* Oxygen is not amenable to electron microprobe analysis and is calculated by difference from 100% (not by stoichiometry).

### 6.3.2 CASSITERITE

Cassiterite is a trace constituent of the ores, that was identified during image analysis of the mill products. Because it was not detected in any of the ore samples, it cannot be ascribed to any of the ore types. It occurs in many concentrator products as  $\leq 25\mu\text{m}$  grains with an approximate mean grain size of 10 to  $15\mu\text{m}$ . It generally occurs locked with chalcopyrite or sphalerite, and was observed with greater frequency in Cu-circuit products (Healy & Petruk 1989). Qualitative microprobe analysis of the cassiterite indicated pure (minor element-free)  $\text{SnO}_2$ .

## 6.4 SULFOSALTS

### 6.4.1 FREIBERGITE

Freibergite is the name applied to argentian tetrahedrite with greater than 20 wt% Ag (Riley 1974), and tetrahedrite when the mineral contains less than 20 wt% Ag. Microprobe analyses of the Trout Lake tetrahedrite/freibergite indicated compositions that span this 20 wt% boundary, but which give an average Ag content of 21.7 wt% Ag. For convenience all compositions observed in this study that lie within the tetrahedrite-freibergite solid solution series are referred to as freibergite.

Freibergite is a trace constituent of the ores, and was found only in samples of the Massive Sphalerite, Layered Pyrite + Sphalerite and the Massive Pyrite ore types. Therefore, freibergite is concentrated in the hangingwall to central parts of the stratigraphic sequence. It is most commonly observed in the Layered Pyrite + Sphalerite ores, where it may

constitute 0.1 vol%, as in TLS.2-26, rather than typical quantities of  $\leq 0.05\%$  in the Massive Pyrite and Massive Sphalerite ore types. The freibergite occurs only as inclusions in, or discrete grains associated with galena, and tends to be less abundant where the galena is associated with prominent chalcopyrite. Freibergite along with the other Sb-sulfosalts, sulfantimonides (except costibite) and dyscrasite are concentrated in the hangingwall Zn-rich ores, but only where galena attains prominence. This mineralogical association is consistent with the strong geochemical affinity of Pb, Sb and Ag in the distal, Zn-rich ore, which are the equivalent of the 'Kuroko' or Black' ores of the Kuroko deposits, Japan.

Freibergite is invariably anhedral, and varies from generally fine-grained rounded inclusions in galena, to rare medium-grained ( $\leq 500\mu\text{m}$ ) interstitial grains associated with galena. The dominant textures exhibited by freibergite are (1) extremely fine-grained ( $\leq 25\mu\text{m}$ ) rounded inclusions marginally located within interstitial galena in massive sphalerite (Fig. 8E); (2) anhedral, fine- to medium-grained discrete grains in massive sphalerite (Fig. 13B); (3) interstitial masses of galena and freibergite that envelope, invade, cement and/or replace fractured pyrite in the Layered Pyrite + Sphalerite ores (Fig. 11A, E and G); (4) freibergite associated with galena, pyrrhotite and foliated scaley masses marcasite replacing pyrite (Fig. 11H); and (5) myrmekitic intergrowths in galena (Fig. 27A).

Sixty quantitative EDA of freibergite show the consistent abundance of the major elements Cu, Ag, Fe, Sb and S, and the variably minor to trace (or undetected) concentrations of Zn and As. Seven representative

compositions are given in Table 17, whereas a complete table of the analyses is given in Appendix G.

Because of the position of the  $AsL\alpha$  line on the inclined and structured 'front end' of the spectrum, and also because of the severe absorption of this 'soft' wavelength, the detection limit for the  $AsL\alpha$  line is approximately 0.2% As. Because of the low tennantite component in the freibergite ( $Cu_{12}As_4S_{13}$ ), the analyses suffer from poor sensitivity in the As determinations. In addition, the overlap of the  $CuK\beta$  into the  $ZnK\alpha$  ROI, and its subsequent routine stripping, degraded the peak shape and increased the uncertainty in the Zn determinations, which are based on the small  $ZnK\alpha$  peak. The Ag L-series peaks were also routinely stripped out from the  $SbL\alpha$  ROI. Because of the uncertainties generated in the determinations of these elements, the limitations in the EDA of freibergite, and because of the probability of non-stoichiometric compositions, the number of atoms per unit formula was calculated on the basis of 13 sulfur atoms, rather than a given number of cations.

The most notable deviations in stoichiometry are the consistently (except one analysis) high number of atoms of Fe + Zn per unit formula ( $\bar{x} = 2.23$ ), and the deficiency in the Cu + Ag ( $\bar{x} = 9.88$ ). It is apparent that the widely used general formula for the tennantite-tetrahedrite solid solution  $(Cu,Ag)_{10}(Fe,Zn)_2(Sb,As)_4S_{13}$  (Riley 1974) does not fully describe the substitution of Ag, Fe and Zn into the ideal end-members tetrahedrite ( $Cu_{12}Sb_4S_{13}$ ) and tennantite ( $Cu_{12}As_4S_{13}$ ). The IMA approved unit formula for tetrahedrite  $(Cu,Ag,Fe,Zn)_{12}(Sb,As)_4S_{13}$  (Fleischer 1987) better describes, and is consistent with, the compositions of Trout Lake freibergite.

TABLE 17

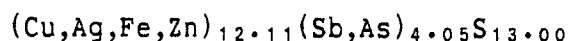
Representative Chemical Compositions (Microprobe Data) of Freibergite

wt% Com- ment	1 Average type	2 High Sb	3 High Ag	4 High Cu, As	5 Low Ag	6 Low Zn	7 High Zn	Uncertainty (95% Confidence)
S	22.53	23.63	21.77	24.24	24.02	23.03	22.19	± 0.1 - 0.2
Fe	5.59	5.67	6.52	5.88	5.98	5.62	4.83	± 0.2 - 0.3
Zn	1.54	1.46	1.20	1.45	1.89	----	2.65	± 0.4 - 0.5
Cu	20.37	23.26	14.73	28.46	27.51	24.12	22.80	± 0.5 - 0.6
Ag	22.22	18.83	30.31	14.76	13.05	18.97	20.21	± 0.2 - 0.4
As	-----	-----	-----	2.83	-----	-----	-----	± 0.0 - 0.5
Sb	26.61	28.10	26.33	23.64	27.97	27.25	26.30	± 0.4 - 0.5
Total	98.86	101.05	100.86	101.26	100.42	98.99	98.98	
Number of atoms								Ideal
S	13.00	13.00	13.00	13.00	13.00	13.00	13.00	13.00
Fe	1.85	1.79	2.23	1.81	1.86	1.82	1.62	} 2.00
Zn	0.44	0.39	0.35	0.38	0.50	----	0.76	
Cu	5.93	6.48	4.44	7.70	7.52	6.87	6.74	} 10.00
Ag	3.81	3.08	5.38	2.35	2.10	3.18	3.52	
As	-----	-----	-----	0.65	-----	-----	-----	
Sb	4.04	4.07	4.14	3.34	3.99	4.05	4.06	4.00

\* Unit formula calculated on the basis of 13 sulfur atoms.

\* A pyrite standard was employed for S and Fe, whereas a chalcopyrite, sphalerite, arsenopyrite, Ag-metal and a stibiotantalite (SbTaO<sub>4</sub>) standard were employed for Cu, Zn, As, Ag and Sb, respectively.

The 60 analyses gave an average composition of 22.78 wt% S, 5.58 wt% Fe, 1.14 wt% Zn, 21.58 wt% Cu, 21.68 wt% Ag, 0.20 wt% As and 26.66 wt% Sb, with a mean total of 99.82%. This composition translates into the unit formula



which constitutes near stoichiometric freibergite close to the tetrahedrite composition.

The compositions show the diadochic substitutions of Sb-As, Cu-Ag and Fe-Zn. The coupled substitution of  $\text{Sb} + \text{Ag} = \text{Cu} + \text{As}$  is not clearly defined because of the detection limit and sensitivity for As. Miller & Craig (1983) point out that the correlation of Ag with Sb is not linear, but merely 'permissive', such that high Sb may be accompanied by high Ag, whereas high As is always accompanied by high Cu and low Ag. This is apparent from analyses 4 and 5, where analysis 5 contains higher Sb, yet lower Ag than analysis 4. The Ag values of all 60 compositions range from 13.05 to 30.31% Ag, yet the As values do not exceed 2.83% As (i.e., 0.65 atoms per unit formula). It is noteworthy that the most Ag-poor analyses were collected on a large mass of freibergite with networked blebs of chalcopyrite interpreted as an exsolution product, and euhedral inclusions of arsenopyrite and abundant associated Au-Ag-Hg alloy (See Fig. 11E).

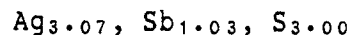
#### 6.4.2 PYRARGYRITE

Pyrargyrite (otherwise known as 'Ruby Silver') is a rare constituent of the ores. It invariably occurs as anhedral inclusions associated with pyrrhotite and/or gudmundite inclusions within interstitial masses of galena in the Massive Sphalerite, and less commonly the Layered Pyrite + Sphalerite ore type (Fig. 27C). The pyrargyrite occurs in sphalerite-rich ores with abundant galena, and is invariably subordinate to freibergite (except in TLS.5-64 i.e., 0.02 vol% pyrargyrite and 0.01 vol% freibergite). It is a characteristic, but non-essential mineral of the Zn, Pb, Sb and Ag geochemical association.

Several microprobe analyses of pyrargyrite were attempted, but the fine-grained ( $\leq 20\mu\text{m}$ ) nature of the pyrargyrite, and calibration and tarnishing problems resulted in only one acceptable analysis. This analysis is given below.

17.25% S, 59.38% Ag and 22.46% Sb (Total = 99.09%).

which translates into the unit formula



No As was detected.

#### 6.4.3 BOULANGERITE

Boulangierite is an extremely rare trace constituent of the hangingwall Layered Pyrite + Sphalerite ores. The mineral was observed as a single 15 $\mu\text{m}$  inclusion that was associated with freibergite within

an interstitial mass of galena in massive sphalerite from sample TLS.2-26. The identity was confirmed by qualitative EDA. No detectable minor or trace elements were observed. Quantitative microprobe analyses were unattainable because of the grain size, resulting in contamination by adjacent phases, and because of the failure to adequately resolve the PbM $\alpha$  and the SK $\alpha$  overlap. The determined variations in stoichiometry may indicate either solid solution towards falkmanite (Pb<sub>3</sub>Sb<sub>2</sub>S<sub>6</sub>), or more probably poor resolution of overlap phenomena. Sample TLS.2-26, the only sample in which boulangerite was observed, contains 0.1 vol% freibergite and 3 vol% galena, and is therefore characterized by the Zn, Pb, Sb and Ag association.

#### 6.4.4 FREIESLEBENITE

Freieslebenite is an extremely rare trace constituent of the hangingwall Layered Pyrite + Sphalerite ores. Only one anhedral grain (approximately 20 x 10 $\mu$ m) associated with pyrargyrite, freibergite, gudmundite and pyrrhotite as inclusions within interstitial galena in the massive sphalerite of TLS.5-84, was observed (Fig. 13A). In addition to galena, freibergite, gudmundite and pyrargyrite sample TLS.5-84 also contains dyscrasite, all of which are characteristic of the Zn, Pb, Sb and Ag geochemical association.

Two microprobe analyses of this one grain failed to detect any minor or trace elements. The analyses were processed by iterative stripping of the overlapping peak flanks of SK $\alpha$  and PbM $\alpha$ , and in the case of one analysis, the PbM $\alpha$  was iteratively stripped and Pb was calculated by difference from 100%. The analyses given in Table 18 are considered

semi-quantitative, but clearly confirm the identification of freieslebenite.

TABLE 18

## Chemical Compositions (Microprobe Data) of Freieslebenite

Analysis	wt%					Number of atoms			
	S	Ag	Sb	Pb	Total	S	Ag	Sb	Pb
Freies-1.	18.50	19.96	23.16	38.38	-----	6.148	1.972	2.028	1.975
Freies-1.	18.35	19.94	23.17	37.03	98.49	6.065	1.971	2.029	1.905
Freies-2.	18.64	21.11	21.97	38.40	100.12	6.183	2.008	1.992	1.905
Uncertainty. (95% Confidence)	± 0.2	± 0.3	± 0.4	± 0.4					

- \* Unit formula calculated on the basis of 4 atoms of Ag + Sb.
- \* A pyrite, Ag-metal, stibiotantalite and an altaite (PbTe) standard was employed for S, Ag, Sb and Pb, respectively.
- \* The first analysis of Freies-1 was processed by iteratively stripping the PbM $\alpha$  and calculating Pb by difference from 100%.

FIGURE 27: PLATE OF PHOTO-MICROGRAPHS.

A. Sample TLN.1-87: A mass of myrmekitic freibergite (Fr) within a grain of galena (Gal) from a Massive Sphalerite (Sp) ore. This mass is spatially associated with graphic clausthalite-galena solid solution in Fe-poor sphalerite. Plane Polarized Reflected Light (PPRL). Scale bar = 40um.

B. Sample TLS.5-64: A thin reaction rim of myrmekitic pyrrhotite (Po) and gudmundite (Gud), and associated freibergite and sphalerite forming on a corroded pyrite (Py) porphyroblast. Probably produced by reaction of late Sb- and Ag-rich fluids with pyrite. PPRL. Scale Bar = 40um.

C. Sample TLS.5-64: Interstitial galena containing inclusions of pyrrhotite (Pyr), pyrrhotite, sphalerite and gudmundite, within a matrix of sphalerite. PPRL. Scale bar = 40um.

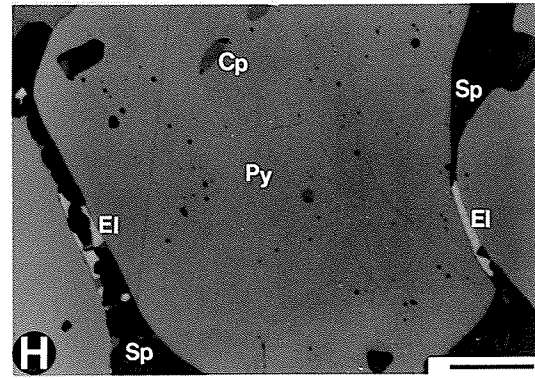
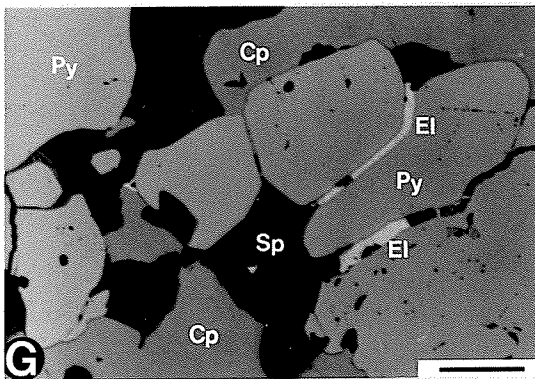
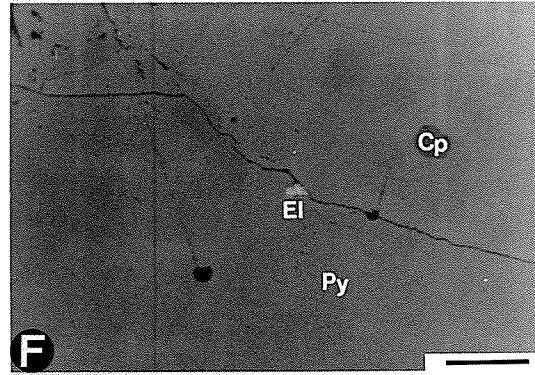
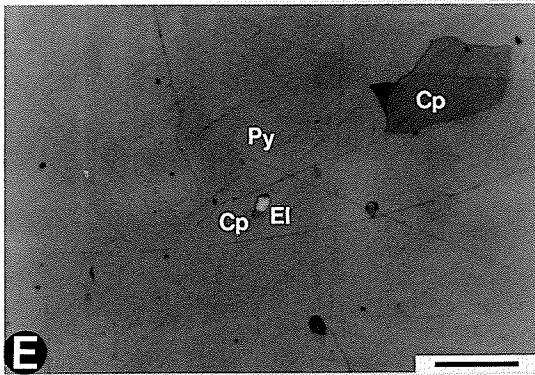
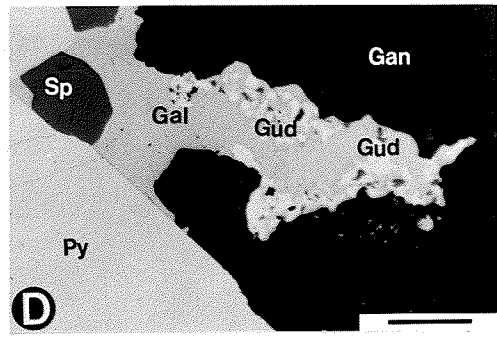
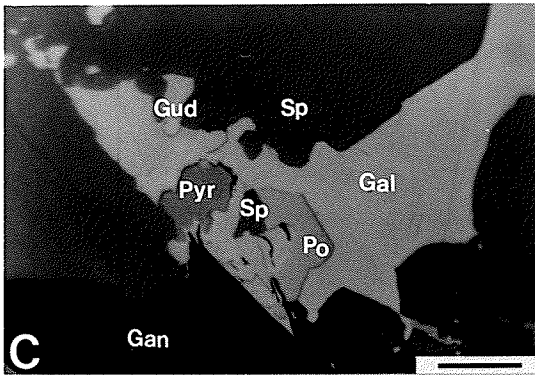
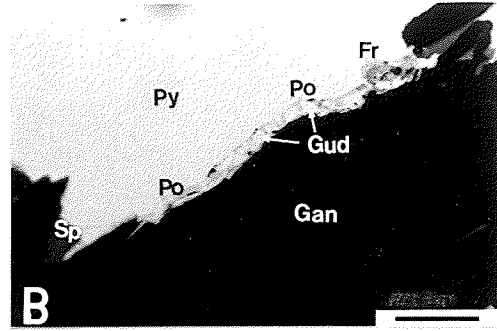
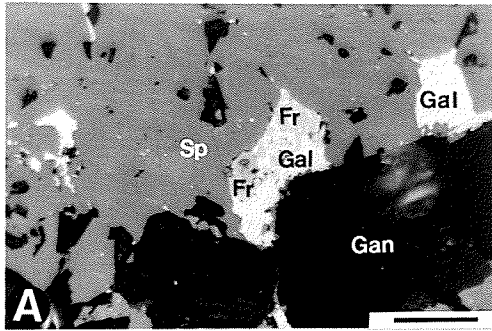
D. Sample TLS.5-84: Myrmekitic gudmundite in galena, which is associated with sphalerite and forms the interstitial matrix material to a large pyrite grain. PPRL. Scale bar = 40um.

E. Sample TLN.2-8: A composite, fine-grained inclusion of Type 1A Au-Ag-Hg alloy (E1) and chalcopyrite (Cp) in pyrite. PPRL. Scale bar = 40um.

F. Sample TLN.2-8: A fine-grained inclusion of Type 1A Au-Ag-Hg alloy forming on a fracture in pyrite. Note the rounded inclusions of chalcopyrite. PPRL. Scale bar = 40um.

G. Sample TLN.2-8: Type 1A Au-Ag-Hg alloy forming grain coatings on, and fracture-fillings in pyrite. Sphalerite and chalcopyrite are the dominant matrix sulfides, and fill the interstices to the pyrite. PPRL. Scale bar = 40um.

H. Sample TLN.2-8: Type 1A Au-Ag-Hg alloy forming grain coatings on pyrite. The alloy is associated with interstitial sphalerite and lesser chalcopyrite. Note the pyrite grains are well rounded. PPRL. Scale bar = 40um.



#### 6.4.5 BOURNONITE

Bournonite is an extremely rare constituent of the ores, that was identified during image analysis of several of the concentrator products. Because it was not detected in any of the ore samples, it cannot be ascribed to any of the ore types. It occurs in the concentrator products as fine-grained ( $\leq 10\mu\text{m}$ ) euhedral grains with stubby to prismatic habit. It occurs associated with freibergite as inclusions in sphalerite. Because of its association with sphalerite and freibergite, and because of the known geochemical association of Sb and Pb with Zn, it is suggested that bournonite probably occurs in the hangingwall Massive Sphalerite and the Layered Pyrite + Sphalerite ore types.

Qualitative electron microprobe analysis of the bournonite detected minor concentrations of Fe, in addition to the major elements Pb, Cu, Sb and S.

#### 6.5 SULFANTIMONIDES

##### 6.5.1 GUDMUNDITE

Gudmundite is observed in several samples and invariably constitutes a trace constituent. It was observed in the hangingwall Layered Pyrite + Sphalerite and Massive Sphalerite ores, where galena attains prominence. However, it was also observed (1) associated with pyrrhotite in a rim of sphalerite at the contact with a quartz vein; and (2) associated with graphic-textured clausthalite-galena solid solution in late Fe-poor sphalerite. Gudmundite is less abundant than freibergite, but more

abundant than pyrargyrite. Both freibergite and gudmundite are characteristic and essential minerals of the Zn, Pb, Sb and Ag geochemical association, whereas pyrargyrite, boulangierite, freieslebenite and dyscrasite are non-essential minerals, only occurring where freibergite and gudmundite are abundant.

The gudmundite varies from fine-grained to rarely medium-grained ( $\leq 150\mu\text{m}$ ), and from euhedral to anhedral depending on the textural association. The dominant textures exhibited by gudmundite are (1) fine-grained, euhedral, bladed to tabular, subhedral to rounded inclusions in galena (Figs. 8E, 13A and 27C); (2) lobate and myrmekitic intergrowths with galena (Fig. 27D); (3) myrmekitic intergrowths with pyrrhotite and associated with freibergite, as a reaction rim on pyrite (Fig. 27B); (4) veinlets of fine-grained, anhedral grains associated with Fe-poor sphalerite and clausthalite-galena solid solution (in TLN.1-87); and (5) rare anhedral grains associated with pyrrhotite disseminated in matrix sphalerite.

Gudmundite was found to contain neither detectable trace elements nor any significant deviations in stoichiometry. Eight compositions are presented in Table 19.

TABLE 19

## Chemical Compositions (Microprobe Data) of Gudmundite

wt%	1	2	3	4	5	6	7	8	Uncertainty (95% Confidence)
S	15.28	15.36	15.20	15.42	15.19	15.13	15.66	15.18	± 0.2
Fe	26.63	26.66	26.96	27.09	26.48	27.25	26.58	26.22	± 0.4
Sb	57.63	57.89	58.12	57.96	57.94	58.29	57.65	57.84	± 0.7
Tot.	99.54	99.91	100.28	100.47	99.61	100.67	99.89	99.24	

## Number of atoms

S	1.00	1.00	0.99	1.00	1.00	0.98	1.02	1.00
Fe	1.00	1.00	1.01	1.01	1.00	1.02	0.99	0.99
Sb	1.00	1.00	1.00	0.99	1.00	1.00	0.99	1.01

\* Unit formula calculated on the basis of 3 atoms.

\* A pyrite and a stibiotantalite standard were employed for Fe and S and Sb, respectively.

## 6.5.2 COSTIBITE

One grain ( $\leq 10\mu\text{m}$ ) of costibite was identified in sample TLN.2-63, through the use of BSE imagery and qualitative EMPA as a check of grey level compositional integrity during routine image analysis. No quantitative microprobe analyses were attempted, as the grain could not be located subsequently. In addition to Co, Sb and S, the presence of minor Fe was also detected. Sample TLN.2-63 is classified as a Sheared Chalcopyrite + Sphalerite ore and contains negligible pyrite. It is suggested that during the deformation and breakdown of pyrite, Co in solid solution in pyrite is liberated. Much of the Co may have entered the pyrrhotite structure, but some may have combined with available Sb and S. The identification as costibite is tentative, as this composition may correspond to costibite or its polymorphs paracostibite or willyamite.

## 6.6 ALLOYS AND INTERMETALLIC COMPOUNDS

### 6.6.1 Au-Ag-Hg ALLOY

Prior to this study the host of the Au had not been identified with confidence, the sole published reference being to a 'metallic gold' mineral (Muzylowski 1979). A gold-bearing mineral whose optical properties are similar to those of electrum was observed in 37 of 112 samples. The mineral shows a wide range in composition (in wt%): 17.34 to 76.5% Ag, 1.6 to 79.9% Au and 1.3 to 30.9% Hg. This compositional range constitutes an extension of the continuous binary Au-Ag solid-solution into the Ag-Au-Hg ternary system. These ternary alloys have been referred to as gold-silver amalgam (Nysten 1986), mercurian

electrum (Scott 1977, Healy & Petruk 1988, 1989, 1990b), and mercurian gold (Shikazono & Shimizu 1988). However, none of these terms encompass the full range in compositions observed at Trout Lake. Healy & Petruk (1990) used the term Au-Ag-Hg alloy to denote compositions encompassing those of both mercurian gold and mercurian silver, and that term is also used in this study.

The Au-Ag-Hg alloy was found in all the ore types, except the Vein Quartz + Chalcopyrite ore type. The Au-Ag-Hg alloy is invariably a trace constituent, but in sample TLN.1-89 (Chalcopyrite Stringer ore), a 5mm-long anastomosing mass comprises 0.2 area% of the polished section. It occurs in the nose of a mesoscopic, disharmonic fold structure along the contact between laminae of massive chalcopyrite and chlorite schist. Additional sections coplanar to TLN.1-89(a) (i.e., b to k) revealed similar masses on the same, and less commonly also on adjacent fold structures, over a distance of 9cm.

The Au-Ag-Hg alloy occurs in two textural types. Type 1 Au-Ag-Hg alloy is texturally associated with pyrite and consists of: (A) fine-grained inclusions in pyrite (Fig. 27E), fracture-fillings in pyrite (Fig. 27F and G), and grain coatings on the margins of, and as interstitial-fillings between pyrite grains (Fig. 27G and H); and (B) grains encapsulated by and associated with galena, freibergite and minor arsenopyrite, which occur interstitial to, or as fracture-fillings in, fractured pyrite (Figs. 11E, 28A, B, C and D). Type 1B was observed in 3 samples and is thus volumetrically insignificant and restricted to the Massive Pyrite and the Layered Pyrite + Sphalerite ore types. Type 1B is distinguished to emphasize that, although rare at Trout Lake, the

association of electrum or Au-Ag-Hg alloy with galena and freibergite is a distinctive assemblage in many Canadian massive sulfide deposits (Healy & Petruk 1990a). Type 1 alloy is found in all but one ore type, and is by far the most common type. Approximately one third (i.e., 103) of all Type 1A grains were found in a single polished section of TLN.2-8, a sample of Sheared Chalcopyrite + Sphalerite ore that occurs adjacent to a syntectonic quartz-diorite sill.

Type 2 alloy was observed in TLN.1-89(a - k) and TLN.2-11 only, and consists of large (i.e., <5mm) anastomosing masses and lesser disseminations distributed along the contact between laminae of chalcopyrite and chlorite schist (Fig. 28E and G). Type 2 was found only in the Chalcopyrite Stringer ores, and in spite of its scarcity, it undoubtedly constitutes volumetrically the most significant type.

#### **6.6.1.1 Grain Size Distribution of Au-Ag-Hg Alloy**

The grain-size distribution of grains of Type 1 alloy was measured using a Reichert Zetoplan optical microscope with calibrated graticules. Because Au-Ag-Hg alloy of Type 1 tends to assume a rectangular shape in the plane of the section, it is not amenable to measurement by a single dimension. Each grain was measured along its maximum dimension ( $d_m$ ), and then an average dimension ( $d_i$ ) perpendicular to  $d_m$  was estimated. The 'equivalent square diameter' (Petruk 1976) was calculated from the product of  $d_m$  and  $d_i$ . The grain size distribution of Type 1 Au-Ag-Hg alloy is given in Figure 29, and is defined by 80% -18 $\mu$ m.

**FIGURE 28: PLATE OF PHOTO-MICROGRAPHS.**

A. Sample TLS.2-40(#2): A large interstitial mass of freibergite (Fr), in massive annealed pyrite (Py). The freibergite contains galena (Gal), arsenopyrite (Asp), sphalerite (Sp), exsolved networks and blebs of chalcopyrite (Cp) and disseminations of fine-grained Type 1B Au-Ag-Hg alloy (El). The alloy also occurs as fracture-fillings, and as coarser-grained interstitial grains associated with freibergite and galena in pyrite (See point A). Plane Polarized Reflected Light (PPRL). Scale Bar = 160um.

B. Sample TLS.2-40(#2): High magnification view of area indicated by point A in Figure 28A. The Type 1B Au-Ag-Hg alloy is intimately associated with galena and freibergite filling fractures and interstitial spaces in the pyrite. PPRL. Scale bar = 40um.

C. Sample TLS.2-40(#2): High magnification view of area at top left splayed and fractured termination of freibergite mass in Figure 28A. The freibergite contains networked blebs of exsolved chalcopyrite, inclusions of sphalerite, and extremely fine-grained disseminations Type 1B Au-Ag-Hg alloy. PPRL. Scale bar = 40um.

D. Sample TLS.5-83A: Galena, freibergite, sphalerite and Type 1B Au-Ag-Hg alloy invading and replacing a coarse-grained pyrite porphyroclast along a large fracture. Note poorly formed dendritic galena in pyrite (left center of field). PPRL. Scale bar = 160um.

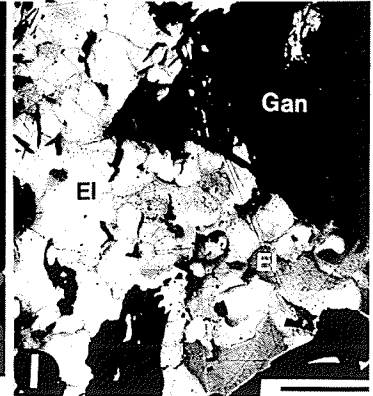
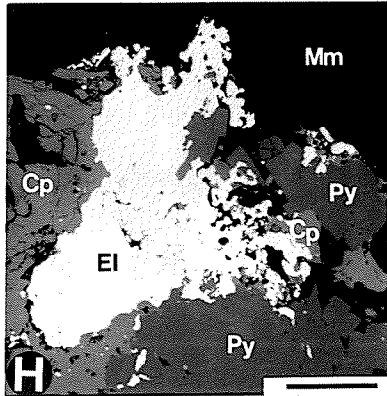
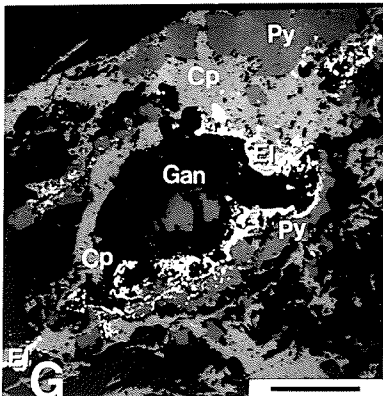
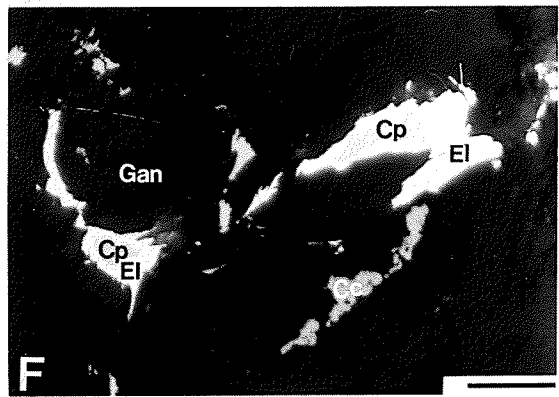
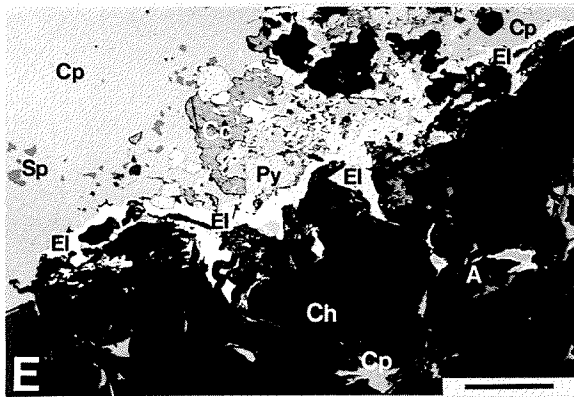
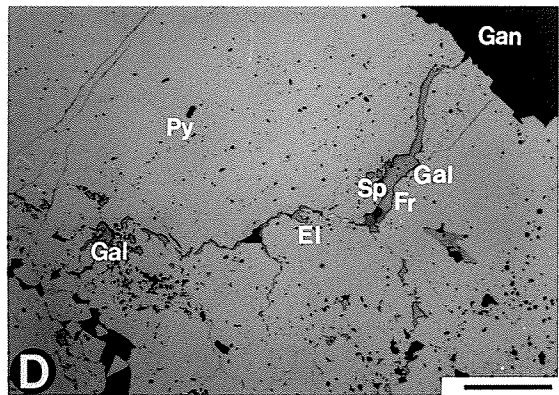
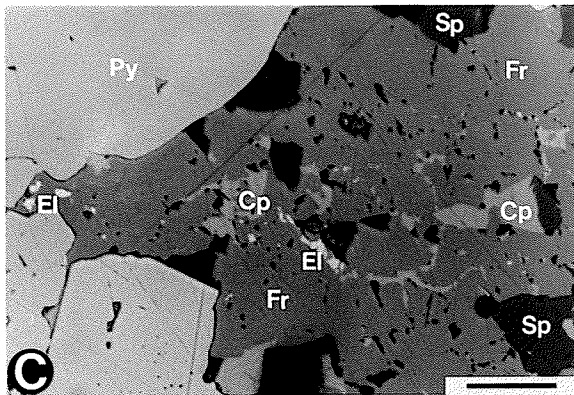
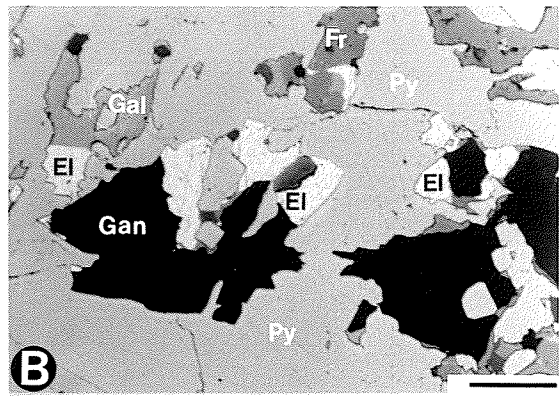
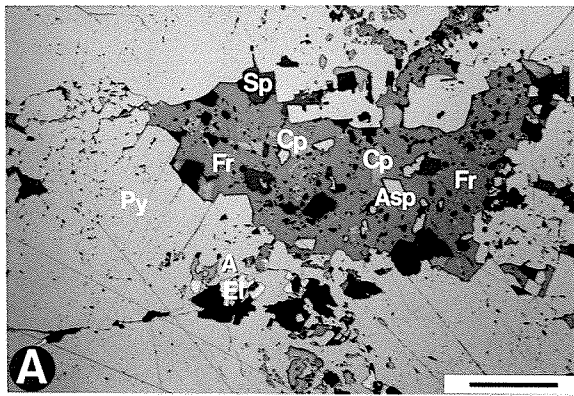
E. Sample TLN.1-89a: A 2mm long anastomosing mass and lesser disseminations of Type 2 Au-Ag-Hg alloy formed along chalcopyrite (Cp) - chlorite schist gangue (Gan) laminae contact. The alloy invades and corrodes chalcopyrite and pyrite. Note carious blebs of sphalerite (far left). Cc denotes persistent carbon coat. PPRL. Scale bar = 160um.

F. Sample TLN.1-89a: Detail of area indicated by point A in Figure 28E. Chalcopyrite is enveloped and corroded by the alloy, which also invades the dilated cleavage traces of some of the chlorite gangue. PPRL. Scale bar = 40um.

G. Sample TLN.1-89k: Large anastomosing mass and lesser disseminations of Type 2 Au-Ag-Hg alloy formed along the strongly folded chalcopyrite - chlorite schist laminae contact. Note granulated, fractured and ruptured pyrite grains. Backscattered electron (BSE) image. Scale bar = 500um.

H. Sample TLN.1-89k: Large mass of Type 2 Au-Ag-Hg alloy invading and replacing pyrite and chalcopyrite. Mm denotes mounting medium. BSE. Scale bar = 140um.

I. Sample TLN.1-89a: Detail of angular lobe of Type 2 Au-Ag-Hg alloy marked by El at the center of the field in Figure 28E. Different grey levels show complex inhomogeneity of mass, with Ag-rich (dark) and Ag-poor (light) grains. High contrast BSE. Scale bar = 30um.



The grain size distribution of Type 2 alloy (sections TLN.2-11 and TLN.1-89a) was determined by image analysis, and is defined by 80% -37 $\mu$ m. The grain size distributions for Types 1 and 2 are given in Fig. 29. The two sections TLN.1-89a and TLN.2-11 contain approximately 600,000  $\mu$ m<sup>2</sup> and 9,000  $\mu$ m<sup>2</sup> of Type 2 alloy, respectively, whereas 417 grains of Type 1 in 35 samples contain approximately 11,000  $\mu$ m<sup>2</sup>. A 'sample' (statistical) of 417 grains in 35 samples is considered representative of Type 1, whereas 2 masses of Type 2 Au-Ag-Hg alloy, especially the overwhelming influence of the mass in TLN.1-89, cannot be considered as a large enough 'sample' to be representative of Type 2. Thus, the abundance of Type 1 relative to Type 2 is not statistically constrained. Consequently, an unweighted average grain size distribution for Trout Lake alloy was calculated by combining the data for Types 1 and 2, and it is defined as 80% -26 $\mu$ m, with a median grain size of 11 $\mu$ m (See Fig. 29).

#### 6.6.1.2 Chemical Composition of Au-Ag-Hg Alloy

A total of 104 EMPA were generated of Au-Ag-Hg alloy, and this compositional data shows the consistent presence of Ag, Au and Hg in widely varying proportions, whereas Fe occurs in minor to undetectable amounts (See Appendix H and I). The analyses gave a mean composition (in wt%) of 49.2% Ag, 38.7% Au, 11.0% Hg and 0.7% Fe (See Table 20). The ranges of elemental concentrations in the alloy are shown as histograms in Figure 30.

The Fe content is anomalous, as Fe is not known to occur in native metals and alloys, as determined by microprobe analyses (L. Cabri, pers.

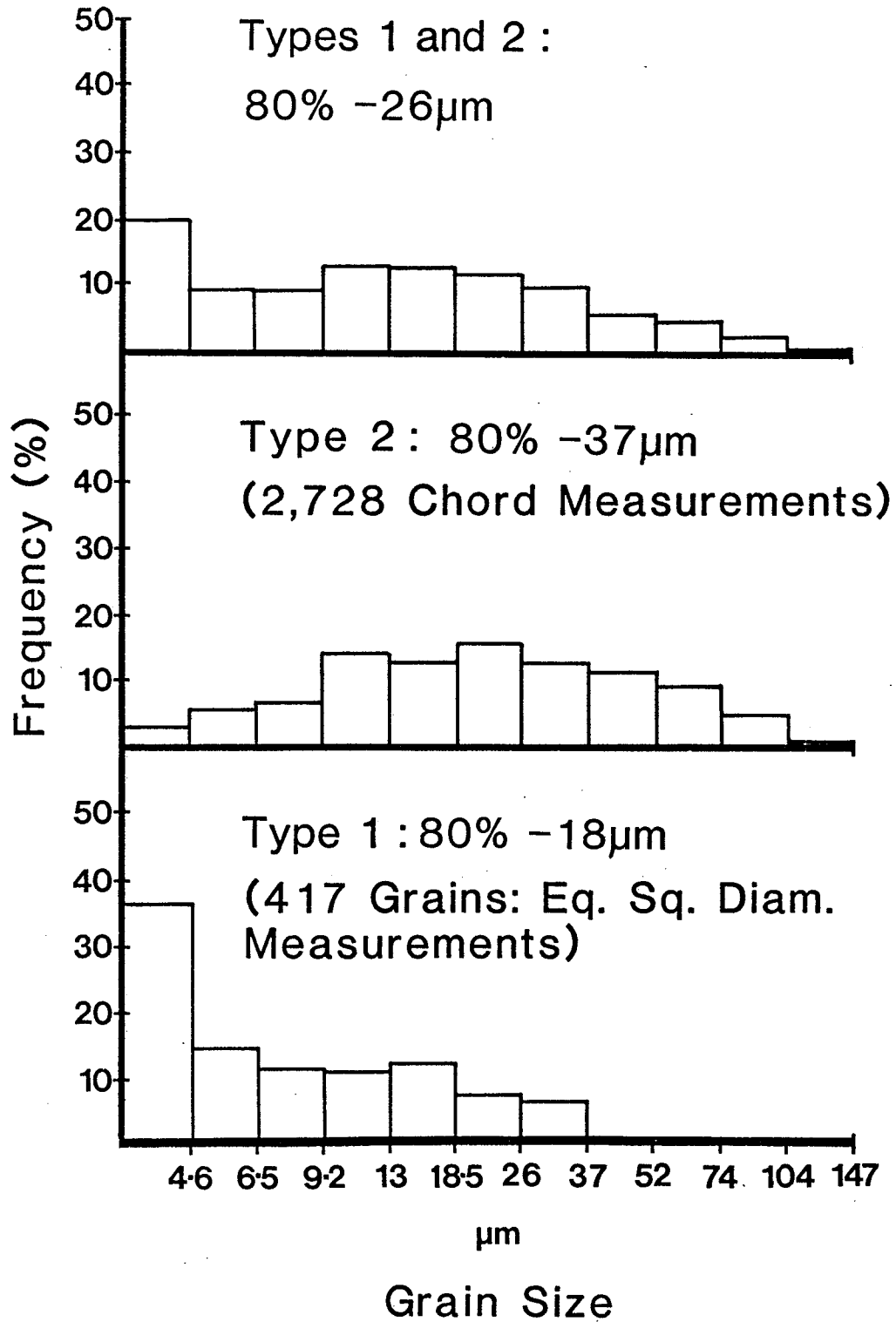


Figure 29: Histograms of the Grain Size Distributions of Au-Ag-Hg Alloy. The 80% passing sizes of Type 1, Type 2 and of the combined distributions of Types 1 and 2 are shown.

comm., 1987). In contrast, Boyle (1979) suggested that Fe is probably a structural constituent of metallic gold. On the basis of the twenty analyses in which Cu and S also were determined, Healy & Petruk (In Prep.) have concluded that the Fe is an analytical contaminant generated in an extensive volume of secondary fluorescence of FeK $\alpha$  (fluoresced principally by AuL $\alpha$ ). Furthermore, it is concluded that microprobe analyses of minute grains (<20 $\mu$ m in diameter) of gold, electrum and Au-Ag-Hg alloys encased in, or adjacent to, pyrite, chalcopyrite, arsenopyrite and pyrrhotite are apt to give contaminant-derived Fe values. Because only 28% of the Trout Lake Au-Ag-Hg alloy occurs as grains or masses greater than 20 microns in diameter, contaminant-free analyses are therefore largely unattainable. Thus, the Fe detected seems not to be due to metallic Fe dissolved in the Au-Ag-Hg alloy.

The inclusion of an extraneous sulfide component in the analyses does not affect the relationship among Au, Ag and Hg, which are of prime interest in our investigation. Consequently, all data were considered. Six representative compositions of the Trout Lake Au-Ag-Hg alloy, which cover the observed range in elemental concentrations, are given in Table 20. The complete set of 104 compositions are plotted on a Ag-Au-Hg triangular diagram in Figure 31.

#### **6.6.1.3 The Ag-Au-Hg Ternary System**

Previous studies have shown that most analyses of naturally occurring alloys of these three elements are related into the Ag-Hg, Au-Hg and Au-Ag binary systems. However, Scott (1977), Nazmova & Spiridonov (1979), Ozerova et al. (1980), Basu et al. (1981), Nysten (1986), Harris (1986),

Shikazono & Shimizu (1988) and others have reported naturally occurring alloys of Ag and Au with minor to major concentrations of Hg. These ternary alloys correspond to the  $\alpha$ -phase binary solid-solutions of the three binary systems extended into the Ag-Au-Hg ternary system.

In the absence of experimental work on the Ag-Au-Hg ternary system, Basu et al. (1981) relied on the three binary systems Ag-Au, Ag-Hg and Au-Hg to estimate the stability field for the face-centered (fcc) ternary  $\alpha$ -phase. The  $\beta$ -phases  $\text{Ag}_5\text{Hg}_4$  and  $\text{Au}_7\text{Hg}_3$ , observed in the corresponding binary systems, are stable below  $276^\circ\text{C}$  and  $419^\circ\text{C}$ , respectively. No such  $\beta$ -phase is observed in the Ag-Au binary system, and therefore below  $419^\circ\text{C}$ , features near the Hg-rich apex of the ternary system are uncertain. Thus, Basu et al. (1981) constructed a schematic  $450^\circ\text{C}$  isothermal section of the ternary system that shows the extrapolated stability field of the  $\alpha$ -phase, presuming no other ternary solid phase (Fig. 31).

The metamorphic grade at Trout Lake corresponds to middle greenschist facies, and being above the biotite isograd indicates temperatures reached at least  $400^\circ\text{C}$  (Aggarwal & Nesbitt 1987). Furthermore, the crystallization of the Au-Ag-Hg alloy is considered to be an essentially retrograde process. Extrapolation of the Au-Ag-Hg system to lower temperatures, assuming no other ternary phases in the Hg-poor region of the system, indicates only minor retraction of the  $\alpha$ -phase stability field. Therefore, the schematic  $450^\circ\text{C}$  isothermal section is a reasonable model for the crystallization of Au-Ag-Hg alloy at Trout Lake.

The compositions of Trout Lake Au-Ag-Hg alloy are plotted on the section, and form a large field with a general trend of slightly increasing Hg with increasing Ag, and decreasing Au. Nazmova & Spiridonov (1979), Nysten (1986) and Shikazono & Shimizu (1988) have also observed this compositional trend, which conforms with the increased solubility of Hg in the Ag end-member. The compositions all plot within the  $\alpha$ -phase stability field, and are thus analagous to the fcc  $\alpha$ -phase solid-solution of Basu et al. (1981). Furthermore, the compositions span much of the field of known compositions compiled by Shikazono & Shimizu (1988), and extends the field for compositions near the Au-Ag join and Ag apex (See Fig. 31). The large range in compositions observed in this study is attributed to the selection of analytical points on the basis of features visible in high-contrast BSE imagery, which allows analysis of otherwise obscured extreme compositions.

#### 6.6.1.4 Zoning and Distribution of Type 2 Au-Ag-Hg Alloy

Basu et al. (1981) and Nysten (1986) have also reported considerable inhomogeneity over distances of fractions of microns within grains of Au-Ag-Hg alloys. The high-contrast BSE photographs in Figures 28I and 33A to F illustrate the extreme compositional inhomogeneity in masses of Type 2 alloy. Points 1 to 4 in Figure 33A correspond to the analyses in Table 21, which were generated in order to confirm the compositions of grains having different levels of grey in the BSE images of Au-Ag-Hg alloy masses. It is apparent from Table 21 that the brightest grains have the highest Au and Hg contents, whereas the darkest grains are Ag-

TABLE 20

Representative Compositions (Microprobe Data) of Au-Ag-Hg Alloy.

wt%	1 Ag- Rich	2 Au- Rich	3 Hg- Rich	4 Hg- Poor	5 Fe- Rich	6 Typical (n=104)	Average (n=104)	Uncertainty (95% Confid- ence)
Ag	76.47	17.34	66.28	27.85	47.59	43.03	49.22	±0.5 - 0.6
Au	11.17	79.86	1.62	67.18	35.24	43.96	38.68	±0.5 - 5.8
Hg	11.14	2.68	30.87	1.29	15.02	11.80	11.00	±0.5 - 3.8
Fe	nd.	0.55	1.59	2.20	2.74	0.30	0.70	±0.7 - nd.
Tot.	98.78	100.40	100.34	98.49	100.57	99.06	99.60	

Note: 'nd.' denotes not detected. Fe is an analytical contaminant.

Operating Conditions:

Excitation Voltage: 20 kV.

Sample Current: 15 nA on the Faraday Cup.

Count Time: 60 secs or until 0.5% standard deviation on the standard and unknown is reached.

Ag: AgL $\alpha$  analytical line; PET crystal; Ag-Au alloy (71.6 wt% Ag, 28.4 wt% Au) standard.

Au: AuM $\alpha$  analytical line; PET crystal; Ag-Au alloy (50.1 wt% Ag, 49.9 wt% Au) standard.

Hg: HgL $\alpha$  analytical line; LIF crystal; synthetic Pd<sub>3</sub>HgTe<sub>3</sub> (Temagamite) standard.

Fe: FeK $\alpha$  analytical line; LIF crystal; Pyrite (FeS<sub>2</sub>) standard.

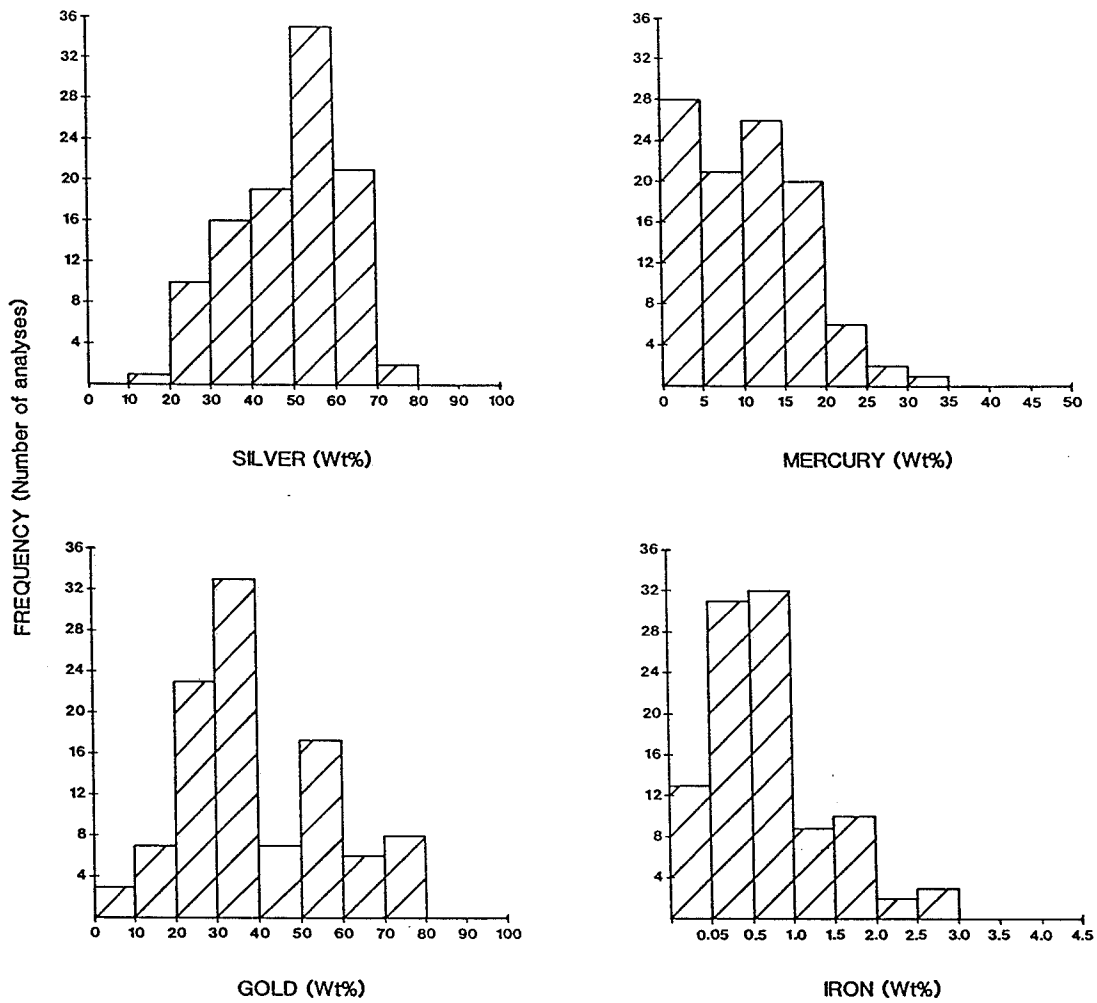


Figure 30: Histograms of Au, Ag, Hg and Fe Concentrations in Trout Lake Au-Ag-Hg Alloy. The range of Au, Ag, Hg and Fe compositions as determined by microprobe analysis are shown. Fe is due to analytical contamination.

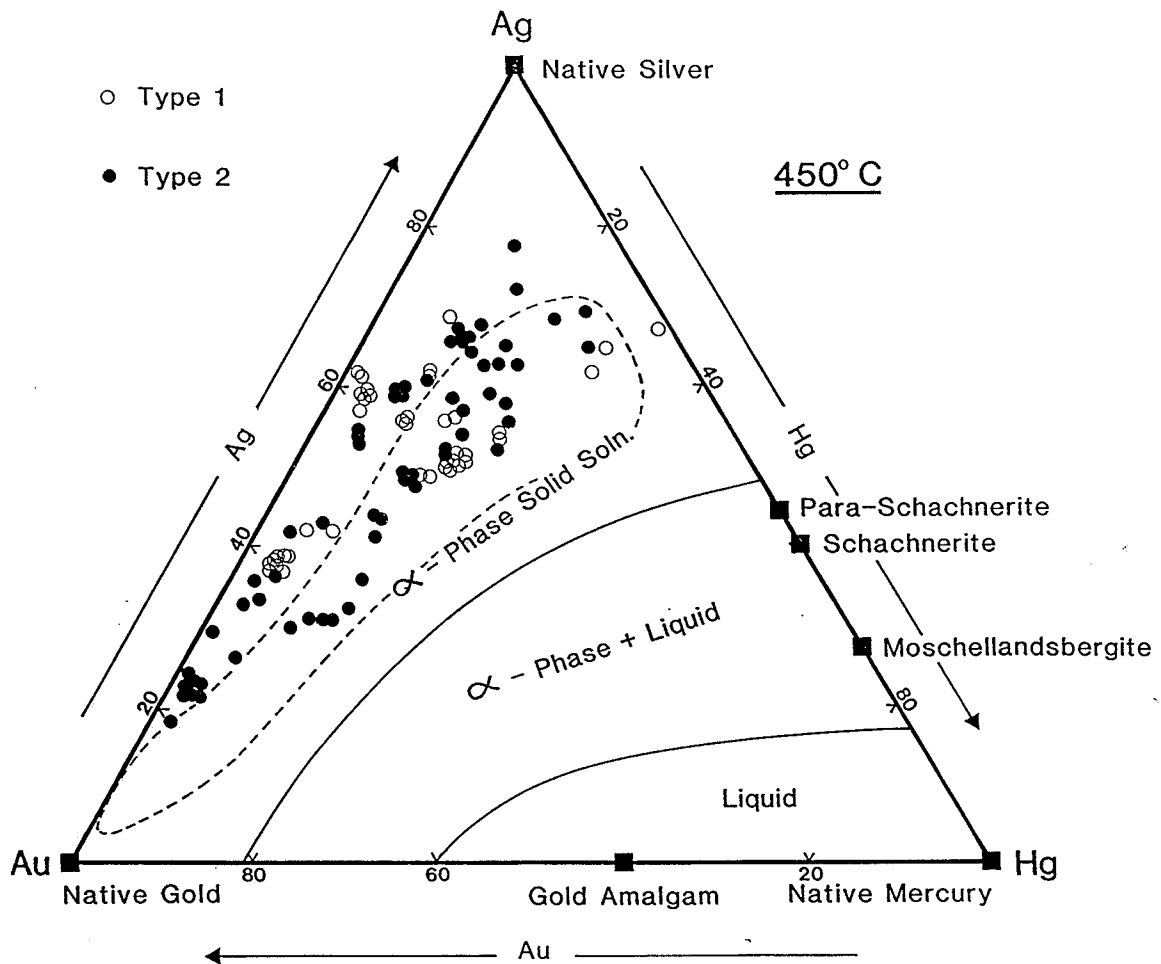


Figure 31: Schematic Isothermal Section of the Au-Ag-Hg Ternary System (in wt%). The phase boundaries for the  $\alpha$ -phase are redrawn from Basu et al. (1981). The composition of several naturally occurring binary alloys with the discrete stoichiometric compositions of intermetallic compounds (e.g. moschellandsbergite) are projected from lower temperatures onto the section, whereas those of the three pure native metals are shown at the apices. The field of known compositions as compiled by Shikazono & Shimuzu (1988) is shown with a dashed line. The compositions from the 104 microprobe analyses of Trout Lake Au-Ag-Hg alloy are designated by type and plotted.

rich. Thus, while the complete set of 104 analyses gives a trend of increasing Hg with increasing Ag, these four analyses from a single mass show Ag inversely related to both Hg and Au. Element profiles across masses of Type 2 alloy consistently show the antipathetic relationship of Ag to Au and Hg (Fig. 32). This suggests a trend toward progressively Ag-rich late compositions at the expense of both Au and Hg, where only the initial composition of each mass parallel the trend of increasing Hg with Ag. Nonetheless, because Au and Hg have a similar atomic number (79 and 80, respectively) much greater than that of Ag (47), the BSE signal and the points selected on the basis of it may not wholly describe the general trend in compositional variation.

In general, within masses of Type 2 Au-Ag-Hg alloy, high Au compositions occur as rare grains ( $\leq 10\mu\text{m}$ ) enveloped in more intermediate compositions (Fig. 33B), the interstices of which are infilled by Ag-rich compositions. In Figure 33C, several grains show pronounced zoning. In subidiomorphic grains e.g., 'm', zoning is parallel to crystal faces. This strong crystallographic control confirms that the range in compositions constitutes solid-solution within the extrapolated  $\alpha$ -phase stability field of Basu et al. (1981), and not that of separate phases produced by subsolidus unmixing. The latter had been postulated in the absence of high contrast BSE imagery by Basu et al. (1981) and Nysten (1986) to explain the inhomogeneity in X-ray dot images. The core of the grain indicated by 'm', which contains oscillatory zoning, is separated from a strongly zoned Ag-rich (dark) rim by a boundary resembling a resorption edge. The grain is cross-cut by a veinlet of intermediate composition 'v', that contains trails of blebs of Au-rich composition

TABLE 21

Chemical Compositions (Microprobe Data) of Au-Ag-Hg Alloy in Section  
TLN.1-89i.

wt%	1	2	3	4
Ag	72.61	54.11	64.19	76.47
Au	14.09	22.91	18.68	11.17
Hg	14.26	21.16	16.08	11.14
Fe	nd.	nd.	nd.	nd.
Total	100.96	98.18	98.95	98.78

- Note: 1. 'nd.' denotes not detected. Fe is an analytical contaminant.  
2. Operating Conditions: As in Table 20  
3. See Figure 33A for location of analytical points.

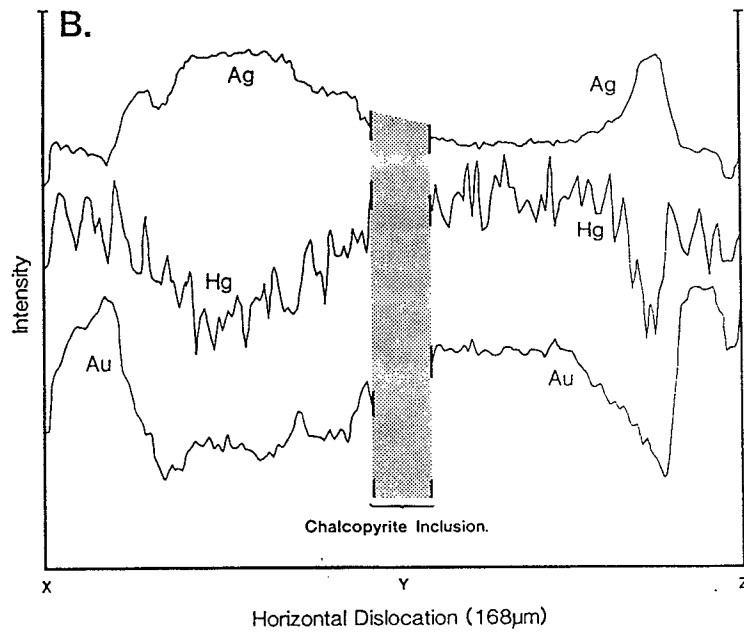
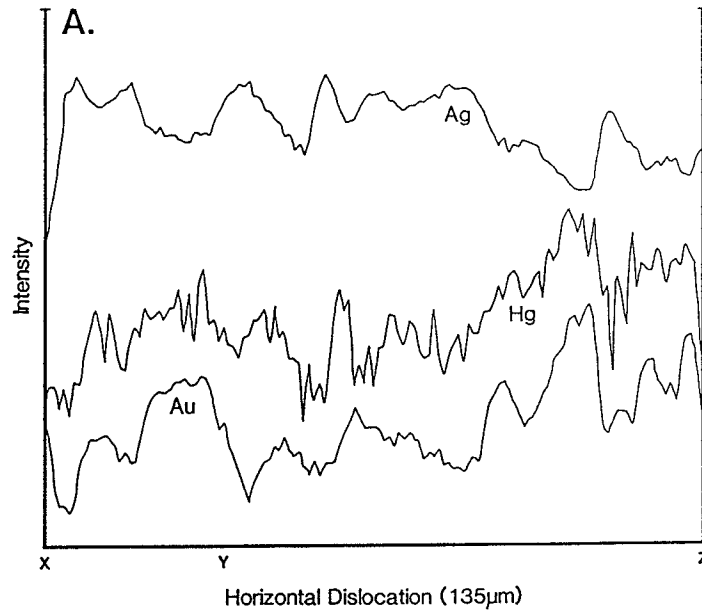


Figure 32: Element Concentration Profiles Across Type 2 Au-Ag-Hg Alloy. Profiles of Au, Ag and Hg concentrations across a mass of Type 2 Au-Ag-Hg alloy in (A) TLN.1-89i, and (B) TLN.1-89b, showing the antipathetic relationship of Ag to both Au and Hg. Continuous, qualitative, wavelength dispersive traverse. Location of traverses shown in Figure 33A and F.

'g' (bright white). These features indicate distinct breaks in the conditions of crystallization, with only partial re-equilibration. In contrast to the general tendency for the later-stage compositions to be Ag-rich, here the final composition 'g' is relatively Au-rich. This composition may be the homogenized product of earlier compositions being redissolved during a localized deformational event, rather than a reversal of the typical sequential crystallization of Ag-rich compositions.

The mass of Type 2 Au-Ag-Hg alloy in Figures 28H and 33D contains a central zone of fractures that are lined by Ag-rich compositions, which contrast with the earlier homogeneous intermediate composition 'm'. Four distinct generations occurring as zones of progressively Ag-rich compositions are observed, with increasing Ag content toward the center of the fractures. A similar pattern of three late Ag-rich zones is also seen in Figure 33E and F. This texture is interpreted as the episodic diffusion of Ag into the earlier formed more intermediate composition.

The contact between laminae of massive chalcopyrite and chlorite schist, along which Type 2 Au-Ag-Hg alloy is concentrated (See Fig. 28E and F), is enriched in clausthalite and naumannite, and contains abundant quartz, calcite, biotite, monazite and particularly coarse-grained ( $\leq 1$ cm) plagioclase within a relatively homogeneous bleached zone of recrystallized matrix chlorite. The plagioclase is variably replaced (commonly occurs as pseudomorphs) by a fine-grained clay mineral (tentatively identified as smectite) and an associated rim of fine-grained adularia. The timing of the clay alteration with respect to the crystallization of Au-Ag-Hg alloy is not clear, as there is no close

spatial association of the clay with the alloy, though the former corrodes chalcopyrite. Pyrite, chalcopyrite, sphalerite and pyrrhotite are invaded and corroded by Type 2 Au-Ag-Hg alloy. The pyrite is also deformed and partially altered to marcasite, which is characteristic of late-stage parageneses associated with the replacement of pyrite in shear zones. Furthermore, marcasite, clausthalite, rucklidgeite and hessite have been observed as interstitial phases associated with Type 1A Au-Ag-Hg alloy. These observations are generally consistent with the paragenesis of gold associated with pyrite, tellurides, quartz and carbonate in discordant veinlets, representing the remobilized fractions in Archean gold deposits (Springer 1983), and suggests that Au, Ag, Hg, Pb, Se, Te, Si, K, Ca and Na were introduced along this contact via a fluid phase.

#### 6.6.2 DYSCRASITE

Dyscrasite is a rare constituent of the ores. It was found in two samples of the Layered Pyrite + Sphalerite ore type. In sample TLS.5-83A, the dyscrasite occurs as fine-grained ( $\leq 10\mu\text{m}$ ) inclusions in freibergite associated with galena cementing large fractures in pyrite porphyroclasts (See Fig. 33G). Dyscrasite was also observed in sample TLS.5-84, as globular, fine-grained ( $\leq 5\mu\text{m}$ ) inclusions in galena that also contain intergrowths of lesser gudmundite. The mineralogical association of dyscrasite with freibergite, galena and gudmundite in Layered Pyrite + Sphalerite ores is consistent with the strong geochemical affinity of Pb, Sb and Ag in Zn-rich ores.

Dyscrasite has a discrete stoichiometric composition, which is characteristic of intermetallic compounds. One quantitative WDA of the dyscrasite was generated using the JEOL 733 at CANMET. The determined composition of 75.43 wt% Ag and 23.61 wt% Sb (total = 99.03 wt%) gives a unit formula of  $Ag_{3.1}Sb_{0.9}$ , which corresponds closely to the composition of stoichiometric dyscrasite. The composition lies within the narrow dyscrasite sub-solidus field (23 to 27 wt% Sb) between 200°C and approximately 500°C on the phase diagram for the Ag-Sb system (Petruk et al. 1969).

## 6.7 TELLURIDES

### 6.7.1 HESSITE

Hessite is a rare trace constituent of the ores, and was observed in the Sheared Chalcopyrite + Sphalerite and the Chalcopyrite Stringer ore types. Hessite occurs as fine-grained ( $\leq 20\mu m$ ) subhedral to anhedral grains in two textural associations. These are (1) subhedral to anhedral grains intimately associated with chalcopyrite and lesser pilsenite and Au-Ag-Hg alloy invading and replacing sphalerite and/or pyrrhotite in sample TLS.1-47 (Fig. 18D); and (2) as anhedral grains associated with galena and enveloped in chalcopyrite, which forms veinlets in fractured gangue (Fig. 20H). Hessite occurs in the Cu-rich footwall ores, and is generally associated with, and forms inclusions in galena and/or chalcopyrite.

Three microprobe analyses of hessite gave compositions with trace S, and apparently slight cation-deficiency. The cation-deficiency may constitute a real deviation from stoichiometry, or more probably

reflects the use of a Ag-metal standard, and the consequent increased errors in the matrix corrections for Ag, as indicated by the low totals.

TABLE 22

## Chemical Compositions (Microprobe Data) of Hessite

wt%	1	2	3	Uncertainty (95% Confidence)
S	0.27	0.25	0.32	± 0.1
Ag	61.38	61.18	61.19	± 0.4
Te	37.21	36.98	36.77	± 0.5
Total	98.86	98.41	98.27	
Number of atoms				
S	0.03	0.03	0.04	
Ag	2.00	2.00	2.00	
Te	1.03	1.02	1.02	

- \* Unit formula calculated on the basis of 2 silver atoms.  
 \* A pyrite, Ag-metal and altaite standard were employed for S, Ag and Te, respectively.

### 6.7.2 PILSENITE

Pilsenite(?) is an extremely rare trace constituent of the ores that was observed in sample TLS.1-47, a Chalcopyrite Stringer ore. Wehrlite has been previously identified at Trout Lake, in what was termed the Pyrite-Chalcopyrite ores (Muzylowski 1979). Ramdohr (1980) considers wehrlite as being possibly identical to pilsenite. Nonetheless, the name wehrlite has been discredited, whilst the mineral name pilsenite ( $\text{Bi}_4\text{Te}_3$ ) has been approved by the IMA (Fleischer 1987). Because the identification of the pilsenite in this study is very tentative (See below), the mineral is referred to as pilsenite(?).

Numerous grains of pilsenite(?) were observed as fine-grained ( $\leq 25\mu\text{m}$ ) euhedral to anhedral grains intimately associated with abundant chalcopyrite, lesser hessite and trace Au-Ag-Hg alloy invading and replacing sphalerite and pyrrhotite (Fig. 18D). Hessite was observed forming rare intricate intergrowths within a single grain of pilsenite. The identification of 'wehrlite' in the Pyrite-Chalcopyrite ores (Muzylowski 1979), and the observation of pilsenite(?) in only one sample of the Chalcopyrite Stringer ores, suggests that the pilsenite(?) is restricted to the footwall Cu-rich ores i.e., the Chalcopyrite Stringer and the Disseminated Pyrite + Chalcopyrite ore types.

The two microprobe analyses of pilsenite(?) given in Table 23 detected several minor and trace elements. The analyses were generated with an  $E_0$  of 20 kV, such that the Bi and  $\text{PbL}\alpha$  peaks could be modelled, and the scaled Bi and  $\text{PbM}\alpha$  peaks stripped off the  $\text{SK}\alpha$  ROI. No  $\text{SK}\alpha$  peak was detected, and both Bi and Pb were analysed by their respective mutually overlapped (partial)  $\text{L}\alpha$  peaks.

TABLE 23

Chemical Compositions (Microprobe Data) of Pilsenite(?)

wt%	1	2	Uncertainty (95% Confidence)
Fe	0.15	1.09	± 0.1
Se	0.71	1.02	± 0.1
Te	33.06	31.31	± 0.3
Pb	3.79	2.72	± 0.3
Bi	60.70	60.92	± 1.4
Total	98.40	97.05	
Number of atoms			
Fe	0.03	0.12	
Se	0.06	0.08	
Te	1.66	1.52	
Pb	0.12	0.08	
Bi	1.87	1.80	

\* Unit formula calculated on the basis of 2 cations.

\* A pyrite, pure-Se, pure-Te, galena and a Bi-metal standard were employed for Fe, Se, Te, Pb and Bi, respectively.

The two compositions give an average of 0.62 wt% Fe, 0.87 wt% Se, 32.19 wt% Te, 3.26 wt% Pb and 60.81 wt% Bi (mean total = 97.73%), which translates into the unit formula  $(\text{Bi}_{1.84}, \text{Pb}_{0.10}, \text{Fe}_{0.07})(\text{Te}_{1.59}, \text{Se}_{0.07})$ . These compositions are non-stoichiometric relative to the known Bi- and Te-bearing minerals (Ramdohr 1980, Miller 1981, Fleischer 1987). The compositions may therefore represent: (1) inferior analyses due to inappropriate standards, poor peak resolution due to inadequate correction of severe peak overlaps, and sample decomposition (indicated by severe scorch marks at the point of analysis), as is indicated by the low totals; (2) intermediate compositions in a solid solution such as Tsumoite ( $\text{Bi}, \text{Te}$ ) and Pilsenite ( $\text{Bi}_4\text{Te}_3$ ); and (3) submicroscopic intergrowths of two or more related Bi-Te-phases.

The observed high reflectivity, white colour and weak brownish anisotropy are characteristic of many of the structurally similar 'Te-Bi compounds' (Ramdohr 1980), but are not sufficiently diagnostic of a given mineral species. The identification as pilsenite therefore remains tentative.

### 6.7.3 RUCKLIDGEITE

Rucklidgeite is a rare trace constituent of the ores, that was observed in sample TLS.3-14, a Chalcopyrite Stringer ore. Abundant fine-grained (approximately 15 $\mu\text{m}$ ) rucklidgeite, clausthalite and lesser Au-Ag-Hg alloy, associated with chalcopyrite and pyrrhotite was observed in sample TLS.3-14. These minerals infilled and corroded deformed pyrite porphyroblasts along fractures and grain boundaries, formed interstitial films and wedges, as well as occurring as variably idiomorphic and

commonly composite inclusions in the pyrite. The rucklidgeite inclusions varied from blocky to rounded, lenticular, lobate and tabular, with aspect ratios varying from 1 to 20 (Fig. 18B and C). The association with clausthalite and Au-Ag-Hg alloy is consistent with the rare occurrences of rucklidgeite "in contact with native gold, galena and pyrite" in the Ashley deposit, Ontario (Harris et al. 1983). Both the rucklidgeite and pilsenite(?) probably correspond to the wehrlite observed by Muzyłowski (1979), and are restricted to the footwall chalcopyrite-rich ores i.e., the Chalcopyrite Stringer ores, and probably also the Disseminated Pyrite + Chalcopyrite ores.

Three microprobe analyses of rucklidgeite, the compositions of which are given in Table 24, were generated with an Eo 20kV, during the same analytical run in which the pilsenite(?) compositions were collected. As with the pilsenite, the Bi and PbL $\alpha$  peaks were modelled, and the scaled Bi and PbM $\alpha$  peaks were stripped off the SK $\alpha$  ROI. No SK $\alpha$  was observed, and both Bi and Pb were analysed by their respective mutually overlapped (partial) L $\alpha$  peaks. Minor to trace amounts of Fe and Se were detected.

The three compositions give an average of 0.55 wt% Fe, 1.69 wt% Se, 41.38 wt% Te, 15.46 wt% Pb and 39.73 wt% Pb (mean total = 98.81%), which translates into the unit formula of (Bi<sub>2.20</sub>, Pb<sub>0.86</sub>, Fe<sub>0.12</sub>)(Te<sub>3.75</sub>, Se<sub>0.25</sub>) or (Bi,Pb,Fe)<sub>3.18</sub>(Te,Se)<sub>4.00</sub>. The slight cation excess probably reflects the poor resolution of the overlapped Bi and PbL $\alpha$  peaks, and also the inappropriate standard selection, resulting in excessive matrix corrections

TABLE 24

Chemical Compositions (Microprobe Data) of Rucklidgeite

wt%	1	2	3	Uncertainty (95% Confidence)
Fe	0.74	0.46	0.44	± 0.1
Se	1.51	1.73	1.84	± 0.1
Te	43.30	39.93	40.92	± 0.4
Pb	15.42	15.43	15.52	± 0.6
Bi	39.36	40.23	39.61	± 1.0
Total	100.32	97.77	98.33	

Number of atoms				Mean
Fe	0.15	0.10	0.09	0.12
Se	0.21	0.26	0.27	0.25
Te	3.79	3.74	3.73	3.75
Pb	0.83	0.89	0.87	0.86
Bi	2.10	2.30	2.20	2.20

\* Unit formula calculated on the basis of 2 anions (Te + Se).

\* A pyrite, pure-Se, pure-Te, galena and a Bi-metal standard were employed for Fe, Se, Te, Pb and Bi, respectively.

#### 6.7.4 VOLYNSKITE

Volynskite is an extremely rare trace constituent of the ores, that was identified during image analysis of the Trout Lake Cu-concentrate TL.MP-12 (See Healy & Petruk 1989). Because it was not identified in the ore samples, it cannot be ascribed to any of the ore types. Volynskite was observed as a single fine-grained (10um diameter) anhedral grain locked with hessite (Fig. 33I). Because of the association with hessite it is probable that volynskite is also restricted to the footwall Cu-rich ores.

Three quantitative WDA of the volynskite were generated using the JEOL 733, CANMET, and the compositions are given in Table 25 The compositions indicate minor element-free volynskite, slightly Ag-poor, Bi-rich stoichiometry.

TABLE 25

## Chemical Compositions (Microprobe Data) of Volynskite

wt%	1	2	3	Average	Uncertainty (95% Confidence)
Ag	17.96	17.55	16.52	17.35	± 0.5
Bi	40.73	40.36	39.57	40.22	± 0.7
Te	44.50	44.63	41.52	43.55	± 0.5
Total	103.19	102.52	97.58	101.10	
at%					
Ag	23.46	23.08	22.96	23.17	
Bi	27.49	27.42	28.39	27.77	
Te	49.05	49.50	48.67	49.07	

\* Standard Deviation quoted at the 95% confidence limits.

\* Operating Conditions :

Excitation voltage : 20 kV.

Sample Current : 15 nA on the Faraday Cup.

Count Time : 60 secs or until 0.5% standard deviation on the standard or unknown is reached.

Ag : AgL $\alpha$  analytical line; PET crystal; Matildite (AgBiSe<sub>2</sub>) standard.

Bi : BiM $\alpha$  analytical line; PET crystal; Bismuthinite (Bi<sub>2</sub>S<sub>3</sub>) standard.

Te : TeL $\alpha$  analytical line; PET crystal; Altaite (PbTe) standard.

## 6.8 SELENIDES

### 6.8.1 CLAUSTHALITE-GALENA SOLID SOLUTION

As stated previously (See GALENA) this section will treat only those 'galenas' that are texturally and/or optically distinguishable from the common, minor element-free, stoichiometric galena. Three distinct varieties of clausthalite-galena are recognized, and will be treated as such below.

1. 'Galenas' with a high reflectivity and a slight blue-white colour (when viewed with a daylight filter) were observed in the Sheared Chalcopyrite + Sphalerite, the Mixed/Layered Chalcopyrite + Sphalerite and the Chalcopyrite Stringer ores. Qualitative EMPA of some of these galenas revealed highly variable Se-contents, varying from trace to major concentrations. The analyses suggest a trend of increasing Se content (clausthalite component) in the galenas passing towards the footwall Cu-rich ores. No Te or Ag was detected.

2. 'Galenas' with a high reflectivity and blue-white colour were observed associated with rucklidgeite and lesser Au-Ag-Hg alloy in sample TLS.3-47 (Fig. 18B). EMPA of two of these galenas generated with an Eo of 20 kV (during the same analytical run in which the pilsenite and rucklidgeite were analyzed), indicate a significant clausthalite component (Se), and a trace altaite component (Te). The compositions are given in Table 26.

The average composition and the calculated unit formula are also presented, and exhibit good stoichiometry despite the stripping procedure employed to generate the SK $\alpha$ , as well as the probable contamination of the analysis by adjacent pyrite, as indicated by the Fe-peak. Analysis 1 corresponds to clausthalite-galena that occurs with chalcopyrite containing myrmekitic pyrrhotite as a composite inclusion in pyrite, whereas analysis 2 corresponds to clausthalite-galena that occurs with Au-Ag-Hg alloy and pyrrhotite, also as a composite inclusion in pyrite. These 'clausthalites' differ significantly from those of the previous variety in that they contain minor Te, consistent with their association with rucklidgeite.

3. Abundant fine-grained ( $\leq 30\mu\text{m}$ ), graphic-textured clausthalite-galena solid solution in low-Fe sphalerite was observed in sample TLN.1-87, a Massive Sphalerite ore (Fig. 26A and B). The sample consists almost entirely of coarse-grained sphalerite with pods of quartzose and carbonate gangue. The sphalerite exhibits abundant deformational twin lamellae, and contains minor blebs and rods of pyrrhotite, but is largely free of chalcopyrite-disease. The sphalerite exhibits a deep red colour in transmitted light (i.e., sphalerite I), which is typical of Trout Lake sphalerites and indicative of Fe-rich compositions.

The monotonous texture of the ore is interrupted by the development of a diffuse zone of graphic galena-clausthalite in sphalerite. The galena-clausthalite comprises approximately 15 vol% of the graphic intergrowth. The host sphalerite exhibits a pale orange to green colour in transmitted light (i.e., sphalerite II), and infills, envelopes,

TABLE 26

Chemical Compositions (Microprobe Data) of Clausthalite-Galena from  
TLS.3-47

wt%	1	2	Average
S	10.96 ± 0.3	3.80 ± 0.3	7.38
Se	5.81 ± 0.3	19.22 ± 0.6	12.52
Te	0.45 ± 0.1	1.55 ± 0.3	1.00
Fe	1.11 ± 0.2	1.69 ± 0.2	1.40
Ag	0.00	0.66 ± 0.2	0.33
Pb	81.74 ± 1.6	70.12 ± 1.7	75.93
Total	100.07	97.04	98.56
Number of atoms			
S	0.82	0.32	0.57
Se	0.18	0.65	0.42
Te	0.01	0.03	0.02
Fe	0.05	0.08	0.07
Ag	0.00	0.02	0.01
Pb	0.94	0.90	0.92

- \* Uncertainty quoted at the 95% confidence limits.
- \* Unit formula calculated on the basis of 1 anion (S, Se and Te).
- \* A pyrite, pure-Se, pure-Te, Ag-metal and galena standards were employed for S and Fe, Se, Te, Ag and Pb, respectively.
- \* The SK $\alpha$  peak was generated by modelling the PbL $\alpha$  peak and stripping the scaled PbM $\alpha$  peak off the SK $\alpha$  ROI.

corrodes and replaces, and thereby postdates sphalerite I (See Fig. 26A and B). These galena-clausthalite masses are associated with minor trails of chalcopyrite blebs, grains and veinlets of gudmundite, and disseminated pyrite and pyrrhotite, which are partly altered to marcasite. Furthermore, several extremely coarse-grained galena-clausthalite grains that are disseminated in the ore beyond the boundary of this intergrowths contain rounded and more rarely myrmekitic inclusions of freibergite (See Fig. 27A).

The galena-clausthalite exhibits textural variation, with areas of (1) fine dustings (i.e., <5um); (2) densely packed and interconnected medium-grained (i.e., 5 to 15um) graphic blebs; (3) coarser-grained (i.e., >15um), more discrete grains lining the boundaries of the masses and defining lineaments within sphalerite II; and (4) rare, extremely coarse-grained (i.e., >100um) grains irregularly disseminated beyond the masses throughout the ore. Type 1 grains probably define features such as fractures and grain boundaries within the pre-existing sphalerite I, which may have acted as the principal conduits for the replacement process. In transmitted light, it is apparent that much of the galena-clausthalite (i.e., Type 2 above) consists of zones and fringes of dendritic threads growing out from internal faces or growth zones in sphalerite II (See Fig. 26B).

Ten analyses of the deep red coloured common sphalerite (I) gave a narrow range in composition (See Table 1 of Appendix J), with an average composition of 33.1 wt% S, 58.8 wt% Zn, 7.62 wt% Fe, 0.13 wt% Cd and 0.03 wt% Cu (total = 99.7%). Fifteen analyses of sphalerite II also gave a narrow range in composition (See Table 2 of Appendix J), with an

average composition of 32.9 wt% S, 64.3 wt% Zn, 2.05 wt% Fe, 0.34 wt% Cd and 0.11 wt% Cu (total = 99.7%). Whereas the Cu values are statistically not significantly different from zero, the Cd values indicate a significant increase in Cd concentration with increased Zn and decreased Fe in sphalerite II.

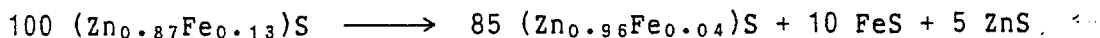
Twenty five analyses of galena-clausthalite gave a large range in composition (See Table 3 of Appendix J), with an average composition of 10.7 wt% S, 6.10 wt% Se, 83.5 wt% Pb and 0.01 wt% Ag (total = 100.3%), and corresponds to a 20% clausthalite component. Because of poor counting statistics, the Ag values are statistically not significantly different from zero, and are not considered further. Bi was undetected in all the analyses. The distribution of Se concentrations seems to be trimodal with peaks at approximately 1 to 2, 5 and 22 wt% Se (See Fig. 34). The peak at approximately 22 wt% Se corresponds to 4 analyses on two grains lining the boundary of the masses (i.e., Type 3). The average composition is thus positively biased by these grains. Nonetheless, it is apparent that inhomogeneity within grains is less than between grains, and that equilibration has not been achieved.

The higher Cd concentration in sphalerite II suggests (1) that sphalerite II did not replace, but grew on, and enveloped sphalerite I, or (2) that sphalerite II is replacive, and that additional Cd was metasomatically introduced during the replacement of sphalerite I. The latter is favoured as sphalerite II crosscuts and corrodes sphalerite I, which occasionally persists as rounded relict islands in sphalerite II (See Fig. 26A). The 3-fold increase in the Cd concentration of sphalerite II cannot be accounted for by mass balance considerations of

the relative volumes of sphalerite I. The reaction that replaces sphalerite I containing 87 mole% ZnS and 13 mole% FeS, with sphalerite II containing 96 mole% ZnS and 4 mole% FeS can be expressed as



This reaction results in a 10 volume% loss of sphalerite, and is isochemical with respect to ZnS, but evolves 10 mole% FeS. However, as the graphic galena-clausthalite comprises 15 vol% of the intergrowth, and assuming identical molar volumes for sphalerite I and II, both FeS and ZnS are evolved according to the reaction



Thus, both Fe and Zn are evolved with much of the excess Fe probably precipitated as the associated gudmundite, pyrite and marcasite. Minor incipient replacement of sphalerite I by sphalerite II is observed irregularly distributed throughout the sample as diffuse apparently opaque (in transmitted light) patches in sphalerite I. The opaque character is produced by the dispersion of light on pits and voids in sphalerite I, which are not infilled by galena-clausthalite.

In their study of the PbS-PbSe system, Wright et al. (1965) found that metastable compositions with excess Se above the bulk composition of the starting material persisted even at higher temperatures, indicating extremely low rates of compositional equilibration. Thus, the wide range in composition does not necessarily indicate growth at extremely low temperatures, where equilibration would be kinetically

constrained, nor do high Se/S ratios necessarily reflect equivalently high Se/S activity ratios in the pore fluid. Czamanske & Hall (1975) propose that the Se concentrations of galena-clausthalite solid solution and other phases in the "late sulfosalt mineralization" at the Darwin mine, simply reflect the availability of Se during late Ag, Bi and Se enrichment. The association of minor freibergite and gudmundite with galena-clausthalite is consistent with this late enrichment of Ag, Sb and Se, but not Bi in TLN.1-87. Bi is conspicuously absent either as distinct Bi-minerals or as a substituent element in any of the associated phases.

In summary, late evolved pore fluids enriched in Pb, Se, Cd, Ag and Sb permeated the massive sphalerite of TLN.1-87 along an irregular zone. The earlier Fe-rich sphalerite (I), equilibrated at higher temperatures, was replaced by low Fe sphalerite (II) with a graphic intergrowth of galena-clausthalite solid solution. The graphic texture is probably the product of simple co-precipitation, accommodated by the negative volume change from sphalerite I to II. The lower Fe content of sphalerite II is consistent with equilibration at higher activities of  $S_2$  or more probably lower temperature.

#### 6.8.2 NAUMANNITE

Naumannite is an extremely rare trace constituent of the ores, that was only identified during image analysis of a Cu-rougher concentrate (i.e., TL.MP-12). Subsequently naumannite was observed in TLN.1-89, occurring intimately associated with clausthalite on the contact of massive chalcopyrite and chlorite schist laminae, along which Type 2 Au-

Ag-Hg alloy is concentrated. In TL.MP-12, the mineral occurs as a single fine-grained (<5um) anhedral grain containing an inclusion of clausthalite (Fig. 33H). Several WDA of the naumannite were attempted, but the fine-grained nature of the grains prohibited contaminant-free compositions. However, compositions of essentially  $\text{Ag}_2\text{Se}$  were indicated.

**FIGURE 33: PLATE OF PHOTO-MICROGRAPHS.**

A. Sample TLN.1-98i: Inhomogeneous mass of Type 2 Au-Ag-Hg alloy showing location of analytical points 1 to 4 presented in Table 21, and location of a major segment (Y to Z) of the wavelength-dispersive traverse (X to Z) shown in Figure 32. High Contrast Backscattered electron (BSE) image. Scale bar = 30um.

B. Sample TLN.1-89i: Type 2 Au-Ag-Hg alloy showing fine-grained, discrete grains of Au-rich alloy (g) enveloped in alloy of intermediate composition (m). High contrast BSE. Scale Bar = 20um.

C. Sample TLN.1-89i: Complex zoning in Type 2 Au-Ag-Hg alloy consisting of oscillatory zoning at 'm', separated from a strongly zoned Ag-rich rim by a resorption edge, and cross-cut by a veinlet of intermediate composition 'v' that contains trails of blebs of Au-rich composition 'g'. High contrast BSE. Scale bar = 10um.

D. Sample TLN.1-89k: High contrast view of large mass of Type 2 Au-Ag-Hg in Figure 28H. Alloy contains episodic diffusion zoning of Ag and Hg (a, b, c and d) into earlier intermediate composition (m) along fractures. High contrast BSE. Scale bar = 60um.

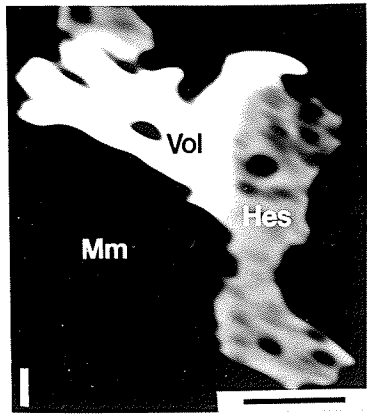
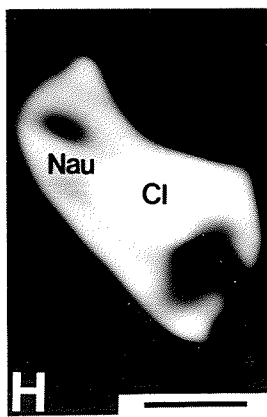
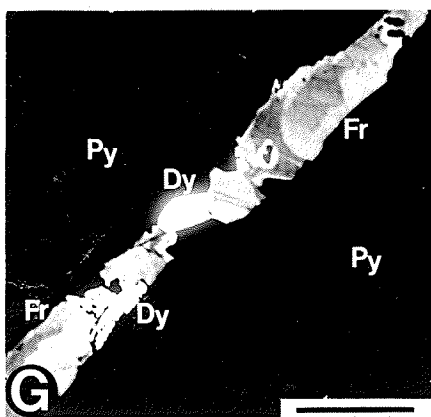
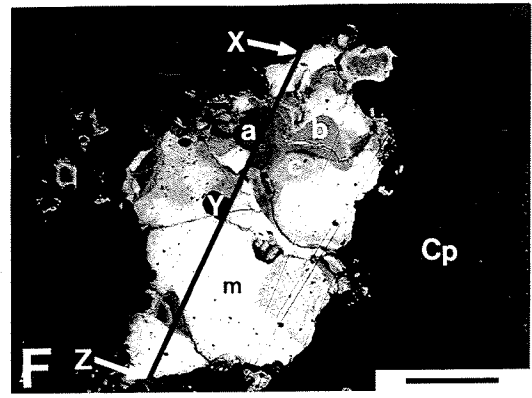
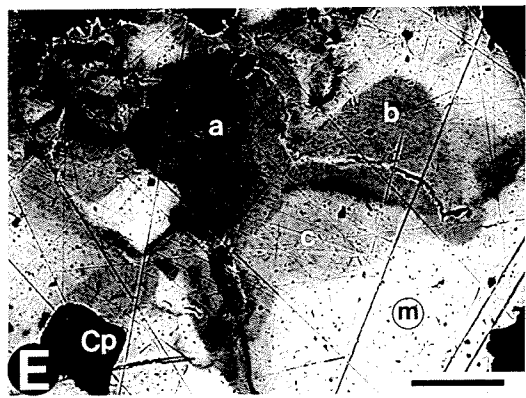
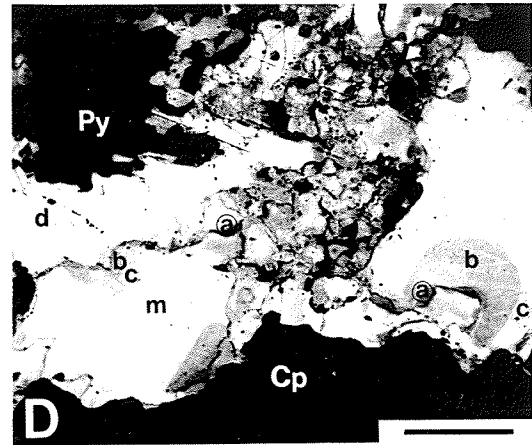
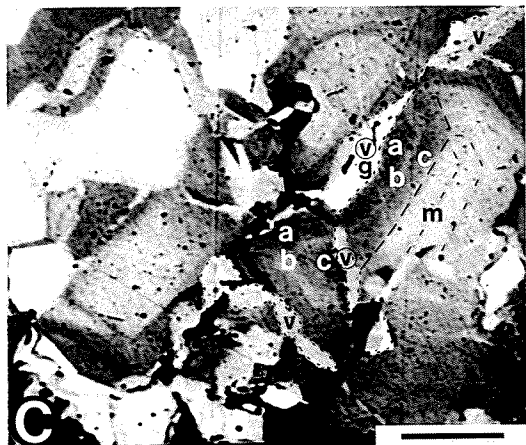
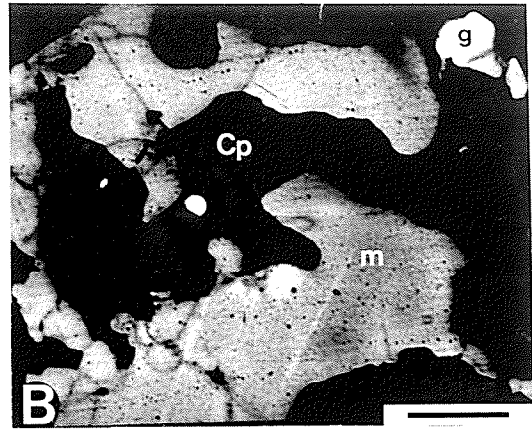
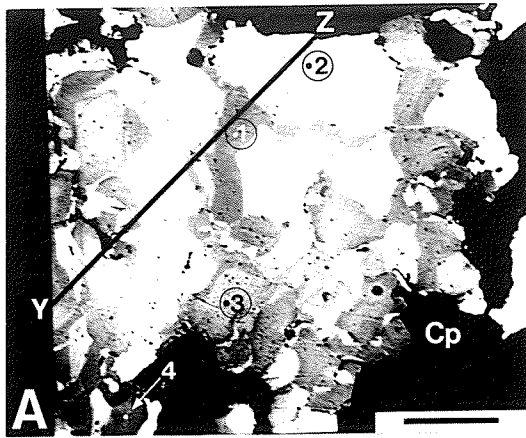
E. Sample TLN.1-89b: Inhomogeneous mass of Type 2 Au-Ag-Hg alloy, showing episodic diffusion zoning of Ag (a, b and c) along fractures into earlier intermediate composition (m). High contrast BSE. Scale bar = 15um.

F. Sample TLN.1-89b: Lower magnification view of mass in Figure 33E, showing location of the wavelength-dispersive traverse (X to Z) shown in Figure 32B, and relation to fractures lined by progressively Ag-rich compositions. High contrast BSE. Scale bar = 45um.

G. Sample TLS.5-83A: Dyscrasite (Ag - bright white) and inhomogeneous freibergite (Fr - light to dark grey) filling a fracture in pyrite. High contrast BSE. Scale bar = 35um.

H. Sample TL.MP-4 (Trout Lake Cu-Rougher Concentrate): Particle of naumannite (Nau) containing an inclusion of clausenthalite (Cl). Mm denotes mounting medium. High contrast BSE. Scale bar = 2um.

I. Sample TL.MP-12 (Trout Lake Cu-1st Cleaner Concentrate): Particle consisting of volynskite (Vol) and hessite (Hess). High contrast BSE. Scale bar = 5um.



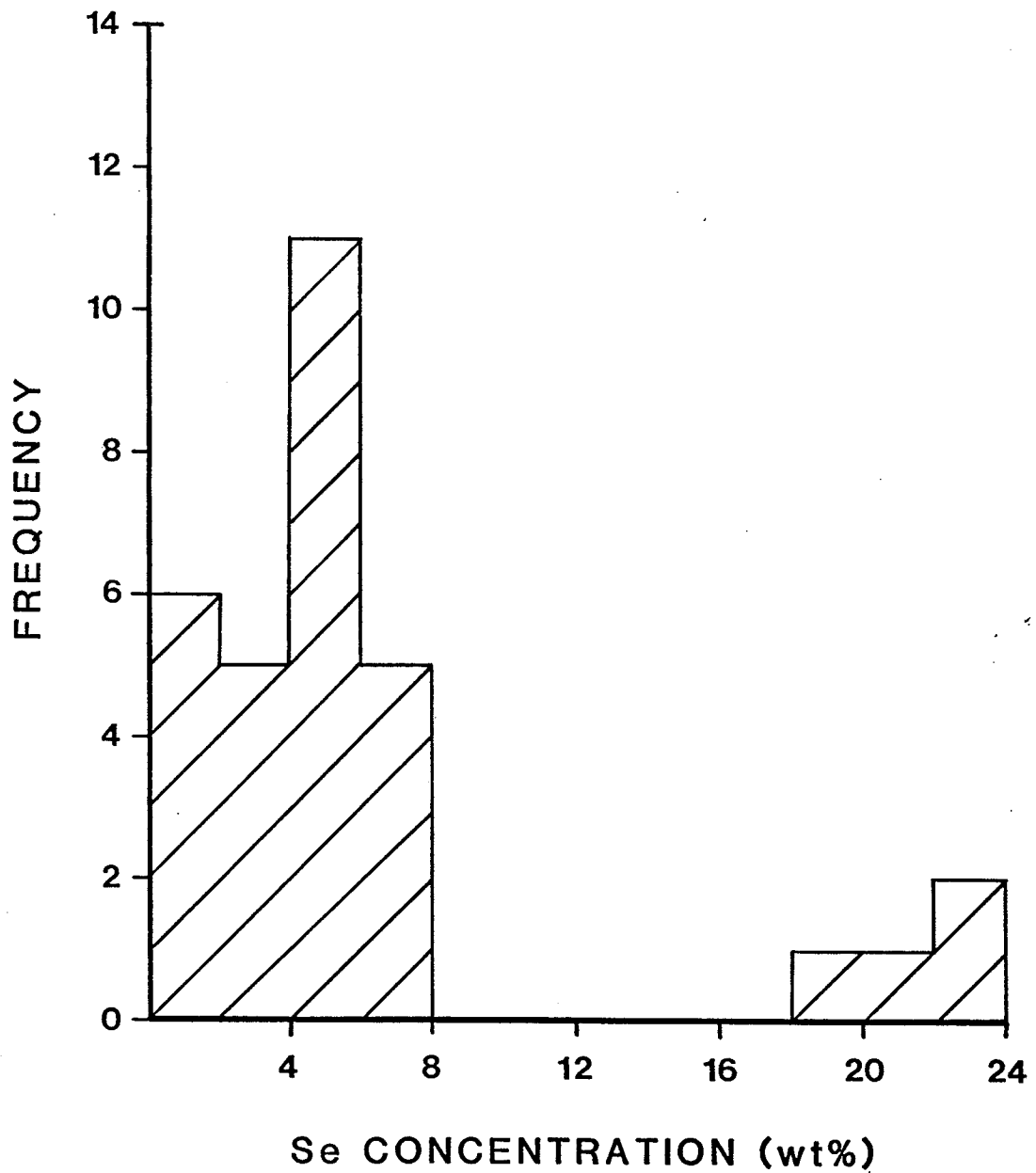


Figure 34: Histogram of Se Concentrations in Clausthalite-Galena Solid Solution. Distribution of Se concentrations in claustralite-galena solid solution as determined by microprobe analysis, indicating a trimodal population.

## Chapter VII

### GEOCHEMISTRY AND METAL ACCOUNTING

In order to elucidate the underlying 'structure' of the chemical composition of the ores, the chemical assays of the 27 representative ore samples were treated statistically using the SAS statistics package. Element distribution statistics, Correlation and R-Mode Factor Analysis were performed on the dataset. In so doing it was hoped to simplify the inter-relationships of the 17 elements, by (1) evaluating the strength of any linear relationship between pairs of elements, through construction of a Correlation Coefficient Matrix, and by (2) clustering the elements into a small number of mutually uncorrelated (orthogonal) generalized factors through Factor Analysis. These techniques provide invaluable information for interpreting the host mineralogy of elements, thus permitting elements to be assigned to previously identified minerals, and particularly for those trace elements whose host mineral(s) had not been previously identified i.e., Indium. In addition, the results are equally important in evaluating the mineral associations that characterize the ore, and which control the differentiation of the ores.

All the analyses for Bi gave concentration levels below the detection limit of 0.001% or 10ppm Bi. The analyses for Ni indicate concentrations of less than 0.003% or 30ppm Ni (except for one analysis of 0.006% Ni). The variance exhibited by Ni is therefore of the same order as the

analytical uncertainty, due to the proximity to the detection limit. In consequence, the Bi and Ni are excluded from the statistical treatment. The mean, maximum and minimum elemental concentrations, and coefficient of variation are provided below in Table 27.

The mean values in Table 27 provide limited information on the relative abundances of the elements in the ores. Clearly the mean values represent elevated values with respect to the mine reserves and analyses of concentrate feed i.e., 14.51% Zn versus 5.6% Zn for the proven ore reserves (See Tables 2 and 3). This disparity reflects (1) that the mean analyses are unweighted with respect to the relative abundances of the ore types, and (2) mine dilution and recovery is not included in the mean analyses. In addition, the preferential elevation of the Zn with respect to the Cu compared to that of the proven reserves, suggests that the suite of 27 samples is biased towards the Zn-rich ores.

Assuming that sphalerite and chalcopyrite are the sole Zn- and Cu-bearing minerals, respectively, then the maximum analysis for Zn and Cu indicate ores with up to 75% sphalerite and 64% chalcopyrite. In addition, a maximum analysis of 44% Fe indicates ores with up to 98% pyrite ( $\pm$  pyrrhotite). The coefficient of variation for Fe and S indicates that these elements exhibit the least range in concentration. This reflects (1) the undifferentiated character of S, being for all intents and purposes the sole anion, irrespective of ore type, and (2) the ubiquitous nature of pyrite and/or pyrrhotite in each ore type, and the generally undifferentiated nature of pyrite. In addition, the lower concentration levels of Fe are sustained by silicate-Fe, Fe in chalcopyrite, sphalerite and pyrrhotite, even where pyrite and/or

TABLE 27

## Basic Statistical Parameters of the Element Distributions

Element	Mean	Maximum	Minimum	Coef of Var
wt%				
Cu	4.97	21.89	0.02	126.
Zn	14.51	44.7	0.19	103.
Mn	0.084	0.270	0.014	81.
Pb	0.688	12.1	0.001	358.
Fe	23.4	44.0	5.6	47.
S	26.5	45.0	3.9	38.
ppm				
Au	3.295	13.75	0.377	108.
Ag	61.05	445.9	4.631	156.
Cd	0.031	0.126	0.001	107.
Co	0.016	0.123	0.001	148.
As	2795.	54000.	<2.	374.
Se	65.	302.	<1.	117.
Te	1.6	5.	<0.2	90.
Hg	38.	114.	7.	60.
Sb	85.	377.	2.	99.
In	34.	63.	<1.	47.
Sn	36.	54.	<1.	44.

\* 'Coef of Var' denotes coefficient of variation, which is a measurement of variation in a population calculated from [Coef of Var = StD / mean . 100]

marcasite are present in minor to trace amounts. Conversely Pb, As and Ag exhibit the largest range in concentrations reflecting the differentiated nature of the ores with respect to these elements, and their respective lognormal distributions. Surprisingly, Au exhibits a coefficient of variation of 108, which is inconsistent with its general tendency for erratic distribution. However, observed abundances of Au-Ag-Hg alloy in samples TLN.1-89, TLN.2-8, TLN.2-11 and TLS.2-40, all of which were not included in the suite of ores for which chemical analyses were done, indicate that the coefficient of variation for Au is unrepresentative of the entire ore population. The Au is erratically distributed and probably also lognormally distributed. For example, the derived Au content of TLN.1-89 (See Table 8 for approximate modal quantities of the Au-Ag-Hg alloy) is 3300ppm Au, at least within the area of the polished section.

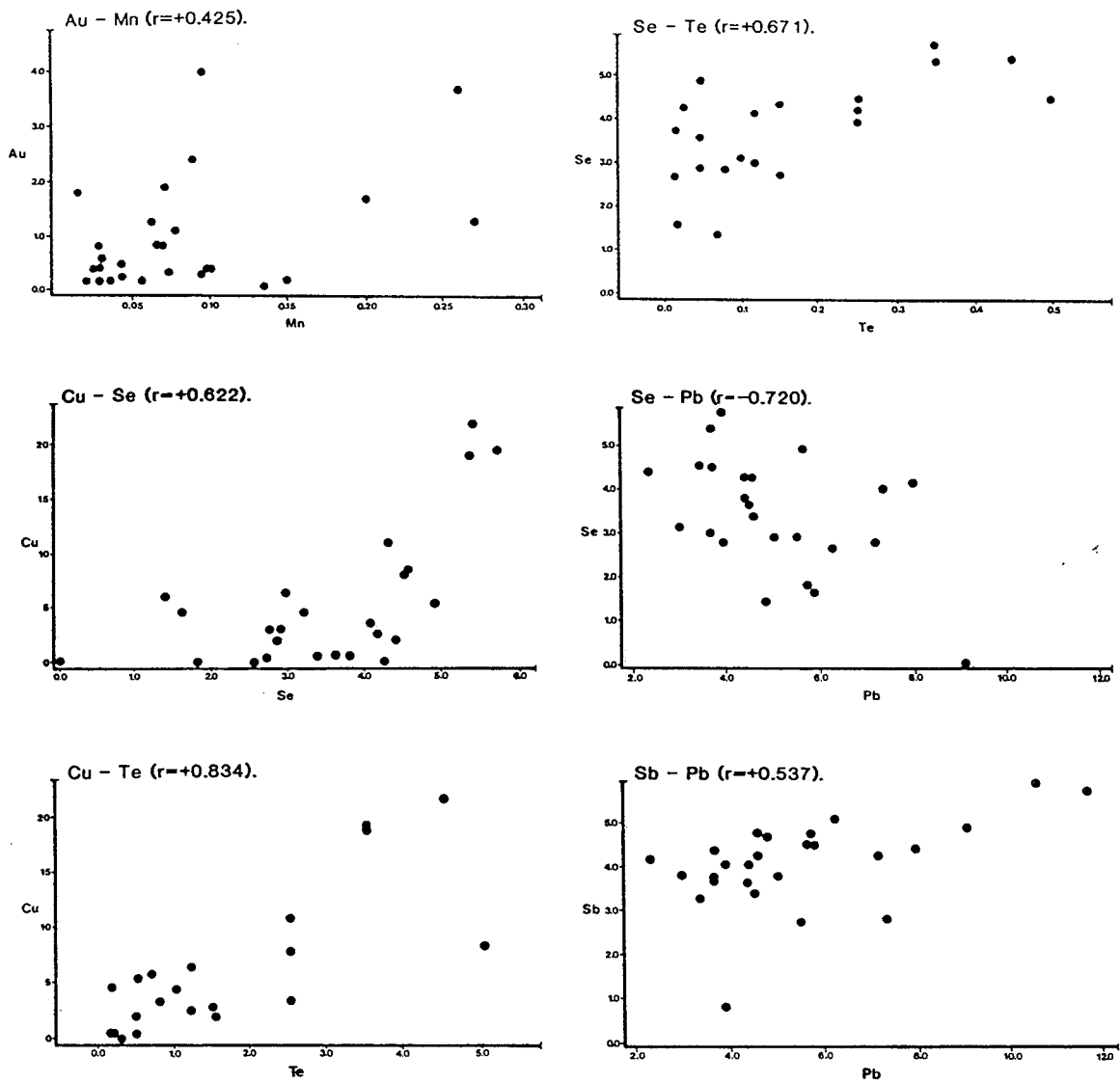


Figure 35: Scatter Diagrams of Selected Element Pairs from the Chemical Analyses. Scatter diagrams for the element pairs (A) Au-Mn; (B) Se-Te; (C) Cu-Se; (D) Se-Pb; (E) Cu-Te; and (F) Sb-Pb are shown with corresponding correlation coefficients ( $r$ ). The data for Sb, Pb and Se are log-transformed.

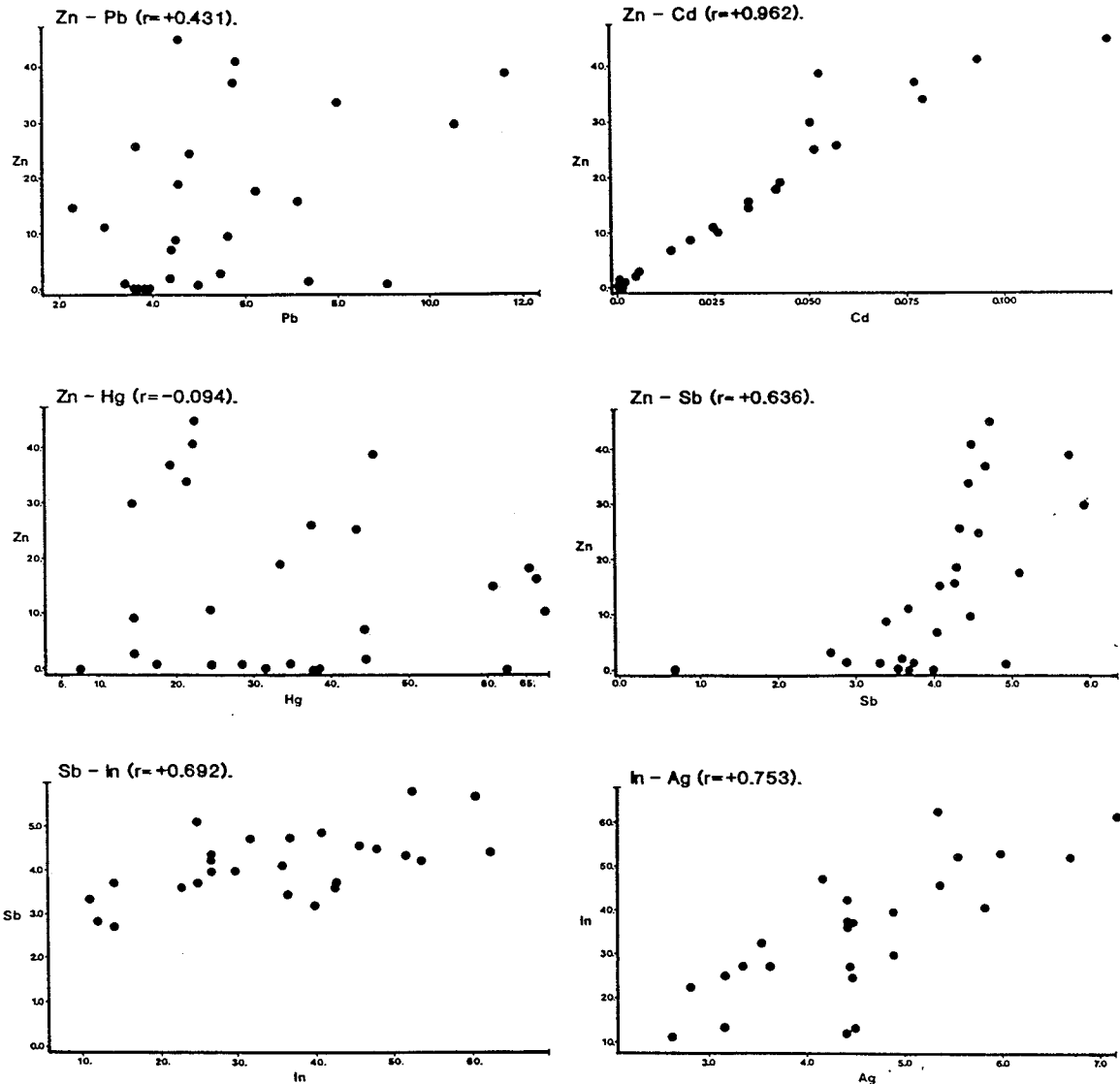


Figure 36: Scatter Diagrams of Selected Element Pairs from the Chemical Analyses. Scatter diagrams for the element pairs (A) Zn-Pb; (B) Zn-Cd; (C) Zn-Hg; (D) Zn-Sb; (E) Sb-In; and (F) In-Ag are shown with corresponding correlation coefficients ( $r$ ). The data for Sb, Pb and Ag are log-transformed.

## 7.1 CORRELATION ANALYSIS

Elements with lognormal distributions i.e., Ag, Sb, Pb, Se, As and Co were log-transformed to normal distribution in preparation for multivariate statistical analysis. Table 28 contains the correlation coefficient matrix consisting of possible 'r-values' of +1.000 to -1.000. For a sample size of 27 observations (the number of samples analyzed) r-values less than  $\pm 0.38$  are not significantly different from zero at the 95% confidence limits. Therefore, interpretation of the relationships for element pairs where the r-values are less than  $\pm 0.38$ , are not attempted. However, even a correlation coefficient of  $\pm 0.38$  indicates that only 14.4% of the total variance in 'X' and 'Y' can be explained by their linear relationship. Of the 120 coefficients in the matrix, 45 give r-values greater than  $\pm 0.38$ , and indicate a significant linear relationship for the respective element pairs. In addition, groups of elements that exhibit a high degree of covariance are readily identified. Two such groups of elements that covary are recognized by their positive correlations between elements of the same group, and negative correlations with elements of the second group. These groups define the fundamental geochemical associations of the ores. These are given below.

1. The Zn-Group: Zn, Cd, Pb, Sb, Ag, Hg, As, In and Sn.
2. The Cu-Group: Cu, Se, Te, Co and Fe.

Au and Mn do not exhibit any significant covariance with the above element groups. Sulfur exhibits marked significant covariance with elements of the Zn-group, and no significant covariance with elements of

the Cu-Group, except Fe. It is interpreted that this reflects the elevated concentration of Hg, Sn, Sb and In in high sulfide, and hence S-rich samples, where the Zn-rich ores tend to consist of more massive sulfides than the Cu-rich ores. This relationship can be considered as a product of induced covariance resulting from S being the sole significant anion in the sulfide ores. Therefore, S is not included in Zn-group. The S-Fe pair gives an r-value of +0.661, and this is readily explained in terms of S being the sole significant anion and Fe being the dominant cation of the sulfides. In addition, the greater weight fraction of S in pyrite (55% S) versus chalcopyrite (35% S) and sphalerite (30% S) also tends to strengthen the positive covariance of Fe with S.

The Au-Mn pair gives an r-value of +0.425, and represents the only apparently significant correlation of Au. The Mn is probably hosted in the gangue, and most probably in chlorite and/or calcite. It may be postulated on the basis of this weak correlation that Au-rich ores are coincident with a primary (non-metamorphic) Mn-rich alteration suite, and/or where the latter is related to the fluid state mobilization of Au during metamorphism. However, it is apparent from Fig. 35A that the Au-Mn correlation is heavily influenced by several extreme datapoints. Most surprisingly Au exhibits no correlation with As or Cu. Gold is commonly associated with As-rich pyrite and arsenopyrite in many types of deposits (Boyle 1979, Gasparrini 1983). Both the petrographic and chemical analyses failed to identify any such association at Trout Lake. Conversely, the apparent tendency of Au to be concentrated in the Cu-rich ores, as observed petrographically, is not substantiated by the

chemical analyses. However, samples TLN.1-89, TLN.2-11 and TLN.2-8, which are Cu-rich and contain abundant Au-Ag-Hg alloy, were not included in the relatively small suite of samples (i.e., n=27) for which chemical analyses were done. The suite was selected on criteria other than those necessary to establish a Au-Cu trend, and is biased away from gold-rich samples. Thus, the Au assays are not wholly representative of this typically lognormally distributed element, which is also characterized by the 'nugget' and 'particle sparsity' effect.

As stated earlier two groups of elements exhibiting marked covariance are recognized, and characterize the ores in terms of their mutual differentiation. These groups can be considered endmembers of a differentiation series from the footwall Cu-rich ores to the hangingwall Zn-rich ores. In addition, each lens may exhibit a greater tendency towards differentiation with a predominance of one association e.g., Lens 5 of the south zone is enriched in the Zn-Group with respect to all other lenses. Table 29 contains the correlation coefficient matrix portraying only the sign of the 40 significant correlations. Groups of elements displaying positive covariance are identified by fields of '+' signs, whereas the field of '-' signs identifies the antipathetic relationship or negative covariance between elements of the different groups. The coherence of the covariance exhibited by the two element groups is given in Table 30, with the elements ordered in terms of the strength of their covariance i.e., geochemical affinity within that group. Sb, Zn, Se, Pb and Te exhibit the highest degree of coherence, Sn, Cu, As, In, and Ag exhibit moderate coherence, while Cd, Co, Hg and Fe exhibit low coherence. Fe exhibits negative covariance with Zn and Cd

TABLE 28

## Correlation Coefficient Matrix of the Chemical Analyses

	Zn	Cd	Ag	Pb	Sb	As	In	Sn	Hg	Cu	Se	Te	Co	Fe	Mn	Au
Zn	1.000															
Cd	<u>0.962</u>															
Ag	0.269	0.107														
Pb	<u>0.431</u>	0.273	<u>0.439</u>													
Sb	<u>0.636</u>	<u>0.545</u>	<u>0.465</u>	<u>0.537</u>												
As	0.136	0.091	0.094	0.371	<u>0.431</u>											
In	<u>0.457</u>	0.364	<u>0.753</u>	0.217	<u>0.692</u>	0.195										
Sn	<u>0.389</u>	0.355	<u>0.423</u>	-0.078	<u>0.662</u>	-0.005	<u>0.743</u>									
Hg	-0.094	-0.104	-0.010	-0.109	0.321	<u>0.493</u>	0.300	<u>0.482</u>								
Cu	<u>-0.381</u>	-0.344	0.160	<u>-0.531</u>	-0.223	<u>-0.591</u>	0.187	0.374	0.051							
Se	<u>-0.503</u>	-0.355	-0.376	<u>-0.720</u>	<u>-0.456</u>	<u>-0.413</u>	-0.222	0.073	0.229	<u>0.622</u>						
Te	<u>-0.507</u>	<u>-0.470</u>	0.104	<u>-0.504</u>	<u>-0.405</u>	<u>-0.512</u>	-0.005	0.212	-0.009	<u>0.834</u>	<u>0.671</u>					
Co	-0.071	0.036	-0.161	<u>-0.503</u>	-0.043	0.064	0.135	0.252	0.303	0.292	<u>0.435</u>	0.273				
Fe	<u>-0.594</u>	<u>-0.562</u>	-0.092	-0.108	0.017	0.110	0.047	0.355	<u>0.611</u>	0.364	<u>0.405</u>	<u>0.380</u>	0.283			
Mn	0.010	0.087	-0.029	-0.164	-0.177	-0.137	-0.060	-0.088	-0.125	-0.018	0.127	0.093	0.229	-0.348		
Au	-0.127	-0.118	0.034	-0.134	-0.190	0.237	-0.036	-0.110	0.107	0.043	0.002	0.053	0.086	-0.054	<u>0.425</u>	
S	0.126	0.127	0.079	-0.020	<u>0.571</u>	0.269	<u>0.473</u>	<u>0.732</u>	<u>0.641</u>	0.063	-0.001	-0.064	0.079	<u>0.661</u>	-0.248	-0.225

TABLE 29

Correlation Coefficient Matrix of the Chemical Analyses. Only the sign of the significant correlations are shown.

	← Group 1. →								← Group 2. →							
	Zn	Cd	Ag	Pb	Sb	As	In	Sn	Hg	Cu	Se	Te	Co	Fe	Mn	Au
Zn																
Cd	+															
Ag																
Pb	+		+													
Sb	+	+	+	+												
As					+											
In	+		+		+											
Sn	+		+		+		+									
Hg						+		+								
Cu	-			-		-					+					
Se	-			-		-					+	+				
Te	-	-		-		-						+				
Co				-								+				
Fe	-	-							+		+	+				
Mn																+
Au																
S					+		+	+	+					+		

and positive covariance with Se, Te, Hg (the latter is a Zn-group element). The groups are discussed below.

TABLE 30

## Coherence of the Geochemical Associations

The number and sign of the significant correlations exhibited by each element within its respective group, and within the opposing group.

Element	Within Respective Group	Within Opposing Group
Sb	+ 7.	- 2.
Zn	+ 5.	- 4.
Se	+ 4.	- 4.
Te	+ 3.	- 5.
Pb	+ 3.	- 4.
Sn	+ 5.	- 0.
Cu	+ 2.	- 3.
As	+ 2.	- 3.
In	+ 4.	- 0.
Ag	+ 4.	- 0.
Cd	+ 2.	- 2.
Co	+ 1.	- 1.
Hg	+ 2.	+ 1.
Fe	+ 2.	- 2, and + 1.

### 7.1.1 THE Zn-GROUP (HANGINGWALL ASSOCIATION)

Elements: Zn, Sb, Pb, Sn, As, In, Ag, Cd, and Hg.

This group contains the highest r-value of any element pair in the matrix i.e., Zn-Cd (+0.962), and is consistent with the universal hypogene<sup>4</sup> geochemical coherence of these two elements (Mielke 1979). Regression analysis of Cd and Zn gives a calculated mean Cd content of 0.14 wt% Cd in sphalerite, assuming that sphalerite is the sole host of Cd. This value is in good agreement with the calculated mean of 0.16% Cd from the microprobe determined compositions of sphalerite, and the 0.14 wt% Cd calculated from the 1983 concentrate assays. The r-value of +0.962 indicates that 93% of the variance in Zn and Cd is explained by their linear relationship. This is interpreted as the systematic diadochic substitution of Cd for Zn in sphalerite (Fig. 36). Despite the high r-value, and thus linearity for the Zn-Cd pair, Cd exhibits distinctly lower covariance than Zn with the other elements of the Zn-group. However, it does exhibit numerous insignificant (note that this is at the 95% confidence level) positive correlations with all other elements of the Zn-group, and conversely negative correlations with elements of the Cu-group. The decreased covariance of Cd is attributed to the higher analytical uncertainty in the Cd determinations, due to proximity to the detection limit at these low levels of concentration. This results in a greater scatter in the Cd determinations relative to

---

<sup>4</sup> The term hypogene refers to geologic processes and resulting features, occurring within and below the crust of the Earth (Bates & Jackson 1980).

the Zn determinations, and probably also results in decreased strength of the covariance of the Zn-Cd pair from the ideal of +1.000 to +0.962, and the decreased coherence in the apparent geochemical coherence of Cd.

The assumption that sphalerite is the sole Hg-bearing phase is not substantiated by the correlation coefficient of -0.094 for the Zn-Hg pair. Hg exhibits no significant covariance with elements of the Cu-group, except with Fe, whereas it exhibits significant positive covariance with the Zn-group elements As and Sn, with which it gives a moderate r-value of +0.498 and +0.482, respectively. The scatter diagram of Zn-Hg (Fig. 36C) shows a distinct lack of linearity, suggesting that the Hg content of sphalerite is highly variable, and/or that additional Hg-bearing phases are present. Hg is known to occur in the Au-Ag-Hg alloy ( $\bar{x}$  = 10.64% Hg), but the contribution of this component to the total variance in Hg is considered insignificant. The Hg content of the ores is a minimum of one order of magnitude greater than can be explained by Hg in content Au-Ag-Hg alloy, i.e., mean analyses of 3.29ppm Au compared to 38ppm Hg, and where the Hg content of Au-Ag-Hg alloy is approximately 25% of the Au content of the Au-Ag-Hg alloy. It is inferred from material balanced assays and mineral quantities in Trout Lake concentrator products (Healy & Petruk 1989) that pyrite hosts approximately 66%, sphalerite 31% and Au-Ag-Hg alloy 3% of the Hg in the ore.

Arsenic exhibits a low positive correlation with Sb (+0.431) and with Hg (+0.493), and a low negative correlation with Cu (-0.591), Se (-0.413) and Te (-0.512). The correlation of As with Sb reflects the greater abundance of arsenopyrite, which is interpreted to be the only

significant host of As, in Sb-rich ores i.e., Massive Sphalerite, and more typically Layered Pyrite + Sphalerite ores with abundant galena, freibergite and pyrargyrite. The trace concentrations of As in freibergite, which behaves antipathetically to the Sb, is relatively insignificant, and is masked by the greater contribution to the total variance in As by the dominant arsenopyrite component. Arsenopyrite is also observed in the footwall Cu-rich ores, but invariably as a trace constituent, resulting in the Cu-As r-value of -0.581. The low chalcopyrite content of Sb- and Ag-rich ores (galena associated with chalcopyrite tends to contain negligible freibergite) is consistent with the negative correlation of As with Cu, Se and Te.

Antimony displays the highest degree of coherent covariance of all the elements, exhibiting significant positive covariance with all elements of the Zn-group except Hg (Sb-Hg r-value = +0.321), and conversely with elements of the Cu-group. Seven Sb-minerals (sulfosalts, sulfantimonides and dyscrasite) were observed in the ores, where freibergite, gudmundite and pyrargyrite are by far the most abundant. Lead exhibits the next highest coherence, while Ag exhibits moderate coherence. Galena is by far the most significant Pb-bearing mineral, while Ag is identified as a major or essential substituent cation in 9 minerals (in 5 of which Sb is also an essential substituent), and as a minor or trace element in an additional 3 minerals. The positive covariance of Sb, Ag and Pb is characterized by moderate r-values, and reflects the wealth of host phases of Sb, Ag and Pb (Fig. 36). In general Sb, Ag and Pb positively covary, and are coupled with the Zn-Cd pair, being enriched in sphalerite-rich ores. The lower coherence of Ag

reflects the occurrence of Ag-minerals such as Au-Ag-Hg alloy, hessite, volynskite and naumannite, and the inferred solid solution of Ag in chalcopyrite, all of which are interpreted to predominate in the footwall Cu-rich ores. This association of Ag with elements of the Cu-group reduces the strength of the linear relationship of Ag with Sb, Pb and Zn. However, the contribution of Ag in sphalerite, freibergite, pyrargyrite, galena and other lesser trace minerals, to the total variance in Ag is dominant.

Indium and tin are also included in the Zn-group, and exhibit moderate coherent covariance. Neither element exhibits significant negative covariance with elements of the Cu-group. Cassiterite is the only Sn-bearing mineral identified, whereas no In-bearing mineral is identified. Both elements exhibit significant positive covariance with Zn, Ag, Sb and one another (Fig. 36). Petruk (1985) reports that sphalerite in complex sulfide ores contains trace In, and that the In is recovered in the Zn concentrate. Petruk also reports that cassiterite in these ores generally occurs as fine-grained inclusions in sphalerite, which is in general agreement with the observations of this study. Thus, the mineral association of cassiterite with sphalerite explains the Zn-Sn r-value of +0.389, whereas the observed occurrence of cassiterite as inclusions in chalcopyrite reduces the strength of this linear relationship, and results in the marginally insignificant r-value of +0.374 for the Cu-Sn pair. Indium is probably hosted largely in sphalerite, though the moderate Zn-In r-value of +0.457 suggests either that the In content of sphalerite is highly variable or that additional In-bearing minerals exist. The moderate to high covariance of In with Ag

and Sb (Fig. 36) tends to confirm the latter, and that In occurs in one or more of the Ag-bearing minerals, or most probably that the In content of sphalerite is elevated in ores with high sulfosalt and sulfantimonide contents.

#### 7.1.2 THE Cu-GROUP (FOOTWALL ASSOCIATION)

Elements: Cu, Se, Te, Co and Fe.

This group of 5 elements is characterized by the coherence of Cu, Se and Te, the less coherent Co, and the loosely included Fe. Cu, Se and Te all exhibit moderate to high ( $> 0.600$ ) positive correlations with one another, Fe exhibits significant positive covariance with Se and Te, whereas Co exhibits only one significant positive correlation with other elements of the Cu-Group i.e., Co-Se pair. Co is included in the Cu-Group because of the one significant and numerous non-significant negative correlations with elements of the Zn-Group, and the converse for elements of the Cu-Group.

Co exhibits significant negative correlations with Pb, but insignificant correlations with Zn and Cd. In addition, the Co-Fe pair yields an r-value of +0.283, suggesting that pyrite the dominant host of Fe is not the dominant host of the Co. Hawley and Nichol (1961) determined that partitioning of Co into pyrite, pyrrhotite and chalcopyrite in the Flin Flon ores to be 0.44 : 1.0 : 0.086. The general tendency for pyrrhotite to be concentrated in the Cu-rich footwall ores,

and the predominance of pyrite as the Fe-sulfide in the galena-, sulfosalt- and sulfantimonide-rich ores, suggests that pyrrhotite may be the dominant host of the Co. The contribution of the pyrrhotite to the total variance in Fe is masked by the dominant contribution of Fe in pyrite, and results in a loss of linearity in the Co-Fe covariance. In contrast however, minor pyrrhotite is commonly associated with galena, freibergite, gudmundite, etc., and Co has been identified along with Sb in costibite. The lack of significant positive covariance between Co and Fe, and the negative covariance of Co with Pb is probably a multi-phase relationship involving pyrrhotite, pyrite ( $\pm$  marcasite), chalcopyrite, costibite and their association with galena and other Sb-minerals.

Fe is loosely included in the Cu-group because of the two significant positive correlations with Se (Fe-Se r-value = +0.405) and Te (Fe-Te r-value = +0.380), and the two significant negative correlations with the Zn-group elements Zn and Cd. Pyrite the dominant host of Fe is observed in all the ore types, though it behaves essentially antipathetically to sphalerite by (1) banding and segregation of pyrite and sphalerite in the Layered Pyrite + Sphalerite ores, and by (2) the tendency towards decreased pyrite content in the Massive Sphalerite ore type, and the converse in the Massive Pyrite ores. This contributes to the negative covariance of the Fe-Zn and Fe-Cd element pairs, while the tendency towards chalcopyrite-, pyrrhotite- and pyrite-rich footwall Cu-rich ores contributes to the positive covariance of Fe with the Cu-group elements. In addition, in Cu-rich samples that contain low abundances of pyrrhotite and pyrite, the Fe content of chalcopyrite sustains the covariance of Fe with the Cu-group elements. The positive covariance of

the Fe-Hg pair ( $r$ -value = +0.611) is consistent with pyrite, the dominant host of Fe, also being the inferred dominant host of Hg (i.e., approximately 66%).

Cu, Se and Te all exhibit moderate to high correlation coefficients with one another (ranging from +0.622 to +0.834), whereas Se and Te exhibit moderate to low positive covariance with Fe. The coherent positive covariance of Se, Te and Cu is surprising in view of the number of Te- and Se-bearing phases identified i.e., hessite (Te), clausthalite-galena (Se), rucklidgeite (Te, Se) pilsenite (Te, Se), volynskite (Te) and naumannite (Se). The Se-Pb pair yields an  $r$ -value of -0.720, suggesting that the clausthalite-galena solid solution contributes an insignificant component to the total variance in Pb and Se (Fig. 35). Hawley and Nichol (1959) determined variable yet comparable ranges (i.e., 200 to 400ppm Se) of Se in pyrite, pyrrhotite and chalcopyrite from the Flin Flon ores. This suggests that the positive covariance of Se and Cu is primarily related to the Se content of chalcopyrite, and the paragenetic association of chalcopyrite with Se-bearing pyrrhotite, pyrite, hessite, clausthalite, rucklidgeite, pilsenite and naumannite in footwall Cu-rich ores. The Cu-Te pair yields the highest  $r$ -value of the Cu-Group i.e., +0.834, and accounts for 70% of the variance in Cu and Te (Fig. 35). The partial covariance of Ag-Te is not exclusive of the Cu-Te covariance, as hessite is concentrated in the Cu-rich ores. In addition, rucklidgeite and pilsenite are concentrated in the Cu-rich ores, such that the covariance of Cu and Te may be explained not only by the paragenetic association of chalcopyrite with Te-bearing phases, but principally by Te in solid solution in

chalcopyrite. Petruk (1985) notes that chalcopyrite in complex sulfide ores may contain a 'few' ppm Te, and this might be sufficient to accomodate much of the Te in the ores, which averages only 1.6ppm Te. The low positive covariance of Fe with all the Cu-group elements reflects the masking effect of the dominant Fe in pyrite on the contribution of the chalcopyrite Fe to the total variance in Fe.

## 7.2 FACTOR ANALYSIS

As stated earlier, R-Mode Factor Analysis was employed to elucidate the structure of the chemical composition of the ores by attempting to define and interpret intercorrelations amongst the elements in the ore samples. R-Mode Factor Analysis is used to analyze the structure within the standardized correlation coefficient matrix of a multivariate dataset (Davis 1973). The technique is applied by clustering a large number of elements into a small number of uncorrelated, generalized factors, such that the elements within each factor are highly correlated, as indicated by high negative or positive factor loadings. The number of factors is ideally small with high factor loadings for each element, such that each element is associated with a minimum number of factors, thus simplifying the relationships in a complex dataset. In this manner the original elements can be replaced by the factors with little loss of information. Each factor describes an 'environmental factor' or geological process that contributes to the variation in the data. In addition, each sample receives a factor score for each extracted factor, and this score expresses the degree to which each sample possesses the property of the individual factors.

The principal factor matrix given in Table 31 contains the factor loadings for all 16 elements (S was excluded) in the dataset, for each of the 7 factors extracted. The communality is the fraction of the variation in each element that is described by the 7 factors. It should be noted that the square of the factor loading equals the fraction of the variation of that element described by the factor. It is also noteworthy that orthogonal varimax factor axis rotation was employed on the grounds that the factors are ideally uncorrelated and may reflect the effects of real phenomena which are postulated as being uncorrelated (Harbaugh & Merriam 1968). For the purpose of interpretation an arbitrary cut-off is adopted, below which value the factor loadings are considered insignificant or unrepresentative. Factor loadings below  $\pm 0.400$  were therefore disregarded, while the sign (denoted by P or N) of the accepted significant factor loadings are presented in Table 32.

Seven factors were extracted, as this was the smallest number of factors to satisfactorily describe over 90% of the variance in the dataset. Extraction of 6 factors was attempted and described less than 90% of the variance in the dataset. However, with the extraction of 6 factors, the essential changes relative to extracting 7 factors, were that Factors 5 and 6 were combined resulting in significant loss of the described variance in the dataset, and specifically in Au and Mn. The element pair scatter diagram for the Au-Mn pair (Fig. 35A) indicates that the r-value of +0.425 is a product of the extreme values distorting the correlation, and does not correctly describe that negligible correlation apparently exists. Thus, the extraction of 6 factors was rejected on the grounds that it excessively compresses the variance in

TABLE 31

## Principal Factor Matrix of the Chemical Analyses

Elem.	Factor							Communality
	1	2	3	4	5	6	7	
Au	-0.017	-0.083	0.026	-0.009	-0.952	0.233	0.020	0.968
Ag	-0.005	0.004	-0.085	-0.956	-0.057	-0.007	-0.115	0.939
Cu	0.900	-0.189	0.092	-0.225	-0.041	-0.073	0.103	0.922
Zn	-0.270	0.910	-0.103	-0.259	0.058	0.003	-0.035	0.983
Cd	-0.197	0.950	-0.088	-0.103	0.058	0.059	0.060	0.971
Co	0.198	0.038	0.192	0.021	-0.012	0.131	0.931	0.963
Mn	0.061	0.048	-0.096	0.038	-0.239	0.948	0.129	0.990
Pb	-0.648	0.092	-0.152	-0.432	0.156	-0.025	-0.408	0.829
Fe	0.218	-0.512	0.758	-0.006	0.157	0.019	0.104	0.919
As	-0.785	-0.057	0.380	-0.138	-0.272	-0.156	0.218	0.928
Se	0.709	-0.200	0.243	0.364	0.008	0.064	0.289	0.822
Te	0.825	-0.377	0.014	-0.147	-0.029	0.046	0.132	0.864
Hg	-0.089	-0.040	0.901	-0.046	-0.142	-0.109	0.175	0.887
Sb	-0.363	0.477	0.416	-0.562	0.213	0.016	-0.073	0.898
In	0.044	0.339	0.274	-0.832	-0.008	-0.055	0.126	0.903
Sn	0.340	0.442	0.598	-0.513	0.096	-0.032	0.061	0.947
Var.	3.49	2.77	2.30	2.68	1.17	1.03	1.29	
%Var.	21.8	17.3	14.4	16.7	7.3	6.4	8.1	
Cum% Var.	21.8	39.1	53.5	70.2	77.5	83.9	92.0	

Note: 'Var' denotes variance, 'Cum% Var.' denotes cumulative% variance.

TABLE 32

## Principal Factor Matrix of the Chemical Analyses

Only the sign of the significant factor loadings are shown.

Elem.	Factor						
	1	2	3	4	5	6	7
Au					N		
Ag				N			
Cu	P						
Zn		P					
Cd		P					
Co							P
Mn						P	
Pb	N			N			N
Fe		N	P				
As	N						
Se	P						
Te	P						
Hg			P				
Sb		P	P	N			
In				N			
Sn		P	P	N			

the dataset into too small a number of factors or geological processes. By extracting 8 or 9 factors a greater amount of the variance in the dataset was described, but with the creation of meaningless additional factors with insignificant low factor loadings and no apparent geological significance.

The values for communality indicate that 99% of the variance in Mn and 98% of the variance in Zn were accommodated for by the 7 factors. Conversely, the 7 factors described only 82% of the variance in Se and 83% of the variance in Pb. The combined variance in the 16 elements described by the 7 factors is 92.0%. One of the more interesting results of the factor analysis is that Factors 5 and 6 contain only one very high significant factor loading for Au and Mn, respectively. This suggests that greater than 90% of the variance displayed by both Au and Mn is controlled by 2 processes that are each independent of the variance in any of the other 15 elements. Factor 6 describes 90% of the variance in Mn, and represents the variance in Mn derived largely from the distribution of the Mn-bearing gangue minerals. Factor 5 describes 91% of the variance in Au, and indicates that the distribution of Au is largely independent of all other 15 elements. Au-Ag-Hg alloy contains approximately 93% of the Au, 10% of the Ag, and 2% of the Hg in the ore. The elements Ag and Hg behave antipathetically with respect to Au within the compositional range of the Au-Ag-Hg alloy, and this together with the minor contribution of the Ag and Hg in Au-Ag-Hg alloy to the total variance in these respective element, results in a complete lack of significant covariance in Ag and Hg with Au. Factor 5 also confirms the results of the correlation analysis, whereby neither Cu nor As exhibit positive covariance with Au.

Factor 1 describes 21.8% of the variance in the dataset, and constitutes the most powerful process controlling the variance in the data. Cu, Se and Te exhibit high positive factor loadings, As exhibits a high negative and Pb exhibits a medium negative factor loading. This indicates that Cu, Se and Te behave essentially sympathetically, and are antipathetic with respect to approximately 62% and 42% of the variance in As and Pb, respectively. This factor is interpreted as describing the distribution of chalcopyrite which is the only significant Cu-carrier and probably the principal host of Se and Te, and the mineral association of tellurides and selenides with the footwall chalcopyrite-rich, and hence Cu-rich ores. Simultaneously, As and consequently arsenopyrite, and Pb and principally galena are depleted in the Cu-rich ores. It is interesting that Sn exhibits a marginally insignificant positive factor loading of +0.340, suggesting that a small portion of the variance in Sn is sympathetic with that of Cu. This may reflect a mineral association of minor cassiterite with chalcopyrite, or stannite (not identified in the ores) with chalcopyrite, or most probably trace Sn in solid solution in chalcopyrite (Petruk 1985, Kase 1987).

Factor 2 describes 17.3% of the variance in the dataset and contains high positive factor loadings for Zn and Cd and moderate to low positive factor loadings for Sb and Sn, and thus the sympathetic relationship of Zn and Cd with a smaller component of the variance in Sb and Sn. The low negative factor loading on Fe indicates that Fe exhibits an antipathetic relationship with the latter 4 elements. As this factor describes 83% and 90% of the variance in Zn and Cd, respectively, it clearly represents the process controlling the distribution of sphalerite. This

process is coupled with a component in the variance of Sb and Sn, which is interpreted to represent the elevated concentration of the many Sb-minerals and cassiterite in the Zn-rich ores. Conversely, the negative factor loading on Fe confirms the antipathetic relationship of the dominant Fe host pyrite, and also pyrrhotite and chalcopyrite with respect to sphalerite and the associated Ag-bearing sulfosalts.

Factor 3 describes 14.4% of the variance in the dataset, and contains a high positive factor loading on Hg, a moderate to low positive factor loading on Sn, As and Sb, and a medium to high positive factor loading on Fe. This factor describes 81% of the variance in Hg. Thus, this factor suggests that the Hg content increases with the abundance of pyrite, arsenopyrite, cassiterite and the Sb-minerals (possibly the more common and non Ag-bearing gudmundite) also increases in the ore. The Layered Pyrite + Sphalerite ore type exhibits the highest factor scores, and thus expression of this factor. This reflects the observed increased abundances of pyrite, arsenopyrite and Sb-minerals in this ore type as it grades along a line of differentiation away from the Massive Sphalerite ores and towards the Massive Pyrite ores. The factor loadings tend to confirm pyrite as the principal host of Hg.

Factor 4 describes 16.7% of the variance in the dataset, and 91% of the variance in Ag. Ag and In exhibit high negative factor loadings, while Sb, Pb and Sn exhibit low negative factor loadings, and thus the sympathetic relationship of Ag and In with a component of the variance in Sb, Pb and In. As this factor includes 91% of the variance in Ag, it clearly constitutes a multi-phase mineral association encompassing 12 Ag-bearing minerals. Material balance calculations on mineral quantities

and assays indicate that chalcopyrite sphalerite and pyrite contain trace but significant concentrations of Ag (Healy & Petruk 1989). This is consistent with the determined (by SIMS and MicroPIXE) ranges of concentrations of many trace elements in common sulfides from Canadian massive sulfide deposits (Cabri et al. 1985, Chryssoulis et al. 1985, 1986). For example, Ag in Kidd Creek sphalerites ranges from not detected (<12ppm) to 308ppm, averaging 45ppm Ag (Cabri et al. 1985). Similarly, the latter authors found that Kidd Creek chalcopyrites contain trace Ag that ranges from not detected (<10ppm) to 1,589ppm Ag (no average value quoted), whereas In is carried in chalcopyrite and to a lesser extent in sphalerite. Factor 4 is interpreted to describe the distribution of Ag and In (and partly that of Sb, Pb and Sn), where Ag and In are partly hosted in chalcopyrite and sphalerite, yet whose concentration is independent of that of Zn and Cu, and hence the abundance of sphalerite and chalcopyrite. In addition, high Ag values are coincident with high Sb, Pb and Sn in the form of elevated abundances of Sb-minerals (many of which are Ag-bearing), galena and cassiterite. The lack of strong Zn-Ag covariance (r-value = +0.269) reflects the independence of this Ag-In-Sb-Pb-Sn association with Zn, although it tends to coincide with Zn-rich ores, in a permissive rather than linear manner. The In-Ag covariance reflected in the r-value of +0.753, and confirmed by Factor 4, may partially reflect the known coupled substitution of  $Ag^+ + In^{3+} = 2Zn^{2+}$  in synthetic sphalerites (McIntyre et al. 1984), and possibly a similar substitution for  $Cu^{2+}$  in chalcopyrite.

Factor 7 describes 8.1% of the variance in the dataset and contains significant antipathetic factor loadings for Co (+0.931) and Pb (-0.408). This factor indicates that 87% of the variance in Co is independent of all other elements, except for a minor (17%) component in the variance in Pb. Costibite is the only Co-bearing mineral identified, although pyrrhotite and possibly also chalcopyrite and pyrite are interpreted as the principal Co-carriers. The lack of Fe-Co covariance is in agreement with the correlation analysis and confirms that pyrite the dominant host of Fe is not a significant Co-carrier, while the complete lack of Co-As covariance indicates that arsenopyrite is not a Co-carrier. It is interpreted that Co is principally hosted in pyrrhotite and that the covariance of Co with the Fe in pyrrhotite is largely masked by the dominant contribution of the Fe in pyrite to the total variance in Fe. The partial antipathy of Pb with Co remains unexplained, though galena and pyrrhotite tend to be concentrated in the hangingwall and footwall, respectively.

Factors 1, 2, 3, 4 and 7 are multi-element factors describing distinct element associations whose behaviour are controlled by five ideally independent geological processes. For example, chalcopyrite and sphalerite tend to be concentrated in different ores, though the relationship is distinctly non-linear. The factors can be regarded as independent processes that are all superimposed on one another in the ores, but that display variable expression independent of the expression of the superimposed factors. Thus a high Zn sample will contain high Cd, but potentially high or low Cu, As, Ag or Hg values. Similarly, a high Cu sample will exhibit high Se and Te values, low As and Pb, but

potentially variable Zn, Cd Ag, Au, etc. These five factors are summarized in to the following associations.

1. Factor 1 : Cu + Te + Se - As - Pb.
2. Factor 2 : Zn + Cd + Sb + Sn - Fe.
3. Factor 3 : Hg + Fe + Sn + Sb.
4. Factor 4 : Ag + In + Sb + Sn + Pb.
5. Factor 7 : Co - Pb.

These five factors describe the independent processes whose combined expression results in the generalized two-fold division of the ores into the Zn-group and the Cu-group elements. Thus, the principal of the ores representing a simple differentiation series from Zn-rich to Cu-rich is a simplified interpretation of the fundamental processes that contribute to their compositions. In addition, if the ores were differentiated primarily on the basis of Cu and Zn, then these two elements would contribute high antipathetic factor loadings on a single factor. Clearly, these elements are not mutually exclusive and do not exhibit a strong linear relationship describing such a negative covariance. However, this generalization is largely valid, because the factors are apparently not truly independent in that Factors 2, 3 and 4 exhibit mutually compatible expression, whereas Factors 1, 5 and 7 exhibit mutually compatible expression. Oblique factor axis rotation is preferred where the factors are partially correlated, as indicated by these non-orthogonal dependent relationship of the factors (Harbaugh & Merriam 1968). However, the R-Mode Factor Analysis program employed in this study does not have an oblique factor axis rotation option.

### 7.3 INVISIBLE GOLD

'Invisible' Au is that which cannot be observed by optical or electron microscopy, which may occur either in solid solution or as sub-micron inclusions in sulfide minerals, and which cannot be recovered directly by cyanidation (Chryssoulis et al. 1987). Romberger (1986) and Huston & Large (1989) postulated that co-precipitation with pyrite of Au carried in solution as bisulfide complexes would generate significant submicroscopic grains of gold in pyrite. Furthermore, Boyle (1979) postulated that high-temperature pyrite and arsenopyrite take up Au and Ag largely as structural constituents which tend to exsolve on cooling. The Au and Ag diffuse to fractures and grain boundaries, where alloys of Au and Ag crystallize. Boyle (1979) also suggested that the frequent occurrence of 'invisible' Au in ores is due the retention of Au and Ag as structural constituents in relatively unfractured and unrecrystallized pyrite and arsenopyrite. Relatively unfractured pyrite metablasts, embedded in a 'soft' matrix of sphalerite, are common in several ore types in which only rare grains of Au-Ag-Hg alloy were observed (e.g., Layered Pyrite + Sphalerite). Conversely, abundant Au-Ag-Hg alloy was observed in Sheared Chalcopyrite + Sphalerite and Chalcopyrite Stringer ore types, where pyrite has typically undergone intense cataclastic deformation and has been partly to completely broken down.

Several lines of evidence, including data obtained by electron and ion microprobe, and results of various metallurgical analyses, show that in both natural and synthetic systems, significant 'invisible' Au (i.e., 1 to 1000ppm) is bound in pyrite and arsenopyrite (Wells & Mullens 1973,

Boyle 1979, Hausen 1981, Springer 1983, Chryssoulis et al. 1987, Cook & Chryssoulis 1989, Cabri et al. 1989). Approximately 30% of the Au in the Trout Lake ore is routinely lost to the tailings during standard froth flotation (Healy & Petruk 1989). Laboratory flotation tests of the tailings (Milojkovic 1983, McEachern 1987) have shown that at least 78% of the Au in the tailings is associated with pyrite and arsenopyrite. Cyanidation of a tailings sample (without regrinding) recovered 30% of the gold, and cyanidation after regrinding to 80% finer than 18um recovered 64% of the gold in the tailings. Thus, 36% of the Au in this tailings is assumed to occur as 'invisible' gold in pyrite and arsenopyrite.

The Au content of arsenopyrite, and the Au and As content of pyrite in the above cyanide-tested tailings sample, were determined by grain discrete secondary ion mass spectrometric (SIMS) analysis of these minerals. The SIMS technique was described by Chryssoulis et al. (1987). The Au concentrations in 46 pyrite grains vary from 0 to 6.80ppm, with a mean value of 0.72ppm. The As concentrations in the same grains vary from < 10 to 4100ppm, with a mean value of 500ppm. The Au and As concentrations show no significant positive covariance. The Au concentrations in 44 arsenopyrite grains vary from 2 to 112ppm, with a mean value of 30.2ppm. The distribution of 'invisible' Au in pyrite and arsenopyrite, and of As in pyrite is shown as histograms in Figure 22.

#### 7.4 DISTRIBUTIONS OF AU-AG-HG ALLOY AND OF INVISIBLE GOLD

The SIMS data and mineral quantities determined by image analysis for pyrite (i.e., 25%) and arsenopyrite (i.e., 0.2%) in the cyanide-tested tailings sample show that the 'invisible' Au in pyrite and arsenopyrite contributes 0.18 and 0.06ppm, respectively to the 0.67ppm Au assay in the tailings. Thus, approximately 27% of the Au in this tailings is due to 'invisible' Au in pyrite and 9% in arsenopyrite, and fully accounts for the 36% of the Au not recovered by cyanidation.

Healy & Petruk (1989) sampled products from the Trout Lake concentrator circuit over a two-hour period. A material-balance procedure adjusted the chemical assays and modal abundances, and simultaneously calculated recoveries of these at each point in the circuit under simulated steady state conditions. They determined that 59, 15 and 26% of the Au was recovered in the Cu-concentrate, Zn-concentrate and tailings, respectively. Fractions of the bulk Au assay in the end products due to pyrite and arsenopyrite were calculated using the material-balance adjusted modal quantities and 'invisible' gold contents of these minerals. This assumes that the 'invisible' gold contents of pyrite and arsenopyrite is identical to those determined by SIMS on the separate tailings sample, and thus that the distribution of 'invisible' gold corresponds to the distribution of these minerals. Pyrite and arsenopyrite were assigned gold assays of 0.12 and 0.02ppm Au in the feed, and account for 6 and 1%, respectively of the Au in the feed. Similarly, pyrite and arsenopyrite account for 20 and 2%, respectively of the Au in the tailings (See Table 33).

Gold due to Au-Ag-Hg alloy was calculated by subtracting the Au assay assigned to pyrite and arsenopyrite from the bulk Au assay of each end product. Fractions of the bulk Au assay in the feed thereby assigned to each mineral indicate that Au-Ag-Hg alloy accounts for 93% of the Au in the feed, with pyrite and arsenopyrite accounting for only 6 and 1%, respectively. Recoveries of Au-Ag-Hg alloy were also calculated on the basis of the distribution of the Au assay assigned to the alloy in each product, and indicates that 63, 16 and 21% of the alloy is recovered in the Cu-concentrate, Zn-concentrate and tailings, respectively (See Table 33). A search for the Au-Ag-Hg alloy, using an EDX-assisted image analyzer search-routine that detects grains larger than 1.5um in diameter (Petruk 1988), failed to find any grains of the alloy in the tailings. This indicates that in the tailings, the alloy is present in grains smaller than 1.5um.

The recovery of 'invisible' Au, which accounts for approximately 7% of the Au in the feed, is assumed to correspond to the recovery of pyrite plus arsenopyrite. Hence, 5 and 7% of the 'invisible' Au is assumed to have been recovered in the Cu-concentrate and Zn-concentrate, respectively, with the remaining 88% having been rejected to the tailings (See Fig. 37).

TABLE 33

**Bulk Au Assays, Modal Quantities and Au Assays Assigned to Pyrite, Arsenopyrite and Au-Ag-Hg Alloy in the Four End Products of the Trout Lake concentrator.**

Product	Modal Quantities and Assigned Au Assays*						Assigned Au Assays due to, and Recovery of Au-Ag-Hg Alloy**	
	Gold Assay (ppm)	Gold Rec. (%)	Pyrite Mod Qts. (wt%)	Pyrite Assay (ppm)	Arsenopyrite Mod Qts. (wt%)	Arsenopyrite Assay (ppm)	Assay (ppm)	Rec. (%)
Feed	2.23	100.0	15.4	0.12	0.06	0.02	2.00	100
Cu-Conc.	18.7	59.2	10.4	0.07	0.10	0.03	18.6	63
Zn-Conc.	7.58	15.3	12.3	0.09	0.45	0.14	7.35	16
Tails	0.65	25.6	17.2	0.13	0.03	0.01	0.51	21

Note: Bulk Au assays and modal quantities of pyrite and arsenopyrite are material balance adjusted (data from Healy & Petruk 1989). 'Mod Qts.' denotes modal quantities.

\* Au assays assigned to pyrite and arsenopyrite are based on the modal quantities of these minerals as determined by image analysis, and their average Au content i.e., pyrite (mean = 0.72 ppm Au) and arsenopyrite (mean = 30.2 ppm Au) as determined by SIMS.

\*\* Au assays due to, and recoveries of, Au-Ag-Hg alloy are estimated by subtracting the Au assay assigned to pyrite and arsenopyrite from the bulk Au assay of the product.

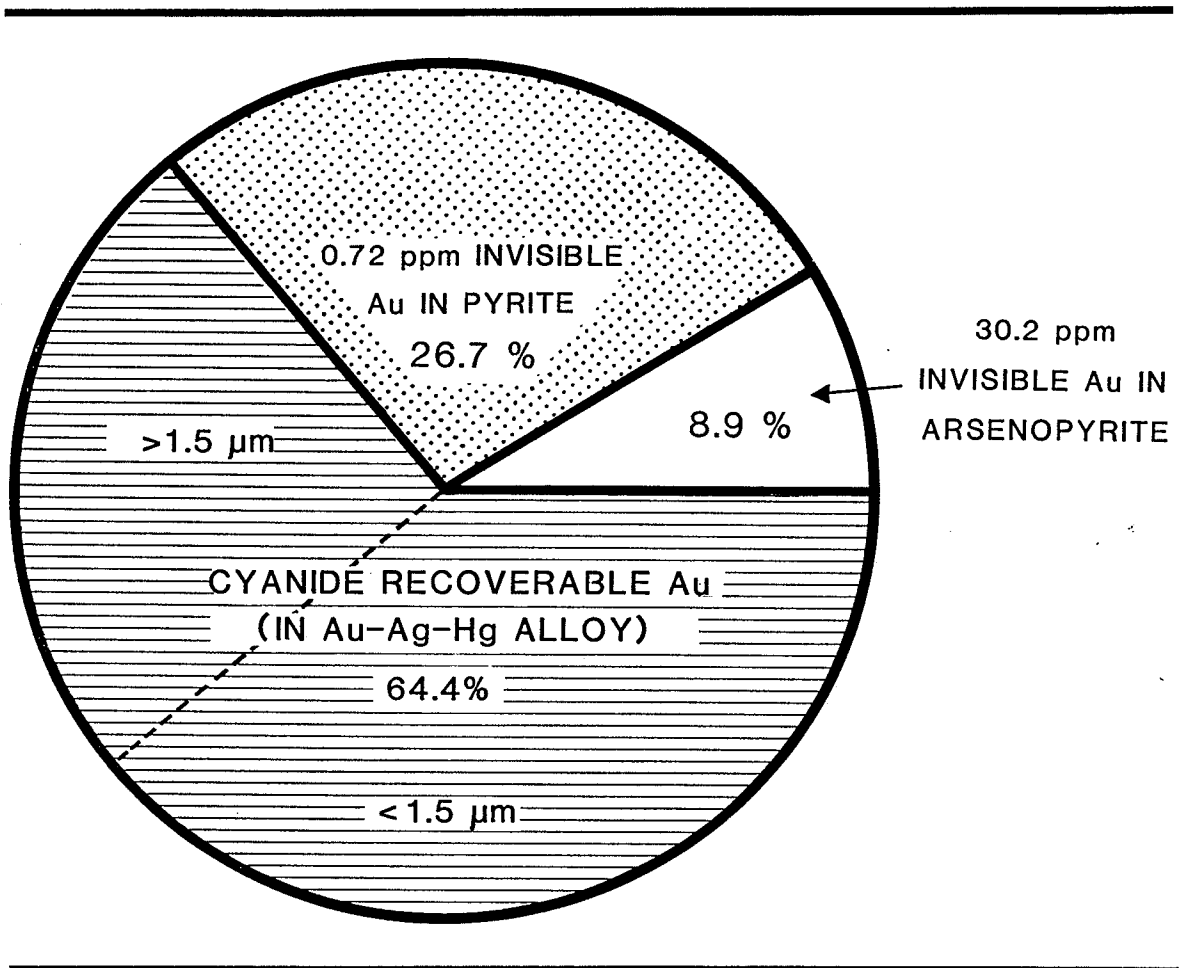


Figure 37: Mineralogical Department of Gold in a Sample of Trout Lake Concentrator Tailings. Department of gold is estimated from a combination of chemical (including cyanidation), electron microprobe, image and SIMS analyses.

## 7.5 SUMMARY

Copper is carried in chalcopyrite, cubanite, bournonite and freibergite, where the latter three phases represent insignificant contributions of Cu to the total Cu tonnage. Te was determined to occur in hessite, rucklidgeite, pilsenite(?), volynskite and in the clausthalite-galena solid solution that is associated with rucklidgeite. The Cu-Te element pair gives the highest r-value of the Cu-Group elements (i.e., +0.834), and is interpreted as the result of the paragenetic association of the Te-bearing minerals with chalcopyrite, and probably with a significant contribution from trace Te in solid solution in chalcopyrite. Selenium was identified in the clausthalite-galena solid solution, rucklidgeite, pilsenite(?) and naumannite. The Se-Pb pair gives an r-value of -0.720, indicating that the clausthalite-galena solid solution contributes an insignificant component to the total variance in Se and Pb. The positive covariance of Cu and Se (r-value = +0.622) is interpreted as resulting from the Se content of chalcopyrite, and the paragenetic association of chalcopyrite with Se-bearing pyrrhotite and pyrite (Hawley & Nichol 1959), rucklidgeite, pilsenite(?) and naumannite in Cu-rich ores.

Zn is carried in sphalerite and freibergite, where the latter is an insignificant contributor to the total Zn tonnage. Cd and probably Hg are also hosted in the sphalerite. The extremely strong positive covariance of Cd and Zn demonstrates that sphalerite is the host of the Cd. The complete lack of Zn-Hg covariance suggests that (1) Hg is only partly hosted in sphalerite. Although Hg in Flin Flon ores occurs dominantly in sphalerite (T. Chen, pers. comm., 1986), it is most

probable that the Hg is largely hosted in pyrite. The sole mineral positively identified as being Hg-bearing is Au-Ag-Hg alloy, which is interpreted to contain approximately 3% of the Hg in the ore.

Au is interpreted to be largely carried in Au-Ag-Hg alloy which is the only Au-bearing mineral identified. The correlation and factor analyses failed to identify any geochemical association of Au with any element, other than Mn, which probably reflects a distorted (non-normally distributed variables) correlation coefficient or an unidentified paragenetic association with a Mn-bearing gangue phase. No association of Au with As was apparent, nor was any association of arsenopyrite with Au-Ag-Hg alloy observed petrographically. The lack of covariance between Au and Hg and Ag reflects the minor contribution of the Ag and Hg in Au-Ag-Hg alloy to the total variance in Ag and Hg, which occur in concentration levels that are at least one order of magnitude greater than can be explained by their occurrence in Au-Ag-Hg alloy.

Arsenic occurs principally in arsenopyrite, but also in solid solution in freibergite, where the level of concentration ( $\bar{x}$  = 0.20 wt% As), and the trace abundance of freibergite in the ores, implies that arsenopyrite can be assumed to be the sole host of As. Pyrite also contains trace amounts of As.

Costibite is the only Co-bearing mineral identified, but is interpreted to be a minor Co-carrier because only one grain was observed, and because of the complete lack of Co-Sb positive covariance. The principal host of Co was not identified, but was interpreted to be pyrrhotite and possibly chalcopyrite.

Cassiterite is the only Sn-bearing mineral identified. Sn is a metallurgically troublesome element, which averages 36ppm Sn in the ores. It is interpreted that Sn is hosted principally in cassiterite associated with sphalerite, and with a subordinate component either as cassiterite or stannite associated with chalcopyrite, or in solid solution in chalcopyrite.

The metallurgically troublesome element Bi occurred consistently at concentration levels below the detection limit of the chemical analyses (0.001 wt% or 10ppm Bi). Bi was detected in the tellurides rucklidgeite, pilsenite(?) and volynskite. Galena is a potential host phase of trace Bi, but the severe Bi and PbMα overlap prohibits detection of less than 1 or 2% Bi.

Indium which occurs at trace concentrations in the ores (mean = 34ppm In) is interpreted to occur in sphalerite, possibly chalcopyrite and/or Sb-minerals. Indium exhibits moderate positive covariance with Zn, but high positive covariance with Ag, Sn, Sb and Pb. The strong covariance with Ag may reflect their geochemical association rather than necessarily being co-hosted in the same mineral. However, it is interpreted that a major component of both In and Ag are carried in sphalerite, especially where associated with Sb-minerals in the Layered Pyrite + Sphalerite ores.

Antimony is carried in freibergite, gudmundite, pyrargyrite, boulangerite, freislebenite, dyscrasite, bournonite and costibite, where the first three most abundant Sb-minerals may be assumed to contribute the only significant fractions to the total variance in Sb. Four of the

above minerals are Ag-bearing, particularly the more abundant freibergite and pyrargyrite, and this together with the association of these minerals with sphalerite and galena, both of which are interpreted as major Ag-carriers, results in a moderately strong Ag-Sb positive covariance.

Silver is carried in freibergite, pyrargyrite, hessite, Au-Ag-Hg alloy, dyscrasite, freieslebenite, naumannite, volynskite, acanthite, galena, and probably chalcopyrite, sphalerite and pyrite. Minor but erratic Ag was also detected in the clausthalite-galena solid solution. Despite the number of Ag-bearing minerals Factor 4 describes 91% of the variance in Ag, suggesting that the distribution of Ag is extremely systematic, covarying with significant components of the variance in In, Sb, Sn and Pb. Both Zn and Cu exhibit insignificant positive covariance with Ag, suggesting that the Ag contents of sphalerite and chalcopyrite are highly variable, and are independent of Zn and Cu abundances in the same samples. However, the strong In-Ag covariance suggests that sphalerite and chalcopyrite are principal hosts of Ag. Chalcopyrite being a simple derivative structure of sphalerite may also demonstrate the known coupled substitution in sphalerite of  $Ag^+ + In^{3+} = 2Me^{2+}$  (McIntyre et al. 1984), where Me denotes Zn and possibly Cu. Microprobe analysis of the Ag in galena gave an average content of 660ppm Ag (Pinard & Petruk 1989), and this suggests that galena hosts approximately 3% of the Ag in the ore. Microprobe analyses of Au-Ag-Hg alloy give an average Au/Ag ratio of 0.82 and indicates that this mineral accounts for approximately 15% of the Ag in the ore, assuming the Au-Ag-Hg alloy is the sole significant Au-carrier. Healy & Petruk

(1989) inferred that chalcopyrite, pyrite and sphalerite contain an average of 45, 11 and 55ppm Ag in solid solution, respectively, and this accounts for 23, 14 and 19% of the Ag in the ore, respectively. Furthermore, freibergite, pyrargyrite and the tellurides account for < 24%, and Au-Ag-Hg alloy for < 19% of the Ag in the ore.

## Chapter VIII

### DISCUSSION

#### 8.1 PREDICTION OF MINERAL LIBERATIONS

The grain size distributions for pyrite, chalcopyrite, sphalerite, freibergite and galena were determined for each of the 27 representative samples (plus the Chalcopyrite Stringer ore sample TLN.1-89) in order to predict liberations that would be obtained at certain grinds. Histograms and cumulative grain curves of the size distributions were plotted for the minerals of interest. The grain size distributions were condensed into mean distributions for each ore type, and histograms and cumulative grain size curves of these were plotted (Fig. 7 to Fig. 21). The 80% 'passing', 'less than' or '-' fraction is given for each mineral in each ore type. Liberation models have been developed by King (1979), Klimpel (1984), Barbery & Leroux (1986), Petruk (1976, 1986) and other workers. Although, these models do not incorporate sufficient parameters to accurately predict liberations, the incorporation of mineral grain size as a principal parameter in all models, allows estimation of the grind required to obtain mineral liberation (Petruk 1986).

Petruk's liberation model was developed to predict the minimum and optimum grinds, and the total liberation of the mineral at specific grinds, from measured surface area data on the mineral in unbroken ore (Petruk 1976, 1986, 1989b). Petruk's liberation model defines the

minimum grind to liberate a mineral as the grind that gives the same size distribution of the mineral in the unbroken ore, and at which approximately 60% of the mineral is liberated. The same model gives the optimum grind as the point on the cumulative grain size curve where the curve flattens, and beyond which point further grinding would not give a significant (>10% per screen size range) increase in liberation (Petruk 1976). The minimum and optimum grinds for the minerals of interest in each ore type and for average Trout Lake ore are presented in Table 34. The average Trout Lake ore is a weighted average in terms of the wt% of the mineral in each ore type (excluding the Vein Quartz + Chalcopyrite ores), and not in terms of the relative abundance of each ore type, which is unknown. Thus, the predicted average grinds for liberating sphalerite are not significantly affected by the minor fine-grained sphalerite in the Chalcopyrite Stringer ores, but are dominated by the the major coarse-grained sphalerite in the Massive Sphalerite ores. The grain size distributions of pyrite, sphalerite, chalcopyrite, galena and freibergite for average Trout Lake ore are presented in Figure 38.

Petruk's liberation model assumes that 60% of the mineral would be liberated at the minimum grind, and provides a method for calculating the approximate liberation that would be produced at finer grinds. The method involves: (1) determining the 95% passing size of the grind; (2) drawing a vertical line on the cumulative size distribution curve for the mineral of interest; and (3) noting the point where the vertical line intersects the cumulative size distribution curve. The predicted liberation is determined using the values on the cumulative size distribution axis. The predicted liberation is  $[(100 - X) + (X \times 0.6)]$ ,

where X is the value at the point of intersection. The predicted liberation that would be obtained when assumed average Trout Lake ore is ground to 95% -147um, the nominal grind used for processing Trout Lake ore, is 64% for pyrite, 69% for chalcopyrite, 73% for sphalerite, 58% for galena, 59% for freibergite and 37% for Au-Ag-Hg alloy.

The above predicted liberations are minimum liberations because they are based on the assumption that all these minerals are cemented in a matrix that is composed of minerals that have the same breakage characteristics as the ore minerals. In practise soft minerals like sphalerite, chalcopyrite and galena will break into finer grains than the hard minerals like pyrite, and thus tend to concentrate in the finer sieve fractions of the grind (Petruk et al. 1985). Consequently, soft minerals and inclusions within these, will achieve higher than predicted liberations (Petruk 1986). Furthermore, hard minerals (i.e., pyrite) initially tend to break dominantly by 'preferred breakage' along grain boundaries, fractures and cleavages, thus releasing the small interstitial minerals. Therefore, liberation of the interstitial minerals depends upon the liberation and size of the host mineral (i.e., pyrite), rather than upon the size of the interstitial mineral. As the ore is ground towards the size distribution of pyrite, the pyrite begins to break by progressively more 'random breakage' within grains. Consequently, minerals that are completely enclosed within pyrite will probably not be liberated unless the ore is ground to an extremely fine size.

Following the above guidelines, it is probable that the sphalerite liberation will be slightly higher than predicted, because of the

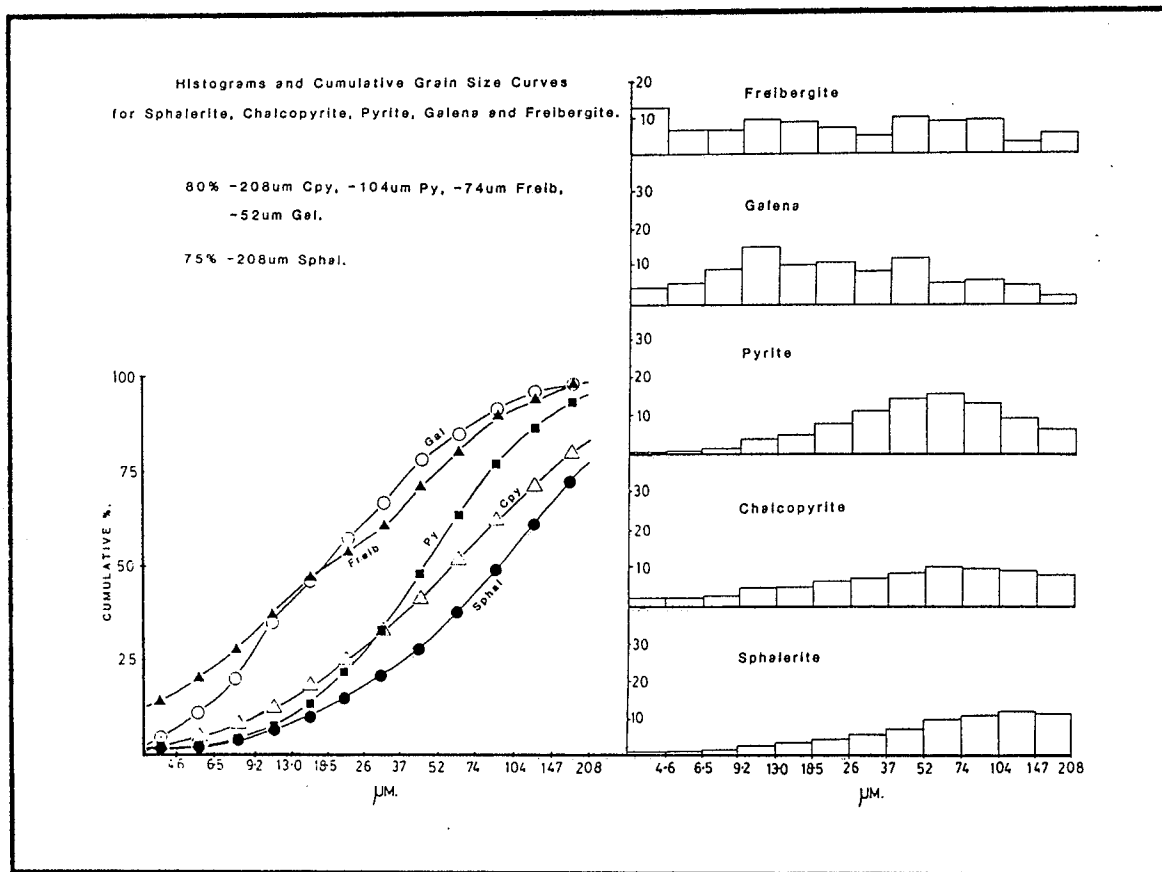


Figure 38: Average Grain Size Distributions for Trout Lake Minerals of Interest. Cumulative grain curves and histograms for the minerals of interest. Data generated from the grain size distributions of the individual ore types by weighting on the basis of the mineral quantities in each ore type. The 80% passing size of each mineral is given, except the 75% passing size of sphalerite is given.

TABLE 34

## Minimum and Optimum Grinds for the Minerals of Interest

Ore Types	Pyrite		Sphalerite		Chalcopyrite		Galena		Freibergite		Au-Ag-Hg Alloy	
	MG	OG	MG	OG	MG	OG	MG	OG	MG	OG	MG	OG
M. Sp.	147	52	>208	147	74	6.5	74	13	13	4.6	-	-
L. Py+Sp.	104	37	208	74	26	4.6	52	13	74	52	-	-
M. Py.	147	37	52	13	18	4.6	18	4.6	26	4.6	-	-
M/L. Cp+Sp.	37	13	147	74	147	52	-	-	-	-	-	-
M. Cp+Po.	104	37	52	13	>208	74	-	-	-	-	-	-
Cp. Stgs.	208	52	52	9.2	>208	104	-	-	-	-	-	-
D. Py+Cp.	104	37	104	26	104	37	-	-	-	-	-	-
S. Cp+Sp.	104	52	74	37	147	18	-	-	-	-	-	-
V. Qtz+Cp.	208	52	104	37	>208	208	-	-	-	-	-	-
Mean	95	26	>208	52	175	52	48	9.2	60	4.6	23	4.6

Note: 'MG' denotes the Minimum Grind, whilst 'OG' denotes the Optimum Grind; both quoted at 80% passing size.

interstitial sphalerite in pyrite. Similarly, the chalcopyrite liberation will be higher than predicted due to: (1) interstitial chalcopyrite in pyrite; (2) veinlets in pyrite; and (3) intergrowths with sphalerite. It is noteworthy that Petruk (1986) found that only a small percentage of chalcopyrite-disease was still present as rods and blebs in Brunswick sphalerite after grinding.

It is probable that galena liberation will be much higher than predicted because it occurs largely as (1) interstitial material or inclusions in sphalerite, and (2) in fractures and interstices in pyrite. Sphalerite is a soft mineral that is readily broken, is concentrated in the finer screen sizes of the grind, and hence would liberate more galena than predicted. The interstitial galena in pyrite would also be liberated from pyrite when pyrite is liberated, regardless of the size of the galena grains. The rare minerals freibergite, Au-Ag-Hg alloy, hessite, etc., occur largely as minute grains associated with galena, chalcopyrite and sphalerite, commonly in fractures and interstices in pyrite. Their liberation therefore depends upon the breakage of ore to the size that will liberate the host mineral e.g., pyrite, as well as the breakage that would release the minute grains. Therefore, the liberation of these minerals will likely be much higher than predicted by the liberation model.

It is possible to make a very generalized prediction on metal recoveries, taking into consideration that the grade-recovery relationship during concentration can substantially affect this prediction, and that actual liberations are dependent on parameters other than simply grain size. In general it can be expected that 95% of

free grains plus 33% of unliberated grains would be recovered in relatively high grade concentrates i.e., 26 to 28 wt% Cu, and 50 to 54% wt% Zn in the respective concentrates. Following these guidelines the predicted recovery for sphalerite from Trout Lake ore is 78% and chalcopyrite 76%. Actual observed recovery of Zn in the Zn concentrate is 77%, whereas 92% of the Cu is actually recovered in the Cu concentrate. However, an additional 14% of the Zn is lost/recovered to the Cu-concentrate (Healy & Petruk 1989).

The unweighted average grain size distribution of Types 1 and 2 Au-Ag-Hg alloy (See Fig. 29) is defined by 80% -26 $\mu$ m. The predicted liberation using Petruk's model is 37% for Types 1 and 2 Au-Ag-Hg alloy, corresponding to predicted recoveries of 56%. It is noted that because of the probable volumetric dominance of the coarser-grained Type 2 Au-Ag-Hg alloy, and the probability of unliberated Type 2 alloy being locked with chalcopyrite, the recovery of Au-Ag-Hg alloy should exceed that predicted. The actual recovery of Au in the Cu-concentrate is 59.2% (Healy & Petruk 1989).

Sample TLS.5-64, a representative Massive Sphalerite ore, contained abundant freibergite, pyrargyrite and gudmundite. Because of their abundances in the sample, image analysis of these three minerals (in addition to the routine mineral list) was undertaken. The analysis was done to determine the mineral quantities and the grain size distributions of these minerals, three of which are Ag-bearing. The results of the chord analyses are plotted in Figure 39, and demonstrate the consistently fine-grained nature of the Sb-minerals i.e., 80% -13 $\mu$ m for freibergite, pyrargyrite and gudmundite. Except for freibergite,

which exhibits a fine- to medium-grained nature in some of the Layered Pyrite + Sphalerite ores, the distributions are considered representative of the bulk of the pyrargyrite and gudmundite in the ores. The partial chemical compositions calculated from the mineral quantities of the complete list of minerals in TLS.5-64 is of particular interest in evaluating the Ag-bearing minerals. The derived compositions compare favourably with the chemical analyses (See Table 7)). The calculated Sb content of 0.03 wt% (300ppm) Sb is in excellent agreement with the chemical analysis of 310ppm Sb, whereas the derived Ag content of 0.02 wt% (200ppm) Ag is approximately half of the chemical analysis of 0.04 wt% (446ppm) Ag. This suggests that despite accommodation of all the Sb-minerals, only 45% of the Ag could be accounted for, and that sphalerite and galena are probably Ag-bearing. If galena is the host of the excess Ag, then it contains approximately 0.15 wt% (1500ppm) Ag, a detectable concentration that was not observed, and which far exceeds the average 660ppm Ag content of Trout Lake galena (Pinard & Petruk 1989). The derived Ag content is subject to large uncertainty due to poor sensitivity in the determination of the area% of freibergite and pyrargyrite at these levels of abundance, as well as the uncertainty due to sample inhomogeneity. However, it is probable that the uncertainty in the derived compositions and the existence of Ag in solid solution in sphalerite and galena, both contribute to the discrepancy between the derived and actual chemical compositions.

As stated earlier the predicted liberations for chalcopyrite, sphalerite, freibergite, Au-Ag-Hg alloy and galena, all of which are known or inferred to be Ag-carriers in that approximate order of

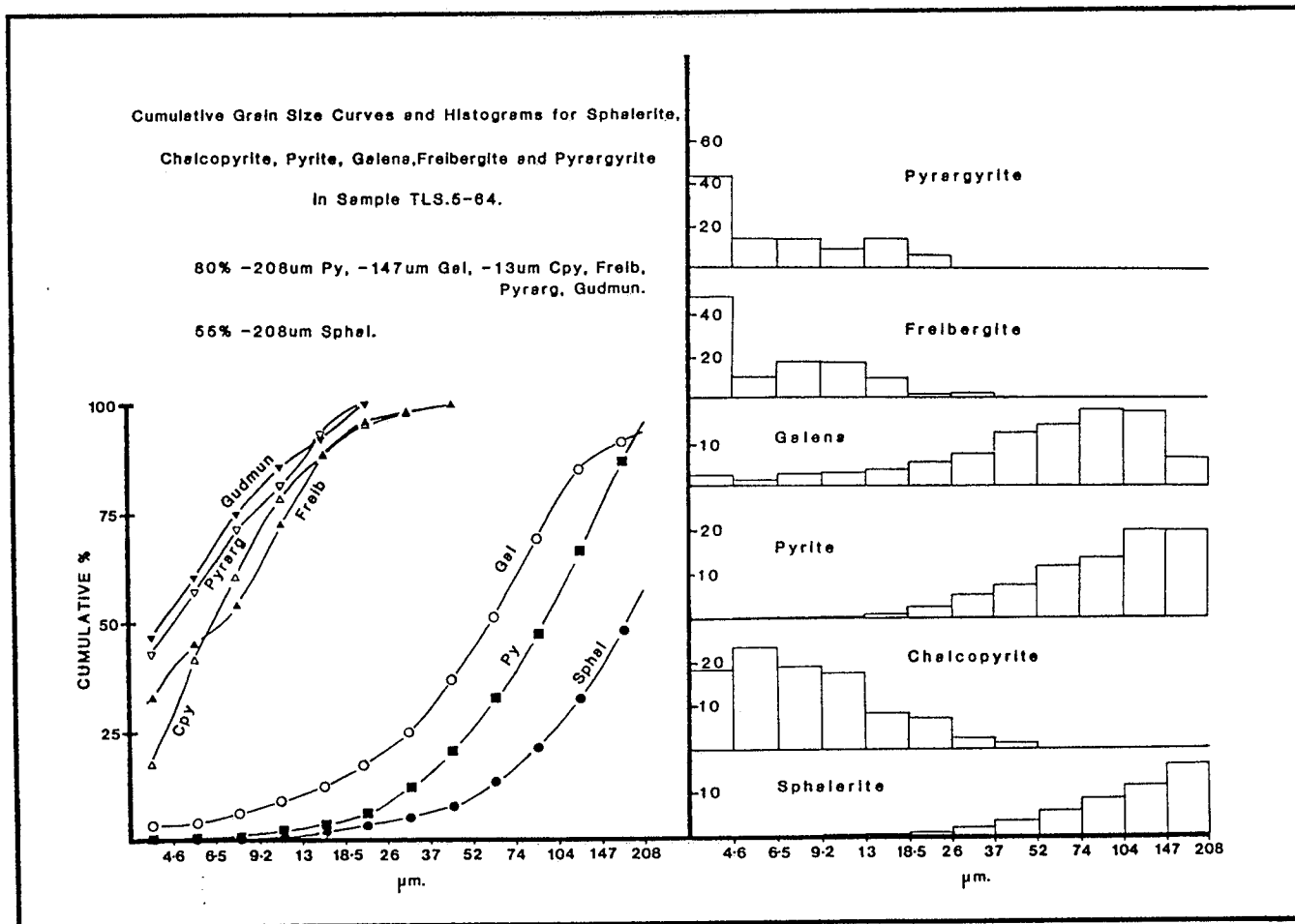


Figure 39: Grain Size Distributions of Minerals of Interest in TLS.5-64. Cumulative grain size curves and histograms of pyrite, sphalerite, chalcopyrite, galena, freibergite, pyrargyrite and gudmundite are shown. The 80% passing size of each mineral is given, except the 55% passing size of sphalerite.

significance, are 69, 73, 59, 37 and 58%, respectively. The predicted liberations for freibergite and pyrargyrite in sample TLS.5-64 are 25% and 20%, respectively, while the petrographic observations on the grain sizes of pyrargyrite, hessite, dyscrasite and other subordinate Ag-bearing minerals suggests that comparable predicted liberations would have been obtained had the grain size distributions been determined. All of these Ag-bearing minerals are 'soft' relative to pyrite and quartz and will tend to preferentially concentrate in the finer sieve fractions of the grind, and thus probably achieve somewhat higher actual liberations. Thus, the flotation behaviour of these minerals (excluding the greater fractions of sphalerite and chalcopyrite which are liberated) will be largely determined by the flotation characteristics of the host mineral.

## **8.2 ORE TEXTURES AND METAMORPHISM**

The Trout Lake ore deposit consists of a series of steeply dipping stacked lenses (6 proven), that are interpreted to represent a metamorphosed volcanogenic massive sulfide deposit as defined by Franklin et al. (1980). The ores were deposited by metal-bearing hydrothermal fluids mixing with seawater, either just below or above an exhalative vent on the Aphebian seafloor. The ore lenses are interpreted to have formed as mounds of fine-grained sulfide mud that precipitated above the vent, with associated deposition of a cross-cutting vein system beneath the vent, representing the 'plumbing system', and generally referred to as the stockwork or stringer mineralization. The lenses (both exhalative and stockwork ores) generally exhibit a

pronounced metal zonation of decreasing Cu/(Cu+Zn) stratigraphically upwards and towards the margins of the lenses. Lenses that exhibit both the Cu/(Cu+Zn) zonation and an underlying stockwork mineralization are termed proximal, having formed in the immediate area of the vent and not having undergone downslope transportation or reworking. The lenses at Trout Lake conform to the configuration of proximal type deposits.

Contemporaneous with the deposition of the sulfide lenses was the deposition of fine-grained subaqueous pyroclastic rocks of quartz-phyric character. These pyroclastic rocks were produced by volcanic extrusions from distant and/or adjacent magmatic bodies, where the latter may have been directly related to the ore deposition, providing the 'heat source' to drive the ore-forming hydrothermal cells. Thus, during each of the hydrothermal cycles, each of which produced one or more ore lenses, a variable amount of pyroclastic rocks were also deposited. The pyroclastic deposits formed the seafloor on which the exhalative vent formed, and the 'capping-rock' that encloses each of the lenses. It also contributed to the interbedded and disseminated wallrock within the lenses.

The supracrustal rocks of the Flin Flon belt, which include the Amisk Group, the host of all the volcanogenic massive sulfide deposits, were deformed and metamorphosed prior to 1,750 Ma during the Hudsonian Orogeny (Syme et al. 1982). The metamorphic grade of the Flin Flon area rocks corresponds to middle greenschist facies (Aggarwal & Nesbitt 1987). The absence of almandine (garnet) and the presence of biotite (and/or phlogopite) in pelitic rocks from the Trout Lake locality indicates that the rocks of this locality were metamorphosed at least to

the biotite isograd, corresponding to the middle greenschist facies. The metamorphic peak occurred during the second of three deformation events (Price 1977, Syme et al. 1982).

The textures displayed by the ores reflect, to varying degrees, the processes of initial deposition, metamorphism and deformation. However, because of the generally large stability fields of the common sulfides, a clear succession of mineralogical changes produced by progressive metamorphism, as observed in silicate rocks, is not observed. In addition, the relatively rapid equilibration times of sulfide minerals facilitates (1) the obliteration of all textures inherited from prior processes and events (i.e., primary ore depositional textures), and (2) the reversion of sulfide minerals (formed at the elevated temperatures of the metamorphic peak) to low temperature minerals, during the period of falling temperature (i.e., retrograde). Thus, the sulfide mineral assemblage we observe today is typically a retrograde assemblage, and not that formed at the temperature maximum (Vokes 1969), whilst the textures principally reflect the latest thermal and/or dynamic event. However, certain minerals and mineral textures produced at each stage in the history of the deposit persist, and permit at least partial deciphering of the history.

#### 8.2.1 RELICT TEXTURES

Two ore textures observed in the Trout Lake ores are possibly relict textures i.e., preserved primary ore depositional textures, that have survived the metamorphic recrystallization and deformation largely unmodified. These textures are (1) spheroidal pyrite, and (2) mineral

banding. Spheroidal pyrite was observed in only two samples and consisted of radiating cracks, pits and/or inclusions of chalcopyrite, sphalerite and/or pyrrhotite in the pyrite (Figs. 16B and 18G). This texture formed during ore deposition and subsequent diagenesis, with recrystallization of the pyrite and the segregation of the chalcopyrite, sphalerite and pyrrhotite into the radiating cracks.

Mineral banding constitutes the most commonly preserved texture in metamorphosed sulfide deposits, and at Trout Lake it is prominent, particularly in the Layered Pyrite + Sphalerite ore type. Such banding is the expression of the alternating types and concentrations of various minerals (Vokes 1969) e.g., sphalerite-rich alternating with pyrite-rich laminae, with variably superimposed banding of arsenopyrite-, galena- and/or gangue-rich laminae (Figs. 11F, G, and 20A). Banding of this type is observed in the 'Black Ores' of the unmetamorphosed Kuroko deposits (Lambert & Sato 1974, Craig & Vaughan 1981, Shimazaki 1974). The latter author also reports banding due to size grading, particularly of pyrite grains. Banding of this type is unlikely to be preserved even during low grade metamorphism, due to the recrystallization which tends to modify grain size, but not the distribution of the mineral components. The banding is generally parallel to the sedimentary stratification in the enclosing wallrocks, which is also parallel to the metamorphic foliation, as is commonly observed in many metamorphosed deposits (Vokes 1969). However, primary banding of this type has not been observed in modern seafloor sulfide mounds (J. Franklin, pers. comm., 1988). Based on the interpretation that the Chalcopyrite Stringer ores represent the tectonically flattened stockwork mineralization, the

constituent, discontinuous banding consisting of alternating chalcopyrite- and gangue-rich laminae (Fig. 16E) cannot be a primary feature of these ores. It is interpreted that this banding is the product of metamorphic segregation under conditions of directed stress in this highly chloritized 'plastic' zone. By corollary, much of the banding in the other ore types may also be the product of metamorphic segregation.

### **8.2.2 CHANGES IN MINERALOGY DUE TO METAMORPHISM**

Despite the tendency of sulfides to re-equilibrate rapidly, much textural and compositional evidence is observed that indicates the prior existence of high temperature minerals, and/or successive stages in a discernible mineral paragenesis.

#### **8.2.2.1 Inversion**

Spindle-shaped or lance-like and doubly concave twin lamellae are discernible without etching in chalcopyrite from Trout Lake ores. These twins are particularly visible in samples containing coarse-grained chalcopyrite. This texture is due to structural transformation from Iss, a high temperature cubic equivalent of similar composition to chalcopyrite, to the low temperature tetragonal chalcopyrite (Craig & Vaughan 1978).

#### 8.2.2.2 Exsolution

Chalcopyrite exhibits textures diagnostic of exsolution due to the decomposition of pre-existing high temperature Iss of homogeneous composition. Coarse-grained chalcopyrite at Trout Lake commonly displays exsolution lamellae of cubanite up to 5mm in length and 50um in width, and which exhibit composite or finely-lamellar habit (Fig. 18A). The cubanite forms by the decomposition of the high temperature Iss with a slight excess of Fe and S relative to stoichiometric chalcopyrite. Naturally occurring cubanite transforms to Iss at  $205 \pm 5^\circ\text{C}$  (Craig & Scott 1976), and this represents the upper stability of cubanite and a minimum temperature estimate for the ores. Ramdohr (1980) reports that the cubanite lamellae commonly overprint the sphalerite stars, indicating that the sphalerite stars had already formed when the chalcopyrite and cubanite still formed homogeneous Iss. Although, this was not observed at Trout Lake, it suggests that the exsolution of sphalerite from Iss is not eutectoidal, as suggested by Vaughan & Craig (1978), because chalcopyrite had not yet formed, with the Iss persisting as the host phase to lower temperatures.

Rare sphalerite stars form clusters and linear features within coarse-grained chalcopyrite, particularly in the Vein Quartz + Chalcopyrite ores. The stars are typically 20um in diameter, although rare exquisitely formed stars up to 90um in diameter are observed (See Figs. 18A and 23A). The similarity in structures between chalcopyrite and sphalerite (chalcopyrite is a derivative structure of sphalerite) provides for crystallographic continuity, and thus coherent exsolution (Craig & Vaughan 1981).

The solid solubility of Zn in chalcopyrite at 500°C, 400°C and 300°C is 0.9, 0.8 and 0.6 at% Zn, respectively, whereas in Iss the solid solubility at 500°C, 400°C and 300°C is 3.3, 1.7 and 1.2 at% Zn, respectively (Wiggins & Craig 1980, Kojima & Sugaki 1985). Heating experiments have shown that the homogenization temperatures of sphalerite stars in chalcopyrite are <500°C (Sugaki et al. 1987). Thus, on cooling the solubility of Zn in Iss decreases resulting in exsolution of sphalerite stars, at temperatures below 500°C, consistent with the middle greenschist metamorphism in the Trout Lake locality. Subsequently, at lower temperatures Iss decomposes to form low temperature chalcopyrite and cubanite. Similarly, CuS is soluble in sphalerite at higher temperatures, resulting in exsolution of chalcopyrite from sphalerite on cooling. Ramdohr (1980) reported that this exsolution can produce the texture known as chalcopyrite-disease (Fig. 8C and D). However, Hutchinson & Scott (1981) demonstrated that significant amounts of chalcopyrite will not dissolve in sphalerite at the temperatures indicated for many deposits exhibiting chalcopyrite-disease. Several studies have since shown that the texture can be largely attributed to replacement of sphalerite by reaction with Cu-rich fluids (Sugaki et al. 1987, Barton & Bethke 1987, Eldridge et al. 1983, 1988). Furthermore, Scott (1983) states that a similar texture exhibited by sphalerite from metamorphic deposits is probably the product of recrystallization of the original chalcopyrite-disease. The chalcopyrite-disease at Trout Lake is therefore interpreted to be essentially a product of the metamorphic recrystallization process.

Fine-grained blebs and rods of pyrrhotite less commonly occur in sphalerite from deformed samples, which also exhibit sphalerite replacement of pyrite (Fig. 23G). This chalcopyrite-disease-like texture may have formed by exsolution of excess FeS from the sphalerite due to recrystallization associated with the deformation, and reduction in the solubility of lower temperature sphalerite to dissolve FeS. Ramdohr (1980) reports a similar texture from metamorphosed ores in Sweden.

#### 8.2.2.3 Composition

The ore mineral assemblages and the compositions of the constituent minerals may be useful in estimating temperature and pressure during the metamorphism of the ores by reference to relevant phase equilibrium diagrams. The equilibrated mineral pair pyrite + arsenopyrite, which is observed in the Trout Lake ores (e.g., polygonal equigranular mosaics in massive pyrite bands) constitutes a fixed point geothermometer. This mineral pair must have formed below 520°C (Sharp et al. 1985). In addition, the As content of buffered arsenopyrite increases with increasing temperature. Because of the refractory nature of arsenopyrite it tends to retain its high temperature composition during cooling (Craig & Vaughan 1981). The effect of pressure on such a composition is not large (Sharp et al. 1985), and can be ignored for the purpose of an estimation based on only eight arsenopyrite compositions. The average As content of these analyses is 32 at% and gives a temperature estimate of 425 ± 30°C. This value for the temperature of crystallization of arsenopyrite is in good agreement with the P + T conditions of middle

greenschist facies metamorphism. Because the effects of pressure and potential trace element contents (i.e., Co, Ni and Sb, which were not determined) are not accounted for, and because of the relatively few compositions used in the temperature estimate, the value of  $425 \pm 30^\circ\text{C}$  is poorly constrained.

Sphalerite constitutes another refractory sulfide which displays compositional dependence on the conditions of formation. Sphalerite may contain up to 30.1 wt% Fe (Craig et al. 1984), and when equilibrated with pyrite and hexagonal pyrrhotite, is temperature independent between 300 and  $600^\circ\text{C}$ , but is pressure dependent. Sphalerite is therefore of use as a geobarometer. In the Fe-Zn-S system, where the activity of FeS is buffered by pyrite + hexagonal pyrrhotite, sphalerite will become enriched in FeS with decreasing pressure (Craig & Scott 1976). However, sphalerite also commonly undergoes partial re-equilibration resulting in decreased FeS contents, and thus higher calculated pressures during formation. Hexagonal pyrrhotite was not observed in this study, though undoubtedly much of the monoclinic pyrrhotite formed by decomposition of the hexagonal pyrrhotite below  $254^\circ\text{C}$ . The Trout Lake sphalerites are generally observed in equilibrium with monoclinic pyrrhotite and corroding and replacing pyrite (Fig. 25D and E), and are therefore unsuitable for geobarometric use. The average Fe content of 56 sphalerite compositions is 6.82 wt% Fe, whereas 15 compositions of an optically and texturally distinct later population of sphalerite (i.e., sphalerite II which replaces the common sphalerite I in sample TLN.1-87) had an average Fe content of 2.05 wt% Fe. This late Fe-poor sphalerite is interpreted as a retrograde reaction during the period of falling

temperature following the metamorphic peak. Sphalerite from Trout Lake exhibits a low, but somewhat variable Fe content due to (1) re-equilibration from the high temperature composition, or (2) initial equilibration with pyrite under conditions of high sulfur activity during the period of pyrite metablastesis. In addition, the abundance of chalcopyrite-disease may adversely affect the sphalerite composition, because Cu is known to affect sphalerite equilibration (Hutchinson & Scott 1981).

#### **8.2.2.4 Replacement**

Replacement of one mineral by another implies that the mineral being replaced predates the one replacing it. It therefore provides information useful in determining the mineral paragenesis. Replacement is produced by one of the following processes (1) dissolution and subsequent re-precipitation, (2) oxidation, and (3) solid state diffusion (Craig & Vaughan 1981).

Several replacement textures of pyrite are common in the Trout Lake ores. Fractured and granulated pyrite with deformation cleavage commonly exhibits replacement (rather than merely injection or infilling and cementing by matrix sulfides) by chalcopyrite, sphalerite, pyrrhotite and galena (Figs. 11A, B, and 25G). In fact, the cataclastic deformation of pyrite porphyroblasts to produce what are termed porphyroclasts facilitates the replacement of the pyrite. Pyrite idioblasts (euhedral metablasts) enveloped in a chalcopyrite matrix commonly display corrosion and replacement resulting in rounded islands

of pyrite in the chalcopyrite (Figs. 13F and 16A). Similarly, pyrite idioblasts in a sphalerite matrix exhibit corrosion and embayment and in an advanced stage, the development of 'atoll' texture (Fig. 8B). The latter forms by preferential replacement of the core of zoned pyrite grains, which is chemically distinct, possibly containing a distinct difference in trace element contents eg., Ni, or a subtle variation from stoichiometry. The core may represent a pre-metamorphic or possibly early stage of metamorphic recrystallization prior to the main pyrite metablastesis (pyrite porphyroblastic growth).

Pyrrhotite is commonly observed replacing pyrite along fractures and grain boundaries (Fig. 25D and E), particularly as rounded islands in a matrix of pyrrhotite and chalcopyrite (Fig. 16A). Further, pyrrhotite-rich ores are generally pyrite-poor and/or exhibit deformed pyrite partially replaced by pyrrhotite, suggesting that much of the pyrrhotite forms by the breakdown of pyrite and the release of S in a partly open system.

Marcasite replaces pyrite along fractures and grain boundaries in a variety of textures. These are (1) fringes of bladed grains and flecks on the pyrite, (2) comb-textured marcasite on pyrite grain boundaries and fractures, (3) 'sooty-textured' pyrite (Fig. 16C), and (4) fine- to medium-grained interlocking aggregates in polygonal masses of recrystallized pyrite (Fig. 16G). These textures are most common in highly deformed samples and are typically concentrated along shear zones or schlieren. Rare foliated scaly masses of marcasite associated with galena, freibergite and pyrrhotite are observed enveloping and corroding cataclastic pyrite along distinct schlieren in some Layered Pyrite +

Sphalerite ores (Fig. 11H). All of these textures, involving the replacement of pyrite by marcasite, are interpreted as retrograde adjustments associated with deformational events that postdate the pyrite metablasteresis, possibly contemporaneous with the D3 event.

A rare fine-grained, concentrically-ringed mixture of marcasite and pyrite replacing pyrrhotite, called 'birds eye' texture, was observed in contact with pyrite grains enveloped in the pyrrhotite (Fig. 16H). This texture is an alteration product of pyrrhotite due to increased oxidation. Pyrite grains commonly display zones and fringes of reticulate textured magnetite in pyrite, known as magnetite-pyrite symplectite (Kieft et al. 1987). This texture is also a product of pyrrhotite alteration due to increased oxidation, with simultaneous growth of pyrite and magnetite.

Pyrite may exhibit dendritic replacement by galena, sphalerite, chalcopyrite and rarely pyrrhotite (Figs. 11D, 18H, 25B and C), particularly in the Massive Pyrite and the Layered Pyrite + Sphalerite ores. This texture is interpreted as resulting from preferential invasion and replacement of pyrite along crystallographically controlled directions, either deformation cleavages or planes of lattice defects i.e., dislocations in the pyrite.

As discussed earlier, the abundant chalcopyrite-disease in Trout Lake sphalerite is interpreted as the product of metamorphic recrystallization of a replacement texture, with a possible minor component from exsolution. Cu-bearing fluids replace the FeS component and possibly ZnS component of sphalerite, and this is generally

developed along grain margins, fractures and twin planes in sphalerite (Eldridge et al. 1983, 1988, Barton & Bethke 1987). This process will tend to deplete the sphalerite in FeS, possibly contributing to low Fe contents. This may render such sphalerites unuseable for geobarometric measurements, depending on the timing of the replacement with respect to the metamorphic peak and latest re-equilibration. The chalcopyrite-disease is commonly observed lying on the bent lamellar twin planes of the sphalerite, where the latter are produced by twin gliding in response to stress. This suggests that the chalcopyrite-disease was imposed on a pre-existing and deformed sphalerite, subsequent to the growth of sphalerite at the metamorphic peak, but probably predates the last compositional re-equilibration. The chalcopyrite-disease is most common and intensely developed in samples displaying intense deformation and abundant matrix chalcopyrite. A discernible trend with increasing deformation is observed from: (1) sphalerite with weak chalcopyrite-disease; to (2) sphalerite with chalcopyrite-disease and interstitial blebs, films and wedges of chalcopyrite to; (3) sphalerite with intense chalcopyrite-disease and abundant interstitial films, wedges and xenoblastic masses of chalcopyrite enveloping the sphalerite (Fig. 8C and D); to (4) where sphalerite develops carious, interpenetrative contacts with the enveloping chalcopyrite (Fig. 20B and G); to (5) where chalcopyrite and sphalerite form fine-grained, myrmekitic intergrowths (Fig. 20A). The development of chalcopyrite-disease is thus facilitated by the deformation of the host sphalerite.

### 8.2.3 CHANGES IN FABRIC DUE TO METAMORPHIC RECRYSTALLIZATION

Metamorphic recrystallization or metablastic growth plays a major role in the ore textures of metamorphic deposits. Recrystallization results from the application of thermal and dynamic energy inducing the growth of strain-free grains and the minimization of the interfacial tension i.e., the area of the grain interfaces. During the process of recrystallization stored energy of strained grains is released, work-hardened minerals are replaced by softer annealed grains, re-orientation occurs, grain size increases, and essentially equidimensional grains in a polygonal mosaic or 'foam' texture are developed. Stanton (1972) strictly defines recrystallization as the process of grain boundary migration. Recrystallization involves: (1) 'nucleation' of strain-free domains by thermal activation at preferred points in the grains; (2) 'primary recrystallization' where new strain-free grains propagate from the nuclei to the point where they mutually impinge; (3) 'normal growth' of the now strain-free grains in order to minimize the total energy of the boundaries i.e., total interfacial surfaces, to produce slightly curved surfaces meeting at the characteristic dihedral angles ( $120^\circ$  in monomineralic aggregates (Fig. 33E), (4) 'secondary recrystallization' where certain grains are coarsened in grain size at the expense of other smaller matrix grains to produce porphyroblasts, and (5) 'differential recrystallization' with temperature dependent recrystallization preferentially producing recrystallization and annealing in one phase and not another.

In general the grain size increases with grade of metamorphism as a direct result of recrystallization. In consequence, the majority of

textures inherited from the period of ore deposition are obliterated. Non-metamorphosed volcanogenic massive sulfide deposits contain fine-grained sedimentary material with abundant pyrite framboids and colliform textured pyrite, whereas the metamorphosed Trout Lake deposit contains pyrite grains up to several cm in diameter, and a calculated median grain size of between 65um. Sato (1974) reports that sphalerite and chalcopyrite usually occur as grains under 10 and 50um, respectively, in the non-metamorphosed Shakanai mine, Japan. This contrasts with the observed grain size distributions of these two minerals at Trout Lake; median grain size of 125um, and 65um, respectively. Therefore, it is interpreted that there is a general increase in grain size of the constituent sulfides due to mineral growth. However, the effects of deformation (discussed in the next section) tend to reduce the grain sizes that were produced by pure metamorphic recrystallization. Thus, the median grain sizes mentioned above are probably lower than those initially produced during the metamorphic peak, prior to the deformation of D3.

The most distinctive texture attributed to metamorphic recrystallization is the development of annealed polygonal mosaics of equidimensional grains displaying  $120^\circ$  triple junction angles. Bands and masses of pyrite at Trout Lake commonly display this recrystallized granuloblastic texture (Fig. 23B). Recrystallized masses of pyrite + arsenopyrite also exhibit this texture, with the development of characteristic (not  $120^\circ$ ) dihedral angles for this polymineralic assemblage. Similarly, massive magnetite commonly displays  $120^\circ$  dihedral angles (Fig. 26G). Minor minerals typically occur within the interstices

between the major mineral (i.e., galena, sphalerite or chalcopyrite in pyrite masses), and rarely as entrapped inclusions (e.g., rounded sphalerite inclusions in pyrite; See Figs. 11C and 25H). This granuloblastic texture is developed in an essentially solid medium where the 'force of crystallization' of the constituent minerals to form euhedral shapes are the same or similar, such that when the growing minerals mutually impinge, one mineral does not develop euhedrism at the expense of another. Stanton (1972) proposed a 'Crystalloblastic Series' for common rock-forming and sulfide minerals, which is based on the 'force of crystallization' or tendency to form euhedral or idiomorphic grains. The series in order of decreasing tendency to euhedrism is garnet, magnetite-arsenopyrite, pyrite, dolomite, tremolite, muscovite, chlorite, pyrrhotite, sphalerite, chalcopyrite and galena. Stanton also points out that other minerals of the same structural groups as those in the series, will likely display equivalent euhedrism and thus positions in the series i.e., pyrite-marcasite.

When grains of pyrite are disseminated in a matrix of sphalerite, chalcopyrite and/or galena, they tend to develop as large euhedral grains with well formed crystal faces (and are termed porphyroblasts) in a matrix of anhedral minerals which rarely develop crystal faces, but tend to form mosaic textures. Thus, disseminated pyrite, arsenopyrite and magnetite develop porphyroblastic texture within matrices of sphalerite, chalcopyrite, pyrrhotite and/or galena (Fig. 23C). This is particularly pronounced in the Layered Pyrite + Sphalerite ores, where pyrite and lesser arsenopyrite form euhedral cubes and prisms with rhombic sections, respectively, in the sphalerite matrix. Within the

matrix, chalcopyrite tends to occupy the interstices between sphalerite grains rather than forming an equidimensional mosaic. Similarly, galena forms as interstitial masses between sphalerite grains, commonly forming on the sphalerite-pyrite, or sphalerite-gangue contacts, in preference to the sphalerite-sphalerite contacts (Fig. 23H). It is noteworthy that when sphalerite forms the interstitial material to pyrite, the pyrite tends to be idiomorphic, whereas as also noted by Vokes (1969), pyrite with interstitial galena has decreased idiomorphism, appearing more rounded (Figs. 11G and 25AA). Paragenetic sequences are commonly constructed on the basis of these textures, which are erroneously interpreted as replacement or cross-cutting textures, rather than merely reflecting the position of the constituent minerals in the 'Crystalloblastic Series'. In this study these textures are interpreted in light of the mineral(s) position within the 'Crystalloblastic Series', and generally imply contemporaneous rather than sequential crystallization.

The grain size of pyrite exhibits a strong dependence on the surrounding matrix in which it grows. Pyrite forming in a chlorite gangue tends to be considerably coarser-grained than pyrite in a sphalerite matrix or in a band of massive pyrite. This phenomena may be attributed to (1) more widely spaced crystallization nuclei from which the pyrite grows, and (2) the lower 'force of crystallization' of the minerals forming the matrix. Thus, there is an observed trend of decreasing pyrite grain size from pyrite in (1) a gangue matrix, (2) a sphalerite or chalcopyrite matrix, where the pyrite is generally porphyroblastic, and in (3) a band or mass of monomineralic pyrite. Less

commonly, the pyrite porphyroblasts overgrow and enclose residual 'foreign' minor minerals, which typically develop rounded or spherical forms to minimize interfacial energies with the host pyrite. When this texture is well developed it is termed poikiloblastic pyrite, and sphalerite is the most common inclusion in pyrite (Figs. 11C and 25H). Similarly, magnetite may exhibit this texture, overgrowing and entrapping pyrite, sphalerite and chalcopyrite (Fig. 26B and C).

#### 8.2.4 CHANGES IN FABRIC DUE TO DEFORMATION

The term deformation is normally used to encompass folding, faulting and other mechanically induced features produced by tectonic forces. Deformation is most pronounced when the stress is applied either at rapid rates or at relatively low temperatures such that the body of rock experiences high strain rates or lacks plasticity, respectively. Deformation tends to reduce the grain size of the constituent minerals, and thus competes with the effect of increased grain size produced by recrystallization. At Trout Lake the textural evidence suggests that deformation accompanied, and also outlasted, the main recrystallization event. This is in general agreement with the known coincidence of the thermal peak with the D2 deformational event, which preceded a third deformational event (D3) at lower temperatures (Price 1977). Therefore, many of the textures developed during the metamorphic peak have been modified by the final deformational event.

The most subtle effects of deformation involve the development of lattice defects, which are occasionally the sole evidence of deformation in moderately deformed ore minerals. Pyrite commonly

displays pronounced anisotropy in deformed samples, suggesting that the anisotropy is due to lattice defects e.g., dislocations. Ramdohr (1980) points out that gliding and twin gliding are not observed in pyrite. Pyrite deforms in a brittle manner, with dislocations and particularly the development of deformation cleavage, whereas lattice bending is improbable. The dendritic replacement of pyrite by galena, sphalerite, chalcopyrite and/or pyrrhotite, which is common in samples exhibiting distinct deformational textures, exhibits distinct crystallographic control by the host pyrite (Figs. 11D, 18H, and 25B and C). Commonly the pyrite does not display deformational cleavage, and thus the dendritic pattern is interpreted as being due to minute lattice dislocations.

Sphalerite commonly displays deformational twinning consisting of straight to curved repeated lamellar twinning of relatively uniform thickness (Fig. 8C). The intensity of twinning seems to vary with the orientation of the grains and the character of the surrounding minerals e.g., galena and chalcopyrite may accommodate and absorb the stress by readily deforming, resulting in less deformed sphalerite.

The brittle idioblastic minerals pyrite, arsenopyrite and magnetite, if subjected to stress above that which merely produces lattice defects, will deform cataclastically with the development of cleavage, granulation, fractures and/or brecciation. Commonly these minerals exhibit granulated margins, where the grain edges are shattered and the dislodged fragments 'float' in the surrounding matrix. Deformation cleavage parallel to (100) in pyrite is common, and becomes highlighted when matrix sulfides, particularly chalcopyrite, cement or replace the

pyrite along the cleavage planes (Fig. 11B). Similarly, irregular fractures are produced by deformation and also become infilled by matrix minerals or by the products of the attrition (Figs. 11A, 20F and 25G). Less commonly 'Blow Apart' texture is well developed, with the drawing apart of the fragments of cataclastic pyrite and the injection or infilling of matrix sulfides, which cement the fragments without replacing them (Fig. 20F). The matrix minerals have behaved plastically, 'flowing' between the fragments of the brecciated brittle sulfide mineral. This texture has been interpreted to mean that the matrix sulfides are younger, although clearly these existed prior to deformation, and merely flowed over minute distances. Even when accompanied by corrosion or minor replacement of the pyrite porphyroclast Vokes (1969) refers to these textures as pseudo-epigenetic. The effects of deformation on the matrix sulfides, which have relatively rapid equilibration rates, are partly obliterated by the subsequent recrystallization and tendency to develop a granuloblastic fabric during the period of falling, yet still elevated temperature that endure after the cessation of deformation.

Elongation and the development of a foliation within the sulfide mass is observed at Trout Lake. Such directed textures are produced by deformation accompanying recrystallization. Numerous ore samples contained coarse-grained elongate pyrite and/or oval rather than equidimensional matrix sphalerite grains exhibiting a preferred orientation parallel to that in the adjacent schist bands i.e., schistosity (Figs. 8A and 20B). Similarly, recrystallized masses of pyrite may exhibit polygonal, yet elongate grains displaying a preferred

orientation, rather than ideally equidimensional grains in a foam texture. This texture is due to growth under conditions of directed stress, and thus a deformational or dynamic component during crystallization. Galena commonly forms on the sphalerite-sphalerite and sphalerite-gangue contacts that are parallel to this foliation, and thus accentuate it (Fig. 23H).

Silicates also define a foliation by (1) the distribution and banding of the wallrock laminae and the orientation of the constituent gangue minerals, and by (2) the preferred orientation of individual gangue grains, particularly chlorite and biotite, that are disseminated within the sulfide matrix (Figs. 8A and 23HH). The banding observed in the Chalcopyrite Stringer ores (Fig. 16E), consisting of alternating chalcopyrite-rich and gangue-rich (e.g., chlorite) laminae is in apparent conflict with the mode of origin of these 'stockwork' ores. However, the stratabound attitude of these ores is interpreted to have resulted from intense compression and probable shearing in this highly chloritized plastic zone. During this event the chalcopyrite probably underwent pressure solution and segregation into distinct layers, thus developing a pseudo-primary banding which constitutes a metamorphic foliation. All these textures are produced by crystallization under a directed stress that is characteristic of compaction and regional metamorphism, resulting in oriented textures rather than purely cataclastic textures.

In ores that have undergone intense deformation the cataclasis affects both the sulfides and gangue minerals to produce thoroughly tectonized ores. This penetrative deformation which is dominated by

internal rotational movements is termed 'Durchbewegung' (literally "move through") (Vokes 1969, Craig & Vaughan 1981). In such ores, lithologic and mineral banding of possible primary origin, is totally disaggregated with a general sequence recognized for the deformation of gangue laminae. These schist laminae become (1) fractured and dislocated, then (2) completely disoriented as rafts floating in a sulfide matrix, then (3) folded and recrystallized detached cores of schist in the sulfide matrix (Fig. 16F), and finally (4) become rotated, rounded and milled to produce 'balls' or augens of gangue (Fig. 20B and C). All these stages are found at Trout Lake. Gangue that was originally disseminated through the sulfide matrix develops a pronounced schistosity, commonly flowing around pyrite porphyroblasts or other competent augen-shaped features in a lepidoblastic texture. The matrix sulfides invade and infill fractures in the augens of gangue, as well as fractures and dilated cleavages in the individual grains of chlorite and biotite. Similarly, pyrite is commonly milled to form pyrite balls or 'pebbles' in a fine-grained tectonized sulfide matrix (Fig. 20G). Under conditions of intense deformation the pyrite breaks down, partially or completely to form pyrrhotite.

In several highly deformed samples swirls of extremely thin ( $\leq 3\mu\text{m}$ ) plates of an unidentified micaceous mineral, possibly chlorite, having almost a filamentous form in the 2 dimensions of the plane of the section are observed around competent augens of gangue and porphyroblasts of pyrite or magnetite (Fig. 26C). These swirls form in the vortices of stress lines within regions adjacent to the terminations of augens during the rotational movements which deformed the host

sulfides. The swirls are thus unfractured, unlike many of those gangue minerals e.g., biotite that are interpreted to have formed earlier at the metamorphic peak.

Deformational textures are observed in most of the ore samples examined, but tend to be concentrated, or are more pronounced along linear features interpreted to be shear zones. However, in several samples the deformation is indeed penetrative, and affects the entire body of the sample.

Whereas pyrite, arsenopyrite, magnetite and many of the gangue minerals deform brittly, sphalerite, chalcopyrite, pyrrhotite and galena deform plastically as suggested by the manner in which they infill fractures in the former more competent minerals. These 'softer' matrix minerals develop a fine-grained myrmekitic texture (Fig. 20A) due to diablastic growth i.e., collection crystallization during and after shearing (Ramdohr 1980). The development of this diablastic texture is characterized by a trend with increasing deformation from straight or curved to carious to myrmekitic interpenetrative contacts between these 'softer' minerals. This texture is variably developed and accompanies many of the other deformational textures in virtually all of the 9 ore types, and in ores from each of the 6 proven ore lenses. In highly deformed Chalcopyrite Stringer ores pyrrhotite and rarely minor sphalerite form carious blebs in, and myrmekitic intergrowths with, chalcopyrite. In highly deformed Layered Pyrite + Sphalerite ores that contain abundant galena, the latter forms blebs in, and subordinate myrmekitic intergrowths with, sphalerite.

The most intense development of *Durchbewegung* texture is observed in sample TLN.2-12, a Sheared Chalcopyrite + Sphalerite ore (See Fig. 20A, C and D). No pyrite is observed, and is interpreted to have been completely granulated and replaced by pyrrhotite. The gangue consists of milled, rounded and fractured augens around which the matrix of chalcopyrite, sphalerite and pyrrhotite flow in a mylonitic texture (Fig. 20C). This matrix consists of fine-grained diablastic-textured chalcopyrite, sphalerite and pyrrhotite, which are admixed to form mutual intergrowths of one another to varying degrees depending on their proportions in a given layer (Figs. 8F and 20E). The layering produced by shearing and plastic flow sweeps across the plane of the section, resembling flow lines. At the termination of the augens coarse-grained matrix sulfides forming in the 'pressure shadows' contrast with the bulk of the fine-grained matrix (Fig. 20D).

The Sheared Chalcopyrite + Sphalerite ore type was defined where the bulk of the constituent chalcopyrite and sphalerite exhibit diablastic texture. The definition of such an ore type, based on a specific textural criteria, is warranted in that it is the fine-grained, intricate intergrowth of the two principal valuable minerals, chalcopyrite and sphalerite. All but one of the samples assigned to this ore type were taken from the Lens 2 of the north zone. This lens is somewhat unique in that (1) it is the largest and richest lens; (2) it lacks a well defined metal zonation i.e., it is disrupted; and (3) it is characterized by the intrusion of a 5 to 25m thick quartz-diorite sill that is discontinuously interlaced with the lens down dip, at least to the 425m level (See Fig. 20E). It is interpreted that the quartz-

diorite was intruded along this highly chloritized, sulfide-rich horizon as a syn-tectonic sill. The sill and the associated deformation are clearly not pre-metamorphic, as recrystallization at the metamorphic peak would have obliterated the diablastic texture (and its association with the intrusion), producing instead a typical mosaic textured sulfide matrix. Similarly, the preserved cataclastic textured pyrite and the diablastic textured matrix sulfides, observed in all the ore lenses, indicate that deformation outlasted (or recurred after) the thermal peak, and the associated major sulfide recrystallization or metablastic event. However, temperature were still somewhat elevated at the time of deformation allowing moderate recrystallization i.e., collection crystallization of the 'smeared' sulfides.

#### 8.2.5 SULFIDE MOBILIZATION

As discussed earlier, the plastic flow of matrix sulfides infilling fractures in pyrite porphyroclasts, gangue, etc., has been observed repeatedly at Trout Lake. This texture may be referred to as mobilization, as might the plastic flow that thickens up sulfides in the nose of folds. However, sulfide movement of this type, although observed at Trout Lake, does not occur over distances greater than probably several centimeters. The preservation of the primary ore depositional Cu/(Cu+Zn) zonation suggests that in general large scale redistribution of elements and thus minerals has not occurred at Trout Lake. The disruption of the Cu/(Cu+Zn) zonation in Lens 2 of the north zone was probably produced by shearing, plastic flow, overfolding and minor faulting, and constitutes redistribution of the metals over relatively short distances, and essentially in the solid state.

However, the Vein Quartz + Chalcopyrite ore type does constitute a mobilization and redistribution of elements over large distances i.e., several tens of meters. These veins consist principally of quartz, carbonate and chalcopyrite with lesser pyrrhotite, sphalerite, pyrite and galena. The veins are interpreted to be a hydrothermally remobilized fraction of metamorphic origin. Quartz is readily 'sweated out' during the metamorphism, and together with sulfides which were selectively dissolved, and migrated over large distances in the pore fluids. Recrystallization occurred as coarse-grained veins that cross-cut the foliation in both the ore lenses and the surrounding wallrock. The sulfide fraction of the veins is relatively enriched Cu, and possibly Au, while other commonly fugitive metals such as Pb, As and Sb do not appear to have been selectively concentrated in these veins.

#### **8.2.5.1 Au-Ag-Hg Alloy and the Transport of Gold, Silver and Mercury**

In order to explain the distribution of Au in volcanogenic massive sulfide deposits, Huston & Large (1989) proposed a model for the transport and deposition of Au, which is consistent with the models for the evolution of the hydrothermal system of Eldridge et al. (1983) and Pisutha-Arnond & Ohmoto (1983). According to this model Au is transported as chloro- and thio-complexes, the dominance of which varies temporally and spatially within the hydrothermal cycle. The association of Au with Zn-Pb-Ag in the upper and outer parts of Zn-rich lenses is attributed to the transport of Au as the bisulfide complex  $Au(HS)_2^-$ , whereas the association of Au with Cu in the stringers and bases of Cu-rich lenses is attributed to transport as the chloride complex  $AuCl_2^-$ . At

Trout Lake, the predominant association of Au with the Cu-rich, footwall, massive sulfide and stringers ores suggests that Au transport as chloride complexes in relatively hot ( $>300^{\circ}\text{C}$ ) fluids dominated, whereas transport as bisulfide complexes in cooler ( $<300^{\circ}\text{C}$ ) fluids passing to the marginal and upper Zn-rich parts of the lenses was subordinate. The distribution of Au at Trout Lake largely reflects this pre-metamorphic hydrothermal history, though significant local migration of the Au during metamorphism, a process suggested by Romberger (1986), is clearly indicated.

Huston & Large (1989) postulated that Au transported as chloride complexes is precipitated by decreasing temperature or increasing pH, and therefore is not intimately associated with sulfide minerals, but occurs as coarse free grains. Romberger (1986) and Huston & Large (1989) argued that precipitation of Au from bisulfide complexes is most efficient by decreasing total reduced sulfur ( $\Sigma\text{S}$ ), either by oxidation or co-precipitation with sulfides such as pyrite. The latter process would produce significant submicroscopic or 'invisible' Au in pyrite. Therefore, this model is consistent with the occurrence of Au at Trout Lake; the probable deportment of Au in the pre-metamorphic deposit, when subjected to recrystallization and local migration during metamorphism, is apt to generate Type 1 Au-Ag-Hg alloy dominantly in the hangingwall ores, and Type 2 in the stringer ores.

Fluid conditions (e.g., salinity, pH,  $f_{\text{O}_2}$  and  $f_{\text{S}_2}$ ) during regional metamorphism of volcanogenic massive sulfide deposits differ significantly from those of the fluids which precipitate the sulfides on or immediately below the seafloor. Textures and mineral assemblages

observed at Trout Lake indicate that conditions during peak and retrograde metamorphism are consistent with pore fluids of moderate to low temperature ( $\leq 400^\circ\text{C}$ ) and oxidation state ( $\log f_{\text{O}_2}$  of -35 to -45), near neutral pH and low salinity. Under these conditions, bisulfide complexes (e.g.,  $\text{Au}(\text{HS})_2^-$ ,  $\text{Ag}(\text{HS})_2^-$ ,  $\text{Hg}(\text{HS})_2^{2-}$ ) are the dominant carriers of Au, Ag and Hg in aqueous solution (Seward 1984, Cathles 1986, Romberger 1986, Shikazono & Shimizu 1987, Sugaki et al. 1987, Wells & Ghiorso 1988). The most efficient mechanisms for deposition from these solutions are a decrease in  $\Sigma\text{S}$  for Au (Seward 1984, Romberger 1986), changes in pH or a decrease in  $\Sigma\text{S}$  for Ag (Sugaki et al. 1987), and boiling and a decrease in  $\Sigma\text{S}$  for Hg (Wells & Ghiorso 1988). Boiling, precipitation of sulfides, dilution and oxidation are effective processes for decreasing  $\Sigma\text{S}$  in the fluid (Seward 1984). Textures such as the alteration of pyrrhotite to pyrite-magnetite symplectite (See Figs. 13G, 16C, and 26E and F) and 'birds-eye' textured pyrite-marcasite (See Fig. 16HH) indicate slightly increasing oxidation states during retrograde metamorphism, whereas the presence of calcite, adularia and argillic alteration (associated with Type 2 alloy) indicate neutral to alkaline pH (Romberger 1986).

The most likely causes of Au, Ag and Hg precipitation from metamorphic pore fluids at Trout Lake are: (1) decrease in  $\Sigma\text{S}$  of the fluid due to continued crystallization of sulfides, and increase in  $f_{\text{O}_2}$ ; (2) decrease in temperature during retrograde metamorphism; (3) adsorption and reduction of Au, Hg (Bancroft & Jean 1982, Jean & Bancroft 1985, 1986) and possibly Ag onto pyrite grains or sheet silicates. Although, the solubility of the Au bisulfide complexes

decreases with increasing temperature, changes in other temperature-dependent variables (e.g.,  $f_{O_2}$  and  $ZS$ ) result in increasing 'geologic' solubility of Au with temperature to 300°C, above which the solubility falls off sharply (Cathles 1986). In addition, the solubility of Ag bisulfide complexes is less sensitive to decreasing temperature than that of Au and Hg (Cathles 1986, Barnes et al. 1967, Sugaki et al. 1987). Thus, the adsorption of Au and Hg by pyrite, the more rapid decrease in the solubilities of Au and Hg bisulfide complexes with falling temperature and slightly increasing oxidation state, and the generally wider range in fluid conditions under which Ag bisulfide complexes are soluble (Hannington & Scott 1986), may tend to generate higher Ag/Au and Ag/Hg activity ratios in evolving pore fluids during retrograde metamorphism. Furthermore, we interpret that 97% of the Hg in the ore is structurally bound in pyrite (66%) and sphalerite (31%), both of which are relatively refractory sulfides. The difference in the covalent radii of Hg (1.49 Å), Au and Ag (1.34 Å), as compared to that of Fe (1.17 Å), may preferentially retard the diffusion of Hg in pyrite. As Au and Ag are released from pyrite by solid state diffusion (Boyle 1979), the availability of Hg in the pore fluids is thus constrained.

Hannington & Scott (1986) note that Ag is transported under similar fluid conditions to those of Au, but the solubility of Ag occurs over a wider range of temperature, pH and salinity. This difference in solubility may generate a broader distribution and less specific host mineralogy for Ag in the pre-metamorphic deposit. Nonetheless; co-precipitation is probably a major depositional process for Ag transported as bisulfide complexes, thereby leading to high

concentrations of Ag in the principal sulfides pyrite, chalcopyrite and sphalerite. The subsequent metamorphic recrystallization of the principal sulfides would then play an important role in the availability of Ag in the pore fluids, though Healy & Petruk (1989) have inferred that these sulfides have retained high concentrations of Ag. However, as the number of inferred and known Ag-bearing minerals at Trout Lake is large (12), the determination of the pre- and peak-metamorphic sites of Ag is highly speculative.

The general trend of increasing Hg with Ag shown in Fig. 31 is not reflected in the composition of alloys crystallizing in successively later generations. Element concentration profiles across masses of Type 2 alloy consistently show the sympathetic variation of Au and Hg concentrations (Fig. 32). This relationship is observed in masses of alloy that are predominantly of the earliest (Fig. 32A) and final (Fig. 32B) compositions. The general trend of the compositional field merely reflects the increasing solubility of Hg in the Ag end-member, rather than a sequence towards later Ag- and Hg-rich compositions (Fig. 40A). Thus, the element profiles across masses containing paragenetically distinguishable features show that the sequence in compositional variation is consistent with increasing Ag/Au and Ag/Hg activity ratios, leading to precipitation of progressively Ag-rich later compositions (Fig. 40B).

The specific association of Au with pyrite in numerous types of deposits (Wells & Mullens 1973, Boyle 1979, Springer 1983, Romberger 1986) suggests that Au is precipitated either by co-precipitation from bisulfide complexes (Romberger 1986, Huston & Large 1989), or by surface

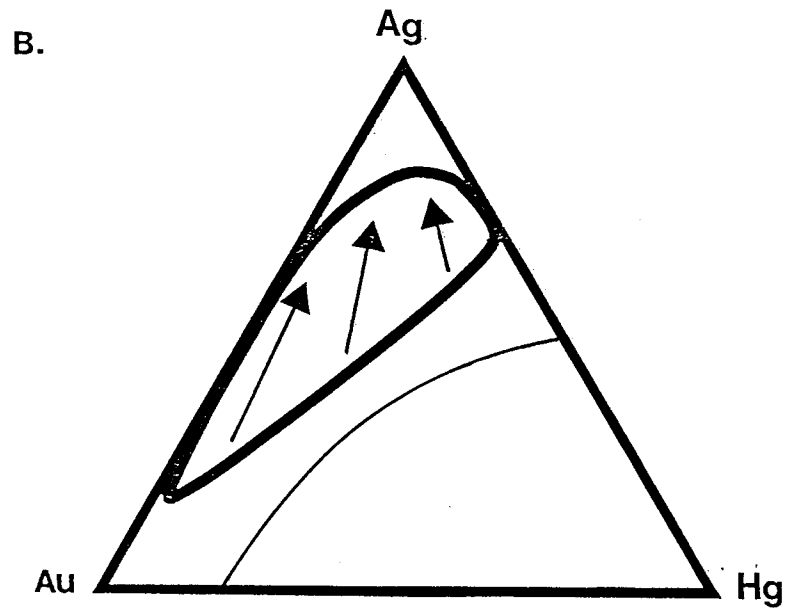
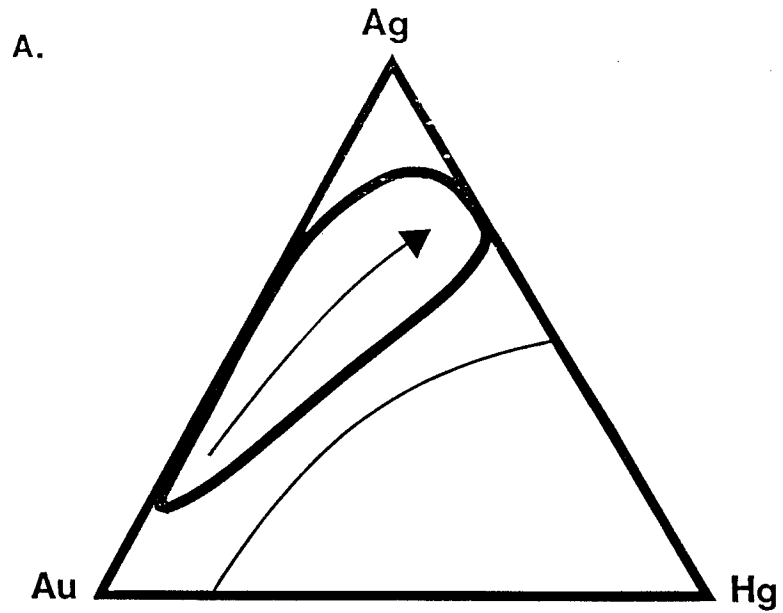


Figure 40: Possible Pathways of Compositional Evolution of Paragenetically Latest Au-Ag-Hg Alloy. The  $\alpha$ -phase field, and the field of Trout Lake Au-Ag-Hg alloy compositions (in wt%) are shown on a schematic triangular diagram of the Au-Ag-Hg ternary system. Two possible trends in composition of alloys crystallizing in paragenetic sequence: (A) later compositions are Ag- and Hg-rich, paralleling the general trend of the field; and (B) later compositions are progressively Ag-rich and Au- and Hg-poor.

adsorption and reduction onto pyrite grains (Bancroft & Jean 1982, Jean & Bancroft 1985), rather than by decreased solubility related to falling temperatures of the fluids. Both these processes explain the high local concentrations of Au with pyrite, and also obviate the need for hydrothermal solutions saturated with Au (Seward 1984, Jean & Bancroft 1985, Romberger 1986). The localized concentration of Au in extremely specific textural types at Trout Lake suggests preferential precipitation of Au at these sites. These sites are areas of potential Au adsorption and reduction by pyrite or sheet silicates, or areas of low stress and strain favoring the precipitation of dissolved components in the metamorphic pore-fluids. In the case of Type 1 Au-Ag-Hg alloys, the dilated fractures and grain boundaries of pyrite porphyroclasts may behave as 'pressure shadows'. Diffusion of Au, Ag and Hg to these sites through pyrite grains as suggested by Boyle (1979), may assist nucleation of the Au-Ag-Hg alloy.

The distribution and localized abundance of Type 2 Au-Ag-Hg alloy are clearly inconsistent with the process suggested by Boyle (1979). It is improbable that these localized concentrations of Au-Ag-Hg alloy were concentrated by solid-state diffusion from pyrite (i.e., 0.2 area% Au-Ag-Hg alloy and 5.25 area% pyrite in TLN.1-89a) or any of the surrounding sulfides, or by plastic flow. Wilson & Rucklidge (1987) and Springer (1985) emphasized the importance of hydrothermal conduits as structural factors controlling the deposition of Au in Archean gold deposits. The contact along which Type 2 Au-Ag-Hg alloy is preferentially concentrated must have acted principally as a locus for high fluid-flow, along which Au-, Ag- and Hg-bearing solutions migrated.

Low stress and strain associated with a dilational contact within the fold nose may have generated chemical potential gradients favoring the precipitation of Au from the fluid phase. Importantly, the noncrystalloblastic nature of these alloys, combined with the idiomorphic character of the weak oscillatory zoning in Figure 33C, strongly suggest open-space growth.

The compositions of Type 2 Au-Ag-Hg alloy (Fig. 31) span virtually the entire composition field of Trout Lake alloy. This suggests that Types 1 and 2 formed by a combination of solid-state diffusion to the margins of pyrite grains (Boyle 1979), coupled with dissolution, local migration and precipitation at preferred sites from late metamorphic pore fluids enriched in Au, Ag and Hg. However, much of Type 2 Au-Ag-Hg alloy probably formed exclusively by hydrothermal remobilization of coarse free 'gold' in the Cu-rich footwall ores. The lack of compositional distinction between Types 1 and 2 Au-Ag-Hg alloy requires at least that Type 1 equilibrated with the pore fluids, even if migration was minimal. However, Type 1 Au-Ag-Hg alloy that occurs as fine-grained inclusions in pyrite, and that could not be quantitatively distinguished on the basis of composition, may have formed solely by solid state diffusion (Boyle 1979). Sample TLN.2-8, which contains 103 grains of Type 1A Au-Ag-Hg alloy (Fig. 27E-H), was taken from adjacent to a syntectonic quartz-diorite sill. The abundance of alloy in this sample seems most readily explained by locally-induced remobilization of the ores and widespread breakdown and replacement of pyrite near the sill (Healy & Petruk 1988), than by the solid state diffusion process. Similarly inconsistent with the latter process is the localized

abundance of Type 1B Au-Ag-Hg alloy in TLS.3-40 (Fig. 28A to C). For the solid state diffusion process of Boyle (1979), we calculate that this cluster requires that Au diffused from up to 1 cm away in massive pyrite. Such an extended diffusion path for Au across numerous pyrite grains is in sharp contrast to the inhomogeneity (over distances of microns) of the Au-Ag-Hg alloy grains, which suggests sluggish solid-state diffusion of Au, Ag and Hg even within the metallic framework of the alloy itself. However, the latter was formed at temperatures below the metamorphic peak, subsequent to pyrite metablastesis.

The distinctive association of Type 1B Au-Ag-Hg alloy with freibergite, galena, sphalerite and minor arsenopyrite is similar to that of Au associated with sphalerite, galena and Ag-bearing sulfosalt assemblages in the Southern Explorer Ridge (Hannington & Scott 1988). Huston & Large (1989) have also identified the association of Au with Zn-Pb-Ag in massive sulfide and other deposit types. These studies attribute this association to precipitation of Au from bisulfide complexes in low temperature (<300°C) fluids. In addition, Seward (1984) and Romberger (1986) speculated on the possible role of thioarsenide (and thioantimonide) complexes in the transport of Au in hydrothermal solutions. Transport and deposition from fluids containing these complexes are likely to generate assemblages similar to Type 1B. However, it is also probable that as the crystallization of Au-Ag-Hg alloy is considered retrograde, the alloy would be preferentially associated with other late stage lower temperature phases crystallizing in available fluid conduits within Zn-Pb-Ag-rich ores.

The oscillatory zoning in Figure 20C probably represents preserved growth zoning produced by equilibration of the evolved fluid composition in the matrix with the edge of the growing grain. This equilibration would have occurred below the peak metamorphic temperature and activity of Au. This texture is not preserved in other sections, suggesting homogenization by intracrystalline volume-diffusion (Schmalzried 1974). Oberthur & Saager (1986) suggested that volume-diffusion caused the pervasive homogenization of the Au-Ag-Hg alloy of the Witwaterstrand placer gold deposits during lower-greenschist-facies metamorphism. However, unlike the placer 'gold' grains in the Witwaterstrand deposits, the Au-Ag-Hg alloy grains at Trout Lake would not have been available during the extensive period of prograde metamorphism.

The zoning illustrated in Figures 28I, and 33A to F, suggests diffusion zoning (Loomis 1983), where the grains of intermediate composition have Ag-rich compositions imposed on them by diffusion from grain surfaces that are in contact and equilibrating with the interstitial fluid. The episodic character of the late Ag-rich compositions may reflect changes in the activity of  $\text{Ag}(\text{HS})_2^-$  related to the crystallization of low temperature Ag-bearing sulfides and sulfosalts. As these phases crystallize, competing equilibrium reactions such as (1)  $\text{Au}(\text{HS})_2^- + \text{Ag}^0 = \text{Ag}(\text{HS})_2^- + \text{Au}^0$ ; (2)  $\text{Ag}(\text{HS})_2^- + \frac{1}{2}\text{H}_2 = \text{Ag}^0 + \text{H}_2\text{S} + \text{HS}^-$ ; (3)  $\text{Ag}(\text{HS})_2^- = \frac{1}{2}\text{Ag}_2\text{S} + \frac{1}{2}\text{H}_2\text{S} + \text{HS}^-$  may have generated stepwise changes, and possibly minor reversals in the general trend of increasing activity of  $\text{Ag}^0$  in the alloy.

The configuration of the diffusion zoning is largely controlled by grain boundaries in Figure 33A and C, and by regions of dislocations

bounding fractures in Figure 33D, E and F. In these regions of the grains, diffusion mechanisms that are structure-sensitive, and which generally have lower activation energies, predominate over simple volume-diffusion at lower temperatures (Schmalzried 1974). Thus volume diffusion, which is kinetically favored and prevails at higher temperatures, tends to erase all evidence of growth zoning. At lower temperatures of metamorphism, and with increased Ag/Au and Ag/Hg activity ratios in the evolved pore fluids, the diffusion zoning is controlled by mechanisms that are structure-defect-dependent, such as surface and dislocation diffusion. Prior to reaching the temperature at which diffusion is effectively stopped, the kinetics of the diffusion mechanisms seem to have progressively impeded the attainment of equilibrium with falling temperature.

## Chapter IX

### CONCLUSIONS

The sulfides pyrite, chalcopyrite, sphalerite, pyrrhotite, marcasite, galena, arsenopyrite, cubanite and acanthite; the oxides magnetite and cassiterite; the Sb-sulfosalts freibergite, pyrargyrite, freieslebenite, boulangerite and bournonite; the sulfantimonides gudmundite and costibite; the alloys and intermetallic compounds Au-Ag-Hg alloy and dyscrasite; the tellurides hessite, rucklidgeite, pilsenite and volynskite; and the selenides clausthalite and naumannite have all been identified in the ores from Trout Lake, in that general order of abundance. The ores are dominated by the textural and spatial distribution of the first three most abundant sulfides, pyrite, chalcopyrite and sphalerite. The differentiation of the ores in terms of Cu and Zn, results in a differentiation series characterized by near end-member mono-mineralic sulfide components of chalcopyrite in the footwall Chalcopyrite Stringer ores, and sphalerite in the hangingwall Massive Sphalerite ores.

The differentiation of Cu and Zn gives a distribution of  $Cu/(Cu+Zn)$  ratios that is characteristic of many volcanogenic massive sulfides (Franklin et al. 1981). Large (1977) and Franklin et al. (1981) attribute this metal zonation to the physiochemical trend encountered by the ore-forming fluids as they emanate upwards and outwards from the point of sea-floor discharge. However, Eldridge et al. (1983) attribute

the zonation to the upward and outward migration of Cu-rich sulfide facies replacing Zn-rich facies in response to chemical and thermal evolution in time of the emanating hydrothermal fluids. Nonetheless, proximal deposits which overlie the emanative center, have well defined stringer zones and prominent vertical compositional gradations of decreasing Cu/(Cu+Zn) ratios, as in Trout Lake. The metal distributions are thus primary and indicate minimal remobilization during middle greenschist facies metamorphism. Limited sulfide remobilization is observed in the form of fluid state remobilization and subsequent deposition as quartz- and chalcopyrite-rich hydrothermal veins of metamorphic origin. Fluid state remobilization is also proposed as the principal mechanism by which Au-Ag-Hg alloy attained its present distribution, possibly in all observed occurrences, but certainly in the highly sheared Chalcopyrite Stringers of TLN.1-89.

Deformational textures are numerous and widespread in the Trout Lake ores. The most conspicuous evidence of deformation on the megascopic scale is the conformable or stratabound attitude assumed by the stockwork ore zones, due to compression and/or shearing in this highly chloritized 'plastic' zone. Open to tightly closed and isoclinal folding are common on the meso- and microscopic scale. The foliated ores commonly consist of lepidoblastic to augen-textured gangue and the enveloping, foliated and less commonly gneissic-textured sulfides. The commonest deformational texture observed in the ores is the cataclastic deformation of pyrite porphyroblasts. Depending on the intensity of the deformation and the nature of the surrounding sulfides, the pyrite texture varies from disaggregated annealed polygonal masses, granulated,

rounded, fractured, deformation cleavage developed, 'blow-apart' textured, schistose pyrite with rare crenulation cleavage developed, and mobilization of pyrite into the cleavages of gangue minerals and veinlets. Such deformation facilitates the cementation and/or replacement of pyrite by sphalerite, chalcopyrite, pyrrhotite, marcasite and galena. Under conditions of intense deformation, the pyrite completely breaks down to form pyrrhotite.

The most significant deformational texture observed in the ores is the development of a myrmekitic texture due to diablastic growth i.e., collection crystallization during and after shearing (Ramdohr 1980). This diablastic texture is characterized by a trend with increasing deformation from straight or curved to carious to myrmekitic interpenetrative contacts between the soft 'matrix sulfides' chalcopyrite, sphalerite, pyrrhotite and/or galena. Most of the ore types exhibit a trend towards this texture, at least locally along shear zones or 'schlieren'. In ores where the bulk of the chalcopyrite and sphalerite exhibit this texture they were assigned to the Sheared Chalcopyrite + Sphalerite ore type.

The diablastic texture is also characterized by reduced grain size distributions relative to the unsheared equivalent, and also reduced optimum grinds i.e., sphalerite 37um, chalcopyrite 18.5um. However, of greater significance is the interpenetrative contacts of the two main minerals of interest chalcopyrite and sphalerite. Petruk's liberation model (Petruk 1976, 1986, 1989b) is partly based on the empirical observation that approximately one third of the unliberated grains will be recovered in the desired concentrate. For most ore types the dominant

contaminant phase in these composite particles are likely to include pyrite, gangue and pyrrhotite, whereas when processing the Sheared Chalcopyrite + Sphalerite ores the predominant contaminant phase is likely to be sphalerite in the Cu-concentrate, where chalcopyrite floatation is first, and chalcopyrite in the Zn-concentrate, where sphalerite is subsequently floated. Consequently, high Zn values may be obtained in the Cu-concentrate, and reduce the availability and resulting recovery of sphalerite in the Zn-concentrate.

All but one of the samples recognized as comprising the Sheared Chalcopyrite + Sphalerite ore type were taken from the lens 2 of the north zone. Nine of the 21 samples from this lens were assigned to this ore type. Lens 2 of the north zone is characterized by disruption of the generalized metal zonation, and also by the intrusion of a 5 to 25m thick quartz-diorite sill that is discontinuously interlaced with the lens down dip, at least to the 425m level. A high grade intersection of the lens at the 425m level confirmed the continuation of the direct relationship between the quartz-diorite and the predominance of the Sheared Chalcopyrite + Sphalerite ore type. This suggests that the quartz-diorite was intruded along this highly chloritized and sulfide-rich horizon as a syn-tectonic sill. The sill is clearly not pre-metamorphic as it is interpreted to cause the deformation and distinctive rounding of the pyrite porphyroblasts, and thus postdates the metamorphic recrystallization of pyrite. In addition, the metamorphic recrystallization of the sulfides would have obliterated the diablastic texture, and its direct association with the intrusion. The quartz-diorite exhibits a schistosity, suggesting that its intrusion was contemporaneous with the metamorphic peak of  $D_2$ , or predates  $D_3$ .

Lens 2 of the north zone is the richest of the 6 proven ore lenses, containing 2,213,000 tons (combined production and reserves) averaging 2.367ppm Au, 17.49ppm Ag, 2.69% Cu and 7.4% Zn (Ko, 1986). This constitutes 35% of the total proven ore tonnage, but also constitutes 48% of the Au, 39% of the Ag, 41% of the Cu and 47% of the Zn (See Table 2). The lens is still open at depth. However, during Part 2 of the Trout Lake project Healy & Petruk (1989) determined that a maximum of approximately 5% of the Zn being recovered in the Cu-concentrate is due to chalcopyrite-sphalerite composite particles. Nonetheless, the texture poses a significant Cu-Zn separation problem during processing of feeds rich, or consisting solely of, Sheared Chalcopyrite + Sphalerite ore.

Another relatively lens-specific texture, although not as exclusively, is the prevalence of fine-grained dendritic sphalerite, galena and freibergite in pyrite porphyroclasts from Massive Pyrite and Layered Pyrite + Sphalerite ores of Lens 5 of the south zone. When ores from stope 2451 of Lens 5 (210 and 215m level) were previously processed, high Zn- and Ag-losses were recorded in the tailings (N. McEachern, pers. comm., 1985). Fine-grained inclusions in pyrite are not liberated until the pyrite is broken to the same size as the mineral inclusions (Petruk 1986). Thus, significant amounts of dendritic inclusions of sphalerite, freibergite and galena in pyrite are probably unliberated, with resultant poor recovery of Zn, Pb and Ag. Because of the limited sampling of Lens 5, inadequate spatial coverage exists to permit predicting losses of this type during processing of ores from the entire lens. However, the low Cu content of this lens (0.29% Cu; See Table 2), and its enrichment in Zn-Group elements (specifically Zn, Ag and Pb) suggests that this texture may persist throughout the lens.

The Au-Ag-Hg alloy, the principal Au-bearing mineral at Trout Lake, is analogous to the  $\alpha$ -phase of the extrapolated Ag-Au-Hg system of Basu et al. (1981). The observed compositional range, inhomogeneity and zoning of the Au-Ag-Hg alloy confirm the existence of a field of extensive solid solution corresponding to the  $\alpha$ -phase. A general sequence of crystallization involving increased Ag-rich compositions suggests increased Ag/Au and Ag/Hg activity ratios with decreasing temperature of metamorphism, decreasing  $\Sigma S$  and increasing  $f(O_2)$  together with disequilibrium conditions of crystallization. Textural and compositional evidence show that the Au-Ag-Hg alloy crystallized from migrating pore fluids and not simply by exsolution from high temperature pyrite. Approximately 7% of the Au is retained as 'invisible' Au in pyrite and arsenopyrite.

Gold is released from pyrite and exposed to pore fluids following metablastesis and subsequent fall in metamorphic temperatures, either by unmixing, as suggested by Boyle (1979,) or by the total breakdown and replacement of pyrite in sheared ores. Primary coarse free grains of 'gold' would also be susceptible to hydrothermal remobilization in the pore fluids. The Au is transported as bisulfide complexes and precipitated from the pore fluids at preferred sites by surface adsorption and reduction onto pyrite grains or in conduits of high fluid flow and low chemical potential in highly sheared Chlacopyrite Stringer ores. Thus, the crystallization of Au-Ag-Hg alloy can be considered a retrograde metamorphic process. The distribution of Au in Trout Lake probably largely reflects its original distribution due to exhalation and diagenesis, modified during metamorphism by limited solid state diffusion, hydrothermal mobilization, local migration and precipitation.

Copper is carried in chalcopyrite, cubanite, freibergite and bournonite, where the latter three minerals constitute insignificant fractions of the total Cu tonnage. The optimum grind for chalcopyrite is 52 $\mu$ m, and this is finer than the particle size of the grinding curve defined by 80% -74 $\mu$ m. However, chalcopyrite will preferentially concentrate in the finer sieve fractions due to its grindability (Petruk et al. 1985), and thereby tend to approach the optimum grind. The total recovery of Cu is 95.2%, with 91.7% in the Cu-concentrate (Healy & Petruk 1989), and constitutes excellent recovery with minimal latitude for recovery improvement. Te was determined to occur in hessite, rucklidgeite, pilsenite(?), volynskite and in the clausthalite-galena solid solution that was associated with rucklidgeite. The Cu-Te element pair gives the highest correlation coefficient (r-value) of the Cu-Group elements i.e., +0.834, and is interpreted to reflect the paragenetic association of Te-bearing minerals with chalcopyrite, but principally due to the contribution from probable trace Te in solid solution in chalcopyrite. Rucklidgeite and the associated Te-bearing clausthalite-galena occurred as fine-grained inclusions along with chalcopyrite and pyrrhotite in pyrite, and may be expected to be recovered in the tailings and/or the Cu-concentrate. Both hessite and pilsenite(?) occur as fine-grained inclusions in chalcopyrite and are expected to report to the Cu-concentrate. Selenium was identified in the clausthalite-galena solid solution, rucklidgeite, pilsenite(?) and naumannite. The Se-Pb pair gives r-value of -0.720, indicating that the clausthalite-galena solid solution contributes an insignificant component to the total variance in Se and Pb. The positive covariance of Cu and Se (i.e., +0.622) is interpreted to reflect the Se content of chalcopyrite, and

the paragenetic association of chalcopyrite with Se-bearing pyrrhotite and pyrite (Hawley & Nichol 1959), rucklidgeite, pilsenite(?) and naumannite in Cu-rich ores. Thus, it may be predicted that the bulk of the Se will be recovered in the Cu-concentrate, and thereby degrade the quality of the copper anodes (Petruk 1985), or to the tailings as solid solution in pyrrhotite and pyrite. The latter is indicated by the findings of (Healy & Petruk 1989), who found that the bulk of the Se is lost to the tailings.

Zn is carried in sphalerite and freibergite, where the latter is an insignificant contributor to the total Zn tonnage. Cd and possibly Hg are hosted in sphalerite. The strong linear relationship of Zn and Cd demonstrates that sphalerite is the host of Cd. The lack of Zn-Hg covariance suggests that Hg is only partly hosted in sphalerite. Hg is known to occur dominantly in sphalerite from Flin Flon ores (T. Chen, pers. comm., 1986). However, on the basis of material balance calculated mineral quantities and assays in the Trout Lake concentrator circuit (Healy & Petruk 1989), it is interpreted that pyrite is the most significant Hg-carrier (i.e., 66%). The elements Zn and Cd are principally recovered in the Zn-concentrate, but also in the Cu-concentrate, because of the 10 to 15% of the sphalerite in the feed that is recovered in the Cu-concentrate. The path of Hg during flotation is partly defined by the behaviour of sphalerite, but principally by that of Hg-bearing pyrite. The calculated optimum grind for sphalerite of 52 $\mu$ m is probably too high, because of the sampling bias towards, and over-representation of, coarse-grained sphalerite from Zn-rich ores. However, this bias may be cancelled by the tendency for sphalerite to

concentrate in the finer sieve fractions. The grinding curve is defined by 80% -74 $\mu$ m, and thus approaches the optimum grind for sphalerite. However, this optimum grind assumes that 28.5% of the sphalerite (See Fig. 38) is finer than the particle size of the grind, and will therefore be partly unliberated (approximately 15%). The total recovery of Zn is 93.4% with 82.5% in the Zn-concentrate, 11.0% in the Cu-concentrate and 6.57% in the tailings (See Table 2).

Healy & Petruk (1989) determined that 86% of the Zn (and hence sphalerite) recovered in the Cu-concentrate occurs as free grains or grains that are sufficiently liberated to behave as free, and that largely fall in the optimum size range for flotation (i.e., 5-100 $\mu$ m). These grains are expected to be recovered in the Zn-concentrate under nominal flotation conditions. Thus, poor liberation is a minor factor in the high Zn losses to the Cu-concentrate. Losses of sphalerite to the Cu-concentrate as composite particles consisting of chalcopyrite-sphalerite (particularly diablastic-textured grains), and entrainment of sphalerite slimes (<5 $\mu$ m grains) are not significant. However, activation of sphalerite by dissolution of reactive secondary Cu-sulfides (e.g., covellite, chalcocite) and marcasite with the flotation reagents may be significant. A linear traverse grain counting procedure was done on a polished section of the float feed, and determined that the ore contains 0.17 wt% marcasite. Marcasite is relatively unstable and may dissolve in the pulp to produce ferrous ions in solution. These ions together with dixanthogen (oxygenated xanthate) at a Ph range of 9.5 to 11, can produce activation of sphalerite (Leroux et al. 1986). However, the minimum storage capacity at the mine and the fast turnover of the 'dry'

ore (1 to 3 days) minimizes the probability of marcasite oxidizing and subsequently reacting in the pulp. Healy & Petruk (1989) identified several reactive Cu-sulfides (principally covellite) in Trout Lake concentrator products, and interpreted that these are derived from entrained Cu-matte in backfilled slag that is re-introduced into the feed through mine dilution. Preliminary flotation tests at Canmet have shown that it may be possible to overcome the Zn losses to the Cu-concentrate by proper conditioning prior to flotation (W. Petruk, pers. comm., 1989), indicating that Cu-activation of sphalerite by Cu-sulfides is responsible for the high Zn losses.

Au is interpreted to be dominantly carried in Au-Ag-Hg alloy which is the only Au-bearing mineral observed petrographically. The correlation coefficient matrix failed to identify any geochemical association of Au with any element, other than Mn, which probably reflects a distorted correlation coefficient (i.e., non-normally distributed variables) or an unidentified paragenetic association with a Mn-bearing gangue phase. No association of Au with As was apparent, nor was any association of arsenopyrite with Au-Ag-Hg alloy observed petrographically. The lack of covariance between Au and Hg and Ag reflects the minor contribution of the Ag and Hg in Au-Ag-Hg alloy to the total variance in these elements, which occur in concentration levels that are at least one order of magnitude greater than can be explained by their occurrence in Au-Ag-Hg alloy. The Au/Ag ratio of the deposit is 0.11 (i.e., 1.73ppm Au and 15.87ppm Ag; Ko 1986), whereas the Au-Ag-Hg alloy gives an average Au/Ag ratio of 0.82 (i.e., 38.68% Au and 49.22% Ag). Thus, Au-Ag-Hg alloy accounts for a maximum of approximately 15% of the Ag in the ore. SIMS

analyses showed that trace concentrations of Au occur as 'invisible' Au in pyrite (i.e., 0.72ppm Au) and arsenopyrite (i.e., 30.2ppm Au), and account for 6 and 1%, respectively of the Au in the ore. These data, together with cyanidation tests of the tailings, and material balanced quantities of pyrite, arsenopyrite and Au-Ag-Hg alloy, show that 36% of the Au in the tailings occurs as 'invisible' Au in pyrite (27%) and arsenopyrite (9%), whereas approximately 40% occurs as <1.5um grains of Type 1 Au-Ag-Hg alloy, and 25% as >1.5um grains of Type 1 Au-Ag-Hg alloy. Thus, Au-Ag-Hg alloy in the size range amenable to flotation and/or regrinding comprises a minor fraction of the Au lost to the tailings. Type 2 Au-Ag-Hg alloy is relatively coarse-grained (80% -37um) and occurs as anastomosing masses in chalcopyrite. Gasparrini (1984) reports that electrum whose grain size is sufficient to ensure liberation, was almost totally recovered in laboratory experiments using standard flotation techniques. The latter author also notes that the electrum generally reports to the Cu-concentrate because of the similar flotation characteristics and spatial association with chalcopyrite. This supports the present findings indicating that the bulk of Type 2, and the coarser fraction of Type 1 Au-Ag-Hg alloy is recovered to the Cu-concentrate. Furthermore, as Au-Ag-Hg alloy locked with chalcopyrite is expected to be recovered, losses of unliberated Type 2 Au-Ag-Hg alloy, which is associated with chalcopyrite and is the dominant form of Au-Ag-Hg alloy, are expected to be negligible.

Arsenic occurs principally in arsenopyrite, but also in solid solution in freibergite, where it's level of concentration ( $\bar{x}$  = 0.20 wt% As), and the trace abundance of freibergite in the ores,

implies that arsenopyrite can be assumed to be the sole host of As. Thus, the environmentally toxic element As is expected to be largely recovered to the tailings, which is then returned to the mine as backfill. Minor As is expected to report to the Zn-concentrate in the form of sphalerite-arsenopyrite composite particles, derived from the common disseminated, fine-grained, euhedral grains of arsenopyrite in matrix sphalerite from the Massive Sphalerite and the Layered Pyrite + Sphalerite ore types.

Costibite is the only Co-bearing mineral identified, but is interpreted to be a minor Co-carrier, because only one grain was observed and because of the lack of Co-Sb covariance. The principal hosts of Co were not identified, but are inferred to be pyrrhotite and pyrite, and thereby suggests that Co should be largely rejected to the tailings. Healy & Petruk (1989) found that 85.6% of the Co was rejected to the tailings.

Cassiterite is the only Sn-bearing mineral identified, although it is inferred that trace yet significant Sn occurs in solid solution in chalcopyrite. The metallurgically troublesome element Sn occurs at trace concentrations ( $\bar{x} = 36\text{ppm Sn}$ ) in the ores. Sn is interpreted to be largely hosted in cassiterite associated with sphalerite, and a lesser component as cassiterite associated with chalcopyrite, or in solid solution in chalcopyrite. Healy & Petruk (1989) found that 65.5% of the Sn was recovered in the Cu-concentrate.

The metallurgically troublesome element Bi occurred consistently at concentration levels below the detection limit of the chemical analyses

(0.001 wt% or 10ppm Bi). Bi was detected by EMPA in the tellurides rucklidgeite and pilsenite(?), which formed inclusions in pyrite and chalcopyrite, respectively. Bi was also detected in volynskite. Consequently, Bi is expected to be recovered at low levels of concentration in the Cu-concentrate and the tailings. Galena is a potential host phase of trace Bi, but because of unresolved line overlaps, determination by EDA was not possible.

Indium which occurs at trace concentrations in the ores ( $\bar{x}$  = 34ppm In) is interpreted to occur in sphalerite, possibly chalcopyrite and/or the Sb-sulfosalts. Indium exhibits high positive covariance with Ag, Sn, Sb and Pb, and moderate covariance with Zn. The strong In-Ag covariance is interpreted to reflect the coupled substitution for Zn in sphalerite, in which it is interpreted that the bulk of the In is hosted. This suggests that In will report principally to the Zn-concentrate, and to a lesser extent to the Cu-concentrate and the tailings.

Antimony is carried in freibergite, gudmundite, pyrargyrite, boulangerite, freislebenite, dyscrasite, bournonite and costibite, where the first three more abundant Sb-minerals are to assumed to contribute the only significant fractions of the total variance in Sb. Pyrargyrite occurs only as fine-grained inclusions in galena, whereas freibergite and gudmundite generally occur as inclusions in galena, but also as discrete grains intimately associated with galena. Gudmundite and pyrargyrite are generally most abundant in Massive Sphalerite ores. The fine-grained inclusions of Sb-minerals are expected to be largely unliberated such that their behaviour will be defined by the host

galena. In the Layered Pyrite + Sphalerite ores, fine-grained dendritic freibergite and galena in pyrite, and fracture-filling and interstitial freibergite and galena in pyrite. These are expected to be partly unliberated and be rejected to the tailings as composite grains of pyrite with galena, freibergite and/or sphalerite. Gasparrini (1984) reports that Ag-rich tetrahedrite is readily recovered by normal flotation techniques, and indicates that liberated freibergite should report to the Cu-concentrate. However, Gasparrini (1984) also reports that lime has a deleterious effect on the recovery of pyrargyrite, which if free, is therefore expected to be rejected to the tailings. The flotation characteristics of gudmundite are unknown. Healy & Petruk (1989) found that 55.4% of the Sb is rejected to the tailings, with 26.2% and 18.4% being recovered in the Zn- and Cu-concentrates, respectively. The Sb rejected to the tailings probably occurs largely as fine-grained Sb-minerals locked in pyrite.

Silver occurs in freibergite, pyrargyrite, hessite, Au-Ag-Hg alloy, dyscrasite, freieslebenite, naumannite, volynskite, acanthite, galena, and is inferred to occur in chalcopyrite, sphalerite, and pyrite. Acanthite may not constitute an ore mineral, but instead be a product of Ag precipitation during flotation. Minor yet erratic Ag was also detected in the clausthalite-galena solid solution. Although, freibergite, Au-Ag-Hg alloy and subordinate pyrargyrite and hessite constitute the most abundant Ag-minerals (as observed petrographically), the Ag-bearing Sb-minerals and tellurides account for < 24%, and Au-Ag-Hg alloy for < 19% of the Ag in the ore.

On the basis of material-balanced mineral quantities and assays in Trout Lake concentrator products, Healy & Petruk (1989) inferred that chalcopyrite, pyrite, sphalerite and galena contain approximately 45, 11, 55 and 750ppm Ag, accounting for 23, 14, 19 and 3%, respectively of the Ag in the ore. Subsequently, Pinard & Petruk (1989) determined by EMPA that the average Ag content of Trout Lake galena is 660ppm Ag, thereby validating in part these inferences. Furthermore, these inferred Ag concentrations fall within the range of known (determined by SIMS and microPIXE) Ag concentrations in chalcopyrite, pyrite and sphalerite from other Canadian massive sulfide deposits (Cabri et al. 1985, Cabri 1988, McIntyre et al. 1984). Thus, it is estimated that 56% of the Ag in the ore occurs in the three most abundant sulfides chalcopyrite, sphalerite and pyrite, such that the distribution of Ag between concentrator products is largely dependent on the behaviour of these minerals. Consequently, a minimum of 32% of the Ag is expected to be routinely lost from the Cu-concentrate; 12% of the Ag to the tailings in pyrite, and 20% of the Ag to the Zn-concentrate in sphalerite. Furthermore, due to the use of lime during flotation (for Ph control), 7.5% of the Ag is expected to be lost to the tailings in pyrargyrite. Healy & Petruk (1989) found that only 48.5% of the Ag was recovered in the Cu-concentrate, with 21.7 and 29.8% being recovered in the Zn-concentrate and tailings, respectively.

The calculated optimum grind for freibergite is 4.6um (See Table 34) with a weighted average grain size curve defined by 80% -60um. Image analysis of pyrargyrite in sample TLS.5-64 gave a grain size distribution defined by 80% -13um, whilst that of hessite in the Cu-rich

ores was not determined, but is probably of equivalent grain size to pyrargyrite. The fine-grained nature of these Ag-bearing phases dictates that they will be largely unliberated, and that their behaviour will be determined by the flotation characteristics of the host phases. Hessite occurs associated with and hosted in chalcopyrite, and is therefore likely to be readily recovered in the Cu-concentrate. Pyrargyrite occurs as fine-grained inclusions in interstitial galena in Massive Sphalerite and Layered Pyrite + Sphalerite ores. Freibergite in the Massive Sphalerite ores occurs as fine-grained rounded inclusions in galena. Thus, freibergite and pyrargyrite will be largely unliberated, and their behaviour will be determined by the flotation characteristics of the host galena. The freibergite and galena in Massive Pyrite and Layered Pyrite + Sphalerite ores assumes two textural styles, which may degrade recovery. These are (1) fine-grained dendritic freibergite and galena (and sphalerite) in pyrite porphyroclasts, and (2) freibergite and galena (and sphalerite) interstitial to and invading, cementing and/or replacing fractured pyrite. The grain size distributions of freibergite and galena from TLS.5-83A, a Layered Pyrite + Sphalerite ore exhibiting strong development of both the above textures, are defined by 80% -74um and 80% -37um, respectively, or 50% -13um for both freibergite and galena. Because of the tendency for pyrite to be concentrated in the coarser-grained sieve fractions, much of the galena and freibergite will be unliberated and be recovered in the tailings. Healy & Petruk (1989) found that 41.4% of the Pb was rejected to the tailings (largely as galena locked with pyrite), and 45.6% to the Zn-concentrate (largely as galena locked with sphalerite). The loss of 87% the Pb (hence galena) from the Cu-concentrate implies losses of (1) a minor proportion of the

Ag in the ore hosted in solid solution in galena; and (2) Ag present as inclusions in, and associated grains of freibergite, pyrargyrite, and other Ag-carriers, with galena.

## BIBLIOGRAPHY

- Aggarwal, P. K. & Nesbitt, B. E. (1987): Pressure and temperature conditions of metamorphism in the vicinity of three massive sulfide deposits, Flin Flon-Snow Lake Belt, Manitoba. *Can. J. Earth Sci.* 24, 2305-2315.
- Ahrlrichs, J. W. (1984): Application of quantitative mineralogy for solving metallurgical problems. In *Applied Mineralogy* (W. C. Park, D. M. Hausen & R. D. Hagni, ed.). TMS-AIME, New York, N.Y., ICAM 84, 279-290.
- Bacon, W. G., Hawthorn, G. W. & Poling, G. W. (1989): Gold analyses - myths, frauds and truths. *Can. Inst. Min. Metall. Bull.*, 82, 931, 29-36.
- Bancroft, G. M. & Jean, G. E. (1982): Gold deposition at low temperature on sulphide minerals. *Nature* 298, 730-731.
- Barbery, G. & Leroux, D. (1986): Prediction of particle composition distribution after fragmentation of heterogeneous materials: influence of texture. In *Process Mineralogy VI* (R. D. Hagni, ed.). TMS-AIME, New Orleans, LA., 415-427.
- Barnes, H. L., Romberger, S. B. & Stemprok, M. (1967): Ore solution chemistry II. Solubility of HgS in sulfide solutions. *Econ. Geol.*, 62, 957-982.
- Barton, P. B. Jr. (1978): Some ore textures involving sphalerite from the Furutobe mine, Akita Prefecture, Japan. *Mining Geol.*, 28, 293-300.
- \_\_\_\_\_ & Bethke, P. M. (1987): Chalcopyrite disease in sphalerite: pathology and epidemiology. *Am. Mineral.*, 72, 451-467.
- \_\_\_\_\_ & Skinner, B. J. (1979). Sulfide Mineral Stabilities. In *Geochemistry of Hydrothermal Ore Deposits*, (H. L. Barnes, ed.). 2nd Ed., Holt, Rinehart and Winston, New York. 236-333.
- Basu, K., Bortnykov, N., Mookherjee, A., Mozgova, N. & Tsepina, A. I. (1981): Rare minerals from Rajpura-Dariba, Rajasthan, India II: Intermetallic compound  $Ag_{74.2}Au_{16.4}Hg_{9.4}$ . *Neues Jahrb. Mineral.*, Abh. 141, 217-223.
- Bates, R. L. & Jackson, J. A. (1980). *Glossary of Geology*. 2nd Ed., American Geological Institute, Falls Church, Virginia.
- Boyle, R. W. (1979): The geochemistry of gold and its deposits. *Geol. Surv. Can. Bull.*, 210.

- Cabri, L. J., Cambell, J. L., Laflamme, J. H. G., Leigh, R. G., Maxwell, J. A. & Scott, J. D. (1985): Proton-microprobe analysis of trace elements in sulphides from some massive-sulphide deposits. *Can. Mineral.*, 23, 133-148.
- \_\_\_\_\_, Chryssoulis, S. L., De Villiers, J. P. R., Laflamme, J. H. G. & Buseck, P. R. (1989): The nature of "invisible" gold in arsenopyrite. *Can. Mineral.*, 27, 353-362.
- Cathles, L. M. (1986): The geologic solubility of gold from 200-350°C, and its implications for gold-base metal ratios in vein and stratiform deposits. In *Gold in the Western Shield* (L. A. Clark, ed.). *Can. Inst. Min. Metall. Spec. Vol. 38*, 187-210.
- Chen, T.T. & Petruk, W. (1980): Mineralogy and characteristics that affect recoveries of metals and trace elements from the ore at Heath Steele Mines, New Brunswick. *Can. Inst. Min. Metall. Bull.*, 73, 823, 167-179.
- Chryssoulis, S., Cabri, L. J. & Salter R. S. (1987): Direct determination of invisible gold in refractory sulphide ores (R. S. Salter, D. M. Wyslouzil & G. W. McDonald, eds.). *Proc. Int. Symp. on Gold Metallurgy*, 1. *Proc. Metall. Soc. of the Can. Inst. Min. Metall.*, 235-244.
- \_\_\_\_\_, Chauvin, W. J. & Surges, L. J. (1986): Trace element analysis by secondary ion mass spectrometry with particular reference to silver in the Brunswick sphalerite. *Can. Metall. Quarterly*, 25, 3, 233-239.
- \_\_\_\_\_, Surges, L. J. & Salter R. S. (1985): Silver mineralogy at Brunswick Mining and Smelting and its implications for enhanced recovery. In *Complex Sulfides* (Zunkel, A. D., Boorman, R. S., Morris, A. E. & Wesely, R. J., eds.). *Proc. TMS-AIME*, New York, 815-830.
- Cook, N. J. & Chryssoulis, S. L. (1989): Mineralogy of 'invisible' gold. *Geol. Assoc. Can.-Mineral. Assoc. Can., Program Abstr.* 14, A134.
- Craig, J. R., Ljokjell, P. & Vokes, F. M. (1984): Sphalerite compositional variations in sulfide ores of the Norwegian caledonides. *Econ. Geol.*, 79, 1727-1735.
- \_\_\_\_\_ & Scott, S. D. (1976): Sulfide phase equilibria. In *Sulfide Mineralogy* (P. H. Ribbe, ed.). *Reviews in Mineralogy*, Vol. 1, *Mineral. Soc. of Amer.* CS1-110.
- \_\_\_\_\_ & Vaughan, D. J. (1981): *Ore microscopy and ore petrology*. Wiley Interscience, John Wiley. New York.
- Czamanske, G. K. & Hall, W. E. (1975): The Ag-Bi-Pb-Sb-S-Se-Te mineralogy of the Darwin lead-silver-zinc deposit, southern California. *Econ. Geol.*, 70, 1092-1110.

- Davis, J. C. (1973). *Statistics and data analysis in geology*. John Wiley and Sons, New York.
- Dunn, P. J., Chao, G. Y., Fleischer, M., Ferraiolo, J. A., Langley, R. H., Pabst, A. & Zilczer, J. A. (1985): New mineral names. *Am. Mineral.*, 70, 214-221.
- Duval, D. (1985): Trout Lake a moneymaker. *The Northern Miner*, Oct. 21, 1985, 1-2.
- Eldridge, C. S., Barton, P. B. & Ohmoto, H. (1983): Mineral textures and their bearing on the formation of the Kuroko orebodies. In *The Kuroko and related volcanogenic massive sulphide deposits* (H. Ohmoto & B. J. Skinner, Jr., ed.). *Econ. Geol. Monogr.* 5, 241-281.
- \_\_\_\_\_, Bourcier, W. L. Ohmoto, H. & Barnes, H. L. (1988): Hydrothermal inoculation and incubation of the chalcopyrite disease in sphalerite. *Econ. Geol.*, 83, 978-989.
- Fleischer, M. (1987): *Glossary of mineral species*. 5th Ed., Mineralogical Record, Tucson, Arizona.
- Franklin, J. M., Lydon, J. W. & Sangster, D. F. (1981): Volcanic-associated massive sulfide deposits. In *75th Anniv. Vol.* (B. J. Skinner, Jr., ed.). *Econ. Geol.*, 485-627.
- Gasparrini, C. (1983): The mineralogy of gold and its significance in metal extraction. *Can. Inst. Min. Metall. Bull.*, 76, 851, 144-153.
- \_\_\_\_\_. (1984): The mineralogy of silver and its significance in metal extraction. *Can. Inst. Min. Metall. Bull.* 77, 866, 99-110.
- Graf, J. L., Jr. (1977): Rare earth elements as hydrothermal tracers during the formation of massive sulfide deposits in volcanic rocks. *Econ. Geol.*, 72, 527-548.
- Groat, L. A., Carter, R. T., Hawthorne, F. C. & Ercit, T. S. (1985): Tantalian niobian titanite from Irgon claim, southeastern Manitoba. *Can. Mineral.*, 23, 569-571.
- Hannington, M. D. & Scott S. D. (1988): Gold and silver potential of polymetallic sulfide deposits on the sea floor. *Mar. Mining*, 7, 271-285.
- Harbaugh, J. W. & Merriam, D. F. (1968): *Computer applications in stratigraphic analysis*, Wiley, New York.
- Harris, D. C. (1986): Mineralogy and geochemistry of the main Hemlo gold deposit, Hemlo, Ontario. In *Gold '86* (A. J. MacDonald, ed.). *Proc. Int. Symp. on Geology of Gold*, Toronto.
- \_\_\_\_\_, Sinclair, W. D. & Thorpe, R. I. (1983): Telluride minerals from the Ashley deposit, Bannockburn township, Ontario. *Can. Mineral.*, 21, 137-143.

- Hausen, D. M. (1981): Process mineralogy of auriferous pyritic ores at Carlin, Nevada. In Process Mineralogy I (D. M. Hausen & W. C. Park, eds.). Proc. SME-AIME Conf., New York.
- Hawley, J. E. & Nichol, I. (1959): Selenium in some Canadian sulphides. Econ. Geol., 54, 608-628.
- \_\_\_\_\_ & \_\_\_\_\_ (1961): Trace elements in pyrite, pyrrhotite and chalcopyrite of different ores. Econ. Geol., 56, 467-487.
- Healy, R. E. & Petruk, W. (1987): An image analysis of the liberation of valuable minerals in the Trout Lake concentrator circuit. Proc. 14th Annual Meeting, Microscopical Soc. of Canada, Winnipeg, 36-37.
- \_\_\_\_\_ & \_\_\_\_\_ (1988): The mineral characteristics that affect metal recoveries from Cu, Zn, Pb and Ag ores in Manitoba. Part I, An investigation of the ore mineralogy of the Trout Lake deposit. CANMET Investigation Rep. MSL 88-61(IR).
- \_\_\_\_\_ & \_\_\_\_\_ (1989): The mineral characteristics that affect metal recoveries from Cu, Zn, Pb and Ag ores in Manitoba. Part II, A mineralogical evaluation of the behaviour of metallic minerals in the Trout Lake concentrator circuit. CANMET Investigation Rep. MSL 89-87(IR).
- \_\_\_\_\_ & \_\_\_\_\_ (1990a): The petrology of Au-Ag-Hg alloy and 'invisible' gold in the Trout Lake massive sulfide deposit, Flin Flon, Manitoba. Can. Mineral., 28, 2, 189-206.
- \_\_\_\_\_ & \_\_\_\_\_ (1990b): Gold mineralization of the Trout Lake massive sulphide ores and it's behaviour during mineral beneficiation. In Process Mineralogy IX (W. Petruk, R. D. Hagni, S. Pignolet-Brandom & D. M. Hausen, eds.), TMS-AIME, Warrendale, PA., 229-239.
- \_\_\_\_\_ & \_\_\_\_\_ (In Prep.): Graphic galena-clausthalite solid solution in low-Fe sphalerite from the Trout Lake massive sulfide ores, Flin Flon, Manitoba. CANMET Investigation Rep.
- Hurley, T. D. & Crocket, J. H. (1985): A gold-sphalerite association in a volcanogenic base-metal-sulfide deposit near Tilt Cove, Newfoundland. Can. Mineral., 23, 423-430.
- Huston, D. L. & Large, R. R. (1989): A chemical model for the concentration of gold in volcanogenic massive sulphide deposits. Ore Geol. Reviews 4, 171-200.
- Hutchinson, M. N. & Scott, S. D. (1981): Sphalerite geobarometry in the Cu-Fe-Zn-S system. Econ. Geol., 76, 143-153.
- Jean, G. E. & Bancroft, G. M. (1985): An XPS and SEM study of gold deposition at low temperatures on sulphide mineral surfaces: Concentration of gold by adsorption/reduction. Geochim. Cosmochim. Acta 49, 979-987.

- \_\_\_\_\_ & \_\_\_\_\_ (1986): Heavy metal adsorption by sulfide mineral surfaces. *Geochim. Cosmochim. Acta* 50, 1455-1463.
- Jonasson, I. R. & Sangster, D. F. (1975): Variations in the mercury content of sphalerite from some Canadian sulphide deposits. In (Elliot, I. L. and Fletcher, W. K. ed.), *Geochemical Exploration 1974*, 313-332, Elsevier, Amsterdam.
- Jones, M. P. (1987): *Applied Mineralogy. A quantitative approach.* Graham & Trotman, London.
- Kase, K. (1987): Tin-bearing chalcopyrite from Izumo vein, Toyoha mine, Hokkaido, Japan. *Can. Mineral.*, 25, 9-13.
- Kieft, C., Holmgren, J. & Eriksson, G. (1987): The silver - mercury - antimony minerals of Sala, Sweden. *Can. Mineral.*, 25, 647-658.
- King, R. P. (1979): A model for quantitative estimation of mineral liberation by grinding. *Int. Jour. Mineral Processing*, 6, 207-220.
- Klimpel, R. R. (1984): Some practical approaches to analysing liberation from a binary system. In *Process Mineralogy III* (W. Petruk, ed.). SME-AIME, New York, N.Y., 65-81.
- Ko, C. B. (1986): *Geology of the Trout Lake Copper-Zinc sulphide deposit.* Hudson Bay Mining & Smelting, Internal Rep.
- Kojima, S. & Sugaki, A. (1985): Phase relations in the Cu-Fe-Zn-S system between 500° and 300°C under hydrothermal conditions. *Econ. Geol.*, 80, 158-171.
- Koo, J. (1973): *Origin and metamorphism of the Flin Flon Cu-Zn sulphide deposit, northern Saskatchewan and Manitoba, Canada.* Unpub. Ph.D Thesis, University of Saskatoon, Saskatchewan.
- \_\_\_\_\_ & Mossman, D. J. (1975): *Origin and metamorphism of the Flin Flon stratabound Cu-Zn sulphide deposit, Saskatchewan and Manitoba.* *Econ. Geol.* 70, 48-62.
- Kullerud, G., Yund, R. A. & Moh, G. H. (1969): Phase relations in the Cu-Fe-S, Cu-Ni-S and Fe-Ni-S systems. In (H. D. B. Wilson, ed.). *Magmatic ore deposits.* *Econ. Geol. Mongr.* 3, 126-175.
- Lambert, I. B. & Sato, T. (1974): *The Kuroko and associated ore deposits of Japan: A review of their features and metallogenesis.* *Econ. Geol.*, 69, 1215-1236.
- Large, R. R. (1977): *Chemical evolution and zonation of massive sulfide deposits in volcanic terrains.* *Econ. Geol.*, 72, 549-572.
- Leroux, M., Rao, S. R. & Finch, J. A. (1986). *Selective flotation of sphalerite from Pb-Zn ore without copper activation.* Paper 20.5, *Proceedings of the 25th Annual Conference of Metallurgists, Can. Inst. Min. Metall., Toronto.*

- Loomis, T. P. (1983): Compositional zoning of crystals: a record of growth and reaction history. In *Kinetics and Equilibrium in Mineral Reactions* (S. K. Saxena, ed.). *Advances in physical geochemistry*, Vol. 3, Springer Verlag, New York.
- Mainwaring, P. R. & Petruk, W. (1984): SEM-based automatic image analysis and its use in mineral beneficiation - A review. *CANMET Rep. MSL 84-43*.
- McEachern, N. C. (1987): Trout Lake - Recovery of Au & Ag from mill tailings. Hudson Bay Mining & Smelting, Internal Rep.
- McIntyre, N. S., Cabri, L. J., Chauvin, W. J. & Laflamme, J. H. G. (1984): Secondary ion mass spectrometric study of dissolved silver and indium in sulphide minerals. *Scanning Electron Microsc. III*, 1139-1146.
- Mielke, J. E. (1979): Composition of the Earth's crust and distribution of the elements. In (F. R. Siegel, ed.). *Review of research on modern problems in geochemistry*. Vol. 16, Int. Assoc. of Geochemistry and Cosmochemistry, UNESCO.
- Miller, R. (1981): Kawazulite  $\text{Bi}_2\text{Te}_2\text{Se}$ , related bismuth minerals and selenian covellite from the Northwest Territories. *Can. Mineral.*, 19, 341-348.
- Miller, J. W. & Craig, J. R. (1983): Tetrahedrite-tennantite series compositional variations in the Cofer deposit, Mineral district, Virginia. *Am. Mineral.*, 68, 227-234.
- Milojkovic, D. (1983): Precious metal recovery from Flin Flon Mill Tailings. Progress Report #1. Cyanidation of Trout Lake zinc tailings. Hudson Bay Mining & Smelting, Internal Rep.
- Muzylowski, M. (1979): Copper-Zinc discovery, Flin Flon, Manitoba. *Can. Mining J.* 100, 5, 65-67.
- Nazmova, G. N. & Spiridonov, E. M. (1979): Mercury-rich gold. *Dokl. Acad. Nauk SSSR* 246, 138-141.
- Nysten, P. (1986): Gold in the volcanogenic mercury-rich sulphide deposit Langsele, Skellefte ore district, northern Sweden. *Miner. Deposita* 21, 116-120.
- Oberthur, T. & Saager, R. (1986): Silver and mercury in gold particles from the proterozoic Witwaterstrand placer deposits of South Africa: metallogenic and geochemical implications. *Econ. Geol.* 81, 20-31.
- Ohmoto, H., Mizukami, M., Drummond, S. E., Eldridge, C. S., Pisutha-Arnond, V. & Lenagh, T. C. (1983): Chemical processes of Kuroko formation. In *The Kuroko and related volcanogenic massive sulphide deposits* (H. Ohmoto & B. J. Skinner, Jr., eds.). *Econ. Geol. Monogr.* 5, 570-604.

- Ozerova, N. A., Petsovic, M. S. & Muravitskaja, G. N. (1980):  
Microcontents of mercury as a typomorphic characteristic of gold deposits. In Scientific Bases and Utilization of Typomorphism of Minerals (A. V. Siderenko, ed.). Nauka, Moscow.
- Petruk, W. (1976): The application of quantitative mineralogical analysis of ores to ore dressing. Can. Inst. Min. Metal. Bull., 69, 767, 146-153.
- \_\_\_\_\_ (1985): Applied mineralogy in ore dressing of volcanogenic massive sulphide ores. In Applied Mineralogy (W. C. Park, D. M. Hausen & R. D. Hagni, eds.). Proc. TMS-AIME, New York, N.Y., ICAM 84, 279-290.
- \_\_\_\_\_ (1986): Predicting and measuring mineral liberations in ores and mill products, and effect of mineral textures and grinding methods on mineral liberation. In Process Mineralogy VI (R. D. Hagni, ed.). Proc. TMS-AIME, New Orleans, LA., 393-403.
- \_\_\_\_\_ (1987): Recent developments in process mineralogy of complex sulphide ores. CANMET Rep. MSL 87-1E.
- \_\_\_\_\_ (1988): Automatic image analysis for mineral beneficiation. Journal of Metals 40, 4, 29-31.
- \_\_\_\_\_ (1989a): Image analysis of minerals. In (W. Petruk, ed.). Image analysis applied to mineral and earth sciences. Short Course Notes 16, Mineral. Assoc. Canada, 6-18.
- \_\_\_\_\_ (1989b): Image analysis for mineral beneficiation. In (W. Petruk, ed.). Image analysis applied to mineral and earth sciences. Short Course Notes 16, Mineral. Assoc. Canada, 86-89.
- \_\_\_\_\_, Cabri, L. J., Harris, D. C., Stewart, J. M. & Clark, L. A. (1969): Allargentum, redefined. Can. Mineral., 10, 163-172.
- \_\_\_\_\_ & Mainwaring, P. R. (1985): The MP-SEM-IPS image analysis system. CANMET Rep. MSL 85-12E.
- \_\_\_\_\_, Pinard, R. G. & Finch, J. (1985): Relationship between observed mineral liberations in screened fractions and in composite samples. SME-AIME Annual Meeting New York, N. Y., 1985.
- Pinard, R. G. & Petruk, W. (1989): Silver content of galena from Trout Lake deposit in Flin Flon. CANMET, Process Mineralogy Section Rep. M-4070.
- Pisutha-Arnond, V. & Ohmoto, H. (1983): Thermal history, and chemical and isotopic compositions of the ore-forming fluids responsible for the Kuroko massive sulfide deposits in the Hokuroko district of Japan. In The Kuroko and related volcanogenic massive sulfide deposits (H. Ohmoto, H. & B. J. Skinner, Jr., eds.). Econ. Geol. Monogr. 5, 523-558.

- Price, D. P. (1977): Geology and economic potential of the Flin Flon-Snow Lake Area. Centre for Precambrian Studies, University of Manitoba, 1977 Annual Rep.
- Ramdohr, P. (1980): The ore minerals and their intergrowths. 2 Volumes, 2nd Ed., Int. Series in Earth Sciences, Vol. 35, Pergamon Press, Oxford.
- Riley, J. F. (1974): The tetrahedrite-freibergite series, with reference to the Mount Isa Pb-Zn-Ag orebody. *Min. Deposita*, 9, 117-124.
- Romberger, S. B. (1986): The solution chemistry of gold applied to the origin of hydrothermal deposits. In *Gold in the Western Shield* (L. A. Clark, ed.). *Can. Inst. Min. Metall. Spec. Vol. 7*, 168-186.
- Sangster, D. F. (1972): PreCambrian volcanogenic massive sulphide deposits in Canada, a review: *Geol. Surv. of Canada, Paper 72-22*, 44p.
- Sato, J. (1974): Ores and ore minerals from the Shakanai mine, Akita Prefecture, Japan. *Mining Geology Spec. Issue 6*, 323-335.
- Schmalzried, H. (1974): *Solid state reactions*. Academic Press. New York.
- Scott, J. D. (1977): Interim report on a mineralogical examination of ore specimens from the Centennial mine, Flin Flon, Manitoba. Hudson Bay Mining & Smelting, Internal Rep.
- Scott, S. D. (1983): Chemical behaviour of sphalerite and arsenopyrite in hydrothermal and metamorphic environments. *Mineral. Mag.*, 47, 427-435.
- \_\_\_\_\_ & Barnes, H. L. (1971): Sphalerite geothermometry and geobarometry. *Econ. Geol.*, 66, 653-669.
- Seward, T. M. (1984): The transport and deposition of gold in hydrothermal systems. In *Gold'82: The geology, geochemistry and genesis of gold deposits* (R. P. Foster, ed.). *Geol. Soc. of Zimbabwe Spec. Pub. 1*, 165-181.
- Sharp, Z. D., Essene, E. J. & Kelly, W. C. (1985): A re-examination of the arsenopyrite geothermometer: pressure considerations and applications to natural assemblages. *Can. Mineral.*, 23, 517-534.
- Shikazono, N. (1985): A comparison of temperatures estimated from the electrum-sphalerite-pyrite-argentite assemblage and filling temperatures of fluid inclusions from epithermal Au-Ag vein-type deposits in Japan. *Econ. Geol.*, 80, 1415-1424.
- \_\_\_\_\_ & Shimizu, M. (1987): The Au/Ag ratio of native gold and electrum and the geochemical environment of gold vein deposits in Japan. *Miner. Deposita* 22, 309-314.

- \_\_\_\_\_ & \_\_\_\_\_ (1988): Mercurian gold from the Tsugu gold-antimony vein deposit in Japan. *Can. Mineral.*, 26, 423-428.
- Shimazaki, Y. (1974): Ore minerals of the Kuroko-type deposits. *Mining Geology Spec. Issue* 6, 311-322.
- Springer, J. S. (1983): Invisible gold. In *The Geology of Gold in Ontario* (A. C. Colvine, ed.). *Ont. Geol. Surv. Misc. Pap.* 110.
- \_\_\_\_\_ (1985): Carbon in Archean rocks of the Abitibi belt (Ontario-Quebec) and its relation to gold distribution. *Can. J. Earth Sci.* 22, 1945-1951.
- Stanton, R. L. (1972): *Ore Petrology. International Series in the Earth and Planetary Sciences.* McGraw-Hill, New York.
- Sugaki, A., Kitakaze, A. & Kojima, S. (1987): Bulk compositions of intimate intergrowths of chalcopyrite and sphalerite and their genetic implications. *Miner. Deposita* 22, 26-32.
- \_\_\_\_\_, Scott, S. D., Hayahsi, K. & Kitakaze, A. (1987):  $Ag_2S$  solubility in sulfide solutions up to 250°C. *Geochem. J.* 21, 291-305.
- Syme, E. C., Bailes, A. H., Price, D. P. & Ziehlke, D. V. (1982): *Flin Flon volcanic belt: Geology and ore deposits at Flin Flon and Snow Lake, Manitoba.* *Geol. Assoc. Can.-Mineral. Assoc. Can., Field Trip 6 Guidebook.*
- Vaughan, D. J. & Craig, J. R. (1978): *Mineral Chemistry of Metal Sulfides.* Cambridge University Press, Cambridge.
- Vokes, F. M. (1969): A review of the metamorphism of sulphide deposits. *Earth Sci. Rev.*, 5, 99-13.
- Wells, J. D. & Ghiorso, M. S. (1988): Rock alteration, mercury transport, and metal deposition at Sulphur Bank, California. *Econ. Geol.* 83, 606-618.
- \_\_\_\_\_ & Mullens, T. E. (1973): Gold-bearing arsenian pyrite determined by microprobe analysis, Cortez and Carlin gold mines, Nevada. *Econ. Geol.* 68, 187-201.
- Wiggins, L. B. & Craig, J. R. (1980): Reconnaissance of the Cu-Fe-Zn-S system: Sphalerite phase relationships. *Econ. Geol.*, 75, 742-751.
- Wills, B. A. (1985): *Mineral process technology.* 3rd Ed., *Int. Series on Materials Sciences and Technology*, Vol. 29, Pergamon Press, Oxford.
- Wilson, G. C. & Rucklidge, J. C. (1987): Mineralogy and microstructures of carbonaceous gold ores. *Mineral. Petrol.* 36, 219-239.

Wright, H. D., Barnard, W. M. & Halbig, J. B. (1965): Solid solution in the systems ZnS-ZnSe and PbS-PbSe at 300°C and above. Am. Mineral., 50, 1802-1815.

## Appendix A

### SAMPLE LOCATIONS AND DESIGNATED ORE TYPES

SAMPLE ID.	ZONE	LENS	LOCATION	ORE TYPE
TLN.1-1.	North.	1.	South End, 110m Level.	Banded Py + Sp.
TLN.1-2.	North.	1.	South End, 110m Level.	Cpy Stringers.
TLN.1-3.	North.	1.	South End, 110m Level.	Vein Qtz + Cp.
TLN.1-4.	North.	1.	North End, 110m Level.	(Not Sectioned).
TLN.1-5.	North.	1.	North End, 110m Level.	Cpy Stringers.
TLN.2-6.	North.	2.	North End, 180m Level.	Sheared Cpy + Sp.
TLN.2-7.	North.	2.	North End, 180m Level.	Cpy Stringers.
TLN.2-8.	North.	2.	South End, 245m Level.	Mixed/Banded Cpy + Sp.
TLN.2-9.	North.	2.	South End, 245m Level.	Sheared Cpy + Sp.
TLN.2-10.	North.	2.	North End, 245m Level.	Msv. Cpy + Po.
TLN.2-11.	North.	2.	North End, 245m Level.	Cpy Stringers.
TLN.2-12.	North.	2.	North End, 245m Level.	Sheared Cpy + Sp.
TLN.2-13.	North.	2.	North End, 245m Level.	Sheared Cpy + Sp.
TLS.3-14.	South.	3.	South End, 210m Level.	Cpy Stringers.
TLS.3-15.	South.	3.	South End, 210m Level.	Banded Py + Sp.
TLS.3-16.	South.	3.	North End, 210m Level.	Msv. Cpy + Po.
TLS.3-17.	South.	3.	North End, 210m Level.	Sheared Cpy + Sp.
TLS.3-18.	South.	3.	North End, 210m Level.	Banded Py + Sp.
TLS.3-19.	South.	3.	North End, 210m Level.	Banded Py + Sp.
TLS.3-20.	South.	3.	Centre/North, 210m Level.	Banded Py + Sp.
TLS.3-21.	South.	3.	Centre/North, 245m Level.	Cpy Stringers.
TLS.3-22.	South.	3.	Centre/North, 245m Level.	Cpy Stringers.
TLS.2-23.	South.	2.	North End, 130m Level.	Diss. Py + Cp.
TLS.2-24.	South.	2.	North End, 130m Level.	Banded Py + Sp.
TLS.2-25.	South.	2.	South End, 130m Level.	Msv. Py.
TLS.2-26.	South.	2.	South End, 130m Level.	Banded Py + Sp.
TLN.1-27.	North.	1.	South End, 155m Level.	Banded Py + Sp.
TLN.1-28.	North.	1.	North End, 80m Level.	Banded Py + Sp.
TLN.1-29.	North.	1.	North End, 80m Level.	Msv. Py.
TLN.1-30.	North.	1.	North End, 80m Level.	Msv. Py.
TLN.1-31.	North.	1.	Centre, 80m Level.	Banded Py + Sp.
TLN.1-32.	North.	1.	South End, 80m Level.	Msv. Py.
TLN.1-33.	North.	1.	Centre, 80m Level.	Diss. Py + Cp.
TLS.3-34.	South.	3.	North End, 80m Level.	Diss. Py + Cp.
TLS.3-35.	South.	3.	North End, 80m Level.	Msv. Py.
TLS.3-36.	South.	3.	North End, 80m Level.	Diss. Py + Cp.
TLS.3-37.	South.	3.	North End, 80m Level.	Diss. Py + Cp.
TLS.2-38.	South.	2.	South End, 80m Level.	Msv. Py.
TLS.3-39.	South.	3.	South End, 180m Level.	Cpy Stringers.
TLS.2-40.	South.	2.	Centre, 180m Level.	Msv. Py.

SAMPLE ID.	ZONE	LENS	LOCATION	ORE TYPE
TLS.3-41.	South.	3.	North End, 180m Level.	Banded Py + Sp.
TLS.3-42.	South.	3.	North End, 180m Level.	Msv. Cpy + Po.
TLS.3-43.	South.	3.	North end, 180m Level.	(Not Sectioned).
TLS.1-44.	South.	1.	South End. 180m Level.	Cpy Stringers.
TLS.3-45.	South.	3.	North End, 210m Level.	Banded Py + Sp.
TLS.3-46.	South.	3.	North End. 210m Level.	Msv. Cpy + Po.
TLS.1-47.	South.	1.	South End, 210m Level.	Cpy Stringers.
TLS.1-48.	South.	1.	South End, 210m Level.	Cpy Stringers.
TLS.1-49.	South.	1.	South End, 210m Level.	Msv. Sp.
TLS.1-50.	South.	1.	South End, 210m Level.	Msv. Cpy + Po.
TLS.1-51.	South.	1.	North End, 210m Level.	Msv. Cpy + Po.
TLS.1-52.	South.	1.	North End, 210m Level.	Msv. Py.
TLS.1-53.	South.	1.	North End, 210m Level.	Msv. Py.
TLS.2-54.	South.	2.	North End, 210m Level.	Banded Py + Sp.
TLS.2-55.	South.	2.	South End, 210m Level.	Banded Py + Sp.
TLS.3-56.	South.	3.	South End, 130m Level.	Cpy Stringers.
TLS.3-57.	South.	3.	Centre, 130m Level.	Msv. Sp.
TLS.3-58.	South.	3.	Centre, 130m Level.	Diss. Py + Cp.
TLS.3-59.	South.	3.	Centre, 130m Level.	Cpy Stringers.
TLS.3-60.	South.	3.	Centre/North, 130m Level.	Msv. Sp.
TLS.3-61.	South.	3.	Centre/North, 130m Level.	Cpy Stringers.
TLN.2-62.	North.	2.	South End, 200m Level.	Sheared Cpy + Sp.
TLN.2-63.	North.	2.	South End, 200m Level.	Sheared Cpy + Sp.
TLS.5-64.	South.	5.	Centre, 215m Level.	Msv. Sp.
TLS.2-65.	South.	2.	North End, 210m Level.	Cpy Stringers.
TLS.1-66.	South.	1.	South End, 210m Level.	Banded Py + Sp.
TLS.1-67.	South.	1.	Centre, 210m Level.	Diss. Py + Cp.
TLS.1-68.	South.	1.	Centre, 210m Level.	Msv. Cpy + Po.
TLS.2-69.	South.	2.	Centre, 130m Level.	Msv. Py.
TLS.2-70.	South.	2.	Centre, 130m Level.	Banded Py + Sp.
TLN.1-71.	North.	1.	Centre, 110m Level.	Cpy Stringers.
TLN.1-72.	North.	1.	Centre, 110m Level.	Msv. Sp.
TLN.1-73.	North.	1.	Centre, 110m Level.	Vein Qtz + Cp.
TLN.2-74.	North.	2.	Centre, 245m Level.	Msv. Sp.
TLN.2-75.	North.	2.	Centre, 245m Level.	Mixed/Banded Cpy + Sp.
TLN.2-76.	North.	2.	Centre, 245m Level.	Msv. Cpy + Po.
TLN.2-77.	North.	2.	North End, 245m Level.	(Not Sectioned).
TLN.2-78.	North.	2.	North End, 245m Level.	Mixed/Banded Cpy + Sp.
TLN.2-79.	North.	2.	Centre/North, 245m Level.	Mixed/Banded Cpy + Sp.
TLN.2-80.	North.	2.	South End, 245m Level.	Cpy Stringers.
TLN.2-81.	North.	2.	South End, 245m Level.	Sheared Cpy + Sp.
TLN.2-82.	North.	2.	Centre/North, 245m Level.	Vein Qtz + Cp.
TLN.2-83.	North.	2.	Centre/North, 245m Level.	Msv. Cpy + Po.
TLS.5-83A.	South.	5.	Sec 12+00E, 210m Level.	Msv. Py.
TLS.5-84.	South.	5.	Sec 12+00E, 210m Level.	Banded Py + Sp.
TLS.5-85.	South.	5.	Sec 11+90E, 210m Level.	Msv. Sp.
TLS.5-86.	South.	5.	Sec 11+90E, 210m Level.	Banded Py + Sp.
TLN.1-87.	North.	1.	Centre/South, 105m Level.	Msv. Sp.
TLN.1-88.	North.	1.	Centre/South, 105m Level.	Banded Py + Sp.
TLN.1-89.	North.	1.	Centre/South, 105m Level.	Cpy Stringers.

SAMPLE ID.	ZONE	LENS	LOCATION	ORE TYPE
TLN.1-90.	North.	1.	Centre/South, 105m Level.	Cpy Stringers.
TLN.2-91.	North.	2.	Centre, 240m Level.	Mixed/Banded Cpy + Sp.
TLN.2-92.	North.	2.	Centre, 240m Level.	Sheared Cpy + Sp.
TLS.2-93.	South.	2.	North End, 80m Level.	Banded Py + Sp.
TLS.2-94.	South.	2.	Centre, 80m Level.	Banded Py + Sp.
TLN.2-95.	North.	2.	South End, 255m Level.	Msv. Sp.
TLN.2-96.	North.	2.	South End, 255m Level.	Sheared Cpy + Sp.
TLN.1-97.	North.	1.	Centre, 80m Level.	Banded Py + Sp.
TLN.1-98.	North.	1.	Centre, 80m Level.	Diss. Py + Cp.
TLN.1-99.	South.	1.	North End, 125m Level.	Banded Py + Sp.
TLS.1-100.	South.	1.	North End, 125m Level.	Banded Py + Sp.
TLS.1-101.	South.	1.	North End, 125m Level.	Banded Py + Sp.
TLS.5-102.	South.	5.	Sec 11+81E, 205m Level.	Banded Py + Sp.
TLS.5-103.	South.	5.	Sec 11+81E, 205m Level.	Msv. Sp.
TLS.5-104.	South.	5.	Sec 11+81E, 205m Level.	Banded Py + Sp.
TLS.5-105.	South.	5.	Sec 12+02E, 205m Level.	Banded Py + Sp.
TLS.5-106.	South.	5.	Sec 12+02E, 205m Level.	Msv. Py.
TLS.5-107.	South.	5.	Sec 12+02E, 205m Level.	Banded Py + Sp.
TLS.5-108.	South.	5.	Sec 11+75E, 205m Level.	Banded Py + Sp.
TLS.5-109.	South.	5.	Sec 11+75E, 205m Level.	Banded Py + Sp.
TLS.5-110.	South.	5.	Sec 11+80E, 205m Level.	Banded Py + Sp.
TLS.5-111.	South.	5.	Sec 12+10E, 205m Level.	Banded Py + Sp.
TLN.2-112.	North.	2.	Sec 11+00E, 425m Level.	Sheared Cpy + Sp.
TLN.2-113.	North.	2.	Sec 11+00E, 425m Level.	Sheared Cpy + Sp.
TLN.2-114.	North.	2.	Sec 11+00E, 425m Level.	Mixed/Banded Cpy + Sp.

Appendix B

GRAIN SIZE DISTRIBUTIONS OF THE MINERALS OF INTEREST

TABLE 1.

## GRAIN SIZE DISTRIBUTION OF PYRITE IN THE SUITE OF ORE SAMPLES

Sample	Grain Size (um)												
	-4.6	-6.5	-9.2	-13.0	-18.5	-26.	-37.	-52.	-74.	-104.	-147.	-208.	+208.
TLS.1-49	0.76	1.72	2.98	6.35	7.46	10.3	13.1	19.4	11.4	12.2	7.06	4.79	2.56
TLS.5-64	0.15	0.35	0.38	0.93	1.30	2.95	5.85	7.99	12.5	14.5	19.5	19.4	14.2
TLS.2-25	0.44	0.70	0.95	2.35	2.89	5.83	9.47	13.4	16.8	15.8	12.3	10.5	8.53
TLS.1-52	0.64	1.05	1.48	4.04	4.98	9.70	14.8	19.9	19.0	14.0	7.87	2.17	0.50
TLS.5-83A	1.18	0.58	1.64	1.81	4.45	6.62	10.7	11.9	13.7	13.6	10.4	10.5	13.9
TLS.2-24	0.45	0.64	0.99	2.55	3.25	6.34	9.96	14.1	18.2	16.5	13.8	8.47	4.77
TLS.2-26	0.56	1.20	2.32	6.67	7.96	12.0	15.1	18.5	17.4	9.34	5.83	1.86	1.26
TLS.2-54	0.54	0.84	1.19	3.20	4.00	7.52	13.0	17.8	19.3	14.9	9.33	5.48	2.92
TLS.2-55	0.44	0.67	1.07	2.54	3.53	6.83	11.4	14.1	17.2	16.7	12.0	8.56	4.93
TLN.2-78	7.52	4.68	9.55	8.30	12.1	9.32	9.87	8.89	8.91	8.41	5.68	2.90	3.90
TLN.2-91	5.42	5.91	7.39	25.1	28.1	22.2	5.91	0.00	0.00	0.00	0.00	0.00	0.00
TLS.3-42	0.61	0.64	1.02	3.21	4.24	7.79	11.5	16.3	17.5	15.5	9.02	6.34	6.29
TLN.2-83(#2)	0.43	0.69	0.90	2.62	4.17	7.43	11.7	16.2	17.0	14.6	9.22	9.29	5.79
TLN.1-2	0.41	0.40	0.69	2.06	1.89	4.47	6.19	8.43	14.3	12.7	13.5	13.2	21.8
TLN.2-11	5.23	6.88	9.49	21.3	11.1	12.9	13.6	11.0	3.99	4.40	0.00	0.00	0.00
TLS.2-65	0.30	0.68	1.08	6.62	11.5	12.2	13.9	21.3	12.0	7.28	5.42	6.20	1.59
TLN.1-71	0.30	0.38	0.44	0.91	1.29	2.77	3.56	5.57	9.33	8.77	11.3	10.1	45.3
TLN.1-89	0.40	0.51	0.52	1.16	1.68	2.24	4.10	6.20	12.3	13.5	15.2	15.5	26.6
TLS.2-36(#2)	0.36	0.63	0.87	2.49	3.61	6.63	9.88	12.1	14.0	12.2	13.0	12.4	11.8
TLS.1-67	0.49	1.08	1.59	4.13	5.79	9.79	14.3	19.3	18.4	14.4	7.03	3.21	0.53
TLN.2-62	0.39	0.82	1.90	3.94	6.26	8.90	11.1	14.4	20.9	15.1	8.05	5.65	2.47
TLN.2-63	20.1	6.22	9.97	6.74	4.97	3.69	6.25	5.17	7.94	12.1	11.1	5.78	0.00
TLN.2-96	0.52	0.64	0.82	2.48	4.24	7.34	10.6	14.9	16.8	13.3	10.5	8.36	9.50
TLN.1-3	0.58	0.71	0.88	2.43	3.44	4.54	5.18	11.6	10.3	18.0	7.48	12.0	22.7

TABLE 2.

## GRAIN SIZE DISTRIBUTION OF CHALCOPYRITE IN THE SUITE OF ORE SAMPLES

Sample	Grain Size (um)												
	-4.6	-6.5	-9.2	-13.0	-18.5	-26.	-37.	-52.	-74.	-104.	-147.	-208.	+208.
TLS. 1-49	9.32	11.0	12.7	20.8	13.4	11.1	8.73	7.07	3.37	2.23	0.29	0.00	0.00
TLS. 5-64	17.9	23.5	19.3	18.1	8.70	7.65	3.09	1.85	0.00	0.00	0.00	0.00	0.00
TLN. 2-74	1.09	1.40	1.88	3.74	3.75	5.19	6.81	8.69	11.7	13.6	14.9	12.5	14.7
TLN. 2-95	4.09	6.14	7.88	13.1	8.29	8.15	7.21	8.58	11.1	11.2	9.15	4.49	0.73
TLS. 2-25	16.6	18.0	18.5	22.0	12.6	7.63	2.70	1.97	0.00	0.00	0.00	0.00	0.00
TLS. 1-52	6.03	10.9	14.2	23.5	16.3	15.1	8.43	4.10	0.94	0.52	0.00	0.00	0.00
TLS. 5-83A	20.8	10.3	11.2	13.0	18.6	26.1	0.00	0.00	0.00	0.00	0.00	0.00	0.00
TLS. 2-24	3.86	5.48	6.81	12.8	11.5	13.1	13.0	11.9	9.78	5.91	3.81	1.74	0.33
TLS. 2-26	18.9	17.8	20.2	22.5	6.43	9.45	3.38	1.24	0.00	0.00	0.00	0.00	0.00
TLS. 2-54	11.9	11.7	14.7	24.0	18.8	9.70	5.77	2.07	1.37	0.00	0.00	0.00	0.00
TLS. 2-55	12.9	14.1	14.0	15.3	10.9	8.47	5.32	5.54	3.52	2.46	2.09	2.33	2.99
TLN. 2-78	4.48	1.92	3.94	3.63	6.38	5.57	8.76	8.31	9.78	10.2	10.8	9.55	16.6
TLN. 2-91	1.34	2.02	2.30	4.95	5.16	8.01	8.48	11.4	16.1	13.4	11.7	7.20	8.02
TLS. 3-42	1.15	2.10	2.73	5.53	5.48	7.83	9.43	10.7	11.5	11.2	9.29	8.92	14.1
TLS. 1-50	0.35	0.47	0.58	1.24	1.26	1.93	2.34	3.82	5.05	6.77	8.28	9.90	58.0
TLN. 2-83(#2)	0.87	1.28	1.81	3.79	3.96	6.82	7.38	10.5	14.5	13.8	13.4	12.2	9.74
TLN. 1-2	2.04	2.45	2.38	4.88	4.39	5.74	6.97	8.62	10.1	11.0	12.0	11.6	17.8
TLN. 2-11	2.01	2.63	2.81	5.90	4.87	6.41	6.92	8.73	9.54	12.1	9.92	10.1	18.0
TLS. 2-65	1.14	1.66	1.91	4.63	5.21	8.08	9.98	12.9	14.5	12.3	10.8	10.1	6.87
TLN. 1-71	0.38	0.47	0.53	1.14	1.23	1.71	2.23	3.22	4.69	5.91	7.43	9.27	61.8
TLN. 1-89	0.61	0.87	1.22	2.52	2.36	3.60	4.66	5.74	8.46	8.70	10.3	11.2	39.7
TLS. 2-36(#2)	1.97	2.79	3.21	7.07	5.62	6.60	8.91	9.40	11.4	12.1	14.3	9.65	6.98
TLS. 1-67	2.35	4.03	5.09	10.1	9.06	12.6	12.8	12.9	12.9	8.38	6.69	2.46	0.65
TLN. 2-12	14.5	5.88	10.4	8.43	12.8	11.3	12.2	7.56	6.19	3.71	2.53	1.93	2.61
TLN. 2-62	3.88	5.45	6.10	13.2	11.2	12.8	11.5	12.6	9.92	7.51	3.72	1.23	0.92
TLN. 2-63	3.60	1.51	3.24	3.24	7.56	8.79	11.8	11.4	12.9	11.4	9.66	7.06	7.81
TLN. 2-96	2.26	2.66	3.36	6.80	6.99	10.0	11.3	14.3	14.8	11.8	7.94	4.62	3.20
TLN. 1-3	0.18	0.21	0.24	0.46	0.49	0.80	1.04	1.61	2.57	3.78	5.36	7.45	75.8

TABLE 3.

## GRAIN SIZE DISTRIBUTION OF SPHALERITE IN THE SUITE OF ORE SAMPLES

Sample	Grain Size (um)												
	-4.6	-6.5	-9.2	-13.0	-18.5	-26.	-37.	-52.	-74.	-104.	-147.	-208.	+208.
TLS.1-49	0.23	0.34	0.44	0.85	0.97	1.61	2.07	3.58	5.30	7.81	10.6	10.3	55.9
TLS.5-64	0.10	0.19	0.21	0.63	0.70	1.21	1.73	2.70	5.54	7.92	11.0	15.7	52.3
TLN.2-74	0.22	0.31	0.39	0.91	0.99	1.67	2.55	4.40	7.23	10.3	14.9	19.3	36.8
TLN.2-95	0.20	0.32	0.43	0.83	0.98	2.04	3.06	5.01	7.76	10.2	13.4	14.9	40.8
TLS.2-25	2.57	5.36	7.04	15.4	13.3	16.1	15.3	12.1	7.58	3.59	1.46	0.33	0.00
TLS.1-52	5.12	11.5	13.3	23.6	5.21	14.1	6.78	9.24	11.1	0.00	0.00	0.00	0.00
TLS.5-83A	5.10	2.66	6.09	6.03	10.5	11.6	13.3	12.5	12.8	8.86	5.35	3.79	1.41
TLS.2-24	0.44	0.82	1.15	2.71	3.02	4.90	6.75	9.70	11.9	14.0	12.1	10.5	22.0
TLS.2-26	0.44	0.61	0.80	1.89	2.01	2.93	3.92	6.15	8.48	10.7	13.4	14.0	34.7
TLS.2-54	0.63	1.07	1.52	3.57	3.75	5.51	6.31	9.13	11.2	12.2	10.6	11.0	23.5
TLS.2-55	1.70	2.13	2.38	4.79	4.42	5.92	7.10	9.17	10.8	11.8	10.8	11.3	17.7
TLN.2-78	2.08	1.17	2.20	2.24	4.42	4.35	7.85	6.07	11.6	11.8	16.5	13.2	16.6
TLN.2-91	0.76	1.10	1.41	3.37	3.28	5.28	7.89	11.4	14.7	17.3	15.1	11.6	6.87
TLS.3-42	1.79	3.46	6.05	14.0	11.7	16.6	15.2	15.7	11.4	3.24	0.00	0.96	0.00
TLS.1-50	2.88	3.95	6.92	14.7	11.9	12.5	12.2	7.58	13.0	6.01	8.28	0.00	0.00
TLN.2-83(#2)	1.36	2.59	4.61	9.40	9.90	15.3	11.7	9.07	13.3	7.36	8.32	5.15	2.01
TLN.1-2	0.97	1.17	1.41	3.22	3.20	4.53	6.57	10.4	13.7	13.5	14.7	14.9	11.8
TLN.2-11	4.55	12.1	19.3	31.8	21.0	9.65	0.74	1.00	0.00	0.00	0.00	0.00	0.00
TLS.2-65	4.48	7.77	10.9	19.1	15.8	16.8	8.37	8.48	6.71	1.61	0.00	0.00	0.00
TLN.1-71	4.63	8.62	13.4	23.4	18.5	19.5	10.4	1.60	0.00	0.00	0.00	0.00	0.00
TLN.1-89	2.21	4.68	6.09	13.1	10.4	10.6	11.2	9.92	13.2	7.85	9.11	1.63	0.00
TLS.2-36(#2)	2.26	3.21	3.66	6.43	5.26	7.13	9.52	11.7	13.3	13.2	11.2	3.53	9.61
TLS.1-67	1.66	3.31	3.91	7.69	4.38	14.9	13.4	13.6	14.4	16.8	5.92	0.00	0.00
TLN.2-12	1.10	0.66	1.47	1.61	3.38	4.03	6.37	8.39	12.7	13.9	14.4	12.9	19.1
TLN.2-62	1.01	1.57	2.44	5.28	5.79	8.48	9.52	12.1	15.7	13.2	12.2	8.56	4.19
TLN.2-63	2.39	1.15	2.90	3.87	6.83	7.77	11.5	12.5	13.2	13.0	13.6	6.65	4.76
TLN.2-96	1.83	2.67	3.25	7.12	7.28	10.3	12.5	13.7	15.6	11.2	9.47	3.50	1.61
TLN.1-3	1.17	2.31	3.10	7.15	8.62	9.33	10.5	11.5	14.0	13.2	11.1	4.60	3.46

TABLE 4.

## GRAIN SIZE DISTRIBUTION OF GALENA IN THE SUITE OF ORE SAMPLES

Sample	Grain Size (um)												
	-4.6	-6.5	-9.2	-13.0	-18.5	-26.	-37.	-52.	-74.	-104.	-147.	-208.	+208.
TLS.1-49	2.63	5.66	9.09	18.6	8.89	8.69	12.7	33.7	0.00	0.00	0.00	0.00	0.00
TLS.5-64	2.20	1.16	2.52	2.68	3.69	5.31	7.13	12.2	14.1	17.3	16.8	6.20	8.83
TLN.2-74	5.32	10.1	17.2	29.4	16.0	14.8	2.93	4.39	0.00	0.00	0.00	0.00	0.00
TLN.2-95	1.40	3.35	5.02	9.29	8.98	12.1	13.2	14.4	11.0	11.0	6.58	3.68	0.00
TLS.1-52	7.81	8.05	18.4	23.4	42.3	0.00	0.00	0.00	0.00	0.00	0.00	0.00	0.00
TLS.5-83A	16.0	6.96	13.5	11.2	12.5	11.4	12.7	5.71	3.47	4.08	2.48	0.00	0.00
TLS.2-26	1.81	4.11	5.23	10.1	8.49	10.1	10.4	10.7	10.7	10.2	11.0	5.99	1.81
TLS.2-55	6.44	11.0	14.0	30.3	16.9	19.4	2.10	0.00	0.00	0.00	0.00	0.00	0.00
TLS.2-36(#2)	4.77	6.13	5.62	14.9	15.7	14.1	11.0	6.89	18.3	2.55	0.00	0.00	0.00
TLS.1-67	0.32	1.90	1.90	4.75	10.1	22.8	36.1	22.2	0.00	0.00	0.00	0.00	0.00
TLN.1-3	1.96	27.5	52.9	17.7	0.00	0.00	0.00	0.00	0.00	0.00	0.00	0.00	0.00

Appendix C

CHEMICAL COMPOSITION (MICROPROBE DATA) OF SPHALERITE IN  
UNBROKEN ORE SAMPLES

wt%	S	Zn	Fe	Cu	Cd	Total
1.	33.32	62.17	5.76	----	----	101.26
2.	33.32	59.42	7.25	----	----	99.99
3.	33.54	59.53	7.43	----	0.26	100.76
4.	33.05	60.25	7.45	----	----	100.75
5.	33.12	60.27	6.54	----	0.34	100.27
6.	32.97	59.57	5.87	0.52	0.20	99.13
7.	33.06	59.29	7.39	----	0.08	99.83
8.	33.07	58.94	7.18	----	0.22	99.41
9.	33.14	59.40	6.35	----	0.27	99.16
10.	32.99	59.02	5.85	0.81	0.04	98.70
11.	33.01	58.66	6.91	----	0.48	99.07
12.	33.28	59.61	6.30	----	0.41	99.60
13.	33.15	57.72	7.22	----	0.23	100.33
14.	33.03	57.17	8.10	----	0.47	98.77
15.	33.01	58.69	6.26	----	0.18	99.40
16.	33.07	58.74	6.47	----	0.32	98.59
17.	33.20	61.46	5.37	----	----	100.03
18.	32.81	61.04	5.80	----	0.28	99.93
19.	34.05	59.74	7.27	----	0.39	101.45
20.	33.85	59.57	6.82	----	0.31	100.54
21.	33.12	60.23	5.72	0.63	0.32	100.01
22.	33.18	59.09	6.38	----	0.11	98.75
23.	32.81	63.21	3.75	----	----	99.77
24.	32.76	62.74	4.08	----	0.23	99.81
25.	32.59	62.10	4.83	----	----	99.52
26.	32.24	61.59	4.85	----	0.12	98.81
27.	32.65	59.55	7.06	----	0.07	99.32
28.	32.93	57.85	7.01	----	0.26	98.05
29.	33.39	57.95	7.43	----	----	98.77
30.	33.20	58.24	7.47	----	----	98.91
31.	33.38	57.88	7.46	----	----	98.71
32.	34.52	59.27	8.11	----	----	101.90
33.	33.64	56.73	8.23	----	0.26	98.86
34.	34.08	58.34	8.24	----	0.14	100.80
35.	33.00	63.58	2.30	----	0.41	99.28
36.	33.10	60.26	5.39	0.85	----	99.60
37.	32.80	63.19	1.85	----	0.50	98.34
38.	31.98	60.09	6.40	----	----	98.47
39.	33.35	65.61	1.72	----	0.39	101.08
40.	33.60	58.77	7.75	----	----	100.12

wt%	S	Zn	Fe	Cu	Cd	Total
41.	33.45	58.06	7.71	----	----	99.22
42.	33.36	60.94	6.78	----	----	101.08
43.	32.86	58.87	7.30	----	----	99.03
44.	33.28	58.99	7.90	----	----	100.17
45.	33.65	59.23	7.50	----	0.27	100.65
46.	33.74	60.43	7.19	----	0.15	101.51
47.	33.55	58.68	8.28	----	----	100.51
48.	33.62	59.15	7.05	----	----	99.81
49.	32.86	59.62	6.31	0.82	----	99.61
50.	33.86	58.70	7.58	----	----	100.14
51.	34.01	59.18	6.80	----	0.40	100.38
52.	33.59	59.64	6.75	----	0.13	100.11
53.	33.31	59.46	7.25	----	0.28	100.30
54.	33.27	60.21	6.42	----	----	99.91
55.	33.43	61.53	6.32	----	----	101.28
56.	33.20	58.46	7.87	----	----	99.53
57.	33.44	58.67	7.76	----	----	99.87
58.	33.36	59.97	7.86	----	0.35	101.54
59.	33.26	59.24	7.22	----	0.36	100.07
n = 59						
Mean	33.25	59.76	6.57	0.06	0.16	99.84
Min	32.24	56.73	1.72	----	----	98.05
Max	34.52	65.61	8.24	0.85	0.50	101.90

Appendix D

CHEMICAL COMPOSITION (MICROPROBE DATA) OF SPHALERITE IN  
THE FLOTATION FEED

wt%	S	Fe	Cu	Zn	Cd	Total
1.	33.17	6.90	----	58.61	0.27	98.95
2.	33.12	7.42	----	58.92	0.15	99.61
3.	33.33	7.09	----	59.20	0.35	99.97
4.	33.19	7.93	0.08	57.76	0.43	99.38
5.	33.22	7.94	----	57.98	0.40	99.54
6.	33.20	8.07	----	57.99	0.39	99.66
7.	33.33	6.99	----	60.07	0.55	100.94
8.	33.21	6.91	----	60.10	0.11	100.32
9.	33.07	6.46	----	59.85	0.27	99.65
10.	33.18	7.05	----	58.72	0.23	99.18
11.	33.23	6.66	----	59.14	0.54	99.56
12.	33.11	2.66	----	64.87	0.48	101.11
13.	32.94	7.96	----	57.92	0.11	98.93
14.	33.17	7.93	----	57.14	0.24	98.48
15.	33.01	6.09	0.54	59.18	0.22	99.05
16.	33.15	7.04	----	59.16	0.14	99.49
17.	33.19	7.10	----	58.73	0.36	99.38
18.	33.34	6.87	----	60.46	0.21	100.88
19.	33.23	5.69	----	61.23	0.10	100.25
20.	32.87	7.00	----	59.58	0.20	99.65
21.	33.33	7.23	----	59.44	0.23	100.23
22.	33.24	6.43	----	59.38	0.29	99.33
23.	33.11	6.11	0.30	60.38	0.08	99.99
24.	33.40	7.32	----	59.79	0.27	100.77
25.	33.17	7.44	----	59.07	0.33	100.01
26.	33.18	6.96	----	60.14	0.12	100.40
27.	32.93	5.94	----	60.13	----	98.99
28.	33.00	6.48	0.43	59.93	0.28	100.12
29.	33.51	7.78	----	59.98	0.15	101.42
30.	33.28	7.11	----	60.11	0.37	100.87
31.	32.93	7.28	----	59.15	0.26	99.62
32.	32.91	7.76	----	58.17	0.47	99.31
33.	33.07	6.38	----	59.29	0.31	99.05
34.	32.87	6.74	0.56	58.53	0.40	99.10
35.	32.84	6.92	----	59.11	0.31	99.18

wt%	S	Fe	Cu	Zn	Cd	Total
36.	33.15	6.82	----	59.98	0.30	99.25
37.	32.87	8.19	----	57.23	0.06	98.34
38.	33.24	7.80	----	57.93	0.21	99.17
39.	32.84	6.68	----	58.89	0.25	98.66
40.	33.24	8.37	----	57.26	0.37	99.25
41.	33.30	7.16	0.16	59.18	----	99.80
42.	33.09	6.84	----	59.20	0.20	99.33
43.	33.35	7.46	----	59.45	0.18	100.44
44.	33.19	7.52	----	58.26	0.45	99.42
45.	33.40	7.53	----	58.82	0.45	100.20
46.	32.87	7.02	----	58.26	0.24	98.40
47.	33.02	6.87	----	58.63	0.26	98.78
n = 47.						
Mean	33.14	7.02	0.05	59.20	0.27	99.68
Max	33.51	8.37	0.56	64.87	0.55	101.42
Min	32.84	2.66	----	57.14	----	98.34

Appendix E

AU AND AS CONCENTRATIONS IN PYRITE (SIMS DATA) FROM THE  
TROUT LAKE CONCENTRATOR TAILINGS

Grain No.	Au (ppm)	As (ppm)	Grain No.	Au (ppm)	As (ppm)
6.	0.07	84	53.	0.62	330
10.	0.02	54	54.	4.49	1100
11.	3.00	150	57.	0.52	14
12.	0.02	54	58.	3.49	4100
13.	0.00	340	60.	0.31	50
15.	1.18	125	61.	0.38	39
21.	0.03	42	62.	0.28	1600
23d.	----	630	64.	0.05	145
24.	0.00	640	65.	0.00	500
25.	0.00	105	68.	0.65	470
27.	0.10	200	69.	0.44	72
29.	0.55	570	74.	0.00	115
29a.	0.34	---	79.	0.35	4100
30.	0.16	490	81.	0.76	96
30d.	----	500	83.	0.46	<10
31.	0.27	---	86.	1.52	<10
33.	----	260	87.	1.50	190
44.	0.28	1000	88.	1.08	25
45.	0.00	58	89.	0.98	420
46.	0.00	460	90.	0.24	200
49.	0.00	110	91.	0.32	1050
50.	0.01	350	92.	6.80	410
51.	0.21	370	93.	0.76	1300
52.	0.22	170	94.	0.29	320
			98.	0.22	130

Au: Mean =  $0.72 \pm 0.38$  ppm Au (n = 46)

As: Mean =  $500 \pm 247$  ppm As (n = 47)

Appendix F

AU CONCENTRATIONS IN ARSENOPYRITE (SIMS DATA) IN THE TROUT  
LAKE FLOTATION TAILINGS

Grain No.	Au (ppm)	Grain No.	Au (ppm)	Grain No.	Au (ppm)
1.	68.	28.	23.	66.	27.
2.	19.	31.	30.	67.	26.
3.	112.	31a.	18.	70.	49.
4.	50.	34.	16.	71.	42.
7.	18.	35.	44.	72.	104.
8.	9.7	36.	6.0	73.	16.
9.	19.	37.	3.	80.	12.
14.	26.	38.	7.8	84.	26.
16.	3.7	39.	10.	85.	80.
17.	80.	40.	100.	95.	11.
18.	15.	41.	6.	97.	23.
19.	4.5	42.	33.	100.	2.0
20.	17.	47.	25.		
22.	23.	50.	2.8		
23.	65.	59.	29.	n = 44	
26.	9.5	63.	18.	Mean = 30.2 ± 8.6 ppm Au	

Appendix G

CHEMICAL COMPOSITION (MICROPROBE DATA) OF FREIBERGITE

Anal.	wt%								Number of Atoms						
	S	Fe	Cu	Zn	As	Ag	Sb	Total	S	Fe	Cu	Zn	As	Ag	Sb
1	23.07	5.73	23.82	2.00	0.00	19.17	26.96	100.77	13.00	1.86	6.77	0.55	0.00	3.21	4.00
2	23.82	5.21	27.02	1.46	0.85	15.54	26.51	100.41	13.00	1.63	7.44	0.39	0.20	2.52	3.81
3	24.24	5.88	28.46	1.45	2.83	14.76	23.64	101.27	13.00	1.81	7.70	0.38	0.65	2.35	3.34
4	23.27	5.42	23.96	1.66	1.03	19.44	23.80	98.58	13.00	1.74	6.75	0.45	0.25	3.23	3.50
5	22.55	5.45	17.60	2.02	0.00	26.34	26.18	100.14	13.00	1.81	5.12	0.57	0.00	4.52	3.98
6	22.07	5.35	16.86	1.75	0.00	27.56	26.69	100.26	13.00	1.81	5.01	0.51	0.00	4.83	4.14
7	22.44	5.51	17.45	1.79	0.00	27.78	25.42	100.40	13.00	1.83	5.10	0.51	0.00	4.78	3.88
8	21.79	5.27	17.18	1.54	0.00	28.50	26.17	100.44	13.00	1.81	5.17	0.45	0.00	5.06	4.11
9	23.42	5.67	23.66	1.29	0.43	19.06	27.36	100.89	13.00	1.81	6.63	0.35	0.10	3.14	4.00
10	23.59	5.81	23.35	1.27	0.80	19.59	26.83	101.25	13.00	1.84	6.49	0.35	0.19	3.21	3.89
11	23.63	5.67	23.36	1.46	0.00	18.83	28.10	101.04	13.00	1.74	6.48	0.39	0.00	3.08	4.07
12	22.56	5.53	18.87	1.38	0.00	24.73	27.06	100.15	13.00	1.63	5.49	0.39	0.00	4.24	4.11
13	23.07	5.90	26.10	0.91	0.91	16.90	26.52	100.31	13.00	1.51	7.42	0.25	0.22	2.83	3.94
14	22.92	5.31	24.18	1.47	0.75	18.36	26.87	99.86	13.00	1.73	6.92	0.41	0.18	3.10	4.01
15	22.19	4.83	22.80	2.65	0.00	20.21	26.30	98.97	13.00	1.62	6.74	0.76	0.00	3.52	4.06
16	23.03	5.62	24.12	0.00	0.00	18.97	27.25	98.99	13.00	1.82	6.87	0.00	0.00	3.18	4.05
17	21.77	5.01	18.36	1.37	0.00	25.47	26.47	98.45	13.00	1.72	5.53	0.40	0.00	4.52	4.16
18	21.78	5.47	18.03	0.78	0.00	26.15	27.19	99.39	13.00	1.88	5.43	0.23	0.00	4.68	4.27
19	22.85	4.87	23.27	1.37	0.00	19.69	26.92	98.97	13.00	1.59	6.68	0.38	0.00	3.33	4.03
20	22.70	4.90	23.19	1.76	0.42	18.37	26.99	98.34	13.00	1.61	6.70	0.50	0.11	3.13	4.07
21	22.62	4.98	23.73	1.90	0.00	18.85	26.24	98.33	13.00	1.64	6.88	0.54	0.00	3.22	3.97
22	23.31	5.37	23.06	1.19	0.00	18.73	27.52	99.18	13.00	1.72	6.49	0.32	0.00	3.10	4.04
23	23.48	5.60	23.54	0.65	0.00	19.06	27.28	99.62	13.00	1.78	6.57	0.18	0.00	3.14	3.97
24	23.30	5.46	23.13	1.04	0.00	19.49	27.02	99.45	13.00	1.75	6.51	0.29	0.00	3.23	3.97
25	23.26	5.68	22.76	0.91	0.31	19.69	27.47	100.08	13.00	1.82	6.42	0.25	0.08	3.27	4.04
26	23.29	5.75	22.14	0.31	0.92	20.03	27.72	100.15	13.00	1.84	6.24	0.09	0.22	3.32	3.32
27	23.26	5.72	22.56	2.49	0.68	19.97	26.97	101.64	13.00	1.84	6.37	0.68	0.16	3.32	3.97
28	22.14	5.69	19.50	1.62	0.00	24.65	26.45	100.05	13.00	1.92	5.78	0.47	0.00	4.30	4.09
29	22.41	6.12	21.54	1.16	0.00	20.70	26.55	98.50	13.00	2.04	6.31	0.33	0.00	3.57	4.06
30	22.13	5.87	20.28	0.64	0.00	23.84	26.29	99.06	13.00	1.98	6.01	0.19	0.00	4.16	4.07
31	22.53	5.59	20.37	1.54	0.00	22.22	26.61	98.86	13.00	1.85	5.93	0.44	0.00	3.81	4.04
32	21.97	5.52	18.02	2.26	0.00	25.19	26.15	99.10	13.00	1.88	5.38	0.66	0.00	4.43	4.08
33	21.77	6.52	14.73	1.20	0.00	30.31	26.33	100.85	13.00	2.23	4.44	0.35	0.00	5.38	4.14
34	23.57	5.42	21.83	1.52	0.00	20.52	27.08	99.94	13.00	1.72	6.08	0.41	0.00	3.36	3.93
35	22.76	5.52	19.43	1.26	0.00	24.39	27.01	100.38	13.00	1.81	5.60	0.35	0.00	4.14	4.06
36	21.79	5.95	16.53	0.84	0.00	28.13	25.96	99.20	13.00	2.04	4.98	0.25	0.00	4.99	4.08
37	22.70	5.43	19.88	1.28	0.00	24.27	27.22	100.78	13.00	1.79	5.74	0.36	0.00	4.13	4.10
38	23.04	6.57	19.64	2.01	0.00	23.15	27.20	101.61	13.00	2.13	5.59	0.56	0.00	3.88	4.04
39	22.16	6.04	18.98	1.00	0.00	24.97	26.65	99.81	13.00	2.04	5.62	0.29	0.00	4.36	4.12
40	22.56	5.57	18.40	1.95	0.00	24.96	26.84	100.27	13.00	1.84	5.35	0.55	0.00	4.27	4.07
41	22.48	5.33	19.41	1.46	0.00	23.72	26.93	99.32	13.00	1.77	5.67	0.42	0.00	4.08	4.10
42	22.82	5.42	19.52	2.24	0.00	23.69	26.69	100.38	13.00	1.77	5.61	0.63	0.00	4.01	4.00
43	22.29	5.33	20.30	1.66	0.00	23.67	27.00	100.25	13.00	1.78	5.97	0.48	0.00	4.10	4.15
44	22.30	5.67	19.26	1.53	0.00	24.25	26.65	99.67	13.00	1.90	5.66	0.44	0.00	4.20	4.09
45	22.82	5.52	20.93	1.56	0.00	21.74	27.33	99.89	13.00	1.81	6.02	0.44	0.00	3.68	4.10
46	23.23	5.57	20.92	0.71	0.00	22.87	27.86	101.17	13.00	1.79	5.91	0.20	0.00	3.81	4.11
47	23.31	5.66	20.75	1.80	0.00	22.92	27.38	101.82	13.00	1.81	5.84	0.49	0.00	3.80	4.02
48	21.88	5.34	17.59	1.32	0.00	27.79	24.17	98.09	13.00	1.82	5.27	0.39	0.00	4.91	3.78
49	22.65	6.14	20.41	0.39	0.00	22.69	27.44	99.73	13.00	2.02	5.91	0.11	0.00	3.87	4.15
50	22.84	5.58	19.53	1.73	0.00	24.04	27.36	101.07	13.00	1.82	5.61	0.48	0.00	4.07	4.10
51	21.81	5.59	16.84	1.31	0.00	28.61	25.75	99.91	13.00	1.91	5.07	0.38	0.00	5.07	4.04
52	23.00	5.50	20.72	1.32	0.00	22.01	27.48	100.03	13.00	1.79	5.91	0.37	0.00	3.70	4.09
53	22.77	5.63	24.44	1.21	0.00	18.41	26.07	98.52	13.00	1.84	7.04	0.34	0.00	3.12	3.92
54	23.08	5.45	23.99	1.09	0.48	18.30	25.95	98.38	13.00	1.78	6.82	0.30	0.12	3.06	3.85
55	22.90	5.67	24.45	1.74	0.00	17.77	26.97	99.51	13.00	1.85	7.00	0.49	0.00	3.00	4.03
56	22.87	5.44	24.29	1.58	0.58	18.97	25.62	99.35	13.00	1.77	6.97	0.44	0.14	3.21	3.84
57	22.69	5.28	23.98	1.05	0.25	18.93	25.84	98.02	13.00	1.74	6.93	0.30	0.06	3.23	3.90
58	23.14	6.10	26.46	1.05	0.00	15.51	26.79	99.04	13.00	1.97	7.50	0.29	0.00	2.59	3.96
59	23.05	5.94	27.94	1.65	0.53	13.37	26.37	98.85	13.00	1.93	7.95	0.46	0.13	2.24	3.92
60	24.02	5.98	27.51	1.89	0.00	13.05	27.97	100.42	13.00	1.86	7.52	0.50	0.00	2.10	3.99
Max	24.24	6.57	28.46	2.65	2.83	30.31	28.10	101.82	13.00	2.23	7.95	0.68	0.65	5.38	4.27
Min	21.77	4.83	14.73	0.00	0.00	13.05	23.64	98.02	13.00	1.59	4.44	0.00	0.00	2.10	3.32
Mean (n=60)	22.78	5.58	21.58	1.41	0.20	21.68	26.66	99.82	13.00	1.83	6.18	0.40	0.05	3.70	4.00

## Appendix H

### CHEMICAL COMPOSITION (MICROPROBE DATA) OF AU-AG-HG ALLOY

wt%	Ag	Au	Hg	Fe	Total	Sample
1.	62.37	21.24	16.42	0.24	100.24	TLN.1-89.
2.	63.80	22.85	12.78	0.30	99.70	TLN.1-89.
3.	23.69	74.48	1.61	0.60	100.35	TLN.1-89.
4.	49.42	38.40	13.06	0.01	100.86	TLN.1-89.
5.	54.56	29.95	16.47	0.01	100.97	TLN.1-89.
6.	68.20	20.79	12.28	0.03	101.27	TLN.1-89.
7.	67.35	23.38	10.99	0.17	101.86	TLN.1-89.
8.	22.15	74.27	1.86	0.54	98.80	TLN.1-89.
9.	51.20	32.96	17.59	0.02	101.74	TLN.1-89.
10.	68.70	8.04	22.71	0.01	99.43	TLN.1-89.
11.	48.51	38.75	13.20	0.01	100.46	TLN.1-89.
12.	43.08	44.06	12.81	0.09	100.01	TLN.1-89.
13.	22.68	74.99	3.02	0.30	100.97	TLN.1-89.
14.	22.19	73.06	2.50	0.45	98.17	TLN.1-89.
15.	48.39	38.62	14.82	0.09	101.88	TLN.1-89.
16.	34.56	60.80	2.89	0.88	99.11	TLN.1-89.
17.	65.22	23.30	11.24	0.05	99.78	TLN.1-89.
18.	64.42	10.46	24.49	0.06	99.41	TLN.1-89.
19.	68.37	12.36	19.63	0.04	100.37	TLN.1-89.
20.	20.92	75.71	2.39	0.52	99.52	TLN.1-89.
21.	20.79	74.86	3.42	0.52	99.57	TLN.1-89.
22.	63.25	23.09	14.81	0.07	101.20	TLN.1-89.
23.	20.82	75.32	3.02	0.30	99.43	TLN.1-89.
24.	50.09	33.19	17.00	0.04	100.30	TLN.1-89.
25.	40.17	45.03	12.89	0.09	98.16	TLN.1-89.
26.	67.36	23.30	10.49	0.19	101.32	TLN.1-89.
27.	67.28	22.90	11.65	0.17	101.97	TLN.1-89.
28.	65.90	24.92	10.06	0.48	100.92	TLN.1-89.
29.	60.26	11.61	26.29	1.53	99.66	TLS.1-52.
30.	66.28	1.62	30.87	1.59	100.34	TLS.1-52.
31.	63.74	8.34	26.52	1.57	100.15	TLS.1-52.
32.	47.59	35.24	15.02	2.74	100.57	TLS.1-52.
33.	48.09	36.22	13.98	2.60	100.86	TLS.1-52.
34.	25.08	67.71	5.43	0.32	98.50	TL.MP-12.
35.	17.34	79.86	2.68	0.55	100.40	TL.MP-12.
36.	29.00	60.65	9.42	0.67	99.72	TLN.2-11.
37.	32.19	64.50	3.13	0.59	100.39	TLN.2-11.
38.	30.22	57.02	10.96	0.61	98.79	TLN.2-11.
39.	43.03	43.96	11.80	0.30	99.06	TLN.2-11.
40.	29.98	56.47	12.40	0.38	99.20	TLN.2-11.

wt%	Ag	Au	Hg	Fe	Total	Sample
41.	40.64	53.40	3.52	0.74	98.27	TLN.2-11.
42.	30.28	55.34	13.12	0.31	99.02	TLN.2-11.
43.	32.03	61.02	4.39	0.82	98.23	TLN.2-11.
44.	36.02	58.33	4.79	0.80	99.92	TLN.2-11.
45.	27.85	67.18	1.29	2.20	98.49	TLN.2-11.
46.	34.30	50.25	14.54	0.74	99.80	TLN.2-11.
47.	42.62	50.33	6.84	0.60	100.37	TLN.2-11.
48.	31.53	52.36	14.06	0.92	98.84	TLN.2-11.
49.	36.91	59.31	3.65	0.72	100.57	TLN.2-81.
50.	36.89	57.68	3.65	0.74	98.93	TLN.2-81.
51.	36.96	57.90	3.46	0.40	98.68	TLN.2-81.
52.	54.75	29.08	14.52	1.14	99.46	TLN.2-81.
53.	55.24	30.48	13.76	0.84	100.30	TLN.2-81.
54.	36.99	57.44	3.98	0.66	99.04	TLN.2-81.
55.	37.38	56.51	3.76	0.51	98.16	TLN.2-81.
56.	40.68	51.15	5.14	1.27	98.24	TLN.2-81.
57.	35.63	57.27	5.05	1.69	99.61	TLN.2-81.
58.	53.79	34.13	9.19	1.98	99.07	TLS.5-83A.
59.	54.00	34.34	9.14	1.39	98.84	TLS.5-83A.
60.	54.15	34.62	9.09	1.22	99.05	TLS.5-83A.
61.	54.62	33.73	9.17	1.50	98.99	TLN.2-40.
62.	49.83	31.52	17.89	0.21	99.43	TLN.2-40.
63.	50.11	31.56	17.06	0.19	98.89	TLN.2-40.
64.	49.41	32.19	16.58	0.29	98.44	TLN.2-40.
65.	49.92	32.45	17.10	0.67	100.12	TLN.2-40.
66.	49.93	30.34	17.71	0.51	98.47	TLN.2-40.
67.	53.32	25.46	20.58	0.49	99.82	TLN.2-40.
68.	53.41	25.10	20.16	0.91	99.56	TLN.2-40.
69.	49.89	33.31	17.09	0.43	100.69	TLN.2-40.
70.	50.82	30.17	18.13	0.39	99.48	TLN.2-40.
71.	50.93	31.07	16.08	0.76	99.59	TLN.2-40.
72.	49.87	30.55	18.58	0.39	99.36	TLN.2-8.
73.	60.84	29.40	9.52	1.51	101.24	TLN.2-8.
74.	68.18	23.36	8.10	1.45	101.07	TLN.2-8.
75.	59.40	35.77	2.00	1.63	98.76	TLN.2-8.
76.	60.34	35.79	1.78	1.68	99.74	TLN.2-8.
77.	40.80	49.08	8.23	0.64	98.72	TLN.2-8.
78.	38.07	56.65	3.99	0.53	99.21	TLN.2-8.
79.	55.47	38.83	3.84	0.51	98.63	TLN.2-8.
80.	58.47	36.61	3.62	0.67	99.35	TLN.2-8.
81.	58.24	36.63	3.79	0.56	99.21	TLN.2-8.
82.	57.62	37.28	2.99	1.26	99.13	TLN.2-8.
83.	57.19	37.24	3.62	0.64	98.67	TLN.2-8.
84.	61.25	28.72	9.11	1.59	100.65	TLN.2-8.
Mean	47.08	41.21	10.71	0.70	99.71	(n = 84)
Max	68.70	79.86	30.87	2.74	101.97	
Min	17.34	1.62	1.29	0.00	98.16	

Appendix I

CHEMICAL COMPOSITION (MICROPROBE DATA) OF AU-AG-HG ALLOY  
IN TLN.1-89I

(Cu and S included in element list)

wt%	Ag	Au	Hg	Fe	Cu	S	Total	Dist	Sulfide
85.	72.61	14.09	14.26	nd.	nd.	0.17	101.13	>10	Cp
86.	54.11	22.91	21.16	nd.	nd.	0.09	98.27	>10	Cp
87.	64.19	18.68	16.08	nd.	nd.	0.19	99.14	>10	Cp
88.	76.47	11.17	11.14	nd.	nd.	0.18	98.96	>10	Cp
89.	52.61	40.77	5.46	0.10	0.11	0.22	99.27	>10	Py
90.	51.48	40.86	5.34	0.10	nd.	0.24	98.02	>10	Py
91.	50.74	26.28	20.65	0.11	nd.	0.23	98.01	>10	Py
92.	49.94	31.92	16.45	nd.	nd.	0.19	98.50	>10	Cp
93.	58.96	33.18	7.69	0.12	0.15	0.24	100.35	8	Cp
94.	61.02	29.90	9.84	0.19	0.13	0.20	101.28	5	Cp/Py
95.	58.87	33.90	6.82	0.49	nd.	0.18	100.26	5	Py
96.	58.67	33.90	7.74	0.64	nd.	0.17	101.12	4	Py
97.	58.09	34.53	6.86	0.84	nd.	0.19	100.51	3	Py
98.	53.00	40.11	4.96	0.97	nd.	0.18	99.22	3	Py
99.	58.09	23.34	17.23	0.92	0.25	0.15	99.98	8	Py
100.	55.76	21.99	19.14	1.29	0.09	0.20	98.47	4	Py
101.	59.97	18.23	17.92	1.34	1.74	0.27	99.47	3	Cp
102.	56.16	26.97	13.28	1.95	nd.	0.24	98.60	5	Py
103.	58.79	31.92	7.81	2.30	nd.	0.41	101.23	2	Py
104.	54.26	26.51	14.71	2.61	nd.	0.46	98.55	3	Py
Mean	58.19	28.06	12.23	0.71	0.23	0.22	99.53	(n = 20)	
Mean	49.2	38.7	11.0					(n = 104)	
Max	76.5	79.9	30.9						
Min	17.3	1.62	1.29						

Appendix J

CHEMICAL COMPOSITION (MICROPROBE DATA) OF SPHALERITE AND  
GALENA-CLAUSTHALITE IN TLN.1-87

TABLE 1. CHEMICAL COMPOSITION (MICROPROBE DATA) OF SPHALERITE I

Anal.	wt%					Total.	at%				
	Zn	S	Fe	Cd	Cu		Zn	S	Fe	Cd	Cu
1.	58.7	33.0	7.88	0.06	0.03	99.6	43.4	49.7	6.82	0.03	0.02
2.	58.6	33.0	7.90	0.17	0.01	99.7	43.4	49.7	6.84	0.07	0.00
3.	58.0	33.3	7.78	0.16	0.05	99.2	42.9	50.2	6.74	0.07	0.04
4.	58.6	32.9	7.91	0.14	0.04	99.6	43.4	49.6	6.86	0.06	0.03
5.	59.0	33.0	7.88	0.21	0.05	100.4	43.3	49.8	6.77	0.09	0.04
6.	59.1	33.2	7.42	0.14	0.02	99.9	43.6	49.9	6.41	0.06	0.01
7.	59.0	33.2	7.77	0.08	0.04	100.1	43.4	49.8	6.69	0.03	0.03
8.	58.8	33.5	7.54	0.18	0.01	100.1	43.2	50.2	6.48	0.08	0.01
9.	59.2	33.4	7.87	0.08	0.03	100.6	43.3	49.9	6.74	0.04	0.02
10.	59.0	32.8	6.29	0.12	0.01	98.2	44.3	50.1	5.53	0.05	0.01
n = 10											
Mean	58.8	33.1	7.62	0.13	0.03	99.7	43.4	49.9	6.59	0.06	0.02
StD	0.35	0.24	0.50	0.05	0.02	0.66	0.35	0.21	0.40	0.02	0.01

TABLE 2. CHEMICAL COMPOSITION (MICROPROBE DATA) OF SPHALERITE II

Anal.	wt%					Total.	at%				
	Zn	S	Fe	Cd	Cu		Zn	S	Fe	Cd	Cu
1.	64.4	32.9	1.78	0.36	0.09	99.5	48.1	50.1	1.55	0.16	0.07
2.	65.0	33.3	2.10	0.35	0.05	100.8	47.9	50.1	1.81	0.15	0.04
3.	63.2	32.7	2.72	0.46	0.02	99.1	47.4	50.0	2.39	0.20	0.02
4.	64.7	32.9	2.32	0.47	0.01	100.4	48.0	49.8	2.02	0.20	0.01
5.	64.7	32.9	2.05	0.36	0.05	100.1	48.1	49.9	1.78	0.15	0.03
6.	64.7	32.6	1.92	0.36	0.12	99.7	48.4	49.7	1.68	0.16	0.09
7.	64.4	32.9	1.75	0.34	0.04	99.4	48.2	50.1	1.53	0.15	0.03
8.	63.4	32.9	2.65	0.46	0.09	99.5	47.3	50.1	2.32	0.20	0.07
9.	62.6	32.7	2.70	0.33	0.13	98.5	47.1	50.2	2.38	0.14	0.10
10.	64.8	32.9	1.72	0.29	0.13	99.8	48.3	50.0	1.50	0.12	0.10
11.	65.3	32.8	1.16	0.25	0.24	99.7	48.8	49.9	1.02	0.11	0.18
12.	63.4	32.4	1.76	0.19	0.41	98.1	48.0	50.0	1.56	0.08	0.32
13.	64.2	33.1	2.19	0.30	0.12	99.9	47.7	50.2	1.91	0.13	0.09
14.	64.6	33.0	1.85	0.22	0.07	99.8	48.1	50.2	1.611	0.10	0.05
15.	64.9	33.5	2.04	0.30	0.07	100.8	47.8	50.3	1.76	0.13	0.05
n = 15											
Mean	64.3	32.9	2.05	0.34	0.11	99.7	48.0	50.0	1.79	0.15	0.08
StD	0.77	0.27	0.43	0.08	0.10	0.74	0.44	0.17	0.37	0.04	0.08

TABLE 3. CHEMICAL COMPOSITION (MICROPROBE DATA) OF GALENA-CLAUSTHALITE

Anal.	wt%					at%			
	Pb	Ag	S	Se	Total	Pb	Ag	S	Se
1.	85.9	0.00	13.1	1.37	100.3	49.4	0.00	48.6	2.07
2.	83.4	0.02	10.6	6.36	100.4	49.5	0.02	40.6	9.90
3.	83.5	0.00	10.7	6.40	100.6	49.4	0.00	40.7	9.92
4.	82.6	0.18	10.1	7.51	100.4	49.2	0.20	38.8	11.8
5.	82.7	0.00	10.5	6.77	99.9	49.2	0.00	40.3	10.6
6.	83.3	0.03	10.6	6.46	100.4	49.3	0.03	40.6	10.0
7.	74.5	0.00	2.18	22.9	99.6	50.1	0.00	9.47	40.5
8.	76.6	0.00	4.42	18.4	99.4	50.0	0.00	18.6	31.4
9.	73.9	0.00	2.90	21.0	97.8	50.0	0.00	12.7	37.3
10.	85.3	0.00	13.1	1.24	99.5	49.3	0.00	48.8	1.89
11.	85.3	0.00	11.6	4.53	101.4	49.5	0.00	43.6	6.90
12.	84.8	0.00	11.8	3.74	100.4	49.6	0.00	44.7	5.74
13.	85.3	0.10	11.6	4.56	101.6	49.4	0.11	43.6	6.93
14.	82.6	0.04	11.5	4.94	99.0	48.7	0.05	43.7	7.64
15.	84.7	0.00	11.4	4.86	100.9	49.6	0.00	42.9	7.46
16.	84.6	0.00	11.0	5.45	101.0	49.9	0.00	41.7	8.42
17.	74.9	0.13	2.11	23.1	100.2	50.2	0.16	9.14	40.5
18.	85.8	0.00	13.2	1.21	100.2	49.4	0.00	48.8	1.82
19.	84.4	0.00	11.2	4.56	100.2	50.0	0.00	43.0	7.10
20.	84.8	0.00	11.5	4.27	100.6	49.7	0.00	43.7	6.57
21.	85.0	0.00	11.5	4.49	100.9	49.8	0.00	43.3	6.89
22.	84.4	0.00	11.5	4.42	100.2	49.5	0.00	43.7	6.81
23.	85.2	0.00	11.6	4.63	101.4	49.5	0.00	43.4	7.07
24.	85.1	0.00	11.6	4.26	101.0	49.7	0.00	43.8	6.52
25.	85.9	0.00	13.1	1.21	100.2	49.4	0.00	48.8	1.82
26.	85.9	0.00	13.0	1.29	100.2	49.6	0.00	48.5	1.95
27.	86.5	0.00	13.4	0.59	100.5	49.5	0.00	49.6	0.89
28.	85.1	0.00	12.7	2.13	100.0	49.3	0.00	47.5	3.24
29.	86.5	0.00	12.6	2.14	101.2	49.9	0.00	46.8	3.24
30.	86.0	0.00	12.7	2.20	100.9	49.5	0.00	47.1	3.33
31.	85.1	0.01	12.5	2.18	99.9	49.5	0.01	47.1	3.33
n = 31									
Mean	81.2	0.02	8.80	9.84	99.8	49.5	0.03	33.9	16.5
StD	4.43	0.06	4.06	7.92	0.82	0.35	0.06	14.6	14.3

Appendix K

LETTER OF WAIVER OF COPYRIGHT FROM DR. W. PETRUK

# MINORETEK

Consulting Applied Mineralogy

**Raymond E. Healy, President**  
219 Waterloo Street  
Winnipeg, Manitoba  
R3N 0S4  
(204) 489-3497

27th - Dec - 1990

To whom it may concern,

I the undersigned Dr. W. Petruk grant Raymond E. Healy permission to use all data from any and all published and unpublished papers and reports, jointly co-authored by R. E. Healy and W. Petruk, in the production of a thesis in partial fulfillment of his requirements for a degree of Master of Science.

Sincerely Yours

Dr. W. Petruk